WASM: Mineral, Energy and Chemical Engineering

Heat Transfer Enhancement in a Parabolic Trough Solar Collector (PTSC) Using Passive Technique and Nanofluids/ Hybrid Nanofluids

Hussein A. Mohammed Mohammed

This thesis is presented for the Degree of
Doctor of Philosophy
of
Curtin University

October 2021

Declaration

To the best of my knowledge and belief, this thesis contains no material previously published by another person or other persons, except where due acknowledgment has been made.

This thesis contains no material that has been accepted for an award of any other degree or diploma in any university.

Signature:

Date: 02 / 10 / 2021

Dedication

Every challenging work needs self-efforts as well as guidance of people especially those who are very close to our heart.

My humble effort, I dedicate to my loving,

Father and Mother

Whose affection, endless love, support, encouragement and prayers of day and night make me able to get such success and honor.

My Family

With special thanks to my wife “Dr Shayma” and my daughters “Danyaa and Lana” each of whom has a special place in my heart.

Brothers and Sisters

I am really grateful to all of you. I could not imagine my life without you.

Acknowledgements

Firstly, I would like to thank Curtin University for giving me the opportunity to study a course in Doctor of Philosophy - Chemical and Energy Engineering. I would like to express my sincere gratitude to my supervisors Prof. Hari Vuthaluru & Prof. Shaomin Liu for their continuous support of my PhD study and related research, their patience, motivation and immense knowledge. There guidance helped me at all times during the research journey, and writing of this thesis. I cannot imagine having better advisors and mentors for my PhD study. Without them, my PhD research would not be possible.

I am deeply grateful to my thesis committee chairperson, Prof. San-Ping Jiang, for his insightful comments and encouragement. I would like to thank the rest of my thesis committee members for their advice, assistance, and help.

My sincere thanks also go to my fellow colleagues for the stimulating discussions, the sleepless nights we worked together to meet deadlines and for all the fun, we shared during the years of study.

Last but not the least; I would like to thank my brother and sisters for their endless love and encouragement. My wife (Dr Shayma), words fail me to thank her for her unconditional support and her endless love. My lovely daughters (Danyaa and Lana) for their support spiritually and emotionally throughout the PhD study.

Abstract

Energy demand in the world is continuously increasing and fossil fuels resources must be replaced by renewable resources with lower environmental risk factors, in particular CO_2 emissions. Concentrating solar collectors appear to be very promising for that purpose. In particular, Parabolic Trough Solar Collector (PTSC) is the most proven industry-scale solar generation technology available today. The main principle of PTSC operation is to reflect direct solar radiation from a parabolic reflector that focusses the solar beam radiation on the receiver tube to heat a Heat Transfer Fluid (HTF). The receiver tube is constructed by encasing the metal absorber tube (through which the HTF flows) with a glass envelope; the space between the absorber tube and glass envelope is evacuated in many existing designs. The thermal performance of such devices is of major interest for optimising the solar field output and increase the efficiency of power plants. Available PTSC suffer from low thermal efficiency and low outlet temperature because of using conventional working fluids and ineffective heat transfer and fluid flow characteristics. Using advanced heat transfer fluids (nanofluids/hybrid nanofluids) and utilisation of passive technique (flow turbulators) are two promising ways to solve these problems. A significant amount of research and development has been carried out to improve the PTSC thermal efficiency and entropy reduction. Numerical based approaches, such as Computational Fluid Dynamics (CFD) modelling is used to have an insight of heat transfer characteristics and fluid flow dynamics associated with various types of inserts structure at minimal cost. This approach is expected to provide a broad range of options to enhance the heat transfer and thermal efficiency, which could eventually lead to the optimisation of PTSC features for a given operating conditions. Therefore, this research was conducted to find ways of improving PTSC performance to enhance its thermal and exergetic efficiencies and find an alternative approach to reduce the entropy generation rate.

Although there have been different working fluids and various passive techniques used to enhance the heat transfer in PTSC, which have advantages over the other techniques, there is still room for improvement to make the heat transfer process more effective. PTSC operations are often confronted with challenges associated with low thermal conductivity

of conventional working fluids and thus low heat transfer characteristics and pressure drop penalty associated with the usage of some flow turbulators. To address these issues there is a need to use special inserts and nanofluids/hybrid nanofluids to alter the flow dynamics and heat transfer within the PTSC structure. The first aim of this research was to improve the PTSC receiver's tube thermal and hydraulic characteristics using different shapes of conical ring inserts (convergent and divergent). Various nanofluid types (Al_2O_3, CuO, SiO_2, and ZnO) with 1- 4% volume fraction and particle diameters from 20 -50 nm suspended in a base fluid (water) were tested. The results were obtained via numerical investigations using finite volume method of three-dimensional model. Two different approaches for simulating nanofluids viz., a single-phase and two-phase mixture were implemented. The results revealed that the highest performance enhancement criteria based on the same pumping power is provided by the divergent ring inserts with 365%. The results demonstrated that SiO_2 particles have achieved the highest heat transfer enhancement in terms of Nusselt number and the friction factor. The Nusselt number was enhanced with the increase of the particle volume fraction and Reynolds number, and with the decrease of nanoparticle diameter. It is found that the comparison of calculated results for different models with the experimental and numerical values shows that the two-phase mixture model is more precise than the single-phase model.

The second aim of this research was to use hybrid nanofluids in order to enhance PTSC's thermal and exergetic efficiencies. In this research, a numerical analysis on three-dimensional PTSC receiver's tube model equipped with conical turbulators was conducted. The Navier-Stokes equations were solved using Finite Volume Method (FVM) coupled with Monte Carlo Ray Tracing (MCRT) method. The flow and thermal characteristics as well as entropy generation of the PTSC's receiver tube were investigated. Three hybrid nanofluids (Ag-SWCNT, Ag-MWCNT, and Ag-MgO) having a mixing ratio of (50:50) dispersed in Syltherm oil 800 were used, Reynolds number (5000 to 100000) and fluid inlet temperatures (400 to 650K) were applied. This research revealed that the conical turbulators effectively augmented the thermal performance by 233.4% utilising Ag-SWCNT/Syltherm oil instead of pure Syltherm oil. Furthermore, the maximum reduction in the absorber's average outlet temperature was in the range of 7-

31°C. The performance evaluation criterion is found to be in the range of 0.9-1.82. The thermal and exergetic efficiencies increased by 11.5% and 18.2%, respectively. The maximum decrement in the entropy generation rate and entropy generation ratio are 42.7% and 33.7%.

To further enhance the PTSC's thermal and exergetic performance, the third aim of this research was to use different hybrid nanofluids with wavy promoters. In this research, a numerical analysis on three-dimensional PTSC receiver's tube model equipped with wavy promoters was conducted. The Reynolds number in the range of 5000 to 100000 with four fluid inlet temperatures in the range of 400 to 650K were utilised. Three different hybrid nanofluids (Fe_2O_3-GO, Fe_2O_3-SiC and Fe_2O_3-TiO_2) dispersed in Syltherm oil 800 with various volume fractions in the range of 1-2% were applied inside the PTSC's receiver tube. The effect of nanoparticle shapes (platelets, blades, cylindrical and bricks) was also examined. The numerical outcomes were verified with the available correlations and with other numerical and experimental data available in the open literature. The numerical results revealed that the utilisation of wavy promoters inside the PTSC's receiver tube could significantly augment the thermal performance, where the overall thermal evaluation criterion (PEC) is found to be in the range of 1.24-2.46 using bricks-shaped nanoparticles of Fe_2O_3-GO/Syltherm oil hybrid nanofluids at 2.0% concentration instead of Syltherm oil. The results show that the thermal efficiency increased by 18.51% and the exergetic efficiency increased by 16.21%. The maximum reduction in the entropy generation rate and the entropy generation ratio were about 48.27% and 52.6% respectively. New correlations for Nusselt number, friction factor and thermal efficiency for PTSC tube having wavy promoters using hybrid nanofluids were developed.

In summary, the results of this thesis are of practical significance for industries aiming for heat transfer enhancement techniques and make their heat transfer equipment operations more effective. It is evident that there is a high potential for enhancing the PTSC's absorber tube thermal effectiveness using conical/wavy turbulators and hybrid nanofluids. A higher useful energy output is obtained and less of the available energy is destroyed due to reduced irreversibilities. The developed receiver tubes have the potential to earn an

additional $3 million/annum for a 100 MW PTSC thermal electric power plant, providing a payback period of less than 4.7 years. These receiver tubes can also be used effectively for PTSC solar thermal plants in addition to other PTSC heating applications. The outcomes of this thesis would be beneficial for the thermal solar parabolic trough collector industry in Australia and the globe. Additionally, the findings in this thesis pave new ways for PTSC design of high thermal and exergetic performance and low entropy generation rate. The improvement in PTSC's performance is essential to make energy from CSP systems cost competitive with energy from other sources. With lower energy costs, increased deployment of this technology will be possible and thus ensuring a cleaner and widely available source of energy.

List of Publications

1. **Hussein A. Mohammed**, Ibrahim A. M. Ali Abuobeida, Hari B. Vuthaluru, Shaomin Liu, Two-phase Forced Convection of Nanofluids Flow in Circular Tubes using Convergent and Divergent Conical Rings Inserts, International Communications in Heat and Mass Transfer, Vol. 101, pp. 10-20, 2019 **(Q1, IF=5.683).**

2. **Hussein A. Mohammed**, F. Fathinia, Hari B. Vuthaluru, Shaomin Liu, CFD based Investigations on The Effects of Blockage Shapes on Transient Mixed Convective Nanofluid Flow over a Backward Facing Step, Powder Technology, Vol. 345, pp.608-620, 2019 **(Q1, IF=5.134).**

3. **Hussein A. Mohammed**, Hari B. Vuthaluru, Shaomin Liu, Parabolic Trough Solar Collectors - Thermal and Hydraulic Enhancement Using Passive Techniques and Nanofluids, A Book to be Published by Springer Nature Switzerland, 2022.

4. **Hussein A. Mohammed**, Hari B. Vuthaluru, Shaomin Liu, Heat Transfer Augmentation of Parabolic Trough Solar Collector Receiver's Tube using Hybrid Nanofluids and Conical Turbulators, Journal of the Taiwan Institute of Chemical Engineers, Vol. 125, pp. 215-242, 2021 **(Q1, IF=5.876).**

5. **Hussein A. Mohammed**, Hari B. Vuthaluru, Shaomin Liu, Thermohydraulic and Thermodynamics Performance of Hybrid Nanofluids based Parabolic Trough Solar Collector equipped with Wavy Promoters, Renewable Energy, Vol. 182, pp. 401-426, 2022 **(Q1, IF=8.001).**

List of Contents

List of Figures

List of Tables

Nomenclature

A	Area, m^2
$\boldsymbol{A}$	Surface area vector, m^2
a	Aperture width, m
$\boldsymbol{a}$	Absorption coefficient
a_p, a_{nb}	Linearized coefficients for $\emptyset$ and $\emptyset_{nb}$
A_a	Collector's projected aperture area, m^2
A_c	Collector area, m^2
A_r	Projected absorber tube area, m^2
A_t	Amplitude of wavy promoter, m
Be	Bejan number
C_p	Specific heat capacity, J/kg.K
$C0,C1$	Cells, having centers C0 and C1 respectively
C_1, C_2, C_μ	Turbulent model constants
CR	Concentration ratio
d_f	Equivalent diameter of a base fluid molecule
d_{gi}	Glass envelope inner diameter, m
d_{go}	Glass envelope outer diameter, m
D	Diameter, m
D_h	Hydraulic diameter, m
d_{np}	Nanoparticle diameter, nm
d_{ri}	Absorber tube's inner diameter, m
d_{ro}	Absorber tube's outer diameter, m
Ex_a	Solar radiation exergy rate absorbed, W/m^2
Ex_u	Absorber tube exergy rate, W/m^2
f	Darcy friction factor
F	Heat exchange efficiency factor
$\boldsymbol{F}$	Force vector, N
F_1	First figure of merit
h	Heat transfer coefficient, $W/m^2.K$

h_w	Glass cover heat transfer coefficient, W/m^2.K
I	Radiation intensity
I_b	Direct solar radiation, W/m^2
I_t	Total instantaneous solar radiation, W/m^2
G_k	Generation of turbulence kinetic energy, kg/m.s^3
$\bar{G}$	Average solar radiation, W/m^2
k	Thermal conductivity, W/m.K.
$\boldsymbol{k}$	Turbulent kinetic energy, m^2/s^2
$K(\theta)$	Frequency edge modifier
L	Length of the absorber, m
L_{ent}	Entrance length, m
L_{exit}	Exit length, m
L_{ts}	Test section length, m
$\dot{m}$	Mass flow rate, kg/s
M	Molecular weight, g/mol
N	Avogadro number, mol^{-1}
n	Refractive index
Ns	Entropy generation ratio
Nu	Nusselt number
P	Pressure, Pa
$\bar{P}$	Time-averaged pressure, Pa
P_h	Wetted perimeter, m
P_p	Pumping power, W
P_t	Pitch of waviness, m
Pr	Prandtl number
PEC	Performance evaluation criterion factor
q	Heat transfer rate per unit length, W/m
q''	Heat flux, W/m^2
Q	Useful heat gain, W
Q_{loss}	Heat loss per meter, W/m
Q_u	Useful energy transferred to the heat transfer fluid, W/m^2
Re	Reynolds number

R	Thermal resistance, K/W
r_r	Rim radius (m)
S	Modules of the mean rate-of-strain tensor, 1/s
$\boldsymbol{S}$	Sources of species in fluid, kg/m^3.s
$S_\emptyset$	Sources of transported property
S_{ij}	Rate of linear deformation tensor, 1/s
S_{gen}	Entropy generation rate, W/K
S'''	Entropy rate, W/K
S_{gen}^F	Entropy generation rate due to fluid friction, W/K
S_{gen}^H	Entropy generation rate due to heat transfer, W/K
S_{gen}^T	Total entropy generation rate, W/K
T	Temperature, K
$\bar{T}$	Time-averaged temperature, K
t	Time, s
t_g	Glass outer tube thickness, m
t_r	Absorber inner tube thickness, m
u,v,w	Velocity components, m/s
u_i ,u_j	Velocity fluctuations, m/s
$\bar{u}_i, \bar{u}_j$	Time-averaged velocity component, m/s
u_m	Mean velocity, m/s
u_τ	Friction velocity, $u_\tau = \tau\ w/\rho$, m/s
v_w	Wind velocity, m/s
$\boldsymbol{v}$	Velocity vector
$\dot{V}$	Volumetric flow rate, m^3/s
w_a	Collector's aperture width, m
W_t	Width of wavy promoter, m
x_i, x_j	Spatial coordinates, m
x, y, z	Cartesian coordinates
$y+$	Dimensionless wall coordinate
Y	Mass fraction of species
$-\rho\overline{u'_i u'_j}$	Reynolds stresses, N/m^2

ΔP	Pressure drop, Pa
Greek letters	
α_{abs}	Absorber tube absorptivity
ε	Turbulent dissipation rate, m^2/s^3
$\boldsymbol{\varepsilon}$	Emissivity
ΔT	Circumferential temperature difference, K
θ	Angle of absorber tube circumference, degrees
α, Γ	Thermal diffusivity, m^2/s
α_t, Γ_t	Turbulent thermal diffusivity, m^2/s
β	Fraction of the liquid volume which travels with a particle
γ	Capture factor of the mirror and HCE cooperation
Γ	End-loss factor
σ, K	Stefan-Boltzmann constant, $W/m^2.K^4$
σ_s	Scattering coefficient
σ_ε	Turbulent Prandtl number for ε
σ_k	Turbulent Prandtl number for k
$\sigma_{h,t}$	Turbulent Prandtl number for energy
δ_{ij}	Kronecker delta
ϕ	Nanoparticle volume fraction
ρ	Density, kg/m^3
μ	Viscosity, Pa.s
μ_t	Eddy viscosity, Pa.s
τ	Transmittance of the glass envelope
τ_w	Shear stress, N/m^2
υ	Kinematic viscosity, m^2/s
η	Turbulence model parameter, $S\boldsymbol{k}/\varepsilon$
η_{el}	Electrical efficiency, %
η_{en}	Energetic efficiency, %
η_{ex}	Exergetic efficiency, %
η_o	Optical efficiency, %
η_{th}	Thermal efficiency, %
Φ	Phase function

$\acute{\Omega}$	Solid angle
φ_r	Rim angle
$\emptyset$	Transported property
$\Gamma_\emptyset$	Diffusion coefficient of $\emptyset$, m^2/s
Subscripts	
Abs	Absorber tube
amb	Ambient state
av	Average
b	Bulk fluid state
bf	Base fluid
cond	Conduction
conv	Convection
dp	Dew point
eff	Effective
f	Fluid
f	Focal length (m)
gi	Glass cover inner wall
go	Glass cover outer wall
hnf	Hybrid nanofluid
i	Initial
in	Inlet
i, j, k	General spatial indices
m	Mixture
nf	Nanofluid
out	Outlet
rad	Radiation
ri	Absorber tube inner wall
ro	Absorber tube outer wall
o	Plain or smooth PTSC tube
p	Particle
s	Sun's surface
sky	Sky

t	Turbulent
w	Wavy
Superscripts	
-	Time averaged value
'	Fluctuation from mean value
Acronyms	
Ag	Silver
Al_2O_3	Aluminum oxide
CFD	Computational fluid dynamics
CPC	Compound parabolic collector
CRS	Central receiver systems
CSP	Concentrated solar power
CTC	Cylindrical trough collector
CTD	Circumferential temperature difference
CNT	Carbon nanotubes
CSP	Concentrated solar power
CuO	Copper oxide
DHW	Domestic heating water
DNI	Direct normal irradiance
DSG	Direct steam generation
EES	Engineering equation solver
ETC	Evacuated tube collector
FLC	Fresnel lens collector
FPC	Flat plate collector
FEM	Finite element method
Fe_2O_3	Ferric oxide
FVM	Finite volume method
GO	Graphene oxide
HCE	Heat collection element
HFC	Heliostat filed reflector
HTF	Heat transfer fluid
IPH	Industrial process heat

LFC	Linear fresnel collectors
LFR	Linear fresnel reflector
MCRT	Monte carlo ray tracing
MgO	Magnesium oxide
MWCNT	Multiwall carbon nanotube
NUHF	Non-uniform heat flux
PDC	Parabolic dish collector
PDR	Parabolic dish reflector
PEC	Performance evaluation criterion
PTR	Parabolic trough receiver
PTSC	Parabolic trough solar collector
SBR	Spherical bowl reflector
SEGS	Solar energy generating systems
SPT	Solar power tower
SiC	Silicon carbide
SiO_2	Silicon dioxide
SWCNT	Single wall carbon nanotube
TiO_2	Titanium dioxide
UHF	Uniform heat flux
ZnO	Zinc oxide

Chapter 1 Introduction

1.1 Background and Motivation

Fossil fuel depletion, the carbon dioxide induced global warming problem or climate change has become a pressing issue over the past 30 years, due to the rapidly increasing global population, increase energy demand and growing environmental degradation of burning fossil fuel. In addition, the global commercial low-temperature heat consumption is estimated to be about 10 EJ per year only for hot water production. The industrial energy consumption in the industrialized countries accounts for 30% of the total required energy; and two-thirds of this energy consists of heat. Therefore, the only promising solution to this problem to meet this global heat demand without contributing to climate change and environmental problems implies the utilization of clean and abundant renewable energy resources, such as solar, wind, geothermal energy, fuel cell and etc. which do not generate any emissions. Renewable energies are sustainable by producing zero greenhouse gas emissions and will be always available, so they seem to be the most suitable energy sources for the future (Tzivanidis et al., 2015) [1] and (Coccia et al., 2016) [2]. Among those, solar energy has received considerable attention, because it is a clean and interminable energy source. Utilization of solar energy has become considerable in many processes due to its advantages, such as reduction of the greenhouse gas emissions and cost of the electricity, and prevention of the global warming through reduction of fossil fuels.

In addition, solar energy (or radiant light and heat from the sun) is currently one of the most important sources of free, abundant and inexhaustible energy source with minimal environmental impact. It is also one of the most sustainable ways for facing the modern problems as fossil fuel depletion, climate change, and increasing energy demand [3]. Solar energy is the most promising energy source among the renewables because it can be converted to electricity or to a useful heat. The power from the sun intercepted by the earth is approximately 1.8×10^{11} MW [4]. About 30% of the solar power actually reaches the earth and at every 20 min, the sun produces enough power to supply the earth with its needs for an entire year. In spite of this huge amount of

available solar energy, approximately 80% of energy used worldwide still predominantly comes from fossil fuels such as coal, petroleum and natural gas [5].

Besides, solar energy is exploited in numerous applications, such as domestic hot water, thermal energy for house heating and cooling, space heating, solar cooling, industrial heat production, chemical processes, methanol reforming, desalination and electricity production in the solar power plants (Bellos et al., 2016) [6]. In addition, solar energy has great economic benefits especially in electricity production applications, photovoltaic panels can be used for direct electricity production or the concentrating solar collector can be used for electricity production through a thermodynamic cycle (Organic Rankine Cycle, 'ORC' or Brayton).

1.2 Solar collectors

Solar collectors can be utilized to produce thermal energy from solar energy. Solar thermal collectors are used to increase fluid temperature in both industrial and residential applications, which depends on the configuration of use, heat transfer fluid, generally water or a mixture of water and glycol. There are several types of solar thermal collectors, which all of them have the common principle of capturing solar radiation, converting it to useful heat and transferring it to a working fluid (Kalogirou, 2004) [7]. Solar water heating (SWH) is the conversion of solar radiation into heat for water heating using a solar thermal collector. SWHs are widely used for residential and some industrial applications.

Generally, solar collectors are divided into two categories: stationary (or non-concentrating) collectors and concentrating collectors. Stationary collectors, such as flat-plate collectors, are not able to provide thermal energy for most industrial processes; because these processes require a temperature of about 100 - 240 °C (Marefati et al., 2018) [8]. In order to solve this problem and achieve higher temperatures up to 400 °C, solar concentrators should be used. Among all the methods of utilizing solar energy, large-scale Concentrated Solar Power (CSP) technology is one of the promising and mature options, because the use of highly concentrated solar irradiation provides lower heat losses from smaller areas and consequently higher

attainable temperature at the receivers (Sarwar et al., 2015) [9]. Concentrating technologies exist in four common forms, namely Parabolic Trough Collector (PTC), Parabolic Dish Collector (PDC), concentrating Linear Fresnel Reflector (LFR), and Solar Power Tower (SPT) (Xiangtao et al., 2017) [10]. By using optical collectors, sunlight is redirected, collected, and focused as a high temperature heat source to power a Stirling engine or steam turbine in order to generate electricity (Fuqiang et al., 2016) [11].

Among the four optical collectors' technologies, the parabolic trough solar collector (PTSC) technology in concentrating solar power (CSP) systems is the most mature and widespread technology for the exploitation of solar energy on a large scale. Thus, the PTSC technology has achieved commercial application for several decades due to the advantages of higher power plant efficiency and lower production cost among solar power systems (Hachicha et al., 2013) [12]. For solar thermal power plant with PTSC technology, the evacuated metal tube with a glass cover (or a glass envelope) when used as Parabolic Trough Receiver (PTR) is the critical component for converting the concentrated solar irradiation into heat by conductive and convective coupled heat transfer. PTSCs are able to supply the useful heat with high thermal efficiency with a reasonable investment cost (~200 $\$/m^2$) and they are characterized as cost-effective and mature technologies. There are two ways to use the PTSCs in solar thermal power plants: first, Direct Steam Generation (DSG) technology, which runs a steam turbine by PTSCs direct steam generation, and second, increasing fluid temperature and use it in a heat exchanger. These technologies can be used in all of the steam turbine power plants, like Rankine with superheat, Rankine with regeneration, Rankine with reheat and organic Rankine cycle (Marefati et al., 2018) [8].

1.3 Parabolic Trough Collector (PTC) Description

Parabolic trough solar collectors (PSTC) are systems with light structures and low cost technology that deliver high temperatures with good efficiency. A PTSC consists of a mirror in the shape of a parabolic cylinder to reflect and concentrate sun radiations towards a receiver tube located at the focus line of the parabolic cylinder. By this idea all the solar energy is focused on the tube (Bellos et al., 2016) [13]. It consists of a

metal tube, covered with a glass tube to reduce heat losses, and is placed along the focal line of the receiver as shown in Figure 1.1. One of the pioneer studies on PTSC type of interest here, is the experimental study done by (Dudley et al., 1994) [14], aiming at calculating the thermal performance and heat losses. Furthermore, over the past decade, ever-increasing capabilities have become available for also addressing PTSC systems numerically, in terms of Computational Fluid Dynamics (CFD). The relevant scientific studies focused mainly on two different flow configurations and respective computational domains: one that comprises the absorber tube and the heat transfer fluid, and a second type that addresses the entire PTSC system (absorber tube, heat transfer fluid, glass cover and annulus space between absorber and glass cover) as shown in Figures 1.2-1.3. A typical concentrated solar power plant with PTSC technology is mainly composed by three modules: PTCs, parabolic trough receivers (PTR) and power generation devices (Xu et al., 2015) [15]. The PTC system uses mirrored surfaces of a linear parabolic reflector to focus direct solar radiation onto a tubular solar receiver as shown in Figure 1.1.

Figure 1.1 Parabolic trough collector with receiver (CSP technologies, 2018) [16].

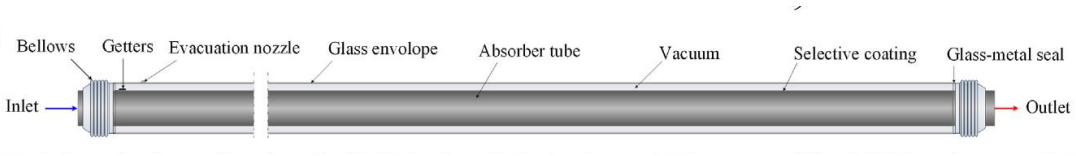

Figure 1.2 Schematic structure of a PTR (Chang et al., 2017) [17].

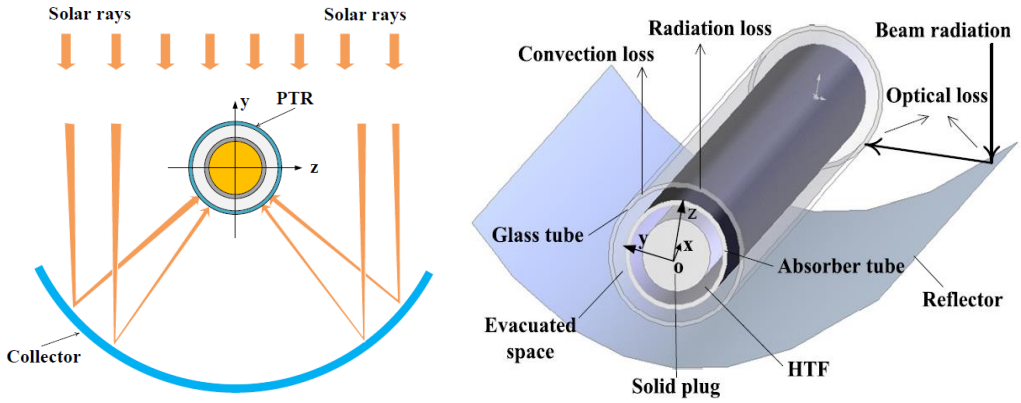

Figure 1.3 Schematic of the physical model of a PTR (Fuqiang et al., 2016) [18].

The receiver is positioned along the focal line of the parabola, and it mainly consists of an absorber tube and a glass cover. The general structure of PTR is an absorber tube (made of metal) surrounded by a glass cover (also named glass envelope), while the annular gap between the absorber tube and glass cover is evacuated as shown in Figure 1.2. In order to absorb the concentrated solar irradiation and decrease the thermal radiation losses effectively, a selective coating is coated on the outer surface of the absorber tube (Wu et al., 2014) [19]. The concentrated solar radiation passes through the glass cover and falls on the outer surface of the metal tube. The metal tube absorbs the concentrated solar radiation and coverts it to heat. The heat is transferred to the Heat Transfer Fluid (HTF) by conductive and convective coupled heat transfer to power steam turbine to generate electricity in turn (Cheng et al., 2015) [20] and (Mwesigye et al., 2013) [21] as shown in Figure 1.3. A small quantity of solar energy is absorbed by the glass cover increasing its temperature slightly during application. A certain amount of energy is released into the environment from the glass cover by natural convection and radiation as shown in Figure 1.4. Therefore, the working process in PTC with tube receiver involves various factors including sunlight concentration and transmission, turbulent flow, conductive, convective, and radiative coupled heat transfer and thermal deformation problems. The whole process of the photo-thermal conversion in the PTC system is very complex, since it includes the physical process of photon energy concentrating, collecting, converting, and coupling nonuniform heat transfers with nonuniform fluid dynamics.

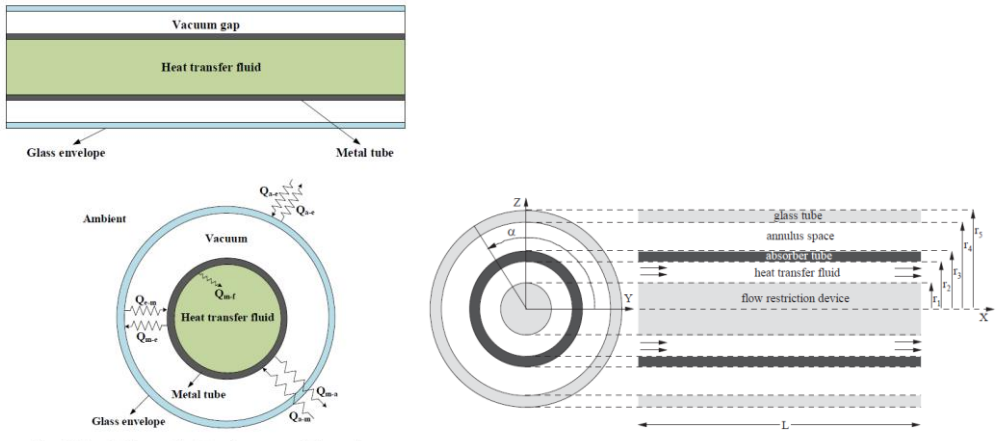

Figure 1.4 Schematic diagram of the heat transfer processes of a PTR (Fuqiang et al., 2016) [18].

It should be noted that the bottom periphery of the PTR is subjected to concentrated solar radiation and the heat flux distribution is highly nonuniform. Whereas the top periphery of the PTR is subjected to low energy density solar irradiation. Therefore, the heat flux distribution on the periphery of the PTR is highly non-uniform, which could induce large high temperature gradients. The large thermal strain, induced by high temperature gradients, can cause the thermal deformations of absorber tube and glass envelope. Due to the large thermophysical and structural property differences between the metal tube and the glass cover, there can be large thermal deformation differences along the longitudinal direction during operation which can induce a rupture in the glass cover (Khanna et al., 2013) [22] and (Patil et al., 2014) [23]. Therefore, the PTR of parabolic trough solar power system is prone to failure during application (Lund, 2003) [24]. Although a series of significant advancements in PTR have been introduced in recent years, the frequently failure of PTR is still a major factor to limit the optimization and application of solar power technologies (Cheng et al., 2012) [25].

Until now, two main methods have been adopted to increase the reliability of PTCs: (1) homogenizing the temperature distribution, and (2) improving the structure of the PTR. Because thermal deformations of the PTC are induced by temperature gradient, homogenizing the temperature distribution on the PTC can effectively minimize the thermal strain and deformation, especially for the metal tube. The temperature gradient on the metal tube can be decreased if the heat transfer performance inside the metal

tube increase, which can benefit for homogenizing the temperature profile of metal tube. On the other hand, improving the structure of the PTR could be made by using surface modification techniques such as corrugation, using inserts, porous materials, vortex generations, etc...

1.4 Working Fluids

The use of PTC in concentrating power plants, in industrial processes, in hydrogen production and in other similar high temperature applications is more and more usual the last years. However, the large temperature gradient is the essential reason of inducing the thermal deformation and damage of PTR. Therefore, many researchers have adopted the method of heat transfer enhancement in absorber tube to decrease the temperature gradient by using different working fluids. The conventional working fluids used in PTC systems such as water, thermal oils and molten salts cannot operate in high temperature levels. Water/steam power plants present important advantages as safety operation, simple storage system and non-toxic working fluid. The limitations of the direct steam generation power plants are based on the need for sophisticated control strategies, as well as on the need for high operating temperatures. The use of thermal oils as Syltherm 800, Therminol VP-1, Therminol 66, Therminol D-12, Marlotherm TH, Sandotherm 59, Dowtherm A and Behran oil is usual in indirect systems with heat exchangers for the heat production. Generally, the thermal oils can operate up to 400 °C with a reasonable pressure level (generally close to 15 bars). However, the use of thermal oils leads to relatively low thermal performance, compared to other working fluids, as well as there is increased maintenance cost. The next generation of working fluids in the CSP plants with PTC is focused on the molten salts (especially nitrate salts) giving higher margin in the solar energy to electricity conversion. Molten salts are usually nitrate salts, for instance (60% $NaNO_3$ - 40% KNO_3), which can easily operate up to 550 °C, giving possibilities for higher thermal efficiency. These working fluids can be exploited as working fluids in PTCs, as well as a storage medium for concentrating solar power plants. However, there is a need for high safety in the operation due to the freezing danger, which can be occurred in temperature levels from 100 - 230 °C. Thus, the molten salts have to be kept upper to a lower limit close to 200 °C due to solidification danger. Other solutions are liquid

metals as sodium and gas working fluids (air, helium, nitrogen and carbon dioxide) for operation at higher temperatures levels without fluid temperature limitation but their operation is not well established yet.

One possible solution to improve the thermal efficiency of such systems could lie in the use of nanofluids as heat transfer fluids. In fact, it is reasonable to expect an increase in the thermal efficiency of PTSCs when the heat transfer base fluid is substituted with a nanofluid of appropriate concentration of nanoparticles. Using nanofluid as a working fluid in solar systems is a novel approach to increase the solar systems efficiency. One of the especially useful applications of nanofluids is in the direct absorption solar collectors where the sunbeams are directly absorbed by the nanofluid. Considering the fact that most base working fluids used in direct absorption solar thermal collectors (e.g., water and ethylene glycol) have low absorption coefficients, it follows that addition of nanoparticles to them not only enhances their optical properties but improves the collector's efficiency as well (Menbari et al., 2017) [26].

Heat transfer can be enhanced by increasing the thermal conductivity of the Heat Transfer Fluid (HTF). It is well-known that the thermal conductivity of metallic particles, metallic oxides and nanotubes is relatively higher than that of liquids. For example, the thermal conductivity of copper at room temperature is about 700 times greater than that of water and about 3000 times greater than that of engine oil. Addition of fine particles (1-100 nm) into heat transfer base fluids (thus forming nanofluids) can significantly increase the heat transfer rate. It is obvious that the research on the applications of nanofluids have been popularized during the recent years. The so called nanofluids, a term which was first introduced by Choi in 1995 at the Argonne National Laboratory, U.S.A (Choi, 1995) [27]. It is also defined as a smart mixture consists from a normal fluid such as (water, engine oil, ethylene glycol, propylene glycol, terpineol, ethanol, glycerol) with a very small amount of solid metallic or metallic oxide nanoparticles (1-100 nm). Nanofluids have significantly improved the fluid thermophysical properties, such as thermal conductivity, viscosity, and convective heat transfer coefficients, compared with conventional fluids.

The most usual nanoparticles are: Al, Al_2O_3, Cu, CuO, TiO_2, SiO_2, Fe, Fe_2O_3, ZnO and Au. The nanofluid was considered as the new generation of advanced heat transfer fluids or a two-phase system, which used for various engineering and industrial applications due to its excellent performance. Some of these applications including nuclear reactors, transportation industry, cooling of transformer oil, electrical energy, mechanical, magnetic, cooling of microchips, improving diesel generator efficiency, solar absorption, microelectronics, paints and coatings, biomedical fields and many other areas where the heat removal is involved. Nanofluids are also called as super-coolant fluids due to their high ability to absorb heat more than any traditional fluids, so they can reduce the size of system and increase its efficiency. The use of these nanoparticles leads to higher thermal conductivity in the flow and consequently to higher heat transfer rate from the warm tube to working fluid, for the case of PTC. Higher heat transfer rate, which means higher heat transfer coefficient, leads to a lower temperature in the collector's absorber and to lower thermal losses, the fact that leads to higher thermal performance (Bellos et al., 2017a) [28]. However, it is essential to determine the heat transfer and the performance enhancement in solar thermal collectors with accuracy in order to evaluate the utilization of nanofluids in solar systems. Thus, a lot of interest has been given in the use of nanofluids as it is among the most efficient working fluids according to the literature studies. The greatest amount of the literature on PTSC includes studies with conventional fluids and mono nanofluids, which include only one dispersed nanoparticle in a base fluid.

1.5 Heat Transfer Passive Techniques

The concept of heat transfer enhancement is quite important and useful in power process, refrigeration, air conditioning, automotive industries etc. In addition to this, heat transfer enhancement techniques are also becoming an important matter of interest in electronics cooling, solar heat collectors, micro chemical processing compact heat exchanger design etc. Generally, heat transfer enhancement techniques may be classified into three main classes i.e., active, passive and compound methods. In active method, external power is used for heat transfer enhancement. It seems an easy method in several applications, however; it is quite complex from design point of view. That is why it is of limited use due to external power requirements as it involves

external power supply. Passive methods utilise energy within the system, which leads to increase fluid pressure drop. The use of special surface geometry gives high thermal performance as compared to plain surface. Twisted tapes, wire coils, dimples, ribs, fins, micro fins, tube with longitudinal inserts, etc. are different passive devices used to enhance heat transfer rate. Compound heat transfer method is a hybrid technique, which involves the use of both active and passive methods. The method is quite complex and have limited applications (Dewan et al., 2004) [29].

The use of twisted tape inserts is one of the important passive methods of heat transfer enhancement. Twisted tapes are generally metallic strips twisted in some specific shape and dimensions and are inserted across the flow. They are also considered as swirl flow devices and act as turbulators used to impart swirl flow, which leads to the increase in heat transfer coefficient. Other techniques focused on geometrical modifications as the use of dimpled absorbers (Huang et al., 2017) [30], the use of internal fins (Bellos et al., 2017b) [28]; (Bellos et al., 2017c) [31] and vortex generators (Cheng et al., 2012) [32]. Moreover, use of inserts in the flow such as porous disks (Ghasemi et al., 2017) [33]; (Satyanarayana, 2008) [34]; Reddy et al., 2015) [35]; (Kumar et al., 2009) [36]; (Kumar et al., 2012) [37]; (Grald et al., 1989) [38], metallic foams, wavy-tape inserts (Zhu et al., 2017) [39], helical coils (Huang et al., 2015) [40]; (Song et al., 2014) [41]; (Muñoz et al., 2011) [42] and perforated plate inserts (Mwesigye et al., 2014) [43]; (Mwesigye et al., 2015) [44] are usually found in the literature, as well as the use of alternative receiver geometries (Okonkwo et al., 2018) [45].

In theory, most of the traditional heat transfer enhancement technologies are also suitable for PTCs because they provide the following advantages: (i) disturb the boundary layer to decrease its thickness and thus decrease the thermal resistance, (ii) increasing flow interruption and thus increase the intensity of turbulence to augment mixing of fluid, (iii) increasing the velocity gradient of fluid near solid walls, and (iv) increase the effective thermal conductivity of fluid due to the high area density and thermal conductivity of the insert's material (Ghasemi et al., 2017) [46]. These techniques have been examined in the literature in order to increase the thermal efficiency of PTC and to make them a more sustainable solution. Moreover, the

circumferential temperature deviation is getting lower with these techniques, the fact that leads to lower thermal stresses and to lower deformation danger (Bellos et al., 2018) [47]. So, the heat augmentation techniques not only increase the thermal efficiency, but also reduce the danger of deformation problems. In this thesis, two heat augmentation techniques are the usage of nanofluids/ hybrid nanofluids as working fluids and the usage of turbulators in the flow were used and thoroughly investigated.

1.6 Research Gap and Novelty

Many techniques have been used to enhance the thermal efficiency, which are mainly focused on the increase of the heat transfer phenomena inside the flow. The use of nanofluids is a recently examined technique, which is under development. The existing experimental results have not fully proved a significant increase in the thermal efficiency of the PTSC and thus they have not been established yet. On the other hand, the use of flow inserts or internal fins in the absorbers of PTSCs is another reliable choice. These techniques aim to increase the mixing of the flow and to create more turbulent conditions in the absorber. However, these techniques lead to high-pressure losses due to the existence of obstacles in the flow. Thus, the thermal enhancement has to be evaluated in every case with proper criteria. Moreover, it is important to state that the use of thermal enhancement techniques decreases the deformation problems in the absorber and in the glass cover, something very important for the lifetime of the PTSCs.

The conventional fluids used as heat transfer medium in solar thermal collectors suffer from poor thermal and heat absorption properties. It was found that these fluids have a limited capacity to carry heat up, which in turn limits the collector's performance. Heat transfer enhancement in solar devices is one of the key issues of energy saving and compact designs. Basically, there are two ways to enhance the heat transfer which involved the use of passive techniques (i.e. surface modifications such as inserts, corrugation, protrusion, addition, fins, etc…) and using additives in base fluids. Recently, as an innovative substance, suspension of nanosized particles has been used in conventional fluids. The fluids with suspended solid particles of nanosized are referred as "nanofluids" (Natarajan et al., 2009) [48]; (Saidur et al., 2011) [49].

Thus, the first aspect of the novelty of this work is that a lot of research has been focused on the evaluation of different modifications with different inserts shapes and configurations in the absorber tubes of PTSCs. However, the studies, which investigate the conical and wavy inserts, are very limited and it is involved conventional fluids. The present study comes to cover this scientific gap and to examine conical and wavy inserts inside the absorbers with different geometrical parameters. This study has high importance for the PTSC design because of the non-uniform heat flux over the absorber, which creates the need for determining the ideal wavy insert locations that would provide the highest thermal efficiency.

Very recently, the term of hybrid nanofluids has been introduced by suspending at least two types of nanoparticles or a composite nanoparticle in a base fluid (e.g. water, ethylene glycol or combinations of these two fluids). Hybrid nanofluids research started around year 2013 and, until now, their development is still in progress. Applications of hybrid nanofluids in renewable energies, especially in solar collectors are extremely low mentioned in the literature and there are very limited technical data available on the usage of hybrid nanofluids in PTSC. Thus, the second novelty of this work is the utilisation of new class of fluid, which is called 'hybrid nanofluids'. The last years, the use of hybrid nanofluids gain more and more attention. These fluids are created by dispersing two kinds of nanoparticles inside the base fluid (e.g. water, ethylene glycol or combinations of these two fluids). The hybrid nanofluid is a homogenous mixture, which presents new physical and chemical bonds, the fact that makes it extremely a promising solution for achieving better heat transfer characteristics. Moreover, it is important to state that the hybrid nanofluids present extra advantages and different hydrodynamic and heat transfer properties, compared to the mono nanofluids due to synergetic effects (Minea et al., 2018) [50]; (Sidik et al., 2016) [51]; (Babu et al., 2017) [52]. Moreover, they give the possibility to utilize cheap nanofluids in order to achieve good thermal properties with a reasonable cost. In the literature, there are very rare studies with hybrid nanofluids implementation in solar collectors. (Menbari et al., 2017) [26] have conducted some studies for the utilization of Al_2O_3-Cu hybrid nanofluid in direct absorption PTCs. (Tahat and Benim, 2017) [53] examined the use of Al_2O_3- CuO in water/ethylene glycol base fluid for operation in

flat plate collector and they found significant thermal enhancement.

Finally, as it is also obvious from the previous paragraphs that the use of mono and hybrid nanofluids in solar collector technologies is a promising and very interesting idea, which is not examined deeply up to today. It also presents many advantages as outlined above and thus it has to be investigated in details in PTSCs. Especially, the examination of hybrid nanofluids in solar collector is practically something new and innovative. On this basis, this study comes to fulfil this scientific gap and to present results about the operation of a PTSC with different hybrid nanofluids. In this thesis, all proposed mono and hybrid nanofluids were evaluated and compared for the operation with pure base fluid in order to determine the thermal efficiency enhancement. The analysis was performed with a developed numerical model using CFD, which was validated with the available numerical or experimental literature.

1.7 Scope and Objectives

Major issues associated with PTC technology are its low thermal efficiency and outlet temperature during normal course of operation. This problem significantly reduces the overall heat transfer, reduces energy harvest from PTC, increases thermal and deformation losses and also has an adverse effect on the PTC useful life period. Therefore, the scope and core objective of this thesis is to improve the heat transfer and fluid flow characteristics as well as the thermal, exergetic efficiencies and the entropy reduction of PTSC based nanofluids/hybrid nanofluids operations. This overarching objective can be broken down into the following specific objectives:

- To develop a 3D computational fluid dynamics model to study the effect of flow restriction device (different inserts conical and wavy tape inserts) on fluid flow and heat transfer characteristics inside a PTSC.
- To utilise the developed model to study the influence of nanofluids consideration using single-phase and two-phase models on the thermal and flow fields of a PTSC's absorber tube.
- To use the developed model to study the effects of nanoparticle type/ combination, volume fraction, nanoparticle shape and inlet fluid temperature on the thermal and flow fields of a PTSC's absorber tube.

- To conduct energy, exergy and entropy analyses to study the influence of the above-mentioned parameters on the PTSC's overall thermal and exergetic performance as well on the entropy generation. Then to propose empirical correlations for the optimum PTSC that provides high thermal, exergetic efficiencies and lowest entropy generation rate based on these analyses.

1.8 Thesis Outline

This thesis contains 7 chapters (including this current chapter) according to the specific objectives as listed above. Each chapter is outlined below:

Chapter 1 provides the background and objectives of the current research.

Chapter 2 includes a comprehensive detailed literature review on the optical, thermal and exergetic analyses along with review of the experimental and numerical studies performed on thermal augmentation methods of PTSCs. This chapter also includes the use of conventional fluids and advanced fluids such as nanofluids and hybrid nanofluids in PTSC. Moreover, the use of passive techniques with different shapes and configurations associated with PTSC is presented in this chapter. Besides, the difficulties and challenges of using nanofluids/hybrid nanofluid-based PTSC frameworks are highlighted in details.

Chapter 3 provides an overview of the research methodology adopted to achieve the research objectives along with the relevant governing equations and the numerical techniques applied.

Chapter 4 presents a numerical study dedicated to the thermal and hydraulic characteristics of turbulent forced convection of nanofluid flow in a PTSC circular tube equipped with different types of conical ring inserts (convergent and divergent). Different nanofluids with different volume fraction and particle diameters are tested. Two different approaches for simulating nanofluids viz., a single-phase and two-phase mixture are implemented.

Chapter 5 provides a numerical analysis on the thermo-hydraulic performance of a PTSC receiver's tube equipped with conical turbulators. The effects of different hybrid nanofluids types, Reynolds number, and fluid inlet temperatures are evaluated on the energetic and exergetic performance as well as the entropy generation rate.

Chapter 6 examines the thermohydraulic and thermodynamic performance of a PTSC receiver's tube equipped with wavy promoters. The effects of hybrid nanofluids, Reynolds number, fluid inlet temperatures, and nanoparticle shape are explored on the energetic and exergetic performance as well as the entropy generation rate.

Chapter 7 summarizes the major findings in this study and gives recommendations for future work in this area.

References

[1] Tzivanidis C., Bellos E., Korres D., Antonopoulos K. A., Mitsopoulos G. Thermal and optical efficiency investigation of a parabolic trough collector. Case Stud Therm Eng 2015; 6: 226–237.

[2] Coccia G., Di Nicola G., Colla L., Fedele L., Scattolini M. Adoption of nanofluids in low-enthalpy parabolic trough solar collectors: Numerical simulation of the yearly yield. Energy Convers Manag 2016; 118: 306–319.

[3] Kreider J. F., Kreith F. Solar energy handbook. New York: McGraw Hill, USA 1981.

[4] Dincer I. Energy and environmental impacts: present and future perspectives. Energy Sources 1998; 20 (4/5): 427–53.

[5] Rosen M. A. The role of energy efficiency in sustainable development. Technol Soc 1996; 15 (4): 21–6.

[6] Bellos E., Tzivanidis C., Antonopoulos K. A., Daniil I. The use of gas working fluids in parabolic trough collectors – An energetic and exergetic analysis. Appl Therm Eng 2016; 109: 1–14.

[7] Kalogirou S. A. Solar thermal collectors and applications. Prog Energy Combust Sci 2004; 30: 231–295.

[8] Marefati M., Mehrpooya M., Shafii M. B. Optical and thermal analysis of a parabolic trough solar collector for production of thermal energy in different climates in Iran with comparison between the conventional nanofluids. J Clean

Prod 2018; 175: 294–313.

[9] Sarwar J., Georgakis G., Kouloulias K., Kakosimos K. E. Experimental and numerical investigation of the aperture size effect on the efficient solar energy harvesting for solar thermochemical applications. Energy Convers Manag 2015; 92: 331–341.

[10] Xiangtao G., Fuqiang W., Haiyan W., Jianyu T., Qingzhi L., Huaizhi H. Heat transfer enhancement analysis of tube receiver for parabolic trough solar collector with pin fin arrays inserting. Sol Energy 2017; 144: 185–202.

[11] Fuqiang W., Qingzhi L., Huaizhi H., Jianyu T. Parabolic trough receiver with corrugated tube for improving heat transfer and thermal deformation characteristics. Appl Energy 2016; 164: 411–424.

[12] Hachicha A. A., Rodríguez I., Capdevila R., Oliva A. Heat transfer analysis and numerical simulation of a parabolic trough solar collector. Appl Energy 2013; 111: 581–592.

[13] Bellos E., Tzivanidis C., Antonopoulos K. A., Gkinis G. Thermal enhancement of solar parabolic trough collectors by using nanofluids and converging-diverging absorber tube. Renew Energy 2016; 94: 213–22.

[14] Dudley V. E., Kearney R., Kolb J. G. SEGS LS2 solar collector-test results. Rep Sandia Natl Lab 1994; SAN94: 1884.

[15] Xu R., Wiesner T. F. Closed-form modeling of direct steam generation in a parabolic trough solar receiver. Energy 2015; 79: 163–76.

[16] CSP technologies, 2018 n.d. https://hub.globalccsinstitute.com/publications/concentrating-solar-power-india/21-csp-technologies Accessed 10 July 2018.

[17] Chang C., Peng X., Nie B., Leng G., Li C., Hao Y., et al. Heat transfer enhancement of a molten salt parabolic trough solar receiver with concentric and eccentric pipe inserts. Energy Procedia 2017: 624–629.

[18] Fuqiang W., Xiangtao G., Jianyu T., Huaizhi H., Bingxi L. Heat transfer performance enhancement and thermal strain restrain of tube receiver for parabolic trough solar collector by using asymmetric outward convex corrugated tube. Energy 2016; 114: 275–92.

[19] Wu L. S., Yuan G., Lei D., Wang Z. Z. Three-dimensional numerical study of heat transfer characteristics of parabolic trough receiver. Appl Energy 2014;

113: 902–911.

[20] Cheng Z. D., He Y. L., Qiu Y. A detailed nonuniform thermal model of a parabolic trough solar receiver with two halves and two inactive ends. Renew Energy 2015; 74: 139–147.

[21] Mwesigye A., Meyer J. P., Bello-Ochende T. Numerical investigation of entropy generation in a parabolic trough receiver at different concentration ratios. Energy 2013; 53: 114–27.

[22] Khanna S., Kedare S. B., Singh S. Analytical expression for circumferential and axial distribution of absorbed flux on a bent absorber tube of solar parabolic trough concentrator. Sol Energy 2013; 92: 26–40.

[23] Patil R. G., Panse S. V., Joshi J. B. Optimization of non-evacuated receiver of solar collector having non-uniform temperature distribution for minimum heat loss. Energy Convers Manag 2014; 85: 70–84.

[24] Lund P. D., Kilpi R. J., Konttinen P. Mechanically manufactured selective solar absorber surfaces. Sol Energy Mater Sol Cells 2003; 79: 273–283.

[25] Cheng Z. D., He Y. L., Cui F. Q., Xu R. J., Tao Y. B. Numerical simulation of a parabolic trough solar collector with nonuniform solar flux conditions by coupling FVM and MCRT method. Sol Energy 2012; 86: 1770–1784.

[26] Menbari A., Alemrajabi A. A., Rezaei A. Experimental investigation of thermal performance for direct absorption solar parabolic trough collector (DASPTC) based on binary nanofluids. Exp Therm Fluid Sci 2017; 80: 218–227.

[27] Choi S. U. S. Enhancing thermal conductivity of fluids with nanoparticles, in: D.A. Siginer, H.P. Wang (Eds.). Dev Appl Non-Newtonian Flows, FED, Vol 231/MD, Vol 66, ASME, New York 1995: 99–103.

[28] Bellos E., Tzivanidis C., Tsimpoukis D. Thermal enhancement of parabolic trough collector with internally finned absorbers. Sol Energy 2017; 157: 514–531.

[29] Dewan A., Mahanta P., Sumithra Raju K., Suresh Kumar P. Review of passive heat transfer augmentation techniques. Proc IMechE Part A J Power Energy 2004; 218: 509–527.

[30] Huang Z., Li Z. Y., Yu G. L., Tao W. Q. Numerical investigations on fully-developed mixed turbulent convection in dimpled parabolic trough receiver tubes. Appl Therm Eng 2017; 114: 1287–1299.

[31] Bellos E., Tzivanidis C., Tsimpoukis D. Multi-criteria evaluation of parabolic trough collector with internally finned absorbers. Appl Energy 2017; 205: 540–561.

[32] Cheng Z. D., He Y. L., Cui F. Q. Numerical study of heat transfer enhancement by unilateral longitudinal vortex generators inside parabolic trough solar receivers. Int J Heat Mass Transf 2012; 55: 5631–5641.

[33] Ghasemi S. E., Ranjbar A. A. Numerical thermal study on effect of porous rings on performance of solar parabolic trough collector. Appl Therm Eng 2017; 118: 807–816.

[34] Reddy K. S., Kumar K. R., Satyanarayana G. V. Numerical investigation of energy-efficient receiver for solar parabolic trough concentrator. Heat Transf Eng 2008; 29: 961–972.

[35] Reddy K. S., Kumar K. R., Ajay C. S. Experimental investigation of porous disc enhanced receiver for solar parabolic trough collector. Renew Energy 2015; 77: 308–19.

[36] Reddy K. S, Kumar K. R. Thermal analysis of solar parabolic trough with porous disc receiver. Appl Energy 2009; 86: 1804–1812.

[37] Kumar K. R., Reddy K. S. Effect of porous disc receiver configurations on performance of solar parabolic trough concentrator. Heat Mass Transf 2012; 48: 555–571.

[38] Gerald E. W., Kuehn T. H. Performance Analysis of a parabolic trough solar collector with a porous absorber receiver. Sol Energy 1989; 42: 281–92.

[39] Zhu X., Zhu L., Zhao J. Wavy-tape insert designed for managing highly concentrated solar energy on absorber tube of parabolic trough receiver. Energy 2017; 141: 1146–55.

[40] Li Z. Y., Huang Z., Tao W. Q. Three-dimensional numerical study on turbulent mixed convection in parabolic trough solar receiver tube. Energy Procedia 2015; 75: 462 – 466.

[41] Song X., Dong G., Gao F., Diao X., Zheng L., Zhou F. A numerical study of parabolic trough receiver with nonuniform heat flux and helical screw-tape inserts. Energy 2014; 77: 771–82.

[42] Muñoz J., Abánades A. Analysis of internal helically finned tubes for parabolic trough design by CFD tools. Appl Energy 2011; 88: 4139–4149.

[43] Mwesigye A., Meyer J. P., Bello-Ochende T. Heat transfer and thermodynamic performance of a parabolic trough receiver with centrally placed perforated plate inserts. Appl Energy 2014; 136: 989–1003.

[44] Mwesigye A., Bello-Ochende T., Meyer J. P. Multi-objective and thermodynamic optimisation of a parabolic trough receiver with perforated plate inserts. Appl Therm Eng 2015; 77: 42–56.

[45] Okonkwo E. C., Abid M., Ratlamwala T. A. H. Effects of synthetic oil nanofluids and absorber geometries on the exergetic performance of the parabolic trough collector. Int J Energy Res 2018: 1–16.

[46] Ghasemi S. E., Ranjbar A. A. Effect of using nanofluids on efficiency of parabolic trough collectors in solar thermal electric power plants. Int J Hydrogen Energy 2017; 42: 21626–34.

[47] Bellos E., Tzivanidis C. Thermal analysis of parabolic trough collector operating with mono and hybrid nanofluids. Sustain Energy Technol Assessments 2018; 26: 105–115.

[48] Natarajan E., Sathish R. Role of nanofluids in solar water heater. Int J Advan ManufactTechn 2009: 3–7.

[49] Saidur R., Leong K. Y., Mohammed H. A. A review on applications and challenges of nanofluids. Renew Sust Energy Rev 2011; 15: 1646–1668.

[50] Minea A. A., El-Maghlany W. M. Influence of hybrid nanofluids on the performance of parabolic trough collectors in solar thermal systems: Recent findings and numerical comparison. Renew Energy 2018; 120: 350–64.

[51] Sidik N. A. C., Adamu I. M., Jamil M. M., Kefayati G. H. .R, Mamat R., Najafi G. Recent progress on hybrid nanofluids in heat transfer applications: a comprehensive review. Int Commun Heat Mass Transf 2016; 75: 68–79.

[52] Ranga Babu J. A., Kumar K. K., Rao S. S. State-of-art review on hybrid nanofluids. Renew Sustain Energy Rev 2017; 77: 551–65.

[53] Tahat M. S., Benim A. C. Experimental analysis on thermophysical properties of Al_2O_3/CuO hybrid nanofluid with its effects on flat plate solar collector. Defect Diffus Forum 2017; 374: 148–56.

Chapter 2 Literature Review

2.1 Introduction

Solar energy exploitation is considered one of the most encouraging solutions for solving the current energy management and environmental problems. Solar Concentrating Technologies (SCT) can provide valuable heat in different temperature levels for various applications such as industrial heat, space-cooling, chemical processes and power generation. Thermal oils, molten metals, several gases, nanofluids or recently reported hybrid nanofluids can be applied as one of the best ways for upgrading the exhibition of the sun-powered collectors. Among different sun-powered collectors, the Parabolic Trough Solar Collector (PTSC) is viewed as the best alternative for moderate temperature range (150-400 °C). PTSC is one of the mature technologies to harness solar energy for various usages such as power generation systems. The popularity of PTSC technology has generated wide interest due to its higher efficiency energy recovery potential. Many approaches have been tried to improve the thermal transport process in the recipient tube section of a PTSC, which involve passive techniques and a variety of working fluids. The objective of this chapter is to provide a comprehensive review of the experimental and numerical studies performed on thermal augmentation methods in PTSCs frameworks. The structure of this chapter includes overviews on PTSC types and enhancement methods, thermal performance analysis of PTSC with passive techniques and new fluids candidates (conventional fluids and advanced fluids such as nanofluids and hybrid nanofluids) for high thermohydraulic performance. Then the limitations of incorporating nanofluids into PTSCs, its difficulties and implementation of these fluids in PTSC frameworks are also highlighted.

The contents of this chapter are to be published in a Book by Springer Nature Switzerland, 2022.

2.2 Solar Energy

The sun radiation has high-temperature, and high-exergy energy source, where the amount of its irradiance is approximately about 63 MW/m^2. Notwithstanding, its configuration drastically diminishes the sun-oriented energy on the earth's surface down to approximately about 1 kW/m^2 (Romero and Zarza, 2004) [1]. In any case, under high sunlight flux-based motion, this problem can be solved by utilising solar systems of concentrating type, which change sun-oriented energy into thermal energy. Sun-based radiation can be changed over into helpful thermal energy by solar thermal and electrical processes respectively. Solar concentrating collectors or flat plate collectors are good examples of sun-powered thermal processes, which could be used to transform sun-oriented radiation into valuable heat. Solar concentrating collector systems can be classified based on center configuration (point-center concentrators) such as central receiver systems (CRS) and parabolic dishes (PD), where the collector packs sunlight-based radiation in a point picture to recipient tube, or based on line-centre concentrators such as parabolic-trough collectors (PTCs) and linear Fresnel collectors (LFC), where the collector amasses sun-powered radiation in a direct picture to recipient tube as appeared in Figure 2.1.

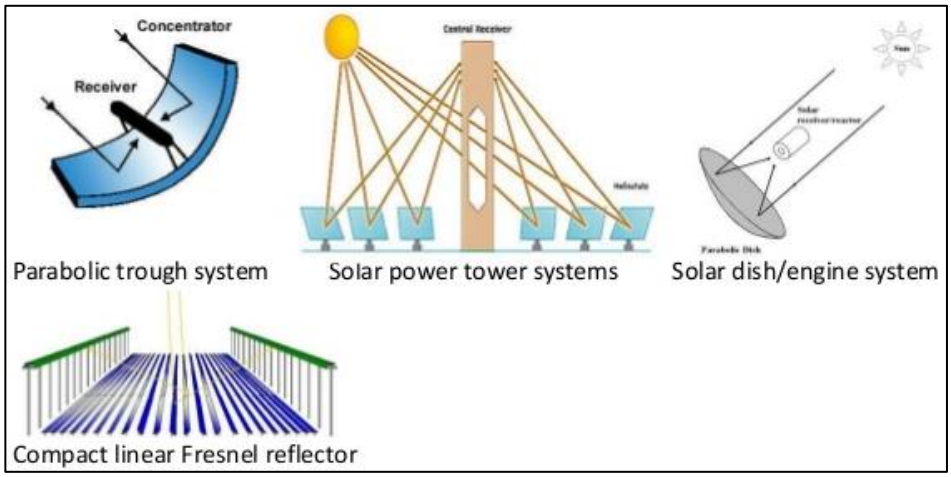

Figure 2.1 Types of Solar thermal power plants (CSP technologies, 2018) [2].

The sun-based radiation is directed onto a central line on the collector axis of PTCs. The liquid streaming inside the recipient tube, which is introduced in the central line, absorbs the concentrated sun-powered energy from the pipe walls and increases its enthalpy. The collector has one-hub sun-oriented tracking to guarantee that the

sunlight-based bar falls parallel to its pivot. PTCs usually utilise direct sun-oriented radiation, named bar radiation or Direct Normal Irradiance (DNI), i.e., which is the portion of sun-powered radiation that arrives as a parallel bar at the earth's surface.

There are two fundamental groups of PTC applications: (i) require a temperature range from 300 to 400°C, and (ii) require a temperature somewhere in the range of 100 and 250°C. The first group is associated with Concentrated Solar Power (CSP) plants, which have been effectively tried under genuine working conditions. CSPs have typical aperture widths and total lengths of around 6 m and 100 to 150 m, respectively, and geometrical proportions are somewhere in the range of 20 and 30. CSP plants combined with PTCs are associated directly and indirectly with steam power cycles. In spite of the fact that the most acclaimed case of CSP plants is the Solar Energy Generating Systems (SEGS) plants in the United States and it is still a work in progress or development around the world. The second group of utilisations are associated with industrial process heat (IPH), heating water for domestic use (DHW), heating, refrigeration and cooling. The second group has standard aperture widths somewhere in the range of 1 and 3 m, complete lengths shift somewhere in the range of 2 and 10 m and geometrical proportions are somewhere in the range of 15 and 20. The vast majority of these facilities are situated in the United States, and other facilities have lately been developed in different nations. These facilities could also be used for different applications such as siphoning water system, desalination and detoxification.

The accuracy and confidence of the predictive theoretical and numerical models are basically dependent on different factors such as applied method type, method structure, geometrical parameters, operational conditions, utilised inputs and etc. Due to this fact, it is crucial to comprehensively investigate the parameters affecting the effectiveness of the suggested methods. In the previous studies, a set of affecting factors are considered and investigated while it is crucial to consider all the influential factors such the required inputs for each case, structure of the model, employed functions in each model and etc. In this regard, a comprehensive overview is performed on the thermal and hydraulic enhancement utilising passive techniques (modification in geometries) and various types of conventional and advanced working fluids (nanofluids and hybrid nanofluids) in PTSC. There are some review research

concerning the applications of PTC using classical fluids and nanofluids (Kalogirou, 2004) [3]; (Jebasingh and Joselin Herbert, 2016) [4]; and (Yilmaz and Mwesigye, 2018) [5]. However, in the current chapter, there is a special focus on the theoretical, experimental and numerical investigations to date in detail including the important aspect of thermal energetic and exergetic analyses and their relations to thermal and exergetic efficiencies of PTC systems. In order to provide deep insight to the important perspectives that ought to be thought of in PTSC future turns of events and to facilitate means for researchers to study this area, several scientific sources concerning the prediction of these performances using different kinds of fluids and gases, are reviewed and their most important outcomes are represented. In addition, according to the results of the reviewed articles, some of the challenges for the utilisation of nanofluids and hybrid nanofluids in PTSC systems are also addressed in this chapter. Moreover, since the present study reflects the results of various researchers, it would be possible to select the approach and inputs for proposing more accurate models in the future. The reviewed studies are categorized based on the investigated passive technique used and also on the working fluid type (conventional, nanofluids and hybrid types).

2.3 Sunlight-based Thermal Collector Types

2.3.1 Sunlight-based Collectors

A few sorts of sun-based collectors are available at present accessible in the commercial center. It can be characterised by their sun-based fixation proportion and following sun’s movement (Tian and Zhao, 2013) [6]; (Thirugnanasambandam et al., 2010) [7]. Non-concentrating collectors (NCC) possess a fixation proportion of around one and work with a temperature range from 30 to 240°C. Regularly, NCC are for all times maintained at a location and do not follow the sun and it depends on their initial direction. In this manner, in the northern half of the globe they face south and they face north in the southern side of the equator. Concentrating sunlight-based collectors (CSC) are intended to follow the sun's situation during the daytime and can utilise either one-hub or two-pivot following designs. Focus proportions are in the range of 10 to 1500, possess large radiation motions and can accomplish high temperatures up to 2000°C as found in Table 2.1. The next sections examine different sorts of collectors as being used around the world.

Table 2.1 Sunlight-based thermal collector types

Collector's Motion		**Collector's Configuration**	**Absorber Type**	**Concentration Ratio (CR)**	**Temperature Range (°C)**	**Reference**
Stationary		Flat plate collector (FPC) Evacuated tube collector (ETC) Compound parabolic collector (CPC)	Flat Flat Tubular	$CR \leq 1$ $CR \leq 1$ $1 \leq CR \leq 5$ $5 \leq CR \leq 15$	$30 \leq T \leq 80$ $50 \leq T \leq 230$ $60 \leq T \leq 240$ $60 \leq T \leq 290$	(Sukhatme and Sukhatme,1996) [8]
Sun Tracking	Single hub	Fresnel lens collector (FLC) Parabolic trough collector (PTC) Cylindrical trough collector (CTC)	Tubular	$10 \leq CR \leq 40$ $15 \leq CR \leq 45$ $10 \leq CR \leq 50$	$60 \leq T \leq 270$ $60 \leq T \leq 400$ $60 \leq T \leq 400$	(Rabl,1976) [9]
	Two hubs	Spherical bowl reflector (SBR) Parabolic dish reflector (PDR) Heliostat filed reflector (HFC)	Point	$100 \leq CR \leq 300$ $100 \leq CR \leq 1000$ $100 \leq CR \leq 1500$	$70 \leq T \leq 700$ $100 \leq T \leq 900$ $150 \leq T \leq 2000$	(Zhang et al., 2013) [10]

2.3.2 Non-Concentrating Solar Collectors (NCC)

The flat plate collector (FPC) is the most widely recognised NCC as appeared in Figure 2.2. This kind of collector is broadly utilized for water-warming and space-warming applications in homes (Kainth and Sharma, 2014) [11]. FPCs are explicitly intended to work in warm and radiant atmospheres. FPCs are rooftop placed, directed and maintained in place for perfect sun-powered presentation. Regularly, an FPC comprises of a protected box fitted with a high transmission properties comparable metal (Hellstrom et al., 2003) [12]. There is an absorber inside the box, which comprises of sheets and pipes dealt with a dull shaded sun oriented specific covering to advance sun-based absorption (Konttinen et al., 2003) [13]. A large portion of the sunlight-based energy going to the FPC is consumed by the sheet-pipe gathering. The subsequent thermal energy will be transferred to working fluid inside the pipes. The FPC's working liquid (normally water) temperature reaches 80°C, with this advantage they become perfect for local boiling water (Sukhatme et al., 1996) [8]. In any case, the operational performance of FPCs is fundamentally decreased during unfavorable climate occasions. For instance, significant lots of chilly, shady and blustery days can incredibly lessen the energy converter efficacy which require additional electrical or gas heating.

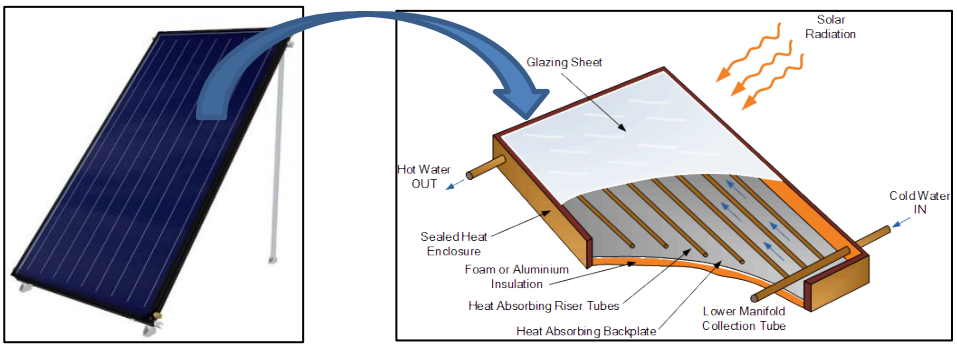

Figure 2.2 Flat-plate collector (FPC) (CSP technologies, 2018) [2].

The evacuated tube collector (ETC) is an elective kind of NCC as appeared in Figure 2.3. An ETC comprises of a focal liquid channel contained inside a vacuum-fixed tube assembly. These tubes comprise of two coaxial pipes made of glass, with empty space between the two pipes to diminish the convection and conduction heat losses from the inner pipe that has the flowing liquid (Vasiliev, 2005) [14]. This advantage of reducing the convection currents by the vacuum envelope makes the ETC to work at higher temperatures than the FPCs. The external surface of the focal heated pipes is coated with special coatings in order to absorb much amount of energy, which will be then transmitted to the working liquid (Alghoul et al., 2005) [15]. The heating pipes are associated with a complex framework that allows the flow of the working liquid along these lines to FPCs.

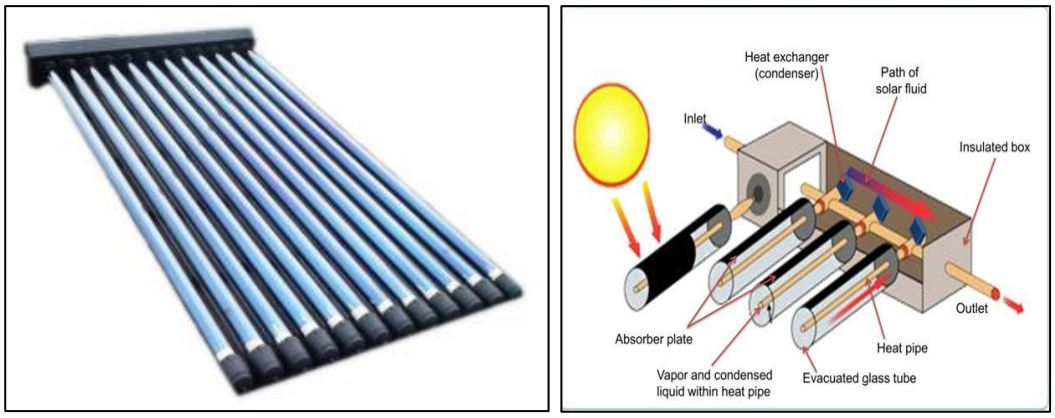

Figure 2.3 Evacuated tube collector (ETC) (CSP technologies, 2018) [2].

Another type of sunlight-based collector is the compound parabolic collector (CPC) as appeared in Figure 2.4. This kind of collector comprises of numerous inward reflecting

parabolic surfaces that immediate sun-powered energy to a receiver pipe situated at the base of the system (Rabl, 1976) [9]. The CPCs are equipped for getting a lot of diffuse radiation with no need to follow the sun. The cylindrical tube shape is another type of solar-based receiver. This collector comprises of a round and hollow tube made of glass that structures the sun-oriented energy receiver and a cylinder that conveys the working liquid. In order to decrease the reflectivity and advance the transmission of sun-based energy to the focal cylinder, the external glass tube is similar to the available one commercially. The barrel glass tube is made empty to keep away from vapor that develops on the inner surfaces, which would lessen the energy transfer. The outside of the cylinder is covered with a particular material that advances greatest sun-absorption, which advances higher temperatures in the working liquid. This working liquid stream rate is managed by valve control in order to get the greatest energy move (Al-Madani, 2006) [16].

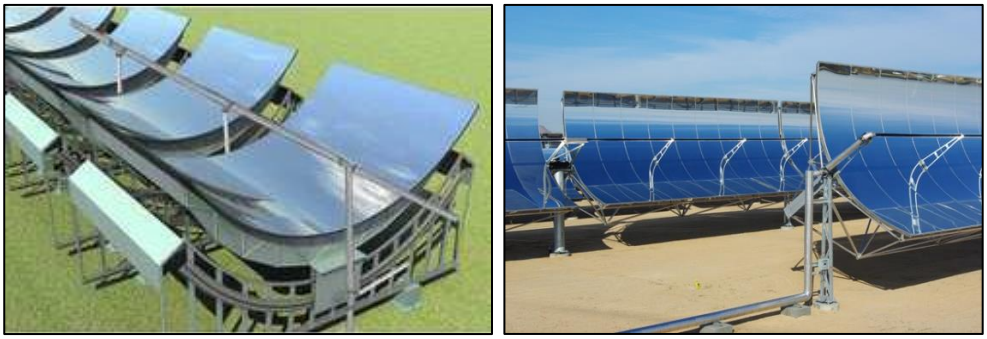

Figure 2.4 Compound parabolic collector (CPC) (CSP technologies, 2018) [2].

The low thermal energy transformation is one of the disadvantages of using NCC, which in turn limits their utilisation in particular applications that require high-temperature. Other disadvantages associated with these types of collectors are its low performance as they experience low fallen sunlight-based energy catch, wasteful heat transfer, and low transport properties of the working liquid (Al-Madani, 2006) [16] and (Minardi et al., 1975) [17]. Moreover, receivers are covered with optically specific layer such as dark chromium to improve absorbance but it represents an ecological peril material (Grasse et al., 1991) [18].

Conversely, CSC has the ability to accomplish high thermal energy moves which could be used in power generation system. However, these CSC arrangements are costly and

require a lot of money if it is applied in an enormous scale. Moreover, during late seventies, significant efforts were made with the aim to design an alternative collector plans to overcome the shortcomings of the available collectors which initiated the advancement of the direct sun-powered absorption collector. This was done to deliver huge energy moves utilising customary sun-powered collector designs (Lee and Sharma, 2007) [19]. However, there were many variables and components limit the productivity of such sun-oriented collectors such as the sort and number of covers used, surface properties and size of the collector, and collector's materials type.

The convective heat flow rate Q is a significant factor in deciding the effective activity of a collector, which must be considered when planning a sun-oriented collector, and it can be assessed utilising this equation:

$$Q = h\,A\,\Delta T \tag{2.1}$$

Where h is the heat transfer factor (W/m^2.K), A is the surface area (m^2), and ΔT is the driving force for the heat flow (K) (Eastop and McConkey, 1977) [20]. By looking at Equation (2.1), it uncovers that the majority of the parameters can be controlled to improve the collector's effectiveness. One of the options is expanding the surface area (A) which looks not practical in light of the fact that the collector's size turns out to be enormous and massive. Another option is expanding ΔT, which requires enhancing the sun-powered concentration proportion, which may not be conceivable because of collector's structure. The third option, which appears reasonable and practical, is to change the heat transfer coefficient by using various working mediums, which have different thermal properties, which will ultimately evaluate the collector's effectiveness. Figure 2.5a shows a schematic of a nanofluid based direct sun-based thermal absorption collector and demonstrates collector's illumination and different heat waste. While Figure 2.5b shows a closed-loop circuit of direct sun-based thermal absorption structure.

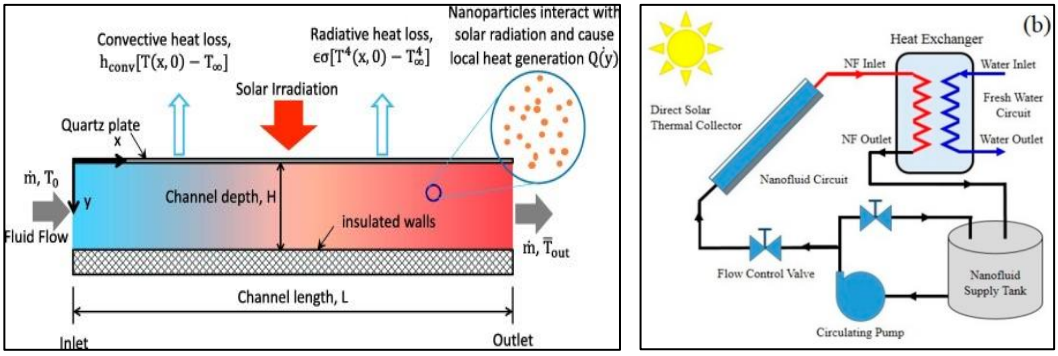

Figure 2.5 Schematic diagrams for solar thermal absorption collector: (a) Collector's illumination and different heat waste, and (b) Closed-loop circuit to transfer heat from nanofluid circuit to water circuit (CSP technologies, 2018) [2].

2.3.3 Concentrating Sun-based Collectors (CSC)

Concentrating sun-based collectors consolidate sun following innovation to keep up the conveyance of focused and centered sunlight-based radiation to the collector. There are four fundamental kinds of CSC: (i) Fresnel linear collectors (FLC); (ii) parabolic trough collectors (PTC); (iii) parabolic dishes (PD), and (iv) heliostats collectors (HC). The FLC can be comprised of either little parabola profile long bended mirrors or from straight sun-powered trackers that have flat reflective strips placed on. The mirrors orient the sun-based light to an optional reflector that focuses and centres the energy onto an absorber pipe. The pipe contains a circulating liquid with temperature in the range of 60 and 250°C (Gouthamraj et al., 2013) [21]. Regularly, FLCs have focus proportions extending in the range from 10 to 40, whereas its direction is accomplished by a single-hub following of the sun's situation during the daytime (Kalogirou, 2004) [3].

The second kind is the PTCs which have been widely examined and its focus proportions is the range of 15 and 45 (Bakos, 2006) [22]. The trough is a parabolic or tube-shaped mirror that reflects and focus the sun-oriented illumination onto a pipe. The PTC consists if concentric pipes one is the inner pipe, that has a circulating liquid, made of a dark metal and the outer pipe is made of a glass. Ordinarily, PTCs are fixed on movable sun-oriented trackers that utilises one-hub sun-following frameworks to pursue the sun's movement. PTCs usually work at the temperatures range of 50 to 400°C (Kalogirou, 2012) [23].

The third type is the PD, which is generally organised to frame a cluster, where the majority of the mirrors are coordinated towards a typical point of convergence. PD is usually fixed with two-pivot sun-following frameworks that keep up the focal point of the sun-powered light on the receiver's pipe in order to pursue the sun's movement during the daytime. PDs has a fixation proportion in the range of 100 and 1000, and it can work at higher temperature of up to 1500°C. This advantage makes the working liquid can convey enormous amounts of thermal energy to run electrical power generation plant (Nixon et al., 2010) [24]. The sunlight-based energy that is generated at the receiver's pipe is then changed over to thermal energy, which is then moved to a reasonable flowing working liquid (Zhang et al., 2013) [10].

The fourth type is the HC, which has organised mirrors to a cluster shape, and these mirrors are driven by two-pivot sun following hardware that empowers the mirrors to reflect and center the sun-oriented energy into a typical tower (Wei et al., 2010) [25]. HC has a fixation proportion up to 1500 and it can operate at higher temperature of up to 2000°C. HFC systems can create steam with high temperature and high pressure that used to generate power when its combined with steam generation system (Behar et al., 2013) [26]. The different types of CSC are displayed in Figure 2.6.

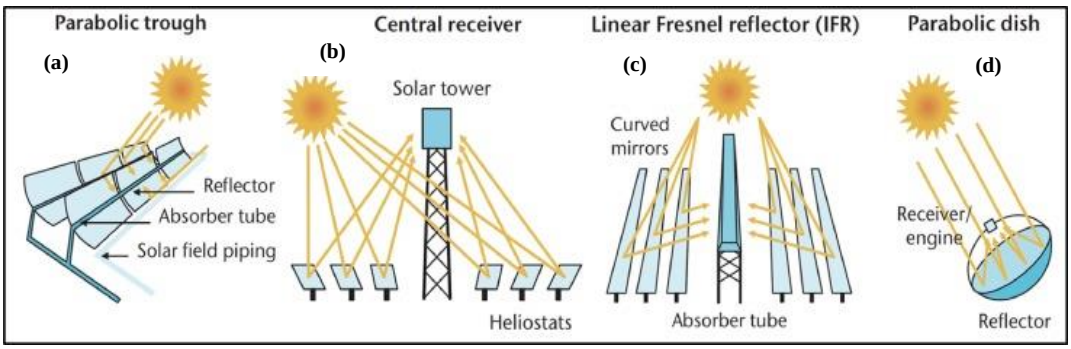

Figure 2.6 Different types of CSC styles: (a) PTC; (b) HC; (c) FLC, and (d) PD (Kalogirou, 2004) [3]; (Nixon et al. 2010) [24]; (Zhang et al. 2013) [10].

2.4 Direct Solar Absorption Collectors Efficiency Improvement

Studies have demonstrated expanding the heat transfer coefficient can fundamentally improve working liquid execution. In any case, available working liquids used to cool down the collectors, for example, water, ethylene glycol, and oils have inherently low thermal conductivity than metals as found in Table 2.2. Because of solids have better thermal conductivity than working liquids; it would be a powerful strategy to include limited quantities of strong particles for improving the liquids thermal conductivity. Late investigations have affirmed suspending little particles in a liquid can enhance its thermal performance (Sureshkumar et al., 2013) [27]. Specifically, the expansion of little micrometer-scale particles to a working liquid would enhance its thermal conductivity and then increase the heat transfer coefficient (Duncan and Peterson, 1994) [28]. Lamentably, two-phase fluids with micrometer-scale particles would have various operational issues in reducing the heat transfer rate such as: (i) molecule sedimentation; (ii) large disintegration rates brought about by circling particles; (iii) particles will in general gather and square tight stream channels; and (iv) expanded stream obstruction and higher-pressure penalty (Das et al., 2006) [29]. Thus, the utilisation of micrometer-scale particles and nanotechnology-based strategies in practical collectors has revived enthusiasm into creating two-phase liquids.

The capacity to produce nanometer-scale materials with thermophysical, chemical and optical properties that are not quite the same as their mass reciprocals has made the chance to build up another type of liquids named as “nanofluids”. It is colloidal suspensions consisting of scattered nanometer-scale particles including metallic, non-metallic, carbides and nitrides. It has a wide assortment of morphologies that incorporate circles, filaments and cylinders (Godson et al., 2010) [30]. In order to improve the direct sun-powered absorption collectors’ efficiency it is believe that nanofluids which have low viscosities, high thermal conductivities and predominant photo-thermal properties are very good option (Saidur et al., 2011) [31]. Another issue with nanofluids preparation is its stability, which needs to be considered as well (Hwang et al., 2007) [32]. That is why a few examinations have detailed the utilisation of nanofluids and their capacity to enhance the effectiveness of direct sunlight-based energy collectors (Shou et al., 2009) [33].

Table 2.2 Thermal conductivities of different particles and fluids at 25 °C.

Particles/fluids		**Thermal conductivity (W/m.K.)**	**Source**
Metal			
	Gold	315	
	Silver	424	
	Copper	398	(Perry and Green, 1997)
	Aluminum	273	[34]
	Iron	80	
	Steel	46	(Alghoul, 2005) [15]
	Stainless steel	16	
Metal Oxide			
	Alumina (Al_2O_3)	40	
	Cupric Oxide (CuO)	77	(Hwang et al., 2007)
	Iron (II, III)	7	[32]
	Titanium Dioxide (TiO_2)	8.37	
	Silicon Dioxide (SiO_2)	1.2	(Kim et al., 2007) [35]
	Zinc Oxide (ZnO)	29	
Carbons			
	Amorphous Carbon	1.59	
	Diamond	900-2320	(Dean, 1992) [36]
	Carbon Nanofibers	13	
	Carbon nanotubes	2000	
	C_{60}-C_{70} Fullerenes	0.4	
	Graphite	2000	
Base fluids			
	Water	0.608	
	Ethylene Glycol	0.257	(Perry and Green, 1997)
	Glycerin	0.286	[34]
	Engine oil	0.145	

2.5 Parabolic Trough Collector (PTC)

A survey of PTC models since the commencement of its innovation, its principle, its applications, producers engaged with their improvement, and business accessibility is highlighted in the following sections.

2.5.1 Background of PTC

The creation of PTC frameworks goes back to the last quarter of nineteenth century. The primary frameworks were utilised in small size offices with lower than 100 kW, similar to steam production and water system. The PTC innovation was popularised in the late seventies and was sent for commercialisation during the eighties (Fernandez-Garcı´a et al., 2010) [37]. In later years, a few organizations fabricated and promoted various PTCs for modern power generation and heat applications. For the period of 1983-1992, nine sunlight-based energy frameworks having 5-85 MWe in size and limit of 354 MWe, were created in Mojave Desert (Price et al., 1999) [38]. These frameworks have been active and their operational encounters have added to PTCs business and developments.

Notwithstanding, the normal yearly development pace of the PTC establishments was right around zero from 1999 to 2006 because of various obstructions against the dispersion of the innovation. The development of the CSP plants rose again in 2006 with 12 MW plant in Spain, and 65 MW plant in Nevada. In year 2007 alone, around 90 frameworks for modern heat application systems were accounted for in 21 nations with limit of 25 MWth. Before the finish of 2014, the quantity of introduced modern plants arrived at 124 everywhere throughout the world with a total limit more than 93 MWth (Yilmaz and Soylemez, 2016) [39]. There are at present several megawatts under development and a large number of megawatts a work in progress around the world. Several countries such as Algeria, Egypt and Morocco have manufactured coordinated sunlight-based plants. While other countries are finishing or arranging their final plants such as Australia, China, India, Iran, Israel, Italy, Mexico, South Africa and United Arab Emirates. Nowadays, there are in excess of 97 plants at various degrees of improvement dependent on the allegorical trough innovation as indicated by NREL database (International Energy Agency, 2009) [40].

2.5.2 Basics of PTC

A PTC is a line-center concentrator, which can be used to change sun-powered energy into high-temperature heat to a temperature up to 550 °C (Tian and Zhao, 2013) [6]. As shown in Figure 2.7, the PTC system fundamentally has a few subsystems to be

practically worked. A sun-based illustrative trough framework comprises of an explanatory formed mirror or reflector bended looking like a parabola which in this manner permits focusing the sun's beams (sun-powered radiation) onto the central line of direct beneficiary framework. The mirror is created from various materials such as glass or aluminum to decrease the assimilation losses. The reflectivity of the mirror, its cost, sturdiness and abradable properties are significant variables in the mirrors creation process. A lot of assembling procedures needs to be conducted in the case of twisting the mirror such as silvering, defensive covering and sticking in order to improve the mirror's reflectivity (Behar et al., 2015) [41].

All beams parallel to the collector's central plane are reflected onto the central hub of the collector. It is fundamentally made of hardened steel tube absorber and an envelope made of borosilicate glass encompassing the absorber. The sunlight-based heat moves to a working liquid circulating through the absorber. The absorber tube is coated with extraordinarily coatings to have a high absorbance of sun-based radiation and low emittance of infrared radiation. A glass spread cylinder is concentrically set around the recipient cylinder and emptied to limit the convective and radiative heat losses from the collector. The envelope is covered by hostile to intelligent layer to diminish the heat losses by infrared radiation. Additionally, the space between the absorber and glass cylinders is considered emptied to a very low vacuum pressure of around 0.013 Pa as appeared in Figure 2.7 (Price et al., 2002) [38].

Getters are usually utilised to guarantee that no hydrogen particles penetrate into the vacuum annulus. The PTC's mirror should be kept stable by bolstering the system by outline with arches with supports to hold the heating element. A control unit is used to drive the collector system by a complete driving setup (apparatus, jackscrew or pressure driven actuator) in order to situate the collector correctly. The temperature at the central line of a PTC can be as high as 400°C with a focus proportion of up to 40. The PTC can be orientated either in an east-west bearing, following the sun from north to south, or a north-south heading, following the sun from east to west (Yilmaz, 2018) [42]. ASHRAE standard 93 is used as a test method to assess the PTC's thermal performance, which can be applied under indoor or outdoor conditions.

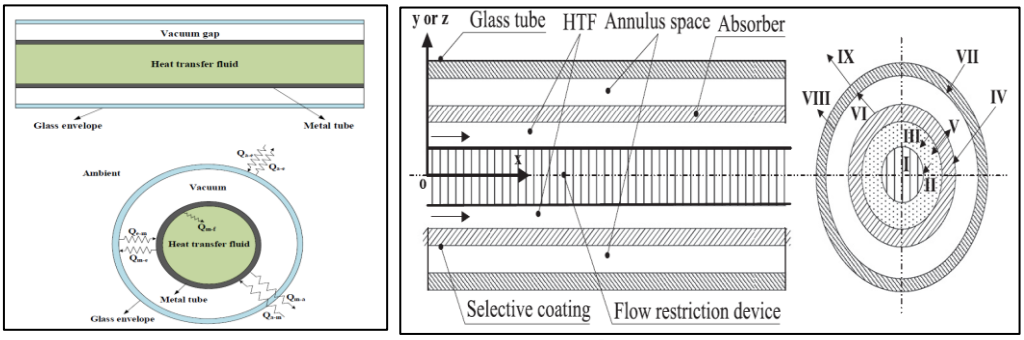

(a) (b)

Figure 2.7 (a) Schematic diagrams of (a) tube receiver's heat transfer mechanisms, (b) PTC's photo-thermal computational model (Price et al., 2002) [38].

Geometrical relations could be utilised to acquire the geometry of the collector by characterising the explanatory shape that makes up the collector framework (Duffie and Beckman, 1991) [43]. The PTC's profile is characterised as shown in Figure 2.8:

$$x^2 = 4\,yf \tag{2.2}$$

Where f is the focal length, which estimates the position of the heating element, can be calculated by:

$$f = \frac{w_a}{4}\tan\left(\frac{\varphi_r}{2}\right) \tag{2.3}$$

Where w_a is the PTC' aperture width and φ_r its rim angle and it can be calculated by:

$$\varphi_r = tan^{-1}\left[\frac{8\,(f/w_a)}{16\left(\frac{f}{w_a}\right)^2 - 1}\right] = sin^{-1}\left(\frac{w_a}{2\,r_r}\right) \tag{2.4}$$

Where r_r is the rim radius. The radius of the local mirror is calculated by:

$$r = \frac{2f}{1+\cos\varphi} \tag{2.5}$$

This provides the rim radius r_r as $\varphi = \varphi_r$:

$$r_r = \frac{2f}{1+\cos\varphi_r} \tag{2.6}$$

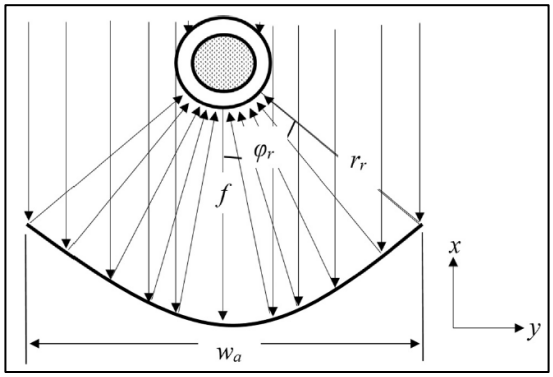

Figure 2.8 Linear PTC-cross section (Duffie and Beckman, 1991) [43].

The heating element diameter is expected to block all the sun-oriented and it is then calculated by:

$$D = 2\, r_r \sin 0.267 = \frac{w_a \sin 0.267}{\sin \varphi_r} \tag{2.7}$$

Where 0.267° indicates the half edge of the cone of light emission radiation. The geometrical relations displayed in Eqs.(2.1-2.6) are very useful in the plan and development of PTC frameworks, which provides precise results. For the examination of PTC frameworks, particularly the optical investigation utilising beam following strategies, is additionally foremost.

There are significant definitions for assessing the thermal, and optical performances of PTCs, which are exhibited and discussed below. Both qualitative and quantitative reviews of energy can be completed by investigating the energy and exergy of PTC frameworks.

2.5.2.1 Optical Analysis

The optical proficiency, η_o is characterised as the proportion of the energy consumed by the heating element to the energy on the collector's opening and it is defined by:

$$\eta_o(\theta = 0) = \rho\, \tau\, \alpha\, \gamma \tag{2.8}$$

Where (ρ) is the capacity of the reflectivity of the mirror, (τ) is the transmittance of the glass envelope, (α) is the absorptivity of the covering on the absorber surface and (γ) is the capture factor of the mirror and heat element.

The variety of all optical properties rely upon on the impact of the rate edge of sun-oriented collectors which is related to a modifier called the frequency edge modifier and it can be calculated by (Gaul and Rabl, 1980) [44],

$$K(\theta) = \frac{\eta_o\,(\theta)}{\eta_o(\theta=0)} \tag{2.9}$$

The incidence angle varies as per the following mode applied. It is important that the episode point can be depicted by different connections given by (Yilmaz and Mwesigye, 2018) [5] contingent upon the tracking kind. The optical effectiveness incorporates the impact of incidence angle and the end-loss factor, is displayed as:

$$\eta_o(\theta) = \rho\, \tau\, \alpha\, \gamma\, \Gamma\, cos\, \theta \tag{2.10}$$

The end-loss factor, Γ is estimated using (Gaul and Rabl, 1980) [44]:

$$\Gamma = 1 - \frac{f}{l}\left(1 + \frac{{w_a}^2}{48f^2}\right) tan\, \theta \tag{2.11}$$

Eq. (2.11) is appropriate for equivalent lengths of the heating element and the collector when heat element is considered evenly. However, the end-loss factor is calculated when the heating element length stretches out past the collector length *l* by a sum *r* on one side, using:

$$\Gamma = 1 + \frac{r}{l} - \frac{f}{l}\left(1 + \frac{{w_a}^2}{48f^2}\right) tan\, \theta \tag{2.12}$$

The end-loss impact for an on a level plane situated north–south pivot framework is resolved in details by (Xu et al., 2014) [45]. The end-loss for short trough collectors was proposed by (Xu et al., 2014) [45] using different technique. The end-loss in tube shaped troughs is given by (Edenburn, 1976) [46] using an alternate way.

The optical plan of the trough collector is practically influenced by a few elements (Guven et al., 1986) [47] including: changes in the sun's width and occurrence angle impacts, thermophysical properties of the materials utilised in heating element and mirror development, blemishes (or blunders), flawed following of the sun, and poor working strategies. (Mokheimer et al., 2014) [48] have envisioned the impacts of the PTC's parts on the optical effectiveness as appeared in Figure 2.9. Taking note of that distinguishing the incomplete impacts of these elements will explain the assurance of the optical productivity.

During the optical examination of PTC frameworks, various factors and their impacts need to be explored such as the assurance of the catch factor, optical productivity, and the heat flux departure from the heating element, rim angle, heating element size, optical error, sun shape, and so on.

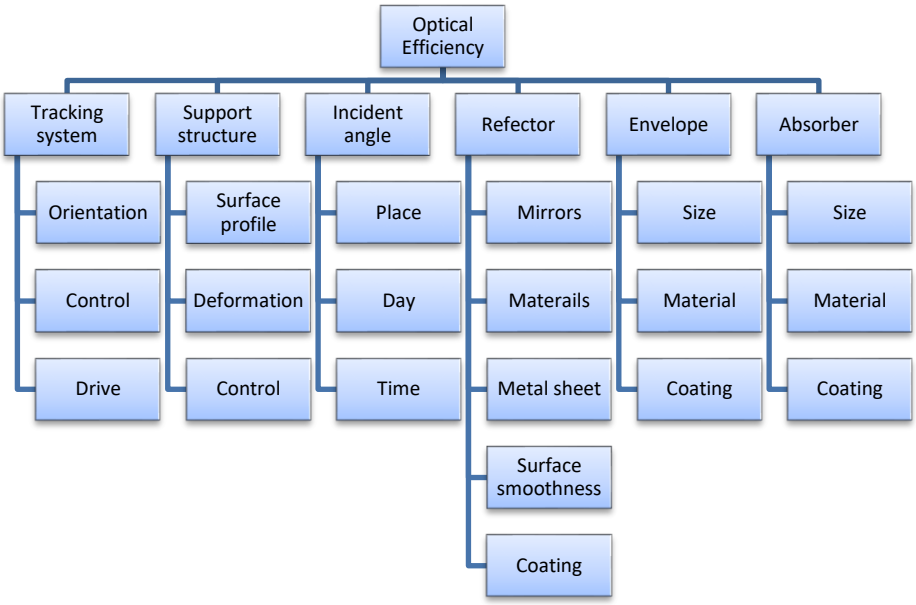

Figure 2.9 Parameters affecting the optical efficiency adapted from (Mokheimer et al., 2014) [48].

The thermal examination of PTC from the energetic and exergetic points of view as well as the entropy generation are discussed next.

2.5.2.2 Thermal Analysis

The PTC's thermal efficiency is calculated by:

$$\eta_{th} = \frac{Q_u}{A_{ap}\, I_D} \tag{2.13}$$

Where Q_u is the useful energy transferred to the working fluid:

$$Q_u = \dot{m}\, C_{p,f}\, (T_{out} - T_{in}) \tag{2.14}$$

The thermal enhancement factor (η) evaluates the effectiveness of heat transfer and flow enhancement methods (Mwesigye et al., 2018) [49].

$$\eta = \frac{(Nu/Nu_p)}{(f/f_p)^{1/3}} \tag{2.15}$$

The Nusselt number could be evaluated by:

$$Nu = \frac{h\, d_{ri}}{k} \tag{2.16}$$

where h is the heat transfer coefficient between working fluid and the absorber tube.

$$h = \frac{Q_u}{(\pi.d_{ri}.L)(T_r - T_{fm})} \tag{2.17}$$

and,

$$T_{fm} = \frac{T_{in} + T_{out}}{2} \tag{2.18}$$

The friction factor could be determined by:

$$f = \frac{\Delta p}{\frac{1}{2}\rho\, u^2}\left(\frac{d_{ri}}{L}\right) \tag{2.19}$$

2.5.2.3 Exergetic Analysis

The exergetic effectiveness can be assessed using the pressure losses and the thermal contribution to PTC:

The entropy generation is calculated by (Mwesigye et al., 2018) [49]:

$$\dot{S}_{gen} = \left(\frac{dS}{dt}\right)_{CV} - \sum_{i=0}^{n} \frac{\dot{Q}_i}{T_i} - \sum_0 \dot{m}_o s_o \geq 0 \tag{2.20}$$

The exergy rate is evaluated by:

$$Ex_u = \dot{m} C_{p,f}\left[(T_{out} - T_{in}) - T_{amb} \ln\left(\frac{T_{out}}{T_{in}}\right)\right] \tag{2.21}$$

The solar radiation exergy is given by:

$$Ex_a = A_{ap} I_D \left[1 + \frac{1}{3}\left(\frac{T_{amb}}{T_s}\right)^4 - \frac{4\,T_{amb}}{3T_s}\right] \tag{2.22}$$

The exergy efficiency is calculated by:

$$\eta_{exr} = \frac{Ex_u}{Ex_a} = \frac{\dot{m} C_{p,f}\left[(T_{out} - T_{in}) - T_{amb} \ln\left(\frac{T_{out}}{T_{in}}\right)\right]}{A_{ap} I_D\left[1 + \frac{1}{3}\left(\frac{T_{amb}}{T_s}\right)^4 - \frac{4\,T_{amb}}{3T_s}\right]} \tag{2.23}$$

2.5.2.4 Entropy Analysis

In any numerical analysis, comprehending the governing equations would give the dispersions for speed, temperature, pressure and turbulent amounts inside the absorber tube (Herwig and Kock, 2007) [50]. The entropy generation comes from irreversibilities of heat transfer $\left(S'''_{gen}\right)_H$ and fluid friction $\left(S'''_{gen}\right)_F$ and its formula is given:

$$S'''_{gen} = \left(S'''_{gen}\right)_F + \left(S'''_{gen}\right)_H \tag{2.24}$$

The entropy generation caused by irreversibility of fluid friction is calculated by:

$$\left(S'''_{gen}\right)_F = S'''_{PROD,VD} + S'''_{PROD,TD} \quad (2.25)$$

Where $S'''_{PROD,VD}$ is the direct dissipation entropy production and $S'''_{PROD,TD}$ is the indirect (turbulent) dissipation entropy production

$$S'''_{PROD,VD} = \frac{\mu}{T}\left(\frac{\partial u_i}{\partial x_j} + \frac{\partial u_j}{\partial x_i}\right) \quad (2.26)$$

$$S'''_{PROD,TD} = \frac{\rho\varepsilon}{T} \quad (2.27)$$

The entropy generation due to irreversibility of heat transfer is calculated by:

$$\left(S'''_{gen}\right)_H = S'''_{PROD,T} + S'''_{gen,TG} \quad (2.28)$$

Where $S'''_{PROD,T}$ is the heat transfer entropy production using mean temperatures and $S'''_{gen,TG}$ is the heat transfer entropy production using fluctuating temperatures

Where $S'''_{PROD,T} = \frac{\lambda}{T^2}\,(\nabla T)^2$ (2.29)

$$S'''_{gen,TG} = \frac{\alpha_t}{\alpha}\,\frac{\lambda}{T^2}(\nabla T)^2 \quad (2.30)$$

Where α and α_t are the thermal diffusivities.

The entropy generation calculation using the direct method (Herwig and Kock, 2007) [50] was given in Eqs. (2.24-2.30). The entropy generation is calculated using with the indirect method given by (Bejan, 1996) [51] as:

$$S'_{gen} = \frac{\acute{q}^2}{\pi\,\lambda\,T_{bulk}^2\,Nu} + \frac{32\,\dot{m}^3 C_f}{\pi^2\,\rho^2\,T_{bulk}\,D^5} \quad (2.31)$$

where q is the heat transfer rate per unit length, $Nu = h\,D/\,\lambda$ with $h = \acute{q}/(T_w - T_{bulk})$, $C_f = \left(-\frac{dp}{dx}\right)\rho D/2G^2$, with G=4 $\dot{m}/\pi D^2$ and T_{bulk} is the bulk fluid temperature $(T_{out} + T_{in})/2$.

The entropy generation rate for a fluid occupying a volume V is calculated by:

$$S_{gen} = \iiint_V S'''_{gen}\,dV \quad (2.32)$$

The Bejan number, presents the irreversibility caused by heat transfer to total entropy generation, is described as:

$$Be = \frac{\left(S'''_{gen}\right)_H}{S'''_{gen}} \quad (2.33)$$

The irreversibility of heat transfer is predominant when Be = 1, and the irreversibility of fluid friction is prevailing when Be = 0 (Amani and Nobari, 2011) [52].

2.6 Performance Enhancement Technique

2.6.1 Passive Techniques

Effective heat transfer framework is one of the significant prerequisites in energy protection (Hojjat et al., 2011) [53]. The improvement of heat transfer prompts growth of high heat motion. Aside from this, improvement in heat movement rate likewise prompts a few focal points like decrease of heat exchanger size and temperature main thrust and so forth. The decreased size of heat exchanger is very significant from financial perspective though decrease of temperature main thrust prompts increment second law proficiency and minimisation of entropy generation or least energy annihilation. The high heat transfer is also useful because of the way that heat exchanger can be worked at low speed and gives impressively higher heat transfer coefficient. Therefore, low working pressure drop is accomplished and working expense is extensively diminished. Thus, in order to improve the productivity of heat exchangers, it is imperative to improve the thermal contact and reduce the pumping power. These advantages related with heat transfer improvement powers to investigate various systems/techniques to improve heat execution of heat exchangers.

The idea of thermal improvement is very significant and valuable in control, refrigeration, cooling, car enterprises, and so on. What's more, heat transfer improvement systems are likewise turning into a significant matter of enthusiasm for electronic cooling, sunlight-based heat collectors, small scale synthetic preparing smaller heat exchanger structure and so forth (Geyer et al., 2007) [54].

The issue of heat transfer improvement has gotten increasingly indispensable in every single mechanical application. The heat transfer upgrade systems can be classified into three categories: active, passive and compound techniques as shown in Figure 2.10. In active strategy, external power is utilised for heat transfer upgrade. It appears to be a simple strategy in a few applications, but it is very perplexing from configuration perspective. That is the reason it is of restricted use because of external power

necessities. Passive strategies use energy inside the framework which prompts increment liquid pressure drop (Dewan et al., 2004) [55]. The utilisation of uncommon surface geometry gives high heat execution when compared with smooth surface. Surface modifications or alterations such as twisted tapes, inserts, coils, ribs, dimples, blades, fins and so forth are distinctive passive types, which are utilised to upgrade heat transfer rate. Likewise, tube with longitudinal supplements is additionally a viable passive technique for heat transfer improvement (Hsieh et al., 2000) [56]. Passive techniques are commonly metallic strips, which are turned in some particular shapes/ measurements and embedded over the flow stream. They are additionally deemed as swirl stream gadgets as turbulators used to confer the swirl stream, which prompt the expansion in heat transfer coefficient. Prior, it was hard to work with complex geometries because of their creation requirements; however, with the headway in assembling innovation, it is presently very conceivable to apply new geometries in heat transfer upgrade strategies. Compound heat transfer strategy is a half-breed system, which includes the utilisation of both active and passive techniques, which is very unpredictable with restricted applications.

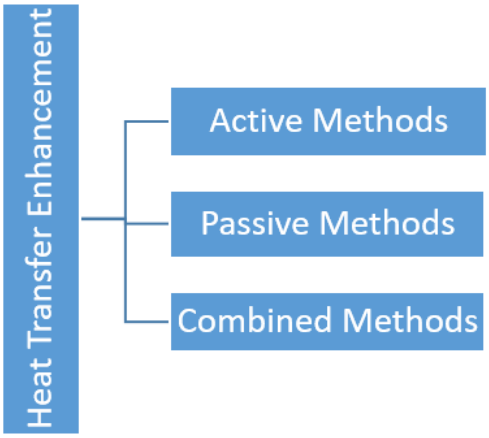

Figure 2.10 Heat transfer augmentation strategies.

Passive strategy is obtained by creating swirl stream of the cylinder side liquid, which gives high speeds close to limit and liquid blending and thus high heat transfer coefficient. In heat transfer frameworks outfitted with aloof procedures, the heat transfer and pressure drop attributes are represented by passive strategy geometrical factors. Additionally, little clearances between a passive system and cylinder limit are significant factor while choosing the width of the passive strategy, which can create sidestep stream, which lead to pressure drop. Utilisation of passive procedure, for

instance twisted tapes and different supplements, causes stream blockage, stream portioning and enlistment of auxiliary stream. Free stream territory is decreased because of stream blockage, pressure drop and viscous impacts are extensively diminished. Furthermore, flow speed additionally increases and, in many cases, secondary stream is actuated. This secondary stream generates swirl and gives compelling blending of liquid stream which enhances the temperature gradient and along these lines heat transfer coefficient (Dewan et al., 2004) [55].

Extensive experimental and numerical research has been conducted chronologically by different investigators on the thermal enhancement using various strategies, which is thoroughly investigated and summarised in the next sections and listed in Table 2.2.

The PTC's performance with different porous shapes (square, triangular, trapezoidal and circular) was numerically studied by Reddy and Satyanarayana (2008) [57] as shown in Figure 2.11. The effects of solar radiation, and porous fin geometrical parameters were examined on the PTC's performance. The optimal thermal and fluid flow characteristics were shown using the trapezoidal shape with 4-mm thickness, 0.25 of tip-to-base thickness ratio (λ) and 1 of fin distance to diameter (*l/d*). The PTC's efficiency remarkably improved with the usage of porous fin receiver and the heat transfer was 13.8% augmented with 1.7 kPa pressure drop losses.

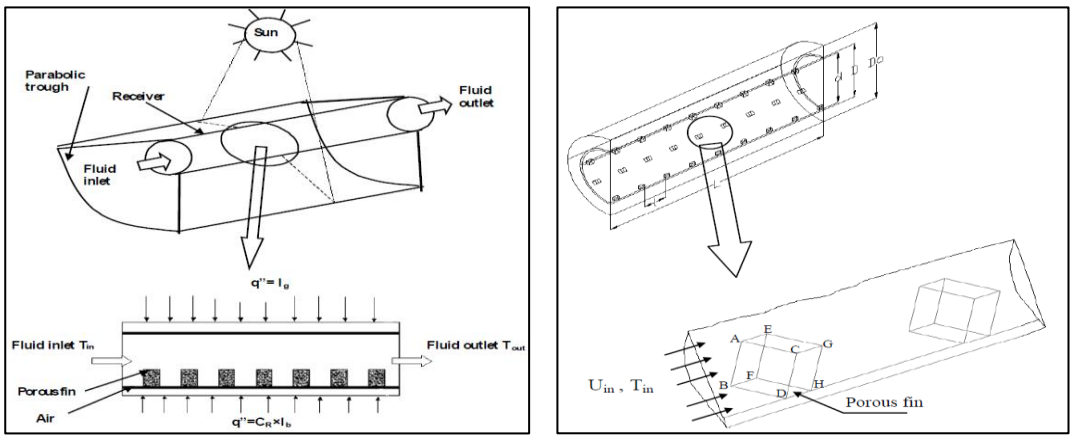

(a) (b)

Figure 2.11 (a) Solar PTC with its boundary conditions, (b) Porous fin receiver with interface boundary conditions Reddy and Satyanarayana (2008) [57] (License Number: 4606940724672).

Reddy et al. (2008) [58] presented a thermal analysis of a porous PTC receiver as shown in Figure 2.12 considering the heat gain and heat loss caused by free convection. CFD-FLUENT package was used to solve the numerical model with the aid of RNG k-ε turbulent model. Different geometrical fin factors were considered in the thermal model such as thickness, porosity, aspect ratio and heat flux. It was observed that the 17.5% of heat transfer improvement and 2 kPa pressure drop loss were achieved. It is also found that the shorter fins were progressively ideal to improve the thermal and hydraulic characteristics. Porous fin receiver having 4 mm of thickness showed a significant increase thermal performance. Empirical correlation for the Nusselt number is suggested dependent on the numerical results.

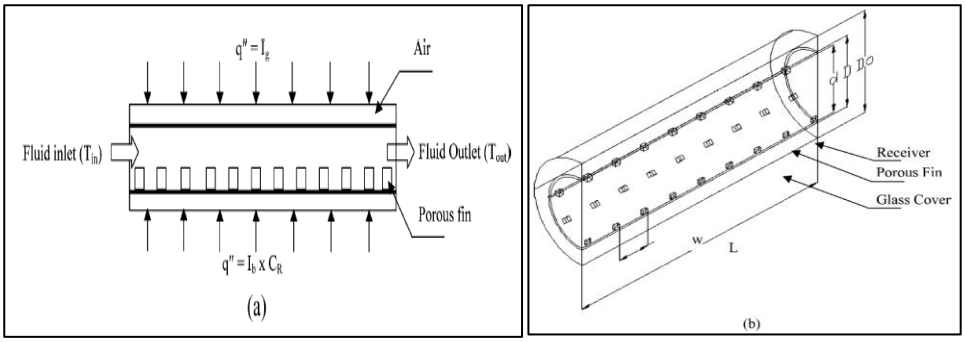

Figure 2.12 Solar PTC with receiver having porous fin: (a) receiver with its operating conditions, (b) receiver with its geometrical factors Reddy et al. (2008) [58] (License Number: 4606940724661).

A three-dimensional numerical simulation of solar PTC having porous disc receiver was conducted by Kumar and Reddy (2009) [59] as shown in Figure 2.13. The effects of Therminol-VP1 as a working fluid, geometrical parameters (disc's angle (h), orientation, height (H) and distance (w)) and solar radiation intensity on the overall thermal performance were involved in the thermal analysis. It was found that higher thermal characteristics were obtained using top porous disc receiver with w = di, H = 0.5di and h = 30 at θ = 30°. The numerical outcomes show that 64.3% and 457 Pa were achieved for Nusselt number improvement and pressure drop loss, respectively, compared with the smooth receiver.

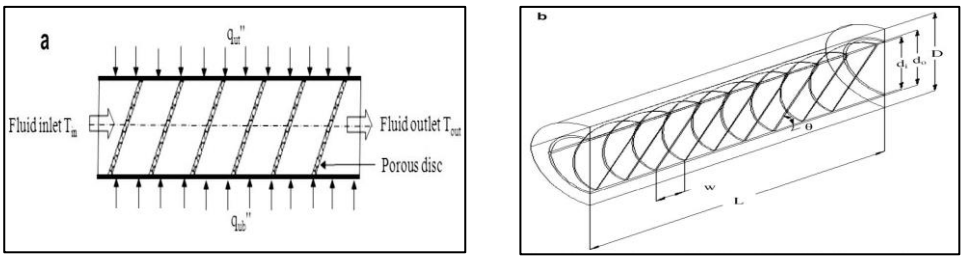

Figure 2.13 Solar porous receiver: (a) with boundary conditions, and (b) with geometrical parameters Kumar and Reddy (2009) [59] (License Number: 4606940725336).

Munoz and Abanades (2011) [60] analysed numerically using CFD tools the impact of helical finned tubes in PTC configuration as shown in Figure 2.14. The thermal stress, fatigue, deformation and pressure losses were considered in the analysis. The results of the finned tube configurations were validated with a reference commercial tube. It is shown that the pressure losses in PTC tube increased when the fins number and its helix angle increased. The thermal and exergetic efficiencies of the collector increased with the decrease of thermal losses and temperature gradients.

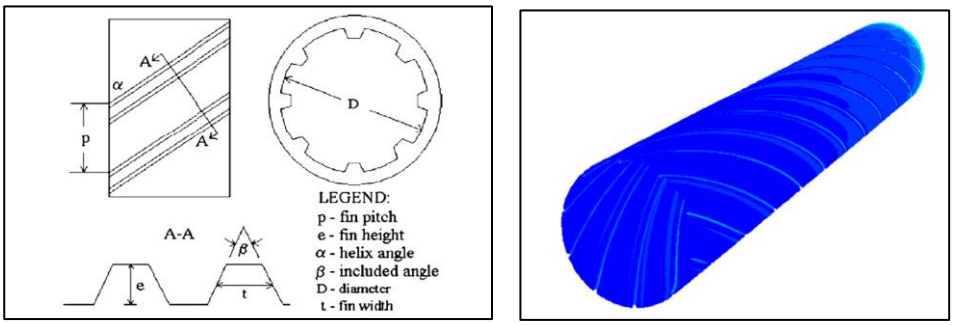

(a) (b)

Figure 2.14 (a) Geometric variables of the helical fin, (b) Tube model corresponding to the length of a helix Munoz and Abanades (2011) [60] (License Number: 4606940725264).

Kumar and Reddy (2012) [61] performed a 3D numerical simulation using CFD-FLUENT package for a porous disc enhanced receiver to find the best configuration with water and therminol oil as shown schematically in Figure 2.15. The performance of the PTC was evaluated by examining the influence of porous disc receiver's location at bottom, top; and alternative porous disc. The porous disc geometric parameters impact and working fluid factors on the PTC's thermal effectiveness were also

investigated. It is found that the flow field caused by the solid/porous discs were remarkably affected the local heat transfer coefficient. The results revealed that the low-pressure drop was attained using porous disc PTC receiver compared to solid disc one. The optimum outcomes were attained at 221 W/m enhanced the heat transfer rate with 13.5% pumping losses for porous disc PTC receiver using water. Conversely, there was 575 W/m of heat transfer rate enhancement with 31.4% pumping losses using therminol oil-55 compared with smooth PTC receiver. Nusselt number and friction factor empirical correlations were developed for porous disc PTC receiver.

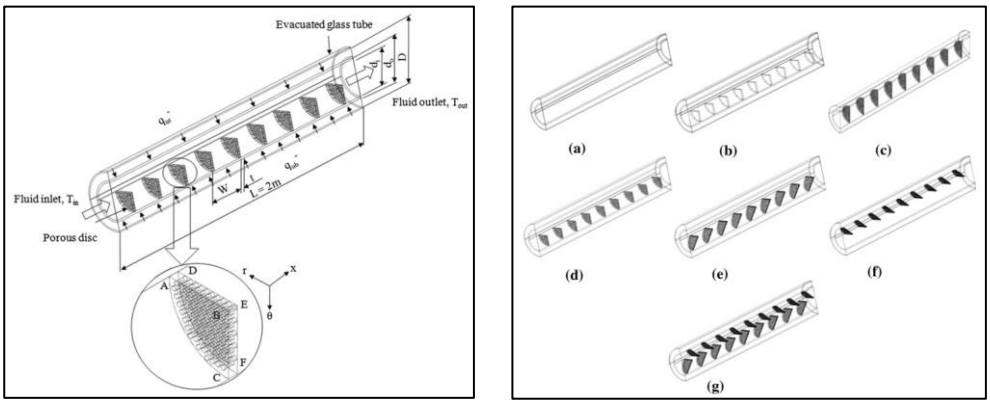

(a) smooth PTC receiver, (b) bottom vertical solid half discs, (c) vertical full porous discs, (d) bottom vertical half porous discs, (e) bottom inclined half porous discs, (f) top inclined half porous discs, and (g) alternative half porous discs

Figure 2.15 (a) Sectional representation of porous disc PTC receiver, (b) Solar PTC configurations Kumar and Reddy (2012) [61] (License Number: 4606940725153).

Cheng et al. (2012) [62] carried out a numerical analysis on combined thermal and turbulent flow in a novel PTC absorber tube using unilateral milt-longitudinal vortexes (UMLVG-PTR) as shown schematically in Figure 2.16. They used finite volume method (FVM) and the Monte Carlo ray-trace (MCRT) method combined with the field synergy principle (FSP). Various parameters such as solar radiation, working fluid inlet temperature, Reynolds number, and LVG geometric factors were further studied. It was found that the thermal loss of the UMLVG-PTR reduced by 1.35-12.10% to that of the SAT-PTR within the range studied, and the larger the Reynolds number is, the better comprehensive enhanced thermal effectiveness is. The increase of incident solar radiation increased the average wall temperature and the thermal loss. The UMLVG-PTR has higher overall thermal effectiveness than the smooth PTR, and it has stable performance within a wide range of incident solar radiation.

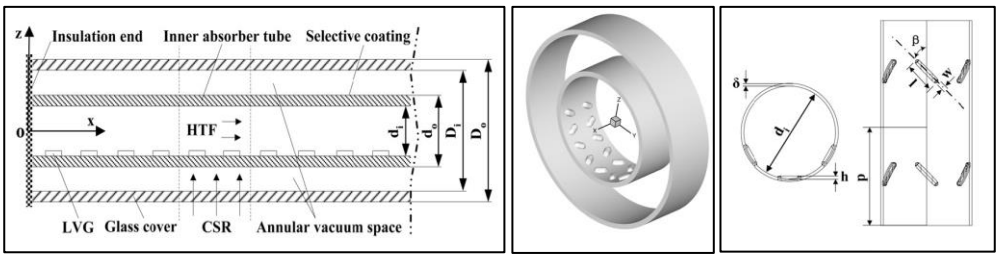

Figure 2.16 (a) The longitudinal cross-section, (b) the computational period model, (c) parameters of LVG Cheng et al. (2012) [62] (License Number: 4606940725615).

Islam et al. (2012) [63] performed a 3-D numerical analysis of PTC receiver using CFD-Fluent package as shown in Figure 2.17. The developed model tackled various physical issues and computational issues associated with PTC system. The physical issues took into consideration non-consistency of the heat flux profile and the temperature profile, and lopsided heating of the working fluid. The most significant numerical issues incorporate the structure of the calculation area, the turbulence models and the near wall physics. They used effectively and proficiently a basic subroutine program to integrate the receiver's optical information and the boundary conditions into the computational domain simulation. Their simulations affirmed that the optical and the computational simulations of the collector can be practiced autonomously.

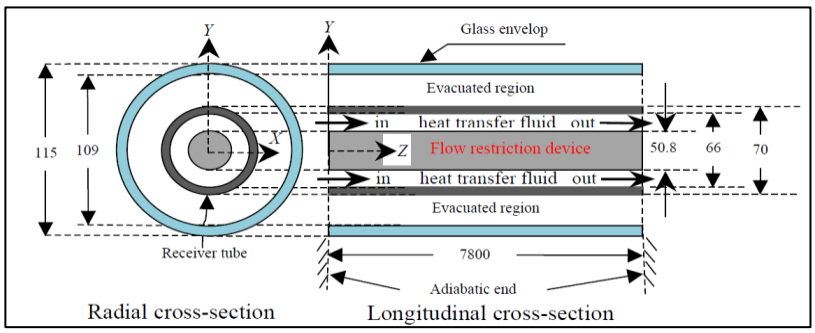

Figure 2.17 Schematic representation of the PTC absorber (all dimensions are in 'mm') Islam et al. (2012) [63] (License Number: 4606940728823).

Aldali et al. (2013) [64] carried out a CFD numerical analysis for three pitch helical fins with 100, 200 and 400 mm, and an aluminum pipe without fins as shown in Figure 2.18. The results revealed that the temperature gradient for the pipe without a helical fin was extensively higher contrasted to the pipes with helical fins. It was confirmed

that the pipe with 100 mm pitch helical fin demonstrated to be superior to 200 and 400 mm pitch helical fins pipes. Nonetheless, the pressure losses for 100 mm pitch helical fin pipe was multiple occasions that recorded for 400 mm pitch helical fin pipe. Moreover, an aluminum pipe indicated the best outcomes, notwithstanding not having any helical fins. This proposes that the conductivity of the material is significant and has more noteworthy bearing than the nearness of the fins. Thus, the pipes with helical fins can efficiently transfer heat to water than that without fins.

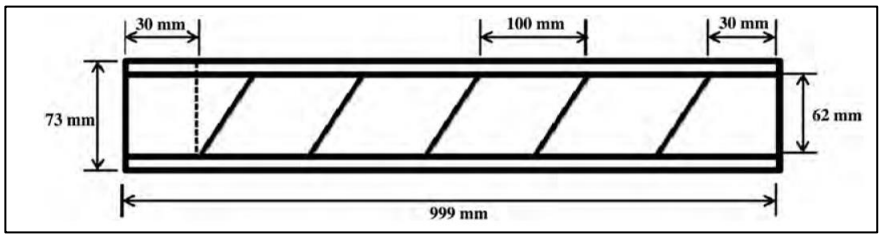

Figure 2.18 Schematic diagram shows the pipe dimensions with inner helical fins Aldali et al. (2013) [64] (License Number: 46069407268531).

Wang et al. (2013) [65] investigated the influence of inserted metal foams on the thermal performance of PTC receiver tube as shown in Figure 2.19. The impacts of metal foams layout, geometrical factor (H), and porosity (u) on the thermal and flow fields were investigated. The thermophysical properties of metal foams and non-constant heat flux were employed to describe the heat transfer characteristic accurately in superheated section of direct system generation (DSG) system. The results revealed that the ‘H’ impact on the thermal effectiveness was substantial, but this is not the case for the impact of ‘u’ at constant layout and ‘H’ as it is somewhat minimal. Furthermore, the heat flux boundary influences the thermal field essentially. There was 45% reduction in the circumferential temperature difference on PTC’s outer surface, which will enormously lessen the thermal stress.

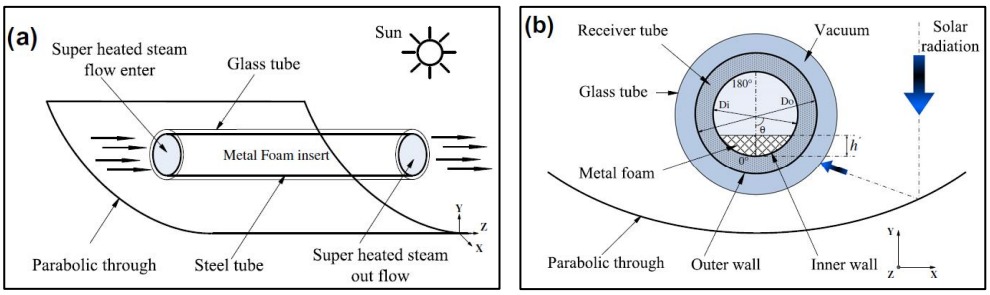

Figure 2.19 (a) Schematic of PTC inserted with metal foams, and (b) PTC cross-section filled with metal foam Wang et al. (2013) [65] (License Number: 4606950012954).

Ghasemi et al. (2013) [66] investigated using CFD FLUENT package the thermal field of PTC having two segmental porous rings as shown in Figure 2.20. The influence of the distance between the rings on the PTC thermal performance was examined suing Therminol 66 as the heat transfer medium. The outcomes show that the thermal effectiveness of the sun powered parabolic framework was enhanced by the inclusion of permeable two segmental rings. The Nusselt number diminished with increments of the separation between the rings. Therefore, the most extreme Nusselt numbers rely upon the Reynolds number, inner diameter and the separation between permeable two rings. The higher thermal improvement was based on the separations between the two permeable rings Q and d/D being 0.75d and 0.6 respectively.

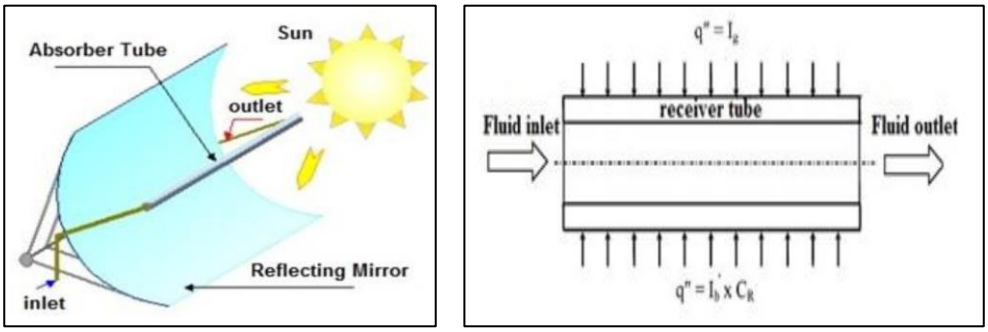

(a) (b)

Figure 2.20 (a) Schematic of PTC system, and (b) Cross-section of receiver tube of PTC Ghasemi et al. (2013) [66] (License Number: 4606940728722).

Ghadirijafarbeigloo et al. (2013) [67] investigated by numerical analysis the thermal effectiveness in PTC receiver pipe fitted with perforated louvered twisted tape (LTT)

with various twist ratios (TR) as shown in Figure 2.21. The results have shown that the thermal and flow fields increased remarkably compared with a pipe having a plain twisted-tape and a smooth pipe. It was found that thermal and flow fields (Nusselt number and friction factor) were higher for LTT tube with a maximum of 150% and 210%, respectively, compared to a smooth pipe. The heat transfer increased with decreasing Re number and TR values, where the optimum results were a TR of 2.67 and Re of 5000.

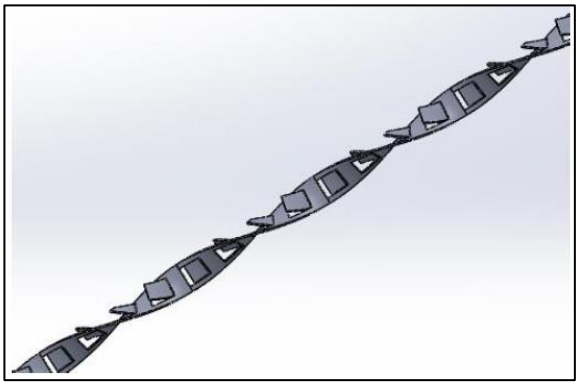

Figure 2.21 Louvered twisted-tape with perforations Ghadirijafarbeigloo et al. (2013) [67] (License Number: 4611221010240).

Too and Benito (2013) [68] conducted a comparative assessment on the thermal and flow fields of solar PTC air absorbers equipped with and without helically coil/wire, twisted tape inserts and dimples as shown in Figure 2.22. They represented the solar tubular air absorbers using simplified steady-state heat transfer model using CO_2 and He gases. This study revealed that the absorber tubes fitted with dimples shows superior overall enhancement performance without substantial pressure drop penalty compared to that of tubes with coil or tape inserts. It is revealed that using these kinds of surface modifications can minimise the temperature gradient between the wall and air flow. Additionally, the pressure loss could be further diminished with the utilisation of CO_2 and He as working gases.

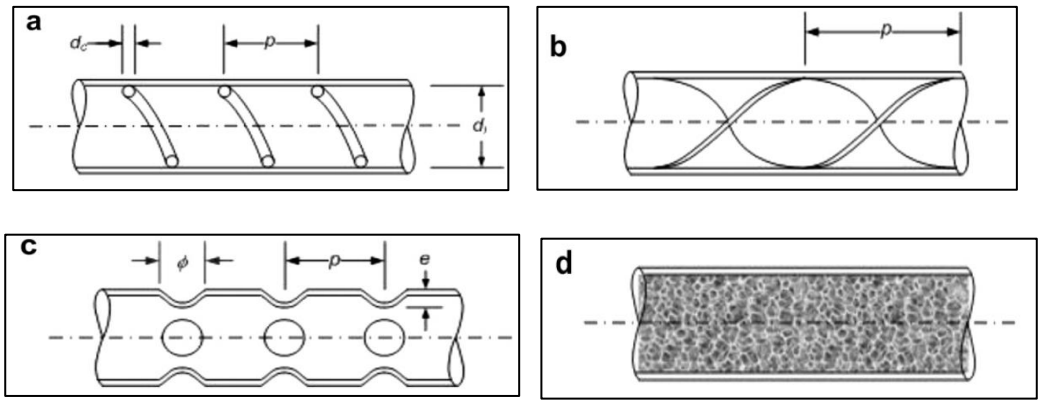

Figure 2.22 Various types of inserts, (a) Helical coil, (b) twisted insert, (c) dimpled tube, (d) porous foam Too and Benito (2013) [68] (License Number: 4611221236456).

Waghole et al. (2014) [69] determined experimentally, using different volume fractions of silver nanoparticles concentrations, the thermal and flow fields data in a PTC absorber tube with and without twisted tape inserts as shown in Figure 2.23. The experiments were conducted using different twist ratios (H/D) and Re number in the laminar range. This study showed that twisted tape insert is an extraordinary guarantee for improving the PTC thermal effectiveness. The experiments show that the Nu number, friction factor and enhancement efficiency were 1.25-2.10 times, 1.0-1.75 times and 135%-205%, respectively, over a smooth PTC absorber. It was seen that the silver nanofluid did not produce higher-pressure loss compared to water at a similar twist ratio. New equations for calculating Nu number and friction factor were proposed for both fluids (water and silver).

Figure 2.23 Actual twisted tape used in the study of Waghole et al. (2014) [69] (License Number: 4611221237634).

Song et al. (2014) [70] analysed numerically the impact of including helical screw-tape (HST) inserts and solar incidence angle of PTC absorber tube as shown in Figure 2.24. Various influence factors including inlet temperature, irradiation level, helical screw-tape inserts parameters and different flux profiles (transversal angle (β)), were considered. The outcomes revealed that β has a significant effect on the flux profile than longitudinal angle (φ). The relative change of heat loss (Q_{loss}) increased when transversal angle (β) of 11.567 was used. However, its impact diminished with the increment of Re number. It was observed that the HST inserts are an appropriate method of enhancing the thermal effectiveness inside the PTC receiver tube as it decreased the Q_{loss}, T_{max} and ΔT. It was concluded that the HST decreased the heat loss 6 times than the smooth PTR, which increased the pressure loss by 23 times than the smooth PTR.

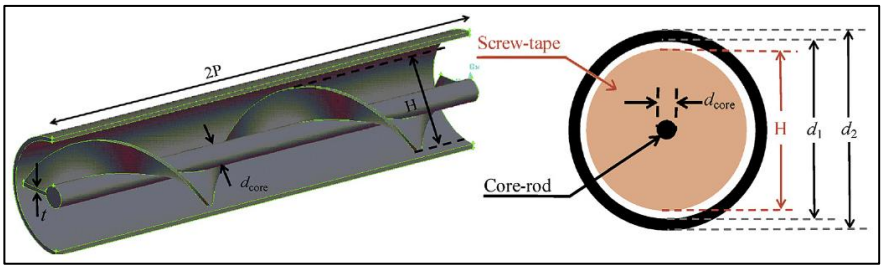

Figure 2.24 Schematic of absorber tube with HST inserts Song et al. (2014) [70] (License Number: 4611230417674).

Mwesigye et al. (2014) [71] and Mwesigye et al. (2015) [72] tested numerically the usage of centrally placed perforated plate inserts (PPI) in a PTC receiver to examine its thermohydraulic performance as appeared in Figure 2.25. The multi-objective optimisation was conducted via the combined utilisation of CFD, design of experiments, response surface methodology and Genetic Algorithm-II. The examination indicated that he with the utilisation of PPI would provide a range of Re numbers at which the PTC thermal effectiveness is improved. In this range, the thermal efficiency increased from 1.2% to 8%, the Nu number increased from 8-133.5% and the friction factor from 1.40-95 times contrasted to a plain PTC receiver tube. Relationships for Nusselt number and friction factor were additionally determined and introduced. It was discovered that the altered thermal efficiency is a progressively reasonable assessment instrument since it thinks about the genuine addition in collector

execution and the relating increment in pumping loss. The utilisation of PPI provided 52.7% reduction in the entropy generation rate.

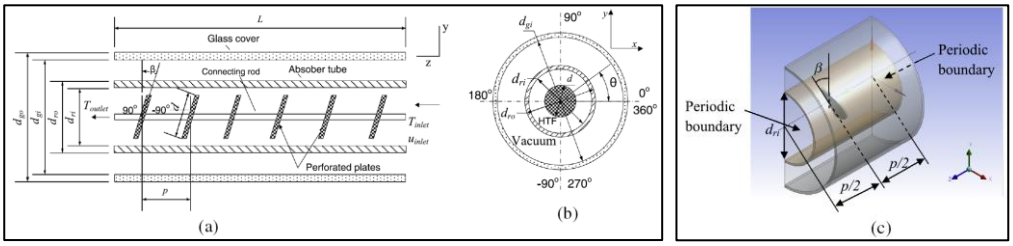

Figure 2.25 Receiver with PPI, (a) longitudinal section, and (b) cross-section, (c) periodic section Mwesigye et al. (2014) [71-72] (License Number: 4611231005708).

Syed Jafar and Sivaraman (2014) [73] investigated experimentally the impact of using a PTC receiver equipped with nail twisted tape (NTT) of two different twist ratios. They studied the effect of Al_2O_3/water nanofluid with 0.1%, and 0.3% particle volume concentration on the thermal and flow fields as shown in Figure 2.26. The tests were conducted using indoor simulation under uniform heat flux condition at Re number range of 710-2130. It was concluded that the NTT absorber with nanofluids can remarkably enhance the PTC thermal effectiveness. The results revealed that the friction factor increased with NNT due to high swirl flow.

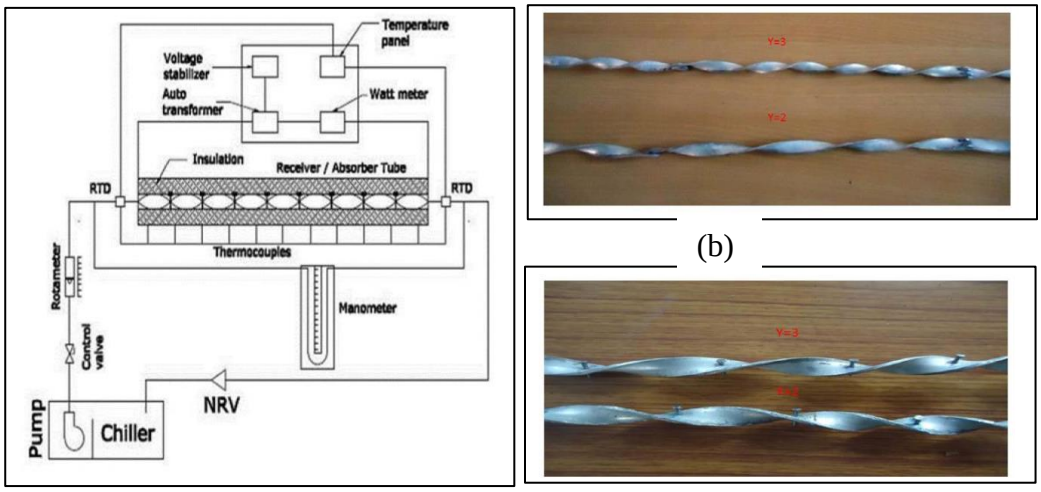

(a)

Figure 2.26 (a) Experimental setup diagram, (b) Plain twisted tapes (PTT), and (c) Nail twisted tapes (NTT) Syed Jafar and Sivaraman (2014) [73] (License Number: 4611231006329).

Mwesigye et al. (2015) [74] performed a thermodynamic analysis and entropy generation for a PTC receiver tube using a synthetic oil-Al_2O_3 nanofluid. The PTC system has of 80° rim angle and 86 concentration ratio. The Re number ranged between 3,560 to 1,151,000 with nanoparticle concentration in the range of 0 to 8%. The results revealed that the thermal efficiency enhanced by up to 7.6% when using nanofluids. It was pointed out that at each inlet temperature and volume fraction there is an optimum value of Reynolds number where minimum entropy is occurred. There was a value of Re number beyond which the utilisation of nanofluids is unfavorable from the thermodynamics point of view.

Huang et al. (2015) [75] studied numerically the thermal effectiveness of a PTC receiver equipped with helical fins, protrusions and dimples as shown in Figure 2.27. The outcomes revealed that the thermal performance was superior for receiver tubes fitted with dimples compared with tubes equipped with either protrusions or helical fins. Then, the impacts of dimples geometrical factors and layouts on the thermohydraulic effectiveness were further studied. The results show that as Re number varies from 1×10^4 to 2×10^4, the value of f/f_0 increased 56%-77% and Nu/Nu_0 increased 44%-64% for the dimpled tubes. The corresponding PEC were varied from 1.23-1.37 which is greater than tubes with protrusions and helical fins. The evaluation of heat transfer enhancement techniques shows that dimples with narrower pitch, deeper depth and larger numbers is beneficial for improving the thermal effectiveness whilst other layouts had insignificant impact.

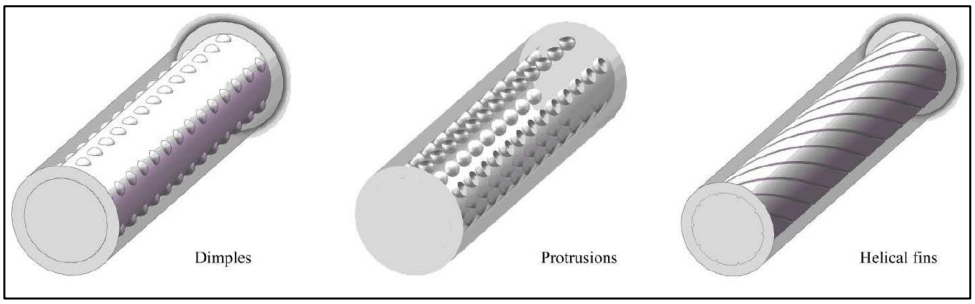

Figure 2.27 The schematic diagram of receiver tube with dimples, protrusions and helical fins Huang et al. (2015) [75] (License Number: 4611231005719).

Chang et al. (2015) [76] examined numerically with FLUENT package the utilisation of twisted tapes inserts (TTI) in a molten salt solar receiver tube to determine the

turbulent thermal effectiveness as shown in Figure 2.28. Various parameters of twisted tapes were studied such as the clearance ratios (*C*) and twist ratios (TR) on the thermal and flow fields under non-uniform heat flux. The outcomes indicated that the TTI remarkably enhanced the consistency of temperature distribution of tube wall and molten salt. The decreases of *C* and TR enhanced the thermal effectiveness effectively and increased the friction factor.

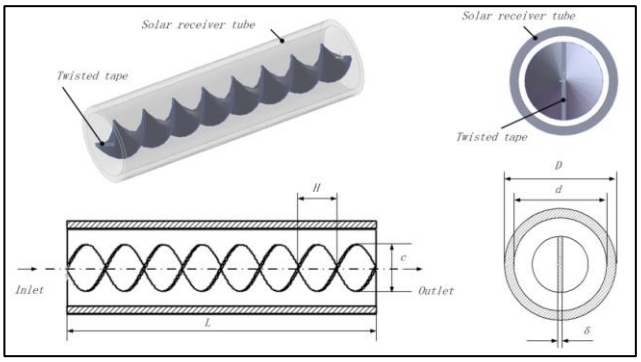

Figure 2.28 The geometry of a PTC receiver tube with TTI Chang et al. (2015) [76] (License Number: 4611231005688).

Lu et al. (2015) [77] analysed theoretically the utilisation of spirally grooved pipe of solar receiver to enhance heat transfer performances. Based on the obtained outcomes, when both the flow velocity and groove height increased, the absorption efficiency increased, whilst the wall temperature decreased. It was found that the heat absorption efficiency of solar receiver fitted with spirally grooved pipe having e/d =0.0475 increased about 0.7%, and the optimum bulk fluid temperature increased to 31.1 °C compared with a solar heat receiver with a smooth pipe. It was concluded that spirally grooved pipe can be an exceptionally viable route for thermal absorption improvement, and it can likewise produce high temperature of molten salt.

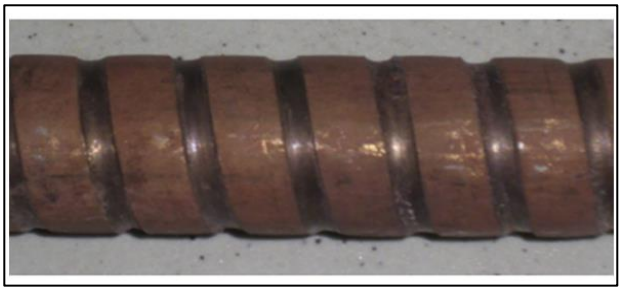

Figure 2.29 Experimental installation and spirally grooved tube Lu et al. (2015) [77] (License Number: 4612900851490).

Reddy et al. (2015) [78] carried out experiments on a 15 m^2 solar PTC equipped with porous disc receiver as shown in Figure 2.30 using six different receiver configurations to evaluate their performance. The experiments were done for different weather conditions and a flow rate in the range of 100-1000 L/h. The results revealed that the time constant for different PTC receiver configurations was in the range of 70s to 260s. The collector acceptance angle is found to be 0.58° and 0.68° respectively for both unshielded receiver (UR) and shielded receiver (SR). The collector efficiencies were in the range of 63.9-66.66% with pumping loss of 0.05 W/m and the heat losses were in the range of 455-1732 W/m^2. It was inferred that the porous disc receiver remarkably enhanced the PTC performance and it thus can be utilised viably for process heat applications.

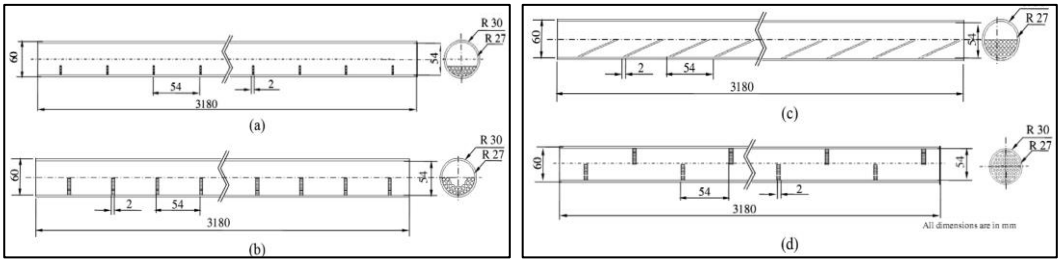

Figure 2.30 Various porous disc receiver configurations, (a) bottom, (b) inclined, (c) vertical, and (d) top Reddy et al. (2015) [78] (License Number: 4612901352313).

Diwan and Soni (2015) [79] utilised PTC absorber tube equipped with wire-coils inserts to examine numerically the thermal and hydraulic characteristics using water as a working medium. The numerical simulations were conducted with the aid of COMSOL Multiphysics 4.4 for different Reynolds numbers and various wire-coils insert pitch values. The results revealed that the Nu number increased by 104% to 330% and the maximum pressure loss ranged between 55.23 to 1311.79 Pa in case of wire-coils with pitch 8 mm. It was concluded that for better thermal effectiveness it is preferable to use wire-coils inserts with pitch value in the range of 6 to 8 mm and more than 8 mm when working with low and high Re numbers respectively.

Mwesigye et al. (2016) [80] utilised wall-detached twisted tape inserts in a PTC absorber tube to investigate numerically the thermal effectiveness based on a FVM as shown in Figure 2.31. It was found that when the twist ratio reduced and the width ratio increased, both the thermal and flow fields increased in the range of 1.05-2.69

times whilst the fluid friction was in the range of 1.6-14.5 compared to a plain receiver pipe. The results have shown significant increase in both thermal efficiency and heat transfer performance of about 10%, 169%, respectively, and reduction in absorber's circumferential temperature up to 68% over a plain receiver pipe. The entropy generation is minimal for each twist ratio and width ratio at the optimum Re number. Empirical equations for thermal and hydraulic performance were also developed.

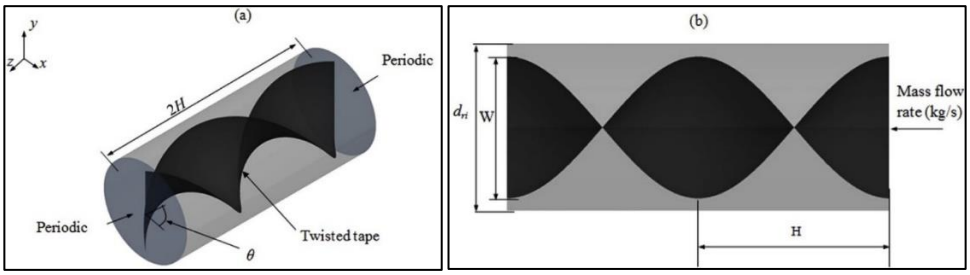

(a) (b)

Figure 2.31 Receiver's absorber tube geometry: (a) full view, (b) section view Mwesigye et al. (2016) [80] (License Number: 4611231005934).

Bellos et al. (2016) [81] utilised a dimpled with sine geometry PTC absorber tube to study its thermal efficiency enhancement as shown in Figure 2.32. Different working mediums were used thermal oil, thermal oil-Al_2O_3 nanofluid and pressurized water to examine its efficacy on the overall thermal effectiveness. The outcomes revealed that the thermal oil-Al_2O_3 nanofluid produced 4.25% improvement of the mean efficiency while 6.34% produced by the use of pressurized water. The results revealed that the mean efficiency enhanced by 4.55% compared to plain tube geometry. Higher fluid temperature levels produced an increase in the efficiency. However, the use of a wavy surface produced negative outcome of high-pressure losses, which needs to be considered.

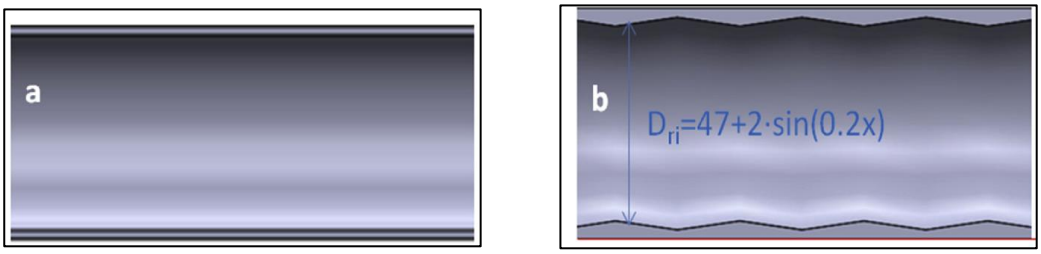

(a) (b)

Figure 2.32 Examined absorber tubes: (a) cylindrical tube, and (b) sine shape tube Bellos et al. (2016) [81] (License Number: 4612941218888).

ZhangJing et al. (2016) [82] utilised porous insert in a solar PTC receiver tube under non-uniform heat flux condition to investigate the thermal enhancement as shown in Figure 2.33. They used an optimisation method, which couples genetic algorithm (GA) and CFD to optimise the layout of porous insert. Three thermal effectiveness evaluation criterions were used such as synergy angle, entransy dissipation and exergy loss. It was observed that the thermal effectiveness of porous receiver insert is always higher than that of the plain receiver. With the use of some materials of high thermal conductivity (Cu, Al and SiC), the solar-to-thermal energy conversion efficiency of GA porous receiver can reach 68%, which is higher than the referenced porous insert receiver is. It was noticed that the energy transfer and exergy loss rate had similar influences on the thermal irreversibility.

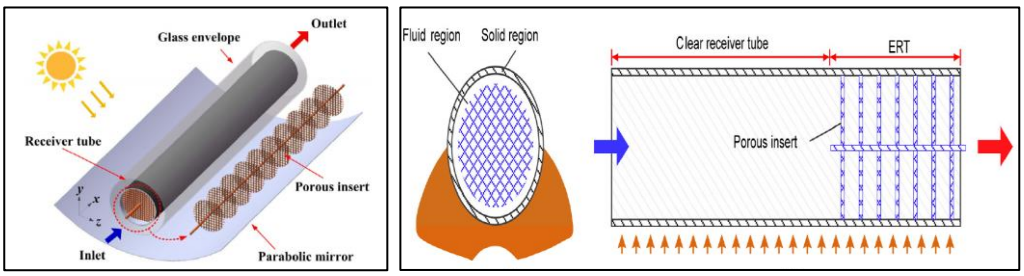

(a) (b) (c)

Figure 2.33 (a) PTC segment diagram, (b) Physical model for simulation transverse cross-section, and (c) Longitudinal cross-section ZhangJing et al. (2016) [82] (License Number: 4612950191523).

Fuqiang et al. (2016) [83] used asymmetric outward convex corrugated tube (AOCCT) tube of PTC receiver to increase its reliability and overall thermal effectiveness as shown in Figure 2.34. The PTC thermal effectiveness and strain was studied by developing an optical-thermal-structural coupled method. It was indicated that the usage of AOCCT can effectively improve the thermal effectiveness and reduce the thermal strain. The results revealed that the maximum augmentation of overall thermal effectiveness factor and restrain of von-Mises thermal strain are 148% and 26.8%, respectively, with the utilisation of AOCCT as receiver.

Figure 2.34 (a) AOCCT as PTC receiver, (b) Diagram of AOCCT used for PTC tube Fuqiang et al. (2016) [83] (License Number: 4612950656289).

Jaramillo et al. (2016) [84] used twisted tape technique (TTT) to study numerically and experimentally, as shown in Figure 2.35, the heat transfer augmentation in the receiver tube for low enthalpy processes by thermodynamics laws. The outcomes revealed that the Nusselt number, removal factor, friction factor and thermal efficiency increased when both the twist ratio (y/w) and Re number reduced compared with the plain receiver tube. However, these quantities do not show an improvement when the twist ratio (y/w) increased. It was concluded that TTT is an effective way to improve PTC thermal effectiveness only under certain conditions. These optimal conditions correspond to a system having a twist ratio close to 1, and low flow rates in the order of 1 L/min. It was clear that the thermal efficiency increased as the volumetric flowrate increased.

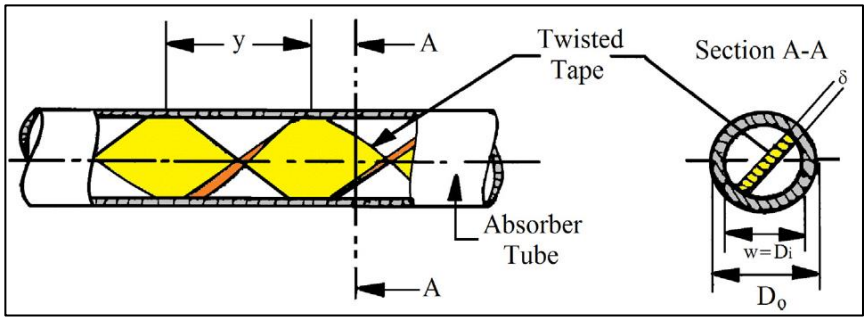

Figure 2.35 Diagram of twisted tape insert used Jaramillo et al. (2016) [84] (License Number: 4612950818541).

Benabderrahmane et al. (2016) [85] investigated numerically the thermal effectiveness of a PTR equipped with longitudinal fins inserts (LFI) and various types of nanofluid as shown in Figure 2.36. The Monte Carlo ray tracing technique was used to obtain the non-uniform heat flux profile. A remarkable thermal enhancement was attained when Reynolds number varied from 2.57×10^4 to 2.57×10^5, and the Nusselt number increased

from 1.3 to 1.8 times. It was found that the metallic nanoparticles significantly enhanced the heat transfer than other nanoparticle types. The friction factor for absorber with fins varied from 1.6 to 1.85 than plain tube. The geometric parameters of the fins have a remarkable effect in heat transfer improvement. At similar condition, using nanofluid in absorber with fins insert offer higher heat transfer performance and higher thermo-hydraulic performance than smooth tube with base fluid.

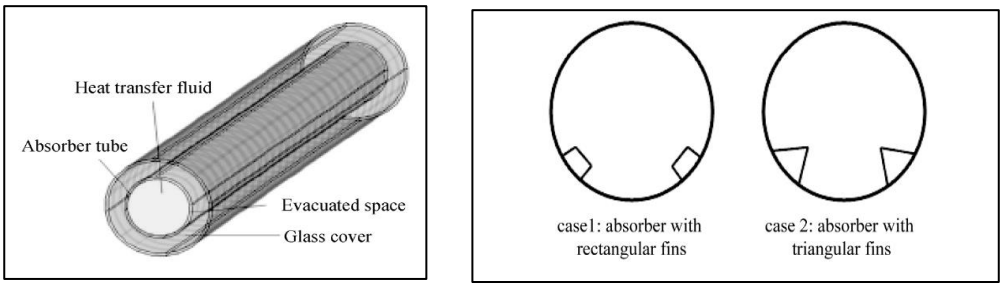

(a) (b)

Figure 2.36 (a) Computational domain diagram, (b) Cross-section of absorber tube with LFI Benabderrahmane et al. (2016) [85] (License Number: 4612960050303).

Chang et al. (2017) [86] utilised concentric and eccentric pipe inserts in a PTR with molten salt as heat transfer medium to examine its performance numerically as shown in Figure 2.37. A 3D simulation model was established, and the combination of a MCRT method and FLUENT software was utilised to obtain the non-uniform heat flux. The results show that the introduction of concentric pipe inserts for PTR augmented the overall thermal effectiveness gradually with maximum augmentation factor of A3 (D=0.04 m) is about 164%. The maximum temperature decrease by A3 can reach more than 19.1K and 2.7K in the absorber tube and the molten salt, respectively. The eccentric pipe inserts of B3 (D=0.04 m and e=0.01 m) performs significantly better than the concentric tube inserts for its excellent performance in decreasing the maximum temperature of absorber tube and molten salt. It enhanced the overall thermal effectiveness dramatically with maximum augmentation factor of B3 is about 165%. The maximum temperature decreased more than 20 K and 2 K in the absorber tube and the molten salt, respectively.

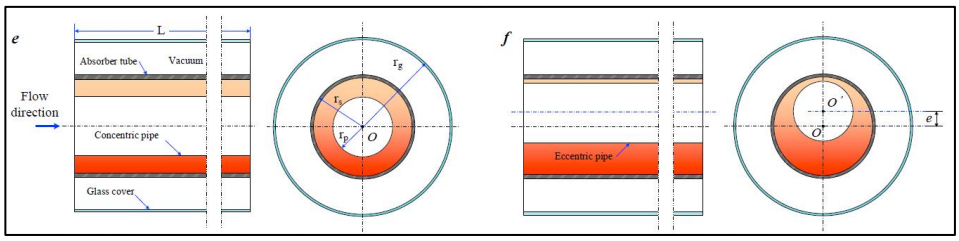

(a) (b)

Figure 2.37 (a) PTC system with concentric pipe inserts, (b) PTC system with eccentric pipe inserts Chang et al. (2017) [86] (License Number: 4611231006837).

Ghasemi and Ranjbar (2017) [87] simulated 3D turbulent flow of Syltherm oil in a PTC absorber tube having porous rings on the thermo-hydraulic characteristics as shown in Figure 2.38. The numerical simulation was carried out using CFD with the aid of ANSYS commercial software. The impact of distance between rings and the rings inner diameter on the thermal effectiveness of the PTC was evaluated. The outcomes have shown that the thermal effectiveness is significantly enhanced by utilising the porous rings. It was found that the thermal characteristics increased by decreasing the distance between the porous rings but the Nusselt number is reduced by increasing the rings inner diameter.

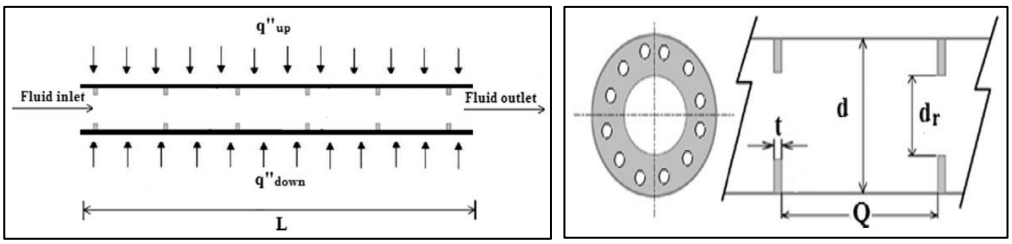

(a) (b)

Figure 2.38 (a) Diagram of PTC absorber tube with porous rings, (b) Cross-section of porous rings Ghasemi and Ranjbar (2017) [87] (License Number: 4613491213097).

Bortolato et al. (2017) [88] tested nanofluids experimentally in a full-scale direct absorber-concentrating collector. The nanofluid used was single wall carbon nanohorns (SWCHNs) suspended in distilled water with volume fraction of 0.02 g/L. A direct absorption receiver was constructed with a flat geometry and installed on an asymmetric PTC using 100 kW/m^2 of solar flux. The results show that the receiver thermal efficiency initially slightly changed and reached 87% and then after 8 h of

exposure it continuously decreased down to 69%. Spectrophotometric analysis on bulk nanofluid samples examined at various times shows that the SWCNHs concentration in water was unstable. This was due to coalescence and precipitation of the aggregates and the polymeric surfactant rapid degradation. The fluid circulation may contribute to the nanoparticles aggregation.

Rawani et al. (2017) [89] used serrated twisted tape insert (STTI) in a PTC absorber tube to investigate analytically its thermal performance. The thermal equations for fully developed flow were developed to study the variation of entropy generation, exergy and thermal efficiencies, and fluid temperature distribution. The temperature rise of fluid for system performance evaluation under specified conditions was calculated by developing a computer program using C^{++} language. The results have shown that the STTIs are a good technique for improving the PTC performance. The results also revealed that for twist ratios x=1, the Nusselt number was shown higher 4.38 and 3.51 times over a plain PTC with corresponding thermal efficiency of 15.7% and 5.41% respectively and exergy efficiency of 12.10% and 12.62%. Jamal-Abad et al. (2017) [90] investigated practically the thermal effectiveness of a PTC filled with copper foam. The experiments were conducted for flow rates (0.5 to 1.5 L/min), the copper foam porosity and pore density were 0.9 and 30 PPI (pores per inch) respectively. The results revealed that the thermal effectiveness was improved and the loss factor reduced by 45% when using copper foam.

Bellos et al. (2017a) [91], Bellos et al. (2017b) [92] and Bellos et al. (2017c) [93] utilised twelve different internally longitudinal fins in an absorbers of PTC module under different operating conditions as shown in Figure 2.39. SolidWorks Flow Simulation was used as the simulation analysis tool and the model results were validated against the literature results. Various operational conditions were tested with the inlet temperature range of 300 to 600 K and the flow rate range of 50 to 250 L/min. They particularly examined internal fins with thicknesses of 2, 4 and 6 mm, whilst their lengths are 5, 10, 15 and 20 mm. They also examined the use of internal longitudinal fins in PTC utilising different gases types (Air, helium and carbon dioxide). It was found that both fin thickness and greater length lead to higher thermal effectiveness and higher-pressure loss. It was concluded that overall optimum absorber had fin

length of 10 mm and fin thickness of 2 mm. It was observed that the thermal efficiency and the Nusselt number were improved by 0.82%, and 65.8%, respectively. Empirical correlations for Nusselt number and friction factor were developed and it was affirmed that both are applicable for smooth and finned absorbers.

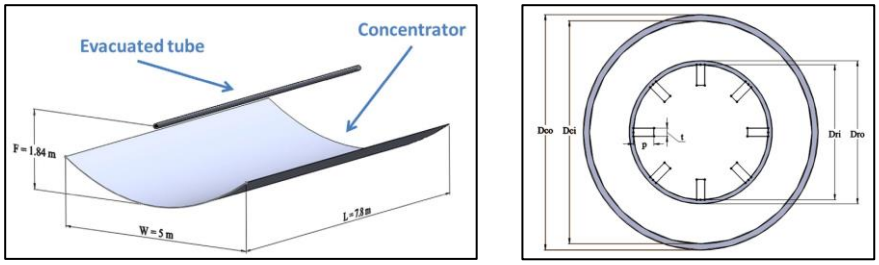

(a) (b)

Figure 2.39 (a) The PTC examined module, (b) Finned absorber cross section Bellos et al. (2017) [91-93] (License Number: 4613500886237).

Zhu et al. (2017) [94] established a comprehensive numerical model using CFD to study the flow and thermal fields inside an absorber tube of PTR equipped with wavy-tape insert using Syltherm-800 as shown in Figure 2.40. It was found that wavy-tape produced high thermal augmentation and lower tube temperature and heat loss. However, the wavy-tape increased the PTR thermal stress and deformation with increased pressure loss. The Nusselt number and friction factor of the wavy PTR increased by 261-310%, and 382-405%, respectively. The wavy-tape produced a performance evaluation index more than 2.11 and heat loss reduction by 17.5-33.1% with entropy generation rate reduction by 30.2-81.8%.

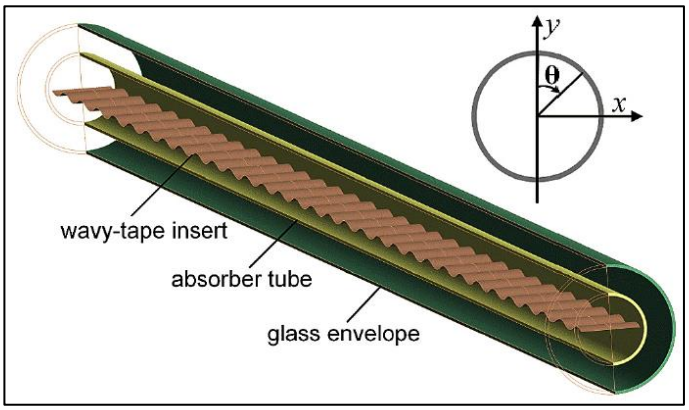

Figure 2.40 Schematic diagram of the PTR equipped with wavy-tape insert Zhu et al. (2017) [94] (License Number: 4613511068043).

Xiangtao et al. (2017) [95] used pin fin arrays insert (PFAI) in a PTC receiver tube to enhance increase the thermal effectiveness as shown in Figure 2.41. The combination of Monte Carlo ray tracing method (MCRT) coupled with Finite Volume Method (FVM) was adopted to perform the simulations. The numerical results indicated that the introduction of PFAI in PTC receiver can significantly improve the thermal effectiveness. The thermal effectiveness factor and the Nusselt number increased up to 12.0% and 9.0% respectively with the utilisation of PFAI. The optimum conditions for higher thermal effectiveness were attained.

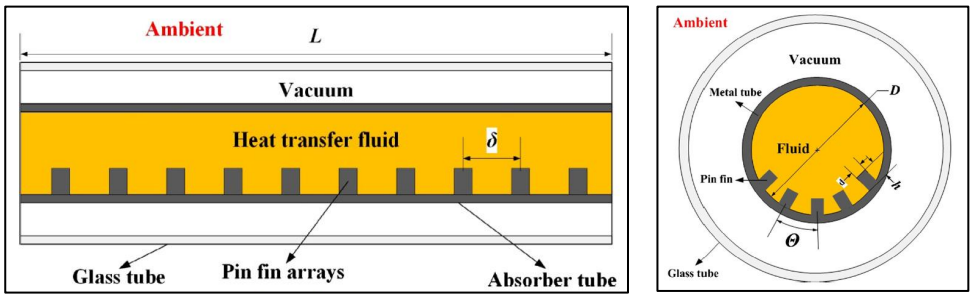

(a) (b)

Figure 2.41 The schematic diagram of PTC tube equipped with PFAI, (a) longitudinal section, (b) cross-section Xiangtao et al. (2017) [95] (License Number: 461351138278).

Huang et al. (2017) [96] studied numerically a 3D turbulent mixed heat transfer in dimpled tubes of PTC tube as shown in Figure 2.42. The impacts of outer wall heat flux profiles and dimple depth on the thermal and flow fields were analysed. The outcomes revealed that the thermal and flow performance in dimpled receiver tubes subjected to non-uniform heat flux (NUHF) were larger than those subjected to uniform heat flux (UHF). It was found that the deep dimples (d/Di = 0.875) were performing much better than the shallow dimples (d/Di = 0.125) at similar Grashof number. It was concluded the impacts of impingement, reattachment and vortex shedding were weakened in the top dimple because of the buoyancy force influence, while the flow was accelerated and the vortex moved backward in the bottom dimple. The higher thermal performance was achieved because of the high reattachment flow, high impingement and vortex shedding.

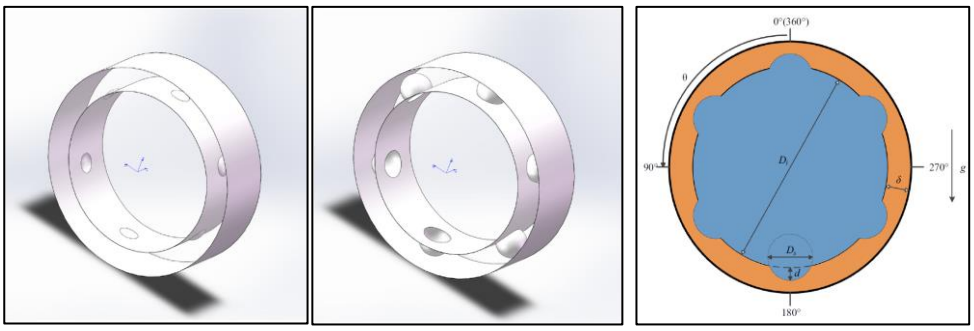

(a) (b) (c)

Figure 2.42 The dimpled tube representation, (a) shallow dimples, (b) deep dimples, (c) parameters of dimpled receivers Huang et al. (2017) [96] (License Number: 4613520033551).

Chang et al. (2018) [97] analysed the reliability and overall convective heat transfer of molten salt flow in a PTC tube with the usage of concentric rod and eccentric rod as turbulators as shown in Figure 2.43. The result showed that both concentric and eccentric rod inserts enhanced the thermal effectiveness effectively. For a PTC with a concentric rod insert, the Nusselt number is about 1.10 to 7.42 times over a plain PTC when the dimensionless diameter (B) increased. The thermal effectiveness factor has a remarkable decrease with Reynolds number increment when B is larger than 0.8. For an eccentric rod insert, the performance effectiveness decreased when Reynolds number increased under a certain dimensionless eccentricity (H). The performance effectiveness decreased from 1.84 to 1.68 times over a plain PTC when H is 0.8. In addition, the absorber tube's optimum temperature decreased dramatically when B and H increased, which eventually reduced the PTC thermal deflection and increased its reliability.

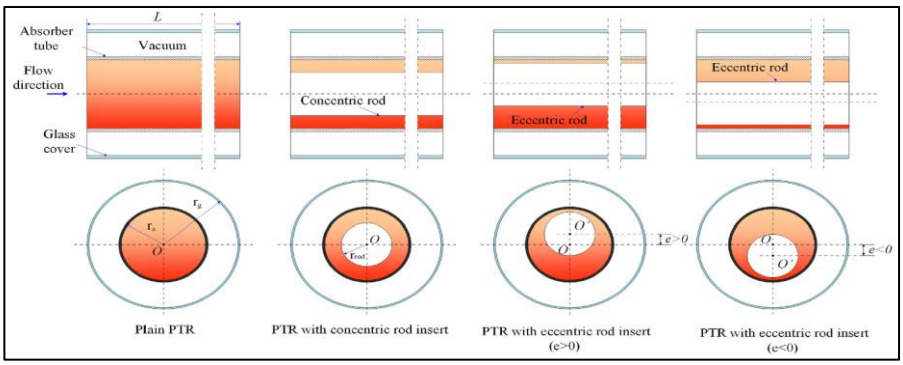

Figure 2.43 The geometry and grid of the plain PTC with concentric rod and eccentric rod inserts Chang et al. (2018) [97] (License Number: 4613530302030).

Bellos et al. (2018a) [98] used a star shape insert for enhancing the thermal performance of PTC. SolidWorks Simulation Studio was used to conduct the the analysis and comapred against a varified model. A total of 16 cases were examined with a fin length range of 15 to 30 mm and fin thickness range of 2 to 5 mm as shown in Figure 2.44. The results revealed that the Nusselt number enhancement is up to 60% with thermal losses decrement up to 14%. It was inferred that the thickness of 5 mm and fin length range of 20 to 30 mm were the optimum paramters for star insert fins. It was also pointed out that the utilisation of flow inserts would decrease the absorber circumferential temperature range and this would in turns decrease the failure danger caused by the thermal stresses. It was observed that about 15% maximum decreament in the temperature range could be achieved with star insert compared to smooth absorber tube.

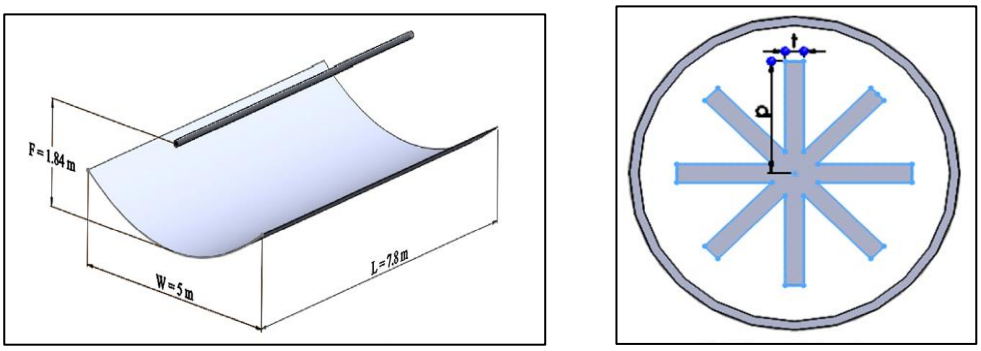

(a) (b)

Figure 2.44 (a) The examined PTC, (b) Star insert shape, (c) Star flow insert cases Bellos et al. (2018a) [98] (License Number: 4613540771277).

Bellos et al. (2018b) [99] exploited the results of their previous studies and investigated the internal fins best number and location in a PTC absorber using multi-objective procedure as shown in Figure 2.45. The analysis was conducted with SolidWorks Flow Simulation using rectangular fins. It was concluded that the internal fins should be located in the absorber tube's lower part where the heat flux is highly concentrated. The results affirmed that the optimum case was with an absorber tube having three fins in its lower part (β=0°, β=45° and β=315°) with thermal efficiency of 68.95% higher than the efficiency of the case with one fin.

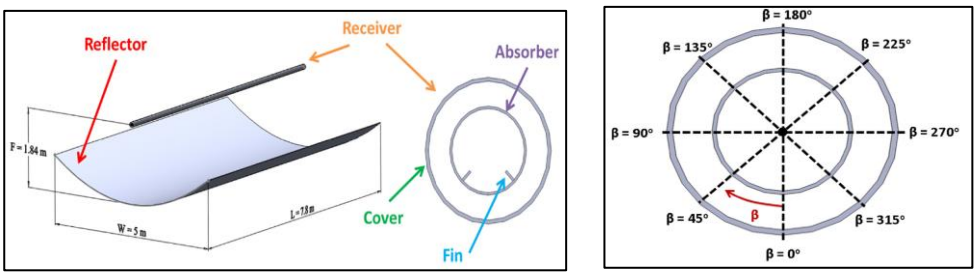

(a) (b)

Figure 2.45 (a) The examined PTC with its internally finned absorber, (b) Internal fins locations in the absorber tube Bellos et al. (2018b) [99] (License Number: 4613540976165).

Bitam et al. (2018) [100] conducted a 3D numerical model to investigate thermal effectiveness in a PTC having conventional straight and smooth tube (CSST) receiver is replaced by a newly designed with a S-curved/sinusoidal tube receiver using synthetic oil as shown in detailed in Figure 2.46. It was noticed that the mean Nusselt number increased by 45%-63%, while the friction coefficient increased by less than 40.8%, which leads to a maximum performance evaluation criterion about 135%. The maximum CTD of the PTR S-curved tube decreased below 35 K for all cases studied which in turns leads to both thermal stresses and heat losses reduction. The thermal augmentation overcomes the corresponding pressure loss by a factor less than 1.35.

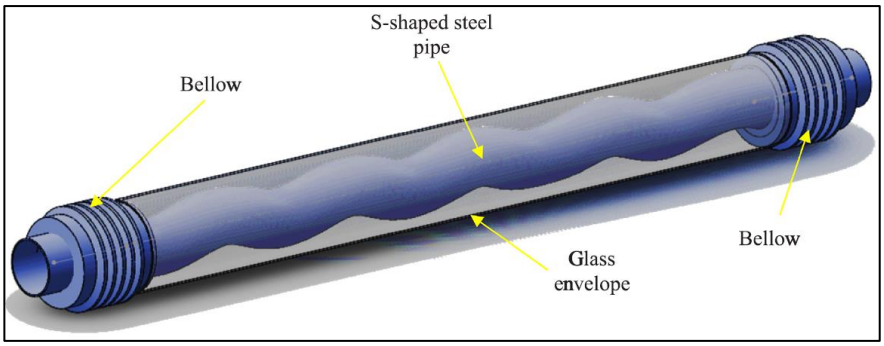

Figure 2.46 (a) The representative cross-section, (b) setup of the novel PTR, (c) 3D schematic view of the PTR Bitam et al. (2018) [100] (License Number: 4615170673264).

Tripathy et al. (2018) [101] performed thermal-fluid and structural analyses of absorber tube used in PTC with different materials using computational approach and utilising Therminol VP1 as shown in Figure 2.47. Steel, copper, aluminum and

bimetallic (Cu-Fe) and tetralayered laminate (Cu-Al-SiC-Fe) were used. It was found that there is no influence for the absorber's material change on the heat transfer, but it does have a remarkable influence on the bending of the tube because of the thermal expansion and self-weight. The results revealed that the steel tube and copper tube absorbers have poor circumferential temperature distributions and higher self-weight and lower mechanical strength respectively. Thus, it was suggested to use a bimetallic tube, which decreases the deflection by 7-15% compared to steel. Besides, tetra-layered laminate absorber tube enhanced the temperature profile and decreased the optimum deflection by 45-49% compared to steel. Hence, this approach could be used as a quick and effective approach to obtain the structural performance under non-uniform thermal conditions.

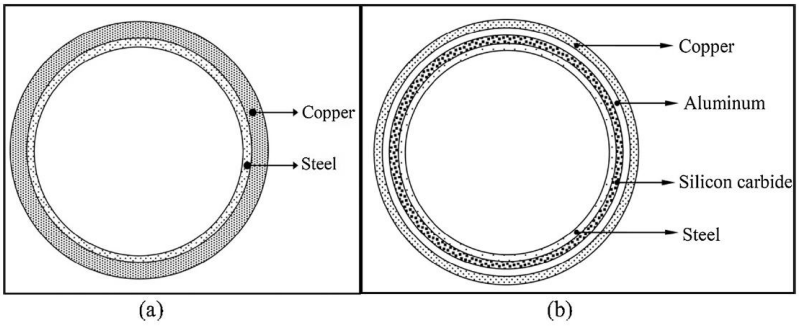

Figure 2.47 (a) Bimetallic absorber tube, (b) Tetra-layered laminate absorber tube Tripathy et al. (2018) [101] (License Number: 4615170858690).

Okonkwo et al. (2018) [102] modelled a commercially available PTC using the engineering equation solver (EES). The study compared the exergetic performance (exergy losses and exergy destruction) of four different geometries: conventional tube, longitudinal finned tube, tube with twisted tape insert, and converging-diverging tube as shown in Figure 2.48. Different combinations of inlet temperature and volumetric flow rate were studied for Therminol VP-1 and Al_2O_3-oil nanofluids. The outcomes have shown that the converging-diverging geometry was observed to achieve the thermal and exergetic efficiencies of 65.95% and 38.24% respectively. It was found that the optical losses accounted for the main cause of exergetic losses with 24.5% for all the examined cases. The exergy destroyed accounted for 59.7% in the converging-diverging tube at 350 K and 54.7% for the smooth absorber tube at the same temperature. It was inferred that the use of Al_2O_3-oil nanofluid with the converging

diverging receiver enhanced the exergetic efficiency of the PTC by 0.73%.

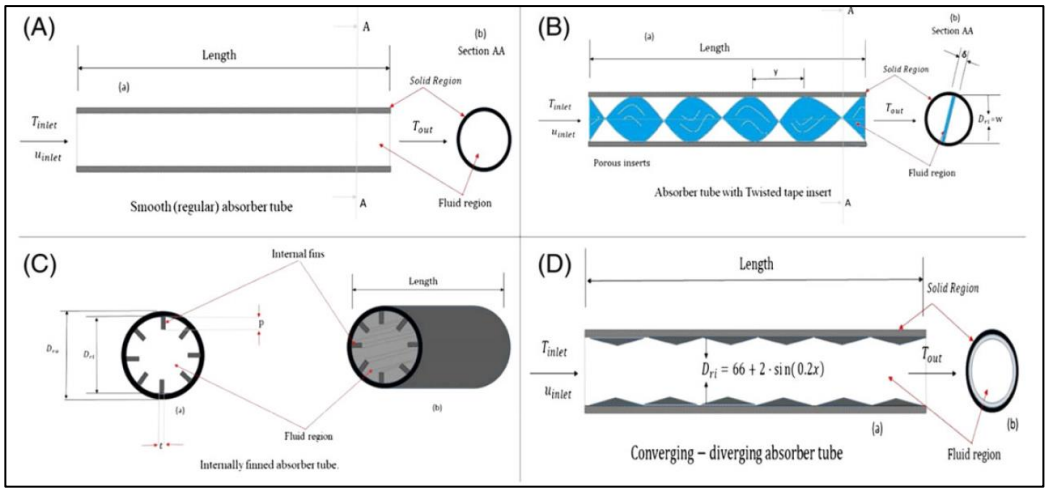

Figure 2.48 Schematic illustration of (A) smooth tube, (B) tube with twisted tape insert, (C) internally finned tube, (D) Converging-diverging tube Okonkwo et al. (2018) [102] (License Number: 4615170858783).

Rawani et al. (2018) [103] compared the performance of various types of twisted tape inserts namely square cut, oblique delta-winglet, alternate clockwise and counter-clockwise, and serrated in PTC absorber tube as shown in Figure 2.49. They used their developed mathematical model with the aid of C^{++} language to assess the PTC thermal performance. The results revealed that the serrated twisted tape inserts with x= 2 provides the highest performance compared with other inserts. It was found that the Nusselt number with serrated twisted tape insert (x=2) is 3.56 times over PTC with plain absorber tube with thermal efficiency enhancement of 13.63 % and exergy efficiency of 15.40 %. It was concluded that the serrated twisted tape provides the lowest entropy generation.

Sl. No	Types of twisted tape	Diagram
1	Plain twisted tape	
2	Square cut twisted tape	
3	Oblique delta-winglet twisted tapes	
4	Alternate clockwise and counter clock wise twisted-tape	
5	Serrated twisted tape	

Figure 2.49 Various twisted tape inserts types used Rawani et al. (2018) [103].

Benabderrahmane et al. (2020) [104] studied numerically the flow and thermal performance of tube receiver with central corrugated insert for PTC system as shown in Figure 2.50. The Monte Carlo ray-tracing method (MCRT) coupled with finite volume method (FVM) was utilised. The outcomes revealed that the utilisation of corrugated insert could significantly augment the overall thermal effectiveness in the range of 1.3-2.6. The increment of corrugation's twist ratio and the decrement of pitch between two corrugations increased the thermal performances.

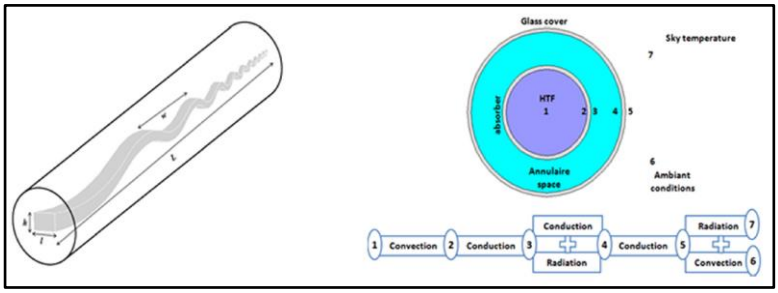

(a) (b)

Figure 2.50 (a) Corrugated PTC system, and (b) heat transfer modes used in their study Benabderrahmane et al. (2020) [104] (License Number: 4031141658252).

Khan et al. (2020) [105] compared numerically energetic and exergetic performance of absorber tube with twisted tape insert and tube with longitudinal fins using Al_2O_3/water with the aid of EES as shown in Figure 2.51. The outcomes revealed that the absorber tube with twisted tape insert has the highest thermal efficiency of 72.26%, compared to a tube with internal fins (72.10%), and smooth absorber tube (71.09%). It was confirmed that the utilisation of nanofluid and passive techniques produced better thermal effectiveness.

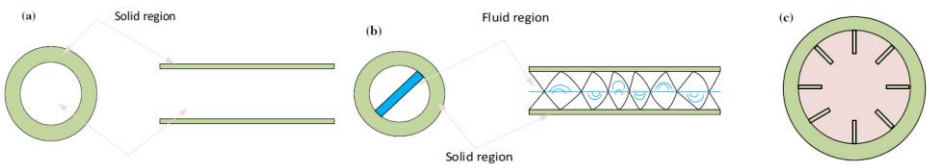

(a) (b) (c)

Figure 2.51 (a) Smooth PTC tube, and (b) PTC tube equipped with twisted tape insert, and (c) PTC tube equipped with internal fins Khan et al. (2020) [105] (License Number: 5030041356315).

A summary of literature studies on PTC utilising various passive techniques are listed in Table 2.3 chronologically.

Table 2.3 Literature studies carried out to date on PTC using various passive techniques.

Reference	Study Type	Passive Technique	Fluid Used	Phase Mode	Flow Type	Remarks
Reddy and Satyanaray ana, 2008 [57]	Numerical	Porous finned receiver	Therminol-VP 1	Single phase	Mass flow rate was in the range of 0.5 - 6.5 kg/s	The natural convection heat loss was lower for porous receiver than the plain receiver. The optimal thermal and flow fields were found with a trapezoidal porous fin of 4 mm thickness, tip-to-base thickness ratio (λ) of 0.25 and a ratio of consecutive fin distance to diameter of the receiver (*l*/*d*) of 1.
Reddy et al. 2008 [58]	Numerical	Porous finned receiver	Therminol-VP 1	Single phase	Turbulent flow Re number was in the range of 150000 - 11500 000	It was found that the porous inserts in PTC receiver improved the heat transfer by 17.5% with a pressure loss of 2 kPa.
Kumar and Reddy, 2009 [59]	Numerical	Porous disc receiver	Therminol-VP 1	Single phase	Turbulent flow Re number was in the range of 40000 - 250000	The maximum heat transfer coefficient is achieved in top half-porous disc receiver with H = 0.5di, w = di at θ = 30° with reasonable drag. The increase in Nusselt number for optimum receiver configuration is 64.2% compared to tubular receive with pressure drop of 457 Pa.
Munoz and Abanades 2011 [60]	Numerical/ CFD	Helical internal fins	Syltherm 800 oil	Single phase	Mass flow rate was 47.7 L/min	The results provide a collector enhancement efficiency of 3% and increase of pressure losses of 40%. This would lead to a 2% plant performance enhancement with a reduction of operation and maintenance costs.
Kumar and Reddy 2012 [61]	Numerical	Porous finned receiver with different inclinations	Therminol-oil 500 and water	Single phase	Mass flow rate was in the range of 0.5 - 1 kg/s	The optimum porous disc receiver improved the heat transfer rate and reduced the pumping power losses using therminol oil-55 higher than water as compared to plain receiver.
Cheng et al. 2012 [62]	Numerical	Unilateral longitudinal vortex generators	Oil syltherm-800	Single phase	Turbulent flow Re number was 3.8×10^4 - 7.0×10^5	The thermal loss of the PTR reduced by 1.35-12.1% to that of the smooth PTR. The comprehensive enhanced heat transfer performance is higher when the Re number is larger at the same inlet temperature.
Islam et al. 2012 [63]	Numerical	Flow restriction device (plug)	Syltherm-800	Single phase	Turbulent flow Re number was in the range of 14235 – 15943	They have identified the non-uniformity of the heat flux and temperature profiles around the tube were physical issues. The results affirmed that the optical simulation and computational heat transfer simulation can be done separately.
Aldali et al. 2013 [64]	Numerical	Helical internal fins	Water	Single phase	Velocity was in the range of 0.257 - 0.354 m/s	The thermal gradient for the pipe without a helical fin is significantly higher compared with the pipe with helical fins. Aluminium pipe has much lower thermal gradient compared to steel pipe.
Wang et al. 2013 [65]	Numerical	Metal porous foam	Superheated steam	Single phase	Re number was in the range of 1×10^5 - 1×10^6	The highest thermal performance is achieved when geometrical parameter (H) equals to 0.75. The Nu number increased 10-12 times associated with friction factor increment of 400-700 times and the PEC increased from 1.1 to 1.5. The thermal stresses were significantly reduced when the circumferential temperature

						difference on the receiver's tube outer surface decreased by 45%.
Ghasemi et al. 2013 [66]	Numerical	Two segmental rings	Therminol 66	Single phase	Re number was in the range of 30000 – 250000	The inclusion of porous rings enhanced the thermal efficiency and the increases of distance between two rings reduced the Nusselt number. The optimum thermal performance was achieved for the case when 'Q' = 0.75d 'the distance between porous two segmental rings' and 'd/D'= 0.6 'inner diameter/inner diameter ratio' respectively.
Ghadirijafarbeigloo et al. 2013 [67]	Numerical	Perforated louvered twisted tape (PLTT)	Behran thermal oil	Single phase	Turbulent flow Re number was in the range of 5000 - 25000	PLTT provided higher Nusselt number and friction factor compared to a smooth tube. It is observed that LLT can provide a maximum of 150% enhancement for Nusselt number and 210% for friction factor.
Too and Benito 2013 [68]	Mathematical	Helical coil /wire insert, twisted tape insert, dimpled tube, porous foam	Air, CO_2 and Helium	Single phase	Turbulent flow Re number was in the range of 7083 - 42499	Unrivaled overall thermal and hydraulic performance was obtained when using tubes with deeper protrusions compared to a plain tube. Working gases such as CO_2 and He can decrease the total pressure drop in a solar tubular gas receiver.
Waghole et al. 2014 [69]	Experimental	Twisted tape inserts	Silver-water Nanofluid	Single phase	Turbulent flow Re number was in the range of 500 - 6000	The thermal and hydraulic performance of silver nanofluid is higher compared to water in a PTC receiver. The Nusselt number, friction factor and enhancement efficiency were observed to be 1.25-2.10 times, 1.0-1.75 times and 135-205%, respectively, compared with the plain receiver of PTC.
Song et al. 2014 [70]	Numerical	Helical screw-tape inserts	Downtherm-A	Single phase	Turbulent flow Re number was in the range of 5000 - 75000	The influence of the transversal angle (β) on the heat flux distribution was found more significant than the longitudinal angle (φ). It is observed that the helical screw-tape inserts remarkably decreased the heat losses and maximum and circumferential temperature differences.
Mwesigye et al. 2014 [71]	Numerical	Perforated plate insert	Sytherm-800	Single phase	Turbulent flow Re number was in the range of 1.02×10^4 - 7.38×10^5	The inclusion of perforated plate inserts was shown to enhance the thermodynamic performance and to reduce the temperature gradients of the receiver. The modified thermal efficiency increased between 1.2% and 8%.
Mwesigye et al. 2015 [72]	Numerical	Perforated plate insert	Al_2O_3- Synthetic oil	Single phase	Turbulent flow Re number was in the range of 3560 - 1.15×10^6	The thermal performance and the thermal efficiency increased up to 38% and 15% respectively. It was found that high inlet temperatures and low flow rates show remarkable enhancement in the receiver's thermal efficiency.
Syed Jafar and Sivaraman 2014 [73]	Experimental	Nail twisted tapes inserts	Al_2O_3 - water nanofluid	Single phase	Laminar flow Re number was in the range of 710 -2130	The insertion of nail twisted tape in an absorber of PTC using nanofluids can greatly enhance its thermal performance and increase its friction factor
Mwesigye et al. 2015	Numerical/ optimisation	Perforated plate insert	Sytherm-800	Single phase	Turbulent flow Re number was in the	It was found that the entropy generation decreased when the orientation angle increased. Increasing the plate size and decreasing

[74]					range of 1.02×10^4 - 1.36×10^6	the plate spacing decreased the optimal Re number. The entropy generation rates are reduced by 53% below the optimal Re number.
Huang et al., 2015 [75]	Numerical	Helical fins, protrusions and dimples	Therminol-VP1	Single phase	Turbulent flow Re number was in the range of 1×10^4 - 2×10^4	The dimpled receiver tubes have unrivalled thermal performance compared with that having helical fins or protrusions. The dimples with deeper depth, narrower pitch and more numbers in the circumferential direction enhanced the thermal performance while other arrangements shown insignificant effect.
Chang et al. 2015 [76]	Numerical	Twisted tape inserts	Molten salt	Single phase	Turbulent flow Re number was in the range of 7485 - 30553	Insert twisted tape significantly improved the uniformity of temperature distribution of tube wall using molten salt. The decreases of clearance rate (*C)* and twisted rate enhanced the heat transfer effectively. The decreases of clearance rate and twisted rate lead to increase the friction factor.
Lu et al. 2015 [77]	Theoretical	Spirally grooved pipe	Molten salt	Single phase	Turbulent flow Re number was in the range of 5000 - 15000	The increment of flow velocity and groove height increased the absorption efficiency and decreased the wall temperature. The heat absorption efficiency increased by 0.7%, and the maximum bulk fluid temperature increased to 31.1 °C.
Reddy et al. 2015 [78]	Experimental work	Porous disc enhanced receiver	Water and oil	Single phase	Turbulent flow Flow rate was in the range of 100 -1000 L/h	The temperature gradient between the receiver's wall surface and fluid was less when using porous disc enhanced receiver compared to classical tubular receiver. The performance of PTC with porous disc enhanced receiver is much better than other receiver configurations.
Diwan and Soni 2015 [79]	Numerical	wire-coils insert	Water	Single phase	Turbulent flow Mass flow rate was in the range of 0.01388 – 0.099 kg/s	The introduction of wire coils increased the Nusselt number by 104% to 330%. Good thermal performance was obtained when using wire-coils inserts with pitch value from 6 – 8 mm at lower flow rates and using pitch of 8 mm at higher flow rate.
Mwesigye et al. 2016 [80]	Numerical	Wall-detached twisted tape inserts	Sytherm-800	Single phase	Turbulent flow Re number was in the range of 10260 - 1353000	The increase of thermal performance of 169%, and increase in thermal efficiency up to 10% were achieved compared with a plain absorber tube. A 58% decrease in the entropy generation rate was also attained.
Bellos et al. 2016 [81]	Numerical	Converging-diverging absorber tube	Thermal oil, thermal oil- nanoparticles (Al_2O_3), pressurized water	Single phase	Turbulent flow Re number was in the range of 4000 - 25000	The utilisation of Al_2O_3-thermal oil nanofluid improved the mean efficiency by 4.25% while the use of pressurized water by 6.34%. The results showed 4.55% mean efficiency enhancement compared to plain tube geometry. At higher fluid temperature levels, the increase in the efficiency was greater.
ZhangJing et al. 2016 [82]	Numerical (optimized by Genetic Algorithm (GA)	Porous insert	Water/steam	Single phase	Turbulent flow Re number was in the range of 50 000- 900 000	The porous insert receiver tube exhibited higher thermal performance than that of the plain receiver. It achieved flawless thermo-hydraulic performance by using similar optimized porous insert, which is difficult to achieve by utilising the plain receiver.

Fuqiang et al., 2016 [83]	Numerical	Asymmetric outward convex corrugated tube	Thermal oil- D12	Single phase	Turbulent flow Re number was in the range of 10×10^3 to 98×10^3	The utilisation of asymmetric outward convex corrugated tube as a receiver of PTC improved the thermal performance and decreased the thermal strain effectively. A maximum 148% and 26.8% of overall thermal performance and von-Mises thermal strain respectively were achieved.
Jaramillo et al. 2016 [84]	Numerical	Twisted tape insert	Water, air	Single phase	Turbulent flow Re number was in the range of 1389.7 - 8338.03	The Nusselt number, the removal factor, the friction factor and the thermal efficiency increased as both the twist ratio (y/w) and the Reynolds number decreased. These quantities did not present an enhancement when the twist ratio increased.
Benabderrahmane et al. 2016 [85]	Numerical 3D	Longitudinal rectangular/ triangular fins	Downtherm-A oil with different nanofluids Al_2O_3, Cu, Sic, C and Cu	Single phase	Turbulent flow Re number was in the range of 2.57×10^4 - 2.57×10^5	It is observed there was a remarkable heat transfer enhancement from 1.3 to 1.8 times. The Cu, and SiC nanoparticles improved heat transfer significantly than C, and Al_2O_3 nanoparticles. The utilisation of fins and nanofluid provided greater thermo-hydraulic performance.
Chang et al. 2017 [86]	Numerical	Concentric and eccentric pipes	Molten salt	Single phase	Turbulent flow Re number was in the range of 1×10^4 - 9×10^4	Inserts can significantly improve heat transfer performance of more than 1.64 times than a PTR without inserts when the PTR is inserted by A3 (larger diameter). The eccentric pipe inserts of B3 (larger eccentricity) performed significantly better than the concentric tube inserts for its excellent performance in decreasing the maximum temperature of absorber tube and molten salt.
Ghasemi and Ranjbar, 2017 [87]	Numerical	Porous rings	Syltherm 800	Single phase	Turbulent flow Re number was in the range of 30000 – 250000	The heat transfer characteristics enhanced by inserting the porous rings in tubular solar absorber. The decrement in the distance between porous rings and the increment of the inner diameter of the porous rings would increase and decrease the heat transfer, respectively.
Bortolato et al. 2017 [88]	Experimental	Flat absorber	SWCNH - water nanofluid	Single phase	Mass flow rate was 350 kg/h	The application of a carbon nanohorn-based nanofluid displayed an efficiency comparable to that obtained with a surface receiver tested in the same system. However, such performance was not maintained for a long time because of lack of stability of the absorbing fluid.
Rawani et al. 2017 [89]	Mathematical	Serrated twisted tape insert	Therminol VP-1	Single phase	Turbulent flow Re number was in the range of 3000- 9000	The thermal efficiency enhancement was 15.7%, while the exergy efficiency was 12.10% and enhancement factor was 1.157 for similar conditions.
Jamal-Abad et al. 2017 [90]	Experimental	Copper porous media	Water	Single phase	Flow rate was in the range of 0.5 - 1.5 L/min	An improvement in Nu number was observed by using metal foam. The friction factor increased considerably when tube was filled with metal foam. The removed energy and absorbed energy parameter of the collector decreased by applying copper foam inside the absorber.
Bellos et al. 2017 [91]	Numerical	Internally finned / evacuated tube absorber	Oil syltherm-800	Single phase	Turbulent flow mass flowrate was in the range of 50 - 250 L/min	The optimum case was achieved with an absorber with 10 mm fin length and 2 mm fin thickness. The thermal efficiency was improved around 0.82%, the Nusselt number increased 65.8%, whilst the friction factor and the pressure losses were doubled compared to the

						smooth case.
Bellos et al. 2017 [92]	Theoretical and Numerical	Internally finned absorber	Oil syltherm-800	Single phase	Turbulent flow mass flowrate was in the range of 50 - 250 L/min	The optimum case with 20 mm fin length and 4 mm fin thickness was achieved. The thermal efficiency and thermal enhancement index were increased by 1.27% and 1.483 respectively, whilst the Nusselt number was confirmed to be 2.65 times higher than the smooth case.
Bellos et al. 2017 [93]	Theoretical	Internal longitudinal fins absorber	Air, Helium, and CO_2	Single phase	Turbulent flow mass flowrate was in the range of 50 - 250 L/min	Higher exergetic efficiency was obtained with fins having 10 mm length. Helium was the suitable working fluid exergetically. Helium was the optimum solution up to 290°C and after this point, carbon dioxide performed better.
Zhu et al., 2017 [94]	Numerical	Wavy-tape insert	Sytherm-800	Single phase	Turbulent flow The mass flowrate was in the range of 240 - 720 L/min	The Nusselt number was improved by 261-310%, which benefits to the decreases of both PTR structure temperature and total heat loss. The heat loss was found to be reduced by 17.5-33.1%, depending on the HTF flow rate.
Xiangtao et al. 2017 [95]	Numerical/ CFD	Pin fin array absorber	Thermal oil- D12	Single phase	Re number was in the range of 2000 to 18000	The utilisation of tube receiver with pin fin arrays inserts increased the Nusselt number up to 9% and the thermal performance factor up to 12%.
Huang et al., 2017 [96]	Numerical	Dimpled receiver	Therminol-VP1	Single phase	Turbulent flow Re number was 2×10^4	The average Nusselt number and friction factor in dimpled receiver tubes under non-uniform heat flux (NUHF) were larger than those under uniform heat flux (UHF). The deep dimples (d/D_i= 0.875) were good performing compared with shallow dimples (d/D_i= 0.125) at similar Grashof number.
Chang et al. 2018 [97]	Numerical	Concentric rod and eccentric rod	Molten salt	Single phase	Turbulent flow Re number was in the range of 10000 – 30000	The temperature profile can be stabilised and the maximum temperature can be significantly decreased with the increasing of dimensionless diameter (B) and dimensionless eccentricity (H), which helps to reduce the PTR thermal deflection and increase its reliability.
Bellos et al. 2018 [98]	Numerical	Insert with star shape	Syltherm 800 (thermal oil)	Single phase	Volumetric flow rate was 150 L/min	The thermal efficiency enhancement increased when the inlet temperature increases. Higher dimensions of the insert provided to higher thermal performance enhancement. The use of inserts increased the pressure drop many times while the pumping loss was low in all cases studied.
Bellos et al. 2018 [99]	Numerical	Fins with different locations and number	Syltherm 800 (thermal oil)	Single phase	Volumetric flow rate was 150 L/min	The optimum absorber was the one with three fins located in its lower part (β=0°, β=45° and β=315°) with thermal efficiency of 68.59%.
Bitam et al. 2018 [100]	Numerical/ CFD	S-curved sinusoidal tube receiver	Synthetic oil	Single phase	Mass flow rate was in the range of 2 - 9.5 kg/s	The Nusselt number and friction factor increased by 45%-63%, less than 40.8%, respectively, which provided 135% maximum performance evaluation criteria. The maximum of 35 K decrement in the circumferential temperature difference resulted in the reduction of thermal stresses and heat losses.
Tripathy et	Numerical	Nil	Therminol VP-1	Single phase	Mass flow rate was in	Steel absorber tube has poor circumfere-ntial temperature profiles;

al. 2018 [101]					the range of 3.4 - 17.6 kg/s	however, copper has better thermal characteristics compared to steel. The bimetallic tube provided 7-15% decline in the deflection compared to steel. A tetra-layered laminate absorber tube improved temperature profile and provided 45-49% decline in the deflection compared to steel.
Okonkwo et al. 2018 [102]	Numerical	Longitudinal finned absorber, twisted tape tube, converging-diverging absorbers	Al_2O_3-Therminol VP-1 nanofluid	Single phase	Mass flow rate was in the range of 25-200 L/min	The converging-diverging absorber produced the best exergetic enhancement of 0.65% using Therminol VP-1 and 0.73% using Al_2O_3/Therminol VP-1 nanofluid.
Rawani et al. 2018 [103]	Mathematical	Square cut, Oblique delta-winglet, alternate clockwise and counter-clockwise, and Serrated	Therminol VP-1	Single phase	Mass flow rate was in the range of 0.06 – 0.16 kg/s	The serrated twisted tape inserts (x=2) produced Nusselt number of 3.56 and 3.19 times over PTC plain absorber. The thermal efficiency enhancement was 13.63% and the exergy efficiency was 15.40%. The serrated twisted tape provided the lowest entropy generation.
Benabderrahmane et al. (2020) [104]	Numerical	Corrugated tube insert	Nitrate salt	Single phase	Turbulent flow Re number was in the range of 10^4- 10^6	The outcomes revealed that the utilisation of corrugated insert could significantly augment the overall thermal effectiveness in the range of 1.3-2.6. The increment of corrugation's twist ratio and the decrement of pitch between two corrugations increased the thermal performances.
Khan et al. (2020) [105]	Numerical	twisted tape insert and longitudinal fins	Al_2O_3/water	Single phase	Turbulent flow Re number was in the range of 10^3- $5*10^5$	The outcomes revealed that the absorber tube with twisted tape insert has the highest thermal efficiency of 72.26%, compared to a tube with internal fins (72.10%), and smooth absorber tube (71.09%).

It can be clearly noticed from Table 2.3 that the vast majority of the research efforts, which have been carried out by different researchers at different countries around the globe using various passive techniques with different shapes and configurations, are mainly done by China with 27%, followed by India with 20%, Greece with 10%, South Africa with 7%, and other countries with 1-3% as can be seen in Figure 2.52.

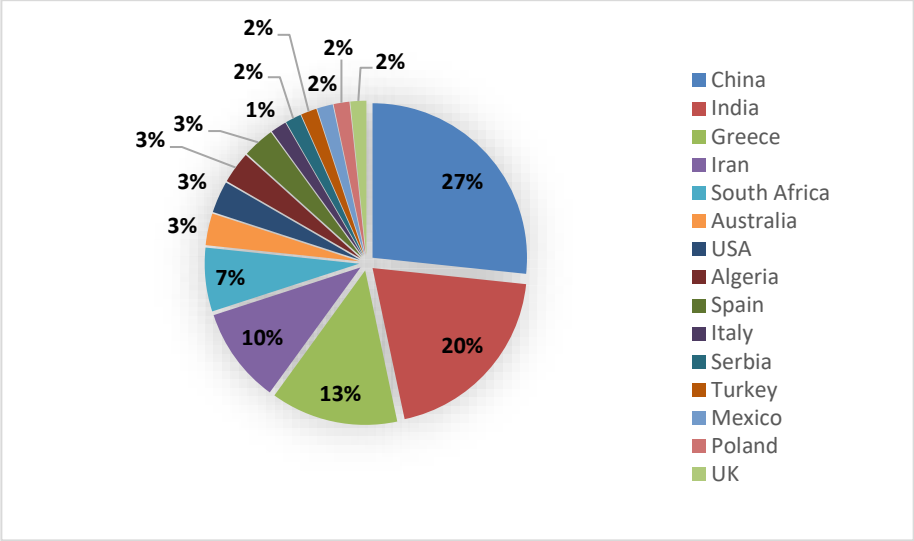

Figure 2.52 Research efforts on PTC equipped with passive techniques around the globe.

2.7 Types of Working Fluids used in PTCs

Recently, PTC technology has been widely applied in concentrating power plants, hydrogen production or other industrial processes with high temperature requirement. In any case, the huge temperature gradient is the basic explanation of instigating the thermal twisting and harm of PTC. Accordingly, numerous scientists have embraced the strategy for heat transfer upgrade to diminish the temperature gradient by utilising diverse operating liquids. The regular working liquids utilised in PTC frameworks, for example, water, thermal oils and molten salts cannot work in high temperatures. However, water/steam power plants depend on the requirements of high operating temperatures and the sophisticated control strategies. The utilisation of thermal oils as Syltherm 800, Therminol VP-1, Therminol 66, Therminol D-12, Dowtherm A and Behran oil is common in indirect frameworks with heat exchangers for the heat creation. Interestingly, the thermal oils can work up to 400 °C with a sensible pressure

level (close to 15 bars). However, the utilisation of thermal oils prompts moderately low thermal execution, and it requires high maintenance cost. The up and coming age of working liquid in PTC systems is molten salts (particularly nitrate salts) giving higher edge in the sun-oriented energy to power conversion. Molten salts are normally nitrate salts, for example (60% $NaNO_3$ - 40% KNO_3), which can work up to 550°C, giving conceivable outcomes for higher thermal effectiveness. However, these working liquids required high security in the activity because of the freezing threat which can be happened in temperature levels from 100-230°C. In this manner, the molten salts must be held upper to a lower limit near 200°C because of solidification threat. Different types of fluids such as liquid metals as sodium and gases (air, helium, nitrogen and CO_2) at higher temperatures can also be utilised but their operation is not yet settled at this point.

2.7.1 Conventional Fluids

There are numerical and experimental research articles have been conducted by diverse investigators on thermal augmentation using different types of classical fluids in PTC, which are comprehensively summarised below, in the following sections.

Cheng et al. (2010) [106] analysed numerically 3D coupled thermal characteristics of Syltherm 800 oil in a PTC receiver tube. The MCRT method and CFD simulation using a commercial FLUENT software were combined and used. Three typical testing models were chosen (no-wall model, no-radiation model and unbridged model) to provide an extra illustration of the thermal mechanism in PTC tube. The outcomes indicated that the radiation loss in Model 3 is up to 153.70 W/m^2. It was revealed that the radiation loss should be decreased as much as possible to enhance the PTC's efficiency. The proposed 3D numerical models and methods can not only be used effectively to study the coupled heat transfer characteristics on known factors but also those difficult or costly to be tested.

Tao and He (2010) [107] developed a 2D numerical model for coupled heat transfer process in a PTC tube. The local temperature gradient, and local Nu number were investigated. The outcomes show that the natural convection influence must be

considered when Ra number is larger than 10^5. When the tube diameter ratio increased, the Nusselt number in inner tube (Nu_1) increased and the Nusselt number in annuli space (Nu_2) decreased. It was found that Nu_1 decreased and Nu_2 increased when the tube wall thermal conductivity increased. However, the Nu number and average temperatures were less affected when thermal conductivity is greater than 200 W/m.K. It was observed that, because of the natural convection influence, the local Nu number on the inner tube increased until it achieved its optimum value then it gradually diminished again.

He et al. (2011) [108] solved the complex coupled heat transfer problem in a PTC system using coupled simulation method of MCRT and FVM. The influences of different parameters such as concentration ratio (CR) and rim angles were investigated. The outcomes revealed that when CR increased, the heat flux profiles look smoother, the angle span became larger and the shadow influence of absorber tube got more vulnerable. However, when the rim angle raised, the heat flux maximum value became lower, and the curve moved towards the direction of φ=90°. Nevertheless, the temperature increase was only improved when CR increased and when the rim angle greater than 15° its impact on the thermal fields was discarded. It was also noticed that when more rays were reflected by the glass tube, and the temperature rise is much lower when the rim angle is around 15°.

Cheng et al. (2012) [109] combined FVM and MCRT method to solve 3D computational domain of PTC framework. Different working fluid types such as Therminol 1P1, Syltherm 800 and residual gas were used. The results show that the properties of these fluids and operating conditions affected the thermal and flow fields and the receiver's temperature profile, thus affected the thermal loss and the collector efficiency. It was concluded that the average Nusselt number of the two synthetic oil increased and the average friction factor decreased when the inlet fluid temperature increased. It was also observed that the two synthetic oil fluids have a better thermal effectiveness and a lower pressure drop than that of the two salts. The thermal loss of four residual gas conditions increased and the collector efficiency decreased when the fluids inlet temperature increased, respectively. The portions of the total thermal loss caused by radiation increased when fluids inlet temperature increased.

Hachicha et al. (2013) [110] presented heat transfer model which includes different detailed elements of the receiver of PTC using finite volume method. The energy balance equation was implemented for each model's element along with the ray trace techniques. They used crossed string method to include the thermal radiative heat transfer. The results obtained were compared with the available experimental ones, with some observed variation at higher temperatures. These variations were caused by the optical properties of the heating element, and potential mistakes came from the utilised heat transfer coefficient relationships. It was thus inferred that the developed model was feasible for estimating the heating element optical and thermal patterns under various working situations.

Mwesigye et al. (2013) [111] and Mwesigye et al. (2014) [112] performed numerical simulation for entropy generation analysis in a PTC receiver at various parameter values. Using the first law of thermodynamics, the results revealed that the Nusselt number and friction factor did not change when the proportion ratios varied. The second law of thermodynamics indicated that the entropy generation values in the receiver's tube increased as the proportion ratios increased. The results also show that at low flow rate values the Bejan number was around 1 and at the highest flow rate it was between 0 and 0.24. It was found that the entropy generation could be minimized when the entropy generation caused by the thermal and fluid irreversibilities in the receiver's tube is minimized.

Chang et al. (2014) [113] presented experimental and numerical analysis of thermal effectiveness in PTC absorber pipes utilising non-uniform heat flux in high Reynolds number range as shown in Figure 2.53. The results revealed that the fluid temperature and pipe wall profiles are very irregular in all three directions. The wall temperature profile of an absorber tube varied with the tubes' angle θ, and the maximum temperature happened at $\theta = 180^{o}$. An empirical correlation for the wall temperature profile was proposed.

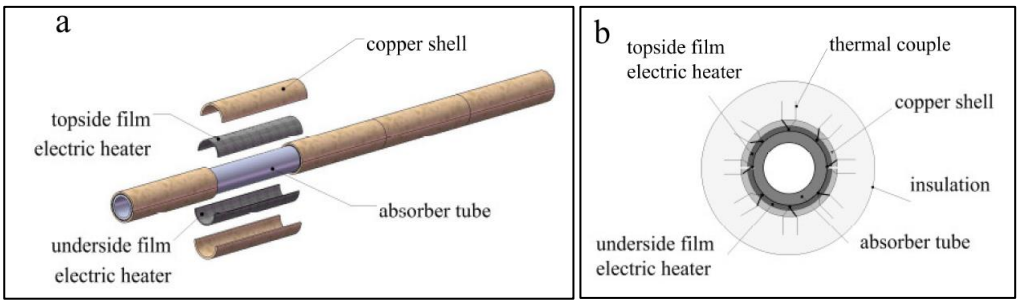

Figure 2.53 (a) Test section diagram, (b) Schematic diagram of the tube cross-section Chang et al. (2014) [113] (License Number: 4615760389838).

Wang et al. (2014) [114] examined the thermal physics mechanisms of PTC systems using a 3D simulation based on FVM to solve the coupled problem as shown in Figure 2.54. The performance of the PTCs using molten salt as a medium fluid was numerically studied, and the influences of other paramount parameters on the PTCs were investigated. The results revealed that the CTD of the absorber increased with DNI rising and decreased with the increase of medium fluid inlet temperature and inlet velocity. Furthermore, the numerical outcomes indicated that the non-uniform heat flux significantly affected the CTD of the absorber while it has a minimal impact on the thermal efficiency. The PTC's thermal efficiency using molten salt at 773 K is 7.90% lower than that using oil for typical work conditions.

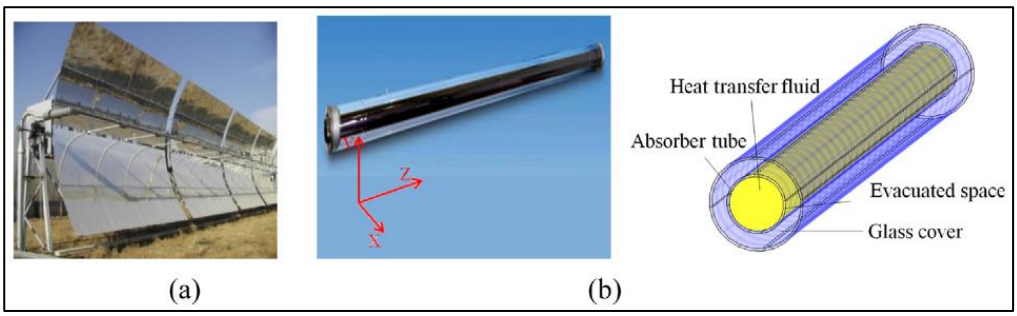

Figure 2.54 (a) Experimental platform with 600 m^2 in Langfang city used for modeling, (b) Schematic diagram of the PTC Wang et al. (2014) [114] (License Number: 4615770404855).

Wu et al. (2014) [115] simulated three-dimensional optics and temperature profile of a PTC receiver using the combination of a MCRT method and commercial software (FLUENT). The coupled heat transfer mechanisms and fluid flow were together considered. The detailed temperature history of the whole PTC receiver was obtained.

It was observed that the heat loss of the bellows was around 7% of the total heat loss if a heat convection coefficient 10 W/m^2 K was subjected on the bellows. The temperature difference with in the metal tube changes inversely with HTF velocity. In addition, the simulation results show the stagnation temperature of PTC receiver increased linearly with time, and can reach at 700 K in 130 s.

Cheng et al. (2014) [116] presented detailed comparative and sensitive analyses for different PTC systems to optimise their thermal and optical effectiveness. They used LAT73 Trough, T6R4 PTC system of different aperture widths, and T6R4 PTC system of different focal lengths under various working conditions. The results revealed that the PTC frameworks had various levels of sensitivity to various optical errors, with consistent optical accuracy requirements. When the aperture width is larger, there will be a high sensitivity of the PTC system to the optical errors. Thus, an ideal optimised focal length of 0.47 m can be determined accordingly, with a maximum optical efficiency of 87.28%. The PTC systems of different active receiver lengths or different glass cover diameters have little effects on the optical performance and little sensitivity to the optical errors. However, the PTC systems of different absorber diameters have relatively larger effects than that of them. It was found that when the absorber diameter is smaller, there will be more sensitivity to the optical errors. However, there may be some contradictory trends in the optical and thermal efficiencies for optimising some geometric parameters, such as the glass cover diameter.

Wang et al. (2015) [117] used a solar ray trace (SRT) and the finite element method (FEM) to analyse the coupled thermal and flow problem in a PTC framework. The heat flux trend was determined by the SRT method, and the influences of various working factors on the PTC's thermal effectiveness were numerically studied. The stress intensity and the thermal deformation profiles of the receiver were also examined. The results indicated that the CTD of the absorber decreased with the increases of inlet temperature and velocity of the working fluid and increased with the increment of the DNI. It was found that the CTD of the absorber tube reached 22-94 K when the inlet velocity was in the range of 1-4 m/s, the DNIs were 500-1250 W/m^2 and the inlet temperature was in the range of 373-673 K as shown in Figure 2.55. It was observed that the PTC's absorber tube thermal stress and deformations were greater than that of

the glass tube.

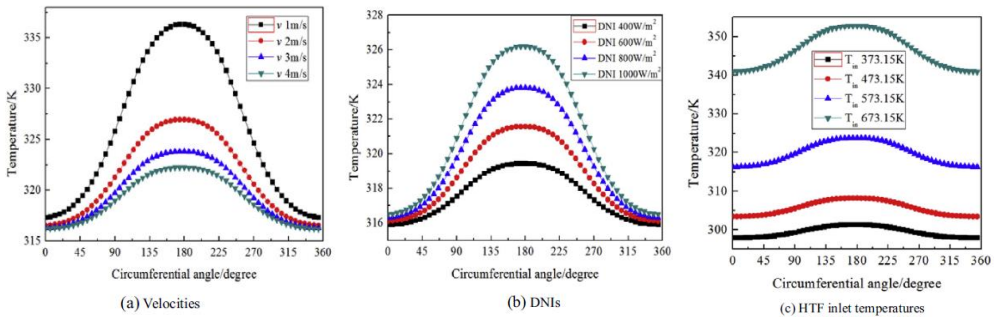

Figure 2.55 Temperature distributions of the outer surface of the cover Wang et al. (2015) [117] (License Number: 4615780671423).

Tzivanidis et al. (2015) [118] designed and simulated a small PTC model for different operating conditions using commercial software Solidworks. The goal of this study was to predict the efficiency of this model and to analyse the heat transfer phenomena that takes place. The results show that the PTC's thermal efficiency is more than 75% for high temperatures. The temperature distribution is non-uniform in the peripheral of the absorber. It was concluded that the Reynolds number is fully reliable on the water inlet temperature. This illustrates that the flow is laminar at low temperature level with a convection coefficient about 300 W/m^{2}K and the flow becomes turbulent at higher temperatures with a greater convection coefficient about 1000 W/m^{2}K.

Li et al. (2015) [119] analysed numerically mixed convective thermal effectiveness in a PTC receiver tube. The influence of buoyancy force under uniform heat flux (UHF) and non-uniform heat flux (NUHF) was analysed quantitatively. The effect of solar elevation angel on the thermal and flow fields was also investigated. The results revealed that there is noticeable difference in flow field and temperature profile between UHF and NUHF. The Nusselt number and friction factor of UHF case is greater than that under NUHF case for φ=0° and 30° and less than that under NUHF case for φ=60° and 90° as shown in Figure 2.56. It was found that it is in appropriate to utilise the experimental correlations for combined/forced convection to carry out the thermal design of a PTC heated by NUHF.

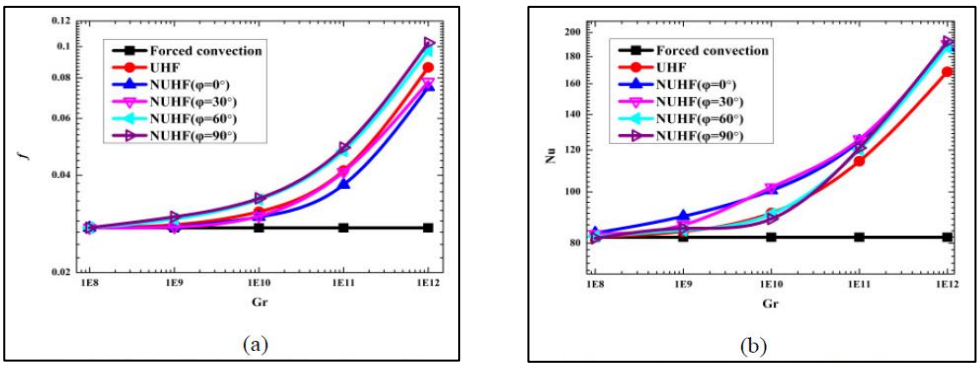

Figure 2.56 (a) Friction factor and (b) Nusselt number versus Gr number at Re=2×10^4 Li et al. (2015) [119] (License Number: 4615760389745).

Li et al. (2016) [120] studied numerically the impact of the free convection of super-heated steam in a PTC receiver tube on the thermal and flow fields. The thermal and flow fields were analysed for uniform (UHF) and non-uniform heat fluxes (NUHF) with wide range of Grashof, Reynolds numbers and solar elevation angles. The outcomes revealed that the free convective boosted the thermal field by more than 10% when the Grashof number is greater than a threshold value. It was concluded that the buoyancy force created a high-speed region at the bottom section of the absorber pipe. The vortex strength under NUHF was greater than that under UHF. They suggested empirical correlations for fRe and Nu number under NUHF to be utilised in practical operation.

Bortolato et al. (2016) [121] used an innovative flat aluminum absorber in small linear solar collector for process heating and direct steam generation system. The absorber width was optimised using a MCRT analysis, and it was constructed using the bar-and-plate technology, including its internal turbulator. It was experimentally placed on an asymmetrical PTC having a concentration ratio of 42. A procedure was applied to examine the PTC during both liquid heating and direct steam generation. The results show that the single- and two-phase flow datasets coincided at decreased temperature. The experimental optical efficiency of this prototype was equal to 82%, while the thermal efficiency at 0.160 K.m^2/W was around 64%, with negligible pressure drop. This is a promising value and can still be improved by using flat absorber and low thermal emittance coating material. It was found that the time constant of the collector is equal to 213 s.

Bellos et al. (2017) [122] developed a thermal model to assess the exergetic performance of commercial PTC using Therminol VP1 and air. It was concluded that the thermal oil exhibited high thermal and exergetic effectiveness with 72.49% and 31.57% respectively. It was noticed that the exergetic efficiency mainly depended on the inlet temperature, while the flow rate is not so paramount. It was pointed out that the exergetic thermal losses were higher in air case due to its lower thermal efficiency. The exergetic frictional losses were higher for air case, which significantly affected the exergy destruction, something was not noticed in thermal oil case. Bellos et al. (2017d) [123] investigated energetically and exergetically a commercial PTC (Eurotrough ET-150). Pressurized water, Therminol VP-1, nitrate molten salt, sodium liquid, air, carbon dioxide and helium were the examined working fluids. The results proved that the liquid working fluids present higher thermal effectiveness than gas working fluids. The pressurized water was the most suitable working fluid for low temperatures up to 550 K, while sodium liquid was the most efficient selection for higher temperatures up to 1100 K. Carbon dioxide and helium perform with similar way and they were the best solutions for extremely high temperatures after 1100 K. The pressure losses have a high impact in gases cases because of its low density, which leads the gases to have optimum exergetic performance in the range of 600 to 650 K, although they can operate up to 1300 K. The global maximum exergetic performance was observed for sodium liquid case at 800 K and then the exergetic efficiency was equal to 47.48%.

Pavlovic et al. (2017) [124] investigated the impact of PTC's geometric dimensions on the optical, energetic and exergetic efficiencies. The module of the commercial LS-3 PTC was examined with Solidworks Flow Simulation in steady-state conditions as shown in Figure 2.57. Various combinations of reflector widths and receiver diameters were tested. The optical and the thermal performance, as well as the exergetic performance were calculated for all the examined configurations. The results have shown that higher widths demand higher receiver diameter for optimum performance. For inlet temperature equals to 200°C with Therminol VP-1, the optimum design was found to be 3000 mm width with 42.5 mm receiver diameter, using a focal length of 1840 mm. The thermal efficiency and the exergetic efficiency were maximised for a

specific receiver diameter, which is fully connected with the width of the collector.

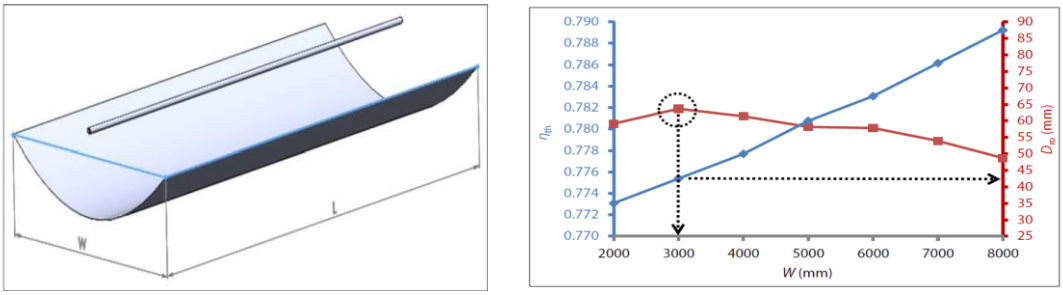

Figure 2.57 (a) The module of LS-2 PTC, (b) Optimum design determination Pavlovic et al. (2017) [124] (License Number: 4615760389821).

An experimental examination was conducted to assess the energetic and exergetic thermal effectiveness of a PTC receiver tube by Chafie et al. (2018) [125]. The PTC was designed, constructed and installed in the research laboratory at Borj Cedria of Tunisia. The useful energy gain, exergy converted to the fluid, energy and exergy efficiencies and exergy factor were measured. The results have shown that the energy gain converted to the fluid and the energy efficiency were smaller than the useful exergy rate and the exergy efficiency. The DNI and the operating temperature were the main parameters affected the exergy factor. The daily average energy, exergy efficiencies and the exergy factor achieved during time of the experiments were 36.10%, 11.85% and 0.11 respectively.

Kumar and Kumar (2018) [126] investigated experimentally the thermal performance of a PTC having a non-evacuated tube and tested using water under the northern Indian weather conditions. Two cases with and without glazing on the PTC's receiver thermal effectiveness were considered. The results revealed that the PTC's effectiveness relied mainly on the fluid's mass flow rate. The PTC's thermal efficiency varied from 25.84% to 53.55% and 13.8% to 47.5%, respectively, in south-facing mode with and without glazing on the receiver's tube. However, in case of tracking mode, these values were 18.5-33.42% and 12.98-25.72%. Good effectiveness was obtained in south-facing mode compared with tracking mode case and the effectiveness enhanced when using glazing on the receiver's tube. There was no noticeable increase in the PTC's efficiency when the mass flow reached a value of 0.024 kg/s.

Fan et al. (2018) [127] proposed a PTC receiver having twin glass tube, and evaluated its effectiveness by a mathematical model as shown in Figure 2.58. Strategies including replacing the selective coating with non-selective one, lowering the fluid's velocity and lowering the inner glass tube emissivity were investigated. The proposed receiver was suggested to be coated with black paint coating having absorptivity (α) of 0.96, and emissivity (ε) of 0.78. The fluid's velocity had an extensive impact on PTC's effectiveness than the transmittance of fluid. Furthermore, the usage of selective coating on the inner glass tube was found beneficial at inlet temperature not higher than 150°C.

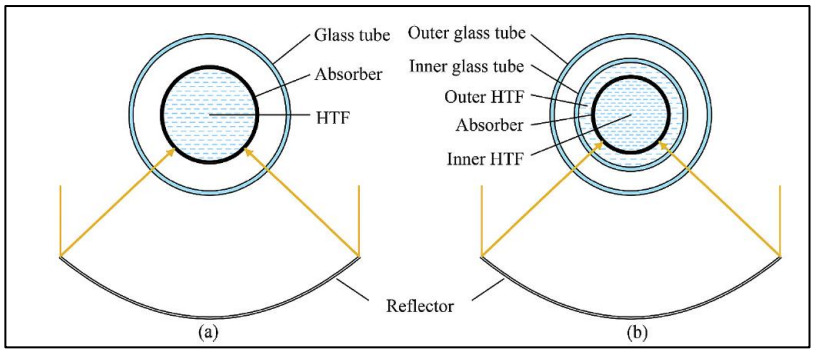

Figure 2.58 Sketches for a cross section of (a) conventional receiver, (b) novel receiver Fan et al. (2018) [127] (License Number: 4616330150735).

2.7.2 Nanofluids

One potential answer for enhancing the thermal productivity of PTCs is the utilisation of nanofluids as working fluids. Actually, it is sensible to anticipate an expansion in the thermal productivity of PTCs when the heat transfer base liquid is subbed with proper grouping of nanoparticles. Utilising nanofluid as a working liquid in sun-based bodies is a novel way to deal with increment the galaxies proficiency. One of the valuable uses of nanofluids is in the absorption sunlight-based collectors where the sun pillars are straightforwardly consumed by the nanofluid. Considering the way that most base working liquids utilised in immediate absorption sunlight-based thermal collectors, for example water, oil, and ethylene glycol, have low absorption coefficients, it follows that expansion of nanoparticles to them upgrades their optical properties as well as enhance the PTC's efficiency too (Menbari et al., 2017) [128].

Expanding the thermal conductivity of the working fluid would improve the heat transfer rate. Metallic particles, metallic oxides and nanotubes have higher thermal conductivity than that of fluids. For instance, the thermal conductivity of copper at room temperature is around multiple times more than that of water and around 3000 times more than that of oil. Expansion of fine particles (1-100 nm) into heat transfer base-liquids (i.e. nanofluids) can fundamentally boost the heat transfer rate. Clearly the exploration on the utilisations of nanofluids have been promoted during the ongoing years. The purported nanofluids, a term that was first presented by Choi in 1995 at the Argonne National Laboratory, U.S.A (Choi, 1995) [129]. It is likewise characterised as a blend comprises from an ordinary liquid, for example water, oil, ethylene glycol, glycerol, with a limited quantity of metallic or metallic oxide nanoparticles. Nanofluids have enhanced the liquid thermophysical properties, for example, thermal conductivity, viscosity, and heat transfer coefficients, contrasted to ordinary liquids.

The most common nanoparticles are: Al_2O_3, CuO, TiO_2, SiO_2, Fe_2O_3, ZnO and Au. The nanofluid was deemed as the new age of cutting-edge heat transfer liquids or a two-stage framework which utilised for different designing and modern applications because of its incredible execution. A portion of these applications including atomic reactors, transportation industry, mechanical energy, cooling of microchips, improving diesel generator effectiveness, sunlight-based absorption, microelectronics, biomedical fields and numerous other applications. Nanofluids are additionally called as extraordinary coolant liquids because of their high capacity to assimilate heat more than any customary liquids, so they can diminish the size of frameworks and boost its proficiency. The utilisation of these nanoparticles prompts higher thermal conductivity and subsequently higher heat transfer rate to the working liquid in PTC system. Higher heat transfer rate, which implies higher heat transfer coefficient prompts a lower temperature in the PTC and to bring down heat losses, the way that prompts higher thermal effectiveness (Bellos et al., 2017a). Therefore, the utilisation of nanofluids is considered among the most effective working liquids as indicated by the literatures, which have been summarised below in the following sections.

Khullar et al. (2012) [130] used sun-based energy via the utilisation of nanofluid in a PTC. Finite difference technique was utilised to solve the governing equations in order to theoretically analyse the PTC performance. The outcomes were validated against the available experimental data of classical PTC under similar conditions. The results revealed that the PTC's thermal efficiency has 5-10% higher compared to the classical PTC using similar external conditions. It was obviously indicated that the PTC based nanofluids has the ability to exploit sun-based energy more effectively than a classical PTC. Kasaeian et al. (2012) [131] studied numerically turbulent flow mixed convective of Al_2O_3-oil nanofluid in a PTC pipe. The used various ranges of nanoparticle volume fraction with less than 5%, and operational temperature of 500 K and pressure of 20 psig. The outcomes revealed that the Nu number has direct reliance on the nanofluid's volume fraction. The heat transfer decreased by increasing the operational temperature at a given mass flowrate.

de Risi et al. (2013) [132] suggested a novel solar Transparent PTC using gas-based nanofluids (mixture of CuO and Ni nanoparticles). They developed a thorough mathematical model considering various aspects of the TPTC and used it to run an optimisation procedure of TPTC. In addition, a genetic algorithm optimisation (MOGA II) was utilised to improve and optimise the solar collector's performance. The results revealed that TPTC based gas-nanofluids can be a promising way compared to classical systems which utilise synthetic oils or molten salts. The optimisation procedure found a maximum thermal efficiency of 62.5% at nanoparticles volume fraction of 0.3% and the minimum solar radiation to run the plant is 133.5 W/m^2 and under this value the power plant has to be stopped. Sokhansefat et al. (2014) [133] studied numerically 3D mixed convective of Al_2O_3-oil nanofluid in a PTC tube subjected to a NUHF. The effects of various Al_2O_3 particle concentrations, and operational temperatures of 300 to 500 K on the thermal field were investigated. The heat flux in the circumferential direction was obtained using the MCRT technique. The numerical results show that the heat transfer has a direct dependency on the nanoparticles volume fraction. In addition, the heat transfer enhancement reduced as the absorber operational temperature increased. The optimum heat transfer was achieved at θ=310° and θ=230° (tube's left and right sides), respectively.

Ghasemi and Ahangar (2014) [134] tested Cu-water nanofluid numerically in a PTC to examine its thermal performance. The thermal field and the thermal efficiency of nanofluids based PTC were evaluated and compared with the classical PTC. Further, the influences of different factors as the mass flow rate, nanoparticle concentration, receiver's geometrical parameters were also investigated. The outcomes show that the addition of limited quantity of copper nanoparticles into water enhanced significantly its absorption characteristics. The thermal, and optical efficiencies were improved and outlet temperatures were higher. The nanofluid based linear PTC has a higher thermal efficiency than a similar conventional collector.

Sunil et al. (2014) [135] investigated experimentally the PTC performance using SiO_2-H_2O based nanofluid with nanoparticle volume fraction in the range of 0.01% to 0.05%. The results revealed that SiO_2-H_2O nanofluid has relatively higher thermal efficiency at high velocities and the instantaneous efficiency increased with the increase in velocity. The maximum instantaneous efficiency obtained for SiO_2-water nanofluid for volume flow rate of 20, 40 and 60 L/h is 10.45%, 21.55% and 30.48% respectively. The corresponding maximum thermal efficiency is 11.27%, 11.61% and 10.95% respectively. The corresponding maximum overall thermal efficiency is 7.76%, 7.73% and 7.48% respectively. Mwesigye et al. (2015) [136] used synthetic oil-Al_2O_3 nanofluid in a PTC to perform a thermodynamic analysis using the entropy generation minimisation method. The PTC used has a rim angle of 80° and a concentration ratio of 86. The results revealed that the thermal efficiency of the PTC enhanced by up to 7.6% when utilising nanofluids. The entropy generated was a minimum at the optimum Reynolds number, at each inlet temperature and nanoparticle concentration, beyond which the utilisation of nanofluids is thermodynamically unreformable. Considerable enhancement in thermal efficiency for all cases was achieved for flow rates lower than 25 m^3/h.

In another study, Mwesigye et al. (2015) [137] used Syltherm800-CuO nanofluid to examine the thermal effectiveness of a PTC having high concentration ratio of 113 compared the available commercial systems of 82. The results revealed that the receiver's thermal effectiveness decreased with both heat loss and CTD increased when the concentration ratios increased as appeared in Figure 2.59. The outcomes also

show that the utilisation of nanofluids remarkably enhanced the receiver's thermal effectiveness. The thermal effectiveness and thermal efficiency increased up to 38% and 15% respectively. Practical correlations for Nu number and friction coefficient were obtained and presented.

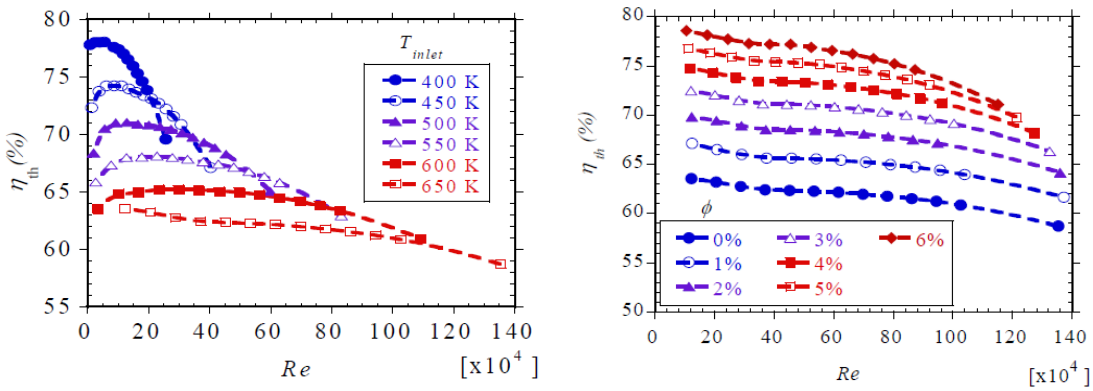

(a) (b)

Figure 2.59 (a) Influence of inlet temperature, and (b) volume fraction on the PTC's thermal efficiency Mwesigye et al. (2015) [137] (License Number: 4616380969157).

Zadeh et al. (2015) [138] focused on the development of an efficient modelling and optimisation of a PTC absorber tube subjected to a NUHF using Al_2O_3/synthetic oil. A genetic algorithm (GA) optimisation method and sequential quadratic programming (SQP) were used in the analysis. The Nu number, pressure drop with Re and Ri numbers were used in the optimisation problem as design constraints. The results have shown that the thermal performance of the absorber tube is improved when nanoparticles volume fraction increased. The thermal effectiveness decreased as the absorber's pipe inlet temperature increased. The hybrid optimisation algorithm (GA-SQP) has provided an efficient technique of obtaining good solution and reducing the calculation time using SQP. Chaudhari et al. (2015) [139] investigated experimentally using Al_2O_3-water on the thermal effectiveness of a PTC. The nanoparticles used have 0.1% of volume fraction and 40 nm particles dimension. The outcomes illustrated that nanofluid-based PTC has higher thermal effectiveness than water-based PTC. It was revealed that the thermal efficiency increased by 7% at 0.1% of nanoparticle volume fraction with heat transfer augmentation of 32% when using nanofluid.

Kasaeian et al. (2015) [140] constructed a standard pilot of trough collector having a 0.7 m width and 2 m in height reflector made of steel mirror to investigate the ways of its performance enhancement. Four kinds of receivers: a black painted vacuumed steel tube, a copper bare tube, a glass enveloped non-evacuated copper tube, and a vacuumed copper tube were used to compare their optical and thermal effectiveness. Multi walled carbon nanotube (MWCNT)/oil nanofluid with 0.2-0.3% volume fraction were utilised in vacuumed copper absorber tube. The outcomes revealed that the vacuumed tube's global efficiency is 11% more than the bare tube. The maximum optical and thermal effectiveness of the vacuumed copper tube were 0.61 and 0.68, respectively. The global efficiency is improved by 4-5% and 5-7%, at 0.2% and 0.3% nanoparticle concentration respectively. The nanofluid shows high thermal potential for further examinations.

Basbous et al. (2016) [141] utilised ultrafine particles Al_2O_3, Cu, CuO and Ag dispersed in Syltherm 800 to examine numerically the thermal effectiveness of a PTC framework. The results revealed that the PTC's heat loss factor declined when using nanofluids. The silver nanoparticles exhibited the optimum PTC's thermal effectiveness with 36% increase in heat transfer coefficient and 21% decrease in heat loss factor. Mwesigye et al. (2016) [142] presented numerically the thermodynamic effectiveness of a PTC using Cu-Therminol VP-1 nanofluid. The outcomes revealed that the thermal efficiency of the system increased by 12.5% and the entropy generation rates reduced significantly as the nanoparticle volume fraction increased. It was observed that the entropy generation rates reduced between 20% to 30% as the nanoparticle concentration increased from 0% to 6% at flow rates lower than 45 m^3/h.

Wang et al. (2016) [143] implemented a combined optical-thermal-stress simulation model based on FEM to examine the PTC effectiveness. The Al_2O_3/synthetic oil nanofluid with NUHF profile were utilised. The effects of particle concentration and other key factors of the PTC system were also investigated. It was found that the utilisation of nanofluid dramatically diminished the temperature gradients, the maximum temperature and deformation in the absorber especially in y-direction. The y-direction displacements decreased from 2.11 mm to 0.54 mm when the volume

fraction increased, this indicates that the new structure solar receiver has a better performance. The new PTC structure has higher thermal efficiency using Al_2O_3/synthetic oil nanofluid contracted to the one using synthetic oil. Moreover, the changes of temperature in the absorber with the direct normal irradiance (DNI), the inlet temperature, and the inlet velocity were remarkably reduced.

Ghasemi and Ranjbar (2016) [144] simulated numerically forced convective turbulent nanofluid flow in a solar PTC receiver. A commercial CFD code was employed to find hydrodynamic and heat transfer coefficients by means of Finite Volume Method (FVM). The effect of nanoparticles volume fraction (ϕ) on the PTC thermal effectiveness was studied. The results revealed that by increasing the nanoparticle volume fraction, the average Nusselt number increased for both CuO and Al_2O_3 nanofluids. Furthermore, it was found that the heat transfer coefficient enhanced up to 28% and 35% when utilising Al_2O_3-water and CuO-water nanofluids (ϕ = 3%), respectively. On the other hand, the friction factor was found lower using nanofluid compared with water.

Kaloudis et al. (2016) [145] used CFD numerical model to study the PTC's thermal effectiveness utilising Syltherm 800/Al_2O_3 nanofluid with concentrations (0%-4%) as shown in Figure 2.60a. In order to address the nanofluid-modeling problem the two-phase approach was preferred (against single-phase model) and validated against experimental and numerical results. In addition, the temperature and velocity fields of the Syltherm 800/Al_2O_3 nanofluid were associated with the enhanced heat transfer occurring at higher nanoparticle concentrations. A boost up to 10% on the collector efficiency was reported for Al_2O_3 concentration of 4% as shown in Figure 2.60b. It was concluded that the two-phase approach was more accurate compared with the single-phase approach which is more common in similar studies. This increase was associated with detailed temperature and velocity fields, showing enhanced mixed convection effects for higher nanoparticle concentrations.

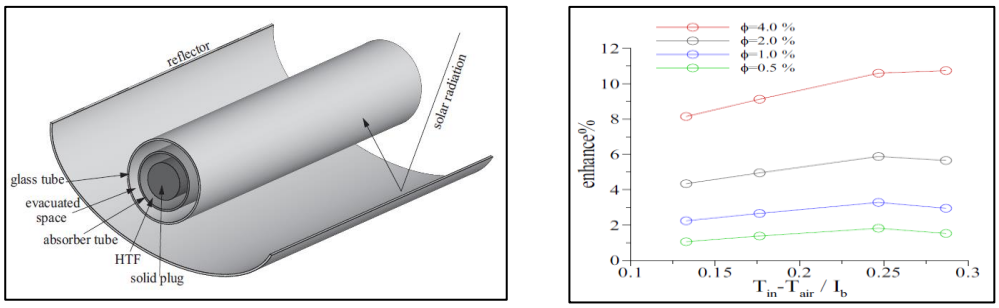

(a) (b)

Figure 2.60 (a) PTC physical model and its absorber tube, (b) Percentage increase in efficiency against inlet temperature for various volume concentrations Kaloudis et al. (2016) [145] (License Number: 4616941148672).

Coccia et al. (2016) [146] analysed the yearly yield assessment of a low-enthalpy PTC using numerical modelling. Six water-based nanofluids at various volume fractions were investigated: Fe_2O_3, SiO_2, TiO_2, ZnO, Al_2O_3, and Au. The results show that small improvements are associated with Au, TiO_2, ZnO, and Al_2O_3 nanofluids at low volume fractions compared with water. However, there was no advantage with respect to water when increasing the nanoparticles concentration as appeared in Figure 2.61. The improvements in thermal efficiency were related to low concentrations of nanoparticles. This is because of the dynamic viscosity tends to considerably increase with the nanoparticle concentration. However, since the dynamic viscosity decreased with temperature while the thermal conductivity increased, it could be of some interest evaluating the potential of nanofluids at higher temperatures. This could be achieved by conducting further experimental investigations at high temperatures on reduced nanoparticle concentration such as TiO_2, ZnO, Al_2O_3, and Au, which did not give negative results at the temperature range investigated in this study.

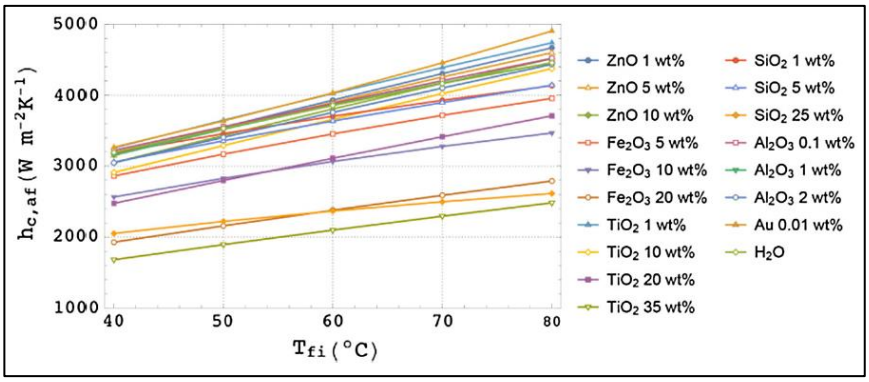

Figure 2.61 Convective heat transfer coefficient $h_{c,af}$ as a function of the inlet fluid temperature T_{fi} Coccia et al. (2016) [146] (License Number: 4616941484393).

Ferraro et al. (2016) [147] analysed the behaviour of a PTC operating with nanofluids, and compared its performance to the more traditional ones using oil. A thermal analysis model was developed and implemented using Matlab. The simulations were performed for a suspension of Al_2O_3 in synthetic oil and its characteristics compared to the corresponding base-liquid. The simulations were carried out for different DNI and variable mass flow, ensuring a temperature at the collector outlet below 400 °C. It was observed that there were only slight differences in the power loss and efficiency, while the main advantage is represented by lowering the pumping power. Mwesigye et al. (2017) [148] investigated the PTC's optimum thermal and thermodynamic effectiveness utilising Cu-Therminol, Ag-Therminol and Al_2O_3-Therminol nanofluids. They used finite volume method with the aid of CFD tool together with MCRT method. The outcomes revealed that the highest and lowest thermal effectiveness was obtained using Ag-Therminol and Al_2O_3-Therminol, respectively. It was found that the thermal efficiency increased by 13.9%, 12.5% and 7.2% for Ag-Therminol, Cu-Therminol and Al_2O_3-Therminol, respectively at a concentration ratio of 113. The maximum thermodynamic effectiveness for low exergy destruction was essentially reliable on the inlet temperature used. Empirical correlations were developed to provide improved thermodynamic performance.

Ghasemi and Ranjbar (2017) [149] simulated numerically 3D turbulent nanofluid flow and heat transfer inside a PTC receiver tube as shown in Figure 2.62a. CFD simulations with the aid of Finite Volume Method (FVM) were carried out to examine the impact of using nanofluid on the PTC's thermal efficiency. The results indicated that, using of nanofluid instead of base fluid as a working fluid causes an increase in the effective thermal conductivity and leads to thermal enhancement. Furthermore, the results revealed that by increasing of the nanoparticle volume fraction, the performance evaluation criteria are increased as shown in Figure 2.62b.

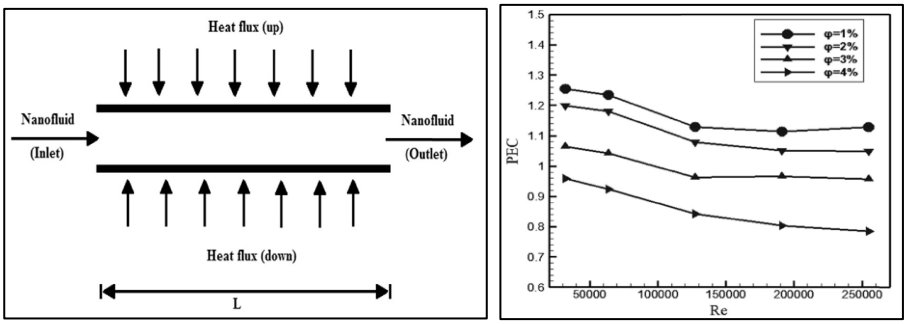

(a) (b)

Figure 2.62 (a) Schematic of nanofluid flowing in a PTC receiver tube, (b) PEC versus Re number Ghasemi and Ranjbar (2017) [149] (License Number: 4616950280403).

Bellos et al. (2017) [150] investigated the use of nanofluids in PTC for various cases as shown in Figure 2.63a. They used nanoparticles (Al_2O_3 and CuO) suspended in Syltherm 800 oil. A detailed thermal model was developed in EES and its results were validated with the experimental results. The results found that the utilisation of nanofluids increased the PTC's effectiveness about 0.5%. The Nusselt number enhancement was about 50% and it was the remarkable for CuO nanoparticles as shown in Figure 2.63b. It was affirmed that high temperature values produced higher thermal effectiveness and it can reach up to 0.6%. Additionally, it was observed that the nanofluids with high concentration and low flow rates provided higher enhancement, which would be paramount criteria to select nanofluids in PTC frameworks.

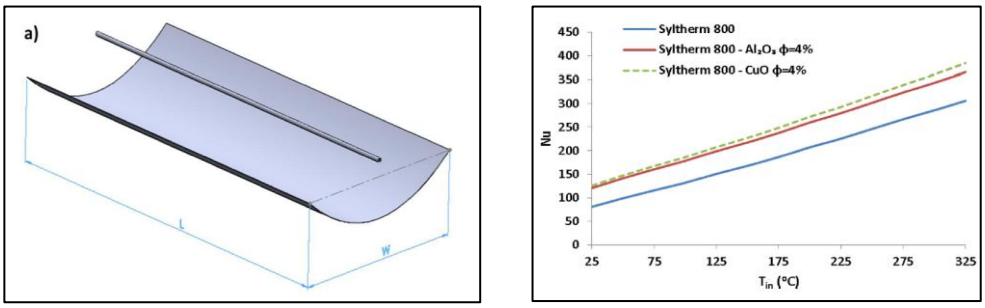

(a) (b)

Figure 2.63 (a) PTC module, (b) Nusselt number comparison for the initial case study Bellos et al. (2017) [150] (License Number: 4619140019400).

Khakrah et al. (2017) [151] performed a comprehensive numerical analysis of 3D turbulent flow of Al_2O_3/synthetic oil nanofluid in a PTC receiver tube. Various governing parameters such as the wind velocity, nanoparticles concentration, inlet temperature, and reflector's angle were investigated. The results revealed that the reflector's orientation significantly affected the Nu number values around the receiver tube. It was observed that the convection heat loss increased by 123.2%, 106.5%, 95.7%, and 86.1% for wind velocities of 5, 10, 15, and 20 m/s, respectively, when using reflector surface with 30° rotation compared with the flow over horizontal reflector. The PTC's efficiency diminished by 8% when the temperature difference (inlet and ambient) was doubled. The efficiency enhancement was 14.3% when 5% volume fraction of Al_2O_3 added to synthetic oil. The wind velocity has no influence on the efficiency enhancement for the rotated reflector cases. Kasaeian et al. (2017) [152] presented new forms of PTC as direct absorption solar collectors with three different receivers made of glass: a bare tube, non-evacuated tube, and a vacuumed tube. The influences of using nanofluids and the properties of the absorber tube on the PTC's thermal effectiveness were investigated. Two nanoparticles of 0.2% and 0.3% MWCNT and nanosilica dispersed in ethylene glycol were utilised. It was found that the maximum outlet temperature and thermal effectiveness in all three receivers was achieved with 0.3% MWCNT/EG. The vacuumed glass-glass receiver exhibited outlet temperature and thermal efficiency of 338.3 K and 74.9%, respectively; which was 20% higher than the bare tube. The carbon nanotubes exhibited maximum values of volume fraction and thermal efficiency at 0.5, and 80.7%, respectively, and it was 0.4 and 70.9%, respectively, for nanosilica.

Mwesigye et al. (2018) [49] investigated numerically using energy and exergy analyses the PTC's thermal effectiveness using SWCNTs-Therminol® VP-1 nanofluid. The results revealed that the thermal effectiveness was augmented about 234% using SWCNT compared with base-fluid. The thermal efficiency raised up to 4.4% as the nanoparticle volume fraction changed from 0 to 2.5%. The thermal efficiency was reasonably improved at flow rates lower than 28 m^3/h. It was observed that SWCNT nanofluid increased the exergetic performance of the PTC system. It was pointed out that the entropy generation rate can be reduced up to 70% due to the significant boost in the thermal effectiveness and the decline in the temperature difference. It was also

affirmed that the higher thermal efficiency or energy output does not necessarily come from higher thermal conductivity. The specific heat capacity has to be taken into consideration as another paramount factor in evaluating the PTC's thermal effectiveness utilising nanofluids.

Subramani et al. (2018) [153] investigated experimentally the performance of TiO_2/water nanofluids in a solar PTC under turbulent flow regime. The thermal and flow fields of nanofluids through the collector were investigated. The outcomes revealed that the Nusselt number, absorbed energy parameter and the maximum efficiency enhancement were augmented up to 22.76%, 9.5% and 57%, respectively, when using TiO_2 nanofluids instead of base-fluid. Practical equations were derived for the Nusselt number, friction factor, and performance index criterion. Bellos et al. (2018) [154] used different types of nanoparticles such as Cu, CuO, Fe_2O_3, TiO_2, Al_2O_3 and SiO_2 dispersed in Syltherm 800 and tested numerically in a PTC system using EES as shown in Figure 2.64a. This study covered a flow rate in the range of 50 to 300 L/min, inlet temperature in the range of 300 to 650 K and nanoparticle volume fraction up to 6%. The results revealed that the most efficient nanoparticle was the Cu, followed by other nanofluids. It was observed that lower flow rates, higher inlet temperatures and higher nanoparticle concentrations provided higher improvement, whilst it is relatively unchanged for various solar irradiation levels. The thermal efficiency improvement was 0.31, 0.54 and 0.74% for Cu volume fractions 2, 4 and 6%, respectively as shown in Figure 2.64b. They suggested a new index, which considered the heat transfer coefficient, the density-specific heat capacity product and the flow rate for the assessment of the thermal performance enhancement.

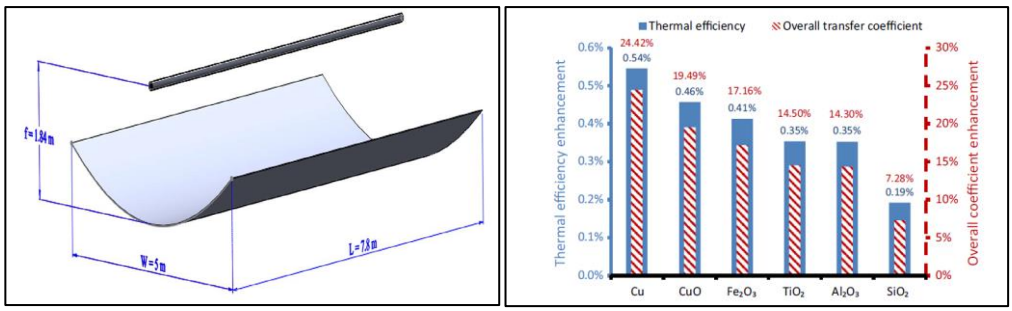

(a) (b)

Figure 2.64 (a) The PTC examined module, (b) Thermal efficiency enhancement and overall heat transfer coefficient Bellos et al. (2018) [154] (License Number: 4620010604035).

Bellos et al. (2018) [155] examined the addition of CuO nanoparticles in Syltherm 800 and in nitrate molten salt and tested its efficacy on a PTC thermal performance. They also evaluated the PTC total effectiveness by considering the hydraulic analysis (pressure losses) and the exergetic analysis. The outcomes revealed that the mean thermal enhancement with the utilisation of Syltherm 800-CuO was 0.65% compared to pure Syltherm, whilst it was 0.13% with the utilisation of molten salt-CuO. The hydraulic analysis affirmed that the pressure drop increased around 50% for Syltherm 800-CuO compared to the pure Syltherm 800 operation, while it was increased around 16% compared to the pure molten salt for molten salt-CuO case. The exergetic analysis confirmed that the molten salts produced higher exergetic performance compared to the oils. It was observed that, for the molten salt case, the maximum exergetic efficiency was achieved at inlet temperature of 650 K and the exergetic efficiency was around 38.4%.

Marefati et al. (2018) [156] analysed the optical and thermal analyses of PTC. Four cities of Iran with different weather conditions were chosen as case studies in order to assess the PTC effectiveness. Effective parameters such as concentration ratio, incident angle correction factor, collector mass flow rate were considered. Numerical modelling of the analysis was done using MATLAB software. The results revealed that Shiraz, with an average annual thermal efficiency of 13.91% and annual useful energy of 2213 kWh/m^2, is the best region to use solar concentrator systems. The utilisation of various nanofluids (CuO, Al_2O_3, and SiC) with volume fraction of 1% to 5% on the PTC's effectiveness was investigated. It was found that the thermal effectiveness using CuO nanofluid is higher than that other nanofluids. The results of this study were useful for the design and implementation of solar systems as the PTC performance changes with geographic region.

Rehan et al. (2018) [157] evaluated the experimental effectiveness of a locally developed PTC system having a concentration ratio of 11 for domestic heating applications. Two types of nanofluids were utilised and prepared Al_2O_3/H_2O and Fe_2O_3/H_2O at different concentrations. The experiments were conducted at Taxila of Pakistan under wide range of working parameters. The results revealed that the

maximum efficiencies were obtained using Al_2O_3 and Fe_2O_3 nanofluids compared to water. It was found that Al_2O_3 nanofluids were preferable in the efficiency enhancement compared to Fe_2O_3 for domestic applications utilising PTC. The results provided essential vision from the commercialisation point of view for developing in-house linear PTC and the impact of utilising nanofluids for space heating applications.

De los Rios et al. (2018) [158] investigated experimentally the impact of Al_2O_3-water nanofluid on the PTC thermal effectiveness. The results revealed that the PTC thermal efficiency was significantly enhanced for all nanofluids examined with relying on the incident angle value. The maximum efficiency of 52.4% was achieved when the incident angle varied from 20° to 30°, whereas it was 40.8% when using water. The maximum efficiency was 57.7% when using an incident angle of 10°, and nanofluid with 1% concentration, while it was 46.5% when using water. The PTC's outlet temperatures were higher using nanofluids than those when using water even when the solar radiation value was very small.

Allouhi et al. (2018) [159] proposed a 1D- mathematical model to study the influence of various nanoparticles in a PTC system. Energetic and exergetic analyses were done using various nanoparticles Al_2O_3, CuO, and TiO_2 with different volume fraction. It was revealed that the existence of nanoparticles enhanced the thermal effectiveness and produced higher values of Figure 2. of Merit (FoM). The FoM value, for CuO nanofluid, was greater than 1 at nanoparticle volume fraction> 1% and it exceeded 1.8 when the volume fraction was 5%. It was observed that CuO nanofluid increased remarkably the outlet temperature contrasted to other nanofluids, which provided similar thermal pattern. The exergy efficiency, for base fluid, ranged between 3.05% to 8.5%, whereas it was significantly enhanced to 9.05% for CuO nanofluid.

Alsaady et al. (2018) [160] used ferrofluids experimentally to test its efficacy on the thermal effectiveness of a small-scale solar PTC. Two working fluids Fe_3O_4 ferrofluids and distilled water were utilised. The outcomes revealed that the thermal efficiency increased by 16% and 25% with the utilisation of ferrofluids without and with external magnetic field compared to base fluid, respectively. It was observed that the ferrofluids show much better thermal efficiency than classical fluids at high temperature levels. It

was noticed that the addition of electromagnetics of 0.01°C m^2/W to the new PTC provided highest thermal efficiency value as it significantly enhanced the ferrofluids thermo-physical properties.

Tagle-Salazar et al. (2018) [161] presented a thermal mathematical model of PTC for heating applications using alumina-water nanofluid with the aid of EES. Furthermore, experimental work was also conducted using a PTC framework. It was noticed that the variation in the simulation results was less than 1% for outlet temperature and 10%-15% for the thermal efficiency. This was attributed to the experimental measurements' uncertainties, combined with a small error in the assumptions used in the mathematical thermal model. For one collector, there were small enhancements in both heat gain (+0.3 W/m) and thermal efficiency (+0.03%). It was inferred that the thermal behaviour of the nonevacuated receiver remarkably enhanced with high thermal losses contrasted to an evacuated receiver.

Kumar et al. (2018) [162] studied experimentally solar PTC with a modified absorber tube with copper fins and using TiO_2 nanofluid. The study was investigated various factors such as DNI, inlet velocity and inlet temperature. The results revealed that the usage of fins increased the thermal effectiveness and the outlet temperature increased with the increases in nanofluid concentration.

Bellos et al. (2020) [163] studied mathematically the thermal augmentation using (Cu/Syltherm 800) nanofluid in a PTC. Three PTC receiver's tube were utilised in the analysis; evacuated, non-evacuated and bare with no cover as shown in Figure 2.65. The results revealed that the bare tube has the maximum enhancements and higher thermal losses and nanofluids enhanced its effectiveness. The optimum augmentation for bare tube, nonevacuated tube and evacuated tube was found 7.16%, 4.87% and 4.06%, respectively, when using cermet coating. These augmentations were accordingly found to be 17.11%, 12.30% and 12.24% for the same tubes types respectively at 25 L/min and when using nonselective receiver.

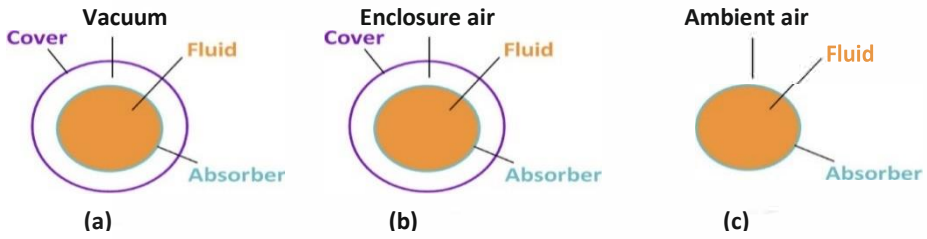

Figure 2.65 Various configurations of PTC receivers, (a) Evacuated tube, (b) Non-evacuated tube, (c) Bare tube Bellos et al. (2020) [163] (License Number: 4920041356616).

A summary of literature studies on PTC utilising conventional fluids and mono nanofluids are listed in Table 2.4. It can be obviously noticed from Table 2.4 that the majority of the research efforts, which have been carried out by different researchers at different countries around the globe, are mainly done using nanofluids with 53% compared with conventional fluids and other fluids with 33% and 14% respectively as can be seen in Figure 2.66. It can also be seen that the vast majority of studies are performed by Iran using nanofluids with 27%, followed by Greece with 17%, South Africa with 12%, China with 10%, and other countries with 2-7%. In contrary, with the usage of conventional fluids as PTC working medium, China has done great efforts in that with 42%, followed by Greece with 19%, then India with 10% and other countries have shared 3-7% as can be seen in Figures 67-68.

Table 2.4 Summary of literature studies on PTC utilising conventional fluids and mono nanofluids.

Reference	Study Type	Heat transfer Enhancement Technique	Fluid Used	Phase Mode	Flow Type	Remarks
Cheng et al. 2010 [106]	Numerical	Nil	Syltherm-oil 800	Single phase	Turbulent flow Re number was in the range from 2000 - 6000	The radiation loss in Model 3 (the unabridged model that includes all of the three-heat transfer type convection-conduction-radiation) was up to 153.70 W/m^2. The collector's efficiency enhanced when the radiation loss reduced as low as possible.
Tao and He 2010 [107]	Numerical/ 2D	Nil	Air	Single phase	Turbulent flow Rayleigh number was in the range of 1000 - 1×10^8	The effect of natural convection should be considered when Ra number is greater than 10^5. The thermal conductivity had less influence on the Nu number and average temperatures when its larger than 200 W/m.K.
He et al. 2011 [108]	Numerical	Nil	Syltherm 800 oil	Single phase	Not specified	The temperature rise only augmented with CR increase when φ<15°, and the influence of rim angle on the heat transfer process could be discarded. However, lots of rays were reflected by glass cover, and the temperature rise was much lower when φ >15°.
Cheng et al. 2012 [109]	Numerical	Nil	Oil syltherm-800, Therminol VP-1, Nitrate Salt, Hitec XL	Single phase	Turbulent flow Re number was in the range of 3×10^3 - 3.08×10^5	The thermal oils used have better thermal effectiveness and a lower pressure loss than the two molten salts. The total thermal radiation loss increased when the fluid's inlet temperature increased.
Hachicha et al. 2013 [110]	Numerical/ CFD	Nil	Thermal oil	Single phase	Mass flow rate was 0.68 kg/s	The developed model was successfully able to determine the heat losses, temperature in the heat collector element (HCE).
Mwesigye et al., 2013 [111]	Numerical	Nil	Sytherm-800	Single phase	Turbulent flow Re number was in the range of 1.19×10^4 - 1.92×10^6	The entropy generation rate decreased when the inlet temperature increased. It is increased when the concentration ratio increased.
Mwesigye et al., 2014 [112]	Numerical	Nil	Sytherm-800	Single phase	Turbulent flow Re number was in the range of 1.02×10^4 - 1.36×10^6	The total entropy generation increased as the rim angle and the fluid temperature decreased, and when the concentration ratio increased. The entropy generation rates were high at low rim angles because of high peak temperatures in the absorber tube.
Chang et al., 2014 [113]	Experimental and Numerical	Nil	Water	Single phase	Turbulent flow Re number was in the range of 1×10^4 - 3.5×10^4	The wall temperature of an absorber tube varied with the circular angle (θ) of cross-section, and the maximum temperature occurred at θ =180°.

Wang et al., 2014 [114]	Numerical	Nil	Molten salt	Single phase	Turbulent flow Velocity was in the range of 1 - 4 m/s	The CTD of the absorber increased with the rising of the DNI and decreased with the increase of fluid's inlet temperature and inlet velocity. The non-uniform distribution of the solar energy flux affected the CTD of receiver while it has less impact on the thermal efficiency.
Wu et al. 2014 [115]	Numerical	Nil	Therminol 55 and Gilotherm 55	Single phase	Turbulent flow Re number was 2 $\times 10^5$	The temperature difference within the metal tube changed inversely with the fluid's velocity. The stagnation temperature of PTC receiver increased linearly with time, and it can reach at 700 K in about 130 s.
Cheng et al. 2014 [116]	Numerical	Nil	Thermal oil	Single phase	Not specified	The PTC of various configurational factors have different sensitivity levels to different optical errors. However, the optical accuracy requirements from various configurational factors of a PTC system were always unchanged.
Wang et al., 2015 [117]	Numerical	Nil	Downtherm-A Synthetic oil	Single phase	Turbulent flow Velocity was in the range of 1- 4 m/s	The CTD of the absorber decreased with the increases of inlet temperature and Reynolds number and it increased with the increment of the DNI. It was found that the absorber's thermal stress and deformations were higher than that of the glass cover.
Tzivanidis et al. 2015 [118]	Mathematical Model (1D)	Nil	Pressurized water (10 - 180 °C)	Single phase	Re number was in the range of 1000-9000	The efficiency of the collector was over 75% for high temperature levels. This was due to very low heat loss factor, which varied from 0.6 to 1.3 $W/m^2.K$, depending on the inlet temperature.
Li et al. 2015 [119]	Numerical/ CFD	Nil	Superheated steam	Single phase	Re number was in the range of 2×10^4 - 10^5	It was not appropriate to utilise the experimental correlations for forced /combined convection to carry out the thermal design and prediction for PTC framework.
Li et al. 2016 [120]	Numerical	Nil	Superheated steam with Pr=1.5	Single phase	Laminar flow Re number was in the range from 250 - 1000	The free convective combined with forced convective increased the thermal rate by more than 10% when the Grashof number was greater than a threshold value. The combined flow and thermal features varied significantly with the solar elevation angle.
Bortolato et al. 2016 [121]	Experimental	Nil	Steam	Single phase	Mass flow rate was 250 kg/h	The optical efficiency was equal to 82%, while the thermal efficiency was around 64%, which was a promising value and can still be improved by using flat absorber and adopting a solar selective coating with a low thermal emittance. The time constant of the collector was equal to 213 s.
Bellos et al. 2017 [122]	Numerical	Nil	Supercritical CO_2	Single phase	Mass flow rate was in the range of 0.5 - 4 kg/s	Low-pressure levels (80 bar) had to be used in low-temperatures while higher-pressure levels (200 bar) were proper for higher temperatures. The maximum exergetic efficiency was 45.3% for inlet temperature of 750 K.
Pavlovic et al. 2017 [124]	Numerical	Nil	Therminol VP-1	Single phase	Mass flow rate was in the range of 0.4 - 5 kg/s	Higher widths demanded higher receiver diameter for optimum performance. For inlet temperature equal to 200°C, the optimum design was found to be 3000 mm width with 42.5 mm receiver diameter, with the focal length of 1840 mm.
Chafie et al.,	Experimental	Nil	Transcal N	Single phase	Flow rate was 0.2	The useful energy gain transferred to the HTF and the exergy

2018 [125]			thermal oil		kg/s	efficiency were proved to be smaller than the useful exergy rate and the exergy efficiency. The exergy factor heavily affected by the DNI and the operating temperature. The average energy efficiency, exergy efficiency and exergy rate for cloudy and sunny days varied between 19.72%, 8.51% and 0.08-36.1%, 11.72% and 0.12, respectively.
Kumar and Kumar 2018 [126]	Experimental	Nil	water	Single phase	Mass flow rate was in the range of 0.001 - 0.024 kg/s	There was no significant effect of the flow rate when it was more than 0.024 kg/s of water. The PTC offered slightly better effectiveness in the south facing mode than the tracking mode.
Fan et al. 2018 [127]	Numerical	Nil	Syltherm 800	Single phase	The mass flow rate was in the range of 100 – 200 L/min	The receiver was useful particularly when the inlet temperature was in the range of 100-120°C. Strategies including replacing the selective coating with non-selective coating, lowering the velocity of outer fluid and lowering the emissivity of the inner glass tube were suggested and verified to be effective in specific conditions.
Menbari et al. 2017 [128]	Experimental	Nil	Al_2O_3, CuO in Water nanofluids	Single phase	Mass flow rate was in the range of 10 - 100 L/h	The thermal efficiency of the PTC system enhanced by increasing nanoparticle volume fraction and nanofluid flow rate.
Khullar et al. 2012 [130]	Mathematical 1D/MATLAB	Nil	Therminol VP-1 – Al nanofluid	Single phase	Volume flow rate was in the range of 0.307×10^{-3} - 0.912×10^{-3} m^3/s	The nanofluid-based PTC had 5-10% higher efficiency than the classical PTC. The solar insolation and incident angle have significant effect on the thermal effectiveness of PTC.
Kasaeian et al. 2012 [131]	Numerical	Nil	Synthetic oil-Al_2O_3 nanofluid	Single phase	Turbulent flow Re number was in the range of 25000 - 100000	The Nusselt numbers had direct reliance on the nanoparticle volume fraction. The thermal characteristics increased as Reynolds number increased.
de Risi et al. 2013 [132]	Mathematical 1 D model with optimisation	Transparent PTC using Quartz	Gas-nanoparticle (Ni-CuO) mixture	Single phase	Velocity was in the range of 5 - 20 m/s	The optimisation procedure provided thermal efficiency of 62.5%. The minimum solar radiation to run the plant was 133.5 W/m^2. Under this value the power plant has to be stopped.
Sokhansefat et al. 2014 [133]	Numerical/ CFD	Nil	Synthetic oil/ Al_2O_3 nanofluid	Single phase	Re number was in the range of 4000 - 18000	The thermal enhancement due to the nanoparticles in the fluid reduced as the absorber operational temperature is increased.
Ghasemi and Ahangar 2014 [134]	Theoretical and Numerical	Nil	Cu- water nanofluid	Single phase	Flow velocity was in the range of 0.5×10^{-3} -11.5×10^{-3} m/s	The nanofluid based linear parabolic concentrator has a higher efficiency than a similar conventional collector.
Sunil et al. 2014 [135]	Experimental	Nil	SiO_2 - water nanofluid	Single phase	Mass flow rate was in the range of 20-60 L/h	The results revealed that SiO_2-H_2O nanofluid has relatively higher thermal efficiency at higher Reynolds numbers.
Mwesigye et al., 2015 [136]	Numerical	Nil	Syltherm oil - Al_2O_3 nanofluid	Single phase	Turbulent flow Re number is in the range of 3560 -	The PTC's thermal efficiency improved by up to 7.6% when using nanofluids. The entropy generated is a minimum at the optimal Reynolds number.

					1.15×10^6	
Mwesigye et al., 2015 [137]	Numerical	Nil	Sytherm 800 - CuO nanofluid	Single phase	Turbulent flow Re number was in the range of 3.84×10^3-1.35×10^6	The thermal performance increased up to 38% while the thermal efficiency increased up to 15%. High inlet temperatures and low flow rates provided remarkable enhancement in PTC's thermal efficiency.
Zadeh et al. 2015 [138]	Numerical	Nil	Al_2O_3-synthetic oil nanofluid	Single phase	Turbulent flow Re number was in the range of 4000-28560	The thermal enhancement has a direct proportion with nanoparticle concentration while it has indirect proportion with the operational temperature.
Chaudhari et al. 2015 [139]	Experimental	Nil	Al_2O_3 in water nanofluid	Single phase	Turbulent flow Re number was 5000	The PTC nanofluid-based has higher efficiency than PTC water-based. The solar thermal efficiency increased about 7% at 0.1% volume fraction. The nanofluid provided thermal enhancement by 32%.
Kasaeian et al. 2015 [140]	Experimental	A black painted vacuumed steel tube, a copper bare tube, a glass enveloped non-evacuated copper tube, and a vacuumed copper tube	Carbon nanotube -oil nanofluid	Single phase	Mass flow rate was not specified	The vacuumed tube has thermal efficiency 11% higher than the bare tube efficiency. The nanofluid showed high thermal potential for further and more complete examinations. A model of global efficiency was proposed and compared with the previous models.
Basbous et al. 2016 [141]	Numerical	Nil	Al_2O_3 in Syltherm 800 nanofluid	Single phase	Mass flow rate was 0.62 kg/s	The nanoparticles improved significantly the convection heat transfer by 18% and decreased the heat losses by 10%. The convection heat transfer factor tended to increase at high temperatures.
Mwesigye et al., 2016 [142]	Numerical	Nil	Cu-Therminol VP-1 nanofluid	Single phase	Turbulent flow flow rate was in the range of 1.22-1.35 m^3/h	The thermal efficiency increased by 12.5% when the nanoparticle volume fraction increased from 0% to 6%.
Wang et al. 2016 [143]	Numerical	Nil	Al_2O_3/synthetic oil nanofluid	Single phase	Flowrate was in the range of 2.8-3.3 L/min	The collector efficiencies Al_2O_3/synthetic oil nanofluid were higher. The changes of temperature in the absorber with DNI, the inlet temperature, and the inlet velocity were remarkably reduced.
Ghasemi and Ranjbar 2016 [144]	Numerical	Nil	CuO-water, Al_2O_3-water, nanofluids	Single phase	Turbulent flow Re number was in the range of 40000 - 250000	Nanofluid enhanced the PTC thermal performance compared with pure water. The heat transfer enhanced 28% and 35% with the utilisation of Al_2O_3-water and CuO-water nanofluids (ϕ=3%), respectively.
Kaloudis et al. 2016 [145]	Numerical	Nil	Al_2O_3 in Synthetic oil	Two phase	Re number was in the range of 4000 - 20 000	The nanoparticles enhanced the PTC's efficiency and it showed enhanced mixed convection effects for higher nanoparticle concentrations. A 10% boost in efficiency was possible for Al_2O_3

						at concentration of 4%.
Coccia et al. 2016 [146]	Numerical	Nil	Fe_2O_3, SiO_2, TiO_2, ZnO, Al_2O_3, and Au in water	Single phase	Mass flow rate is in the range of 0.5 - 1.5 kg/s	The nanoparticles of Au, TiO_2, ZnO, and Al_2O_3 nanofluids at the lower concentrations, presented very slight improvements compared to the use of water. However, there was no advantage when increasing the concentration of nanoparticles.
Ferraro et al. 2016 [147]	Numerical/ MATLAB	Nil	Synthetic oil-Al_2O_3 nanofluid	Single phase	Turbulent flow Mass flow rate was in the range of 1 - 7 kg/s	Only slight differences were observed for the power loss and the efficiency while the main advantage is represented by the lower pumping power.
Mwesigye et al., 2017[148]	Numerical	Nil	Copper/silver/ Al_2O_3-Therminol nanofluids	Single phase	Turbulent flow Re number was in the range of 100 - 2500 000	The thermal efficiency increased by 13.9%, 12.5% and 7.2% for Ag-Therminol, Cu-Therminol and Al_2O_3-Therminol, respectively when the proportion ratio is 113.
Ghasemi and Ranjbar, 2017 [149]	Numerical	Nil	Al_2O_3-Therminol 66 nanofluid	Single phase	Turbulent flow Re number was in the range of 30 000 - 250 000	Nanofluid led to augment the thermal effectiveness. The Nusselt number increased by increasing the nanoparticle volume fraction.
Bellos et al. 2017 [150]	Numerical	Nil	CuO-Syltherm oil 800, Al_2O_3-Syltherm oil 800	Single phase	Volumetric flow rate was in the range of 3 -7 m^3/h	The thermal effectiveness using nanofluids improved about 50% at higher temperatures. The thermal efficiency increased 1.26% and 1.13% with the utilisation of CuO and Al_2O_3 respectively when the proportion ratio was maximised and the flow rate was relatively low.
Khakrah et al. 2017 [151]	Numerical	Nil	Synthetic oil-Al_2O_3 nanofluid	Single phase	Turbulent flow Re number was in the range of 3150 - 21000	The efficiencies reduced by 1-3% by rotating the reflector with 30° relative to wind direction. The addition of small amount of Al_2O_3 led to 14.3% and 12.4% efficiency enhancement, for horizontal and rotated reflectors, respectively.
Kasaeian et al. 2017 [152]	Numerical	A bare glass tube, non-evacuated glass-glass tube, and a vacuumed absorber tube	Carbon nanotube, nanosilica in ethylene glycol nanofluids	Single phase	Mass flow rate was not specified	Carbon nanotubes have higher temperature and efficiency of 338.3 K and 74.9% in the vacuumed glass absorber tube. The carbon nanotubes has optimum point of volume fraction and thermal efficiency at 0.5, and 80.7%, whereas it is 0.4 and 70.9%, respectively, for nanosilica.
Subramani et al. 2018 [153]	Experimental	Nil	TiO_2-wter nanofluid	Single phase	Turbulent flow Re number was in the range of 2950 - 8142	The utilisation of TiO_2 nanofluids provided 22.76% improvement in the thermal effectiveness. The TiO_2 nanofluid provided maximum efficiency enhancement of 8.66% and an absorbed energy parameter 9.5% higher than water-based collector.
Bellos et al. 2018 [154]	Numerical	Nil	3% Al_2O_3 - Syltherm 800, 3% TiO_2 - Syltherm 800,	Single phase	Volumetric flow rate was 150 L/min	The thermal augmentation for hybrid nanofluid was about 2.2 higher compared with pure oil. The thermal efficiency augmentation for hybrid nanofluid reached up to 1.8% compared with only 0.7% for mono nanofluids.

			and 1.5% Al_2O_3 - 1.5% TiO_2 in Syltherm 800			
Bellos et al. 2018 [155]	Numerical	Nil	Syltherm oil 800	Single phase	Volumetric flow rate was in the range of 25-250 L/min	The thermal efficiency augmentation reached up to 2% when the Nu number was about 2.5 times greater compared to the reference case at inlet temperature of 600K. The thermal losses were 22% lower than in the reference case.
Marefati et al. 2018 [156]	Numerical/ MATLAB	Nil	CuO, Al_2O_3, SiC + water nanofluids	Single phase	Mass flow rate was in the range of 0.01 - 0.05 kg/s.m^3	The PTC collector optical performance in Shiraz city was better than the other cities, which was equal to 36.86%. Shiraz was the most suitable area for application of the PTC and the annual efficiency for Shiraz was 13.91% and highest monthly efficiency was 19.01%. Increase in heat transfer with CuO nanofluid was more than with Al_2O_3 nanofluid and the increase in heat transfer with Al_2O_3 nanofluid was more than with SiC nanofluid.
Rehan et al. 2018 [157]	Experimental	Nil	SiO_2, Fe_2O_3, in water nanofluids	Single phase	Mass flow rate was in the range of 1.15 - 2 L/min	The Al_2O_3 and Fe_2O_3 nanofluids achieved maximum efficiencies of 13% and 11% higher, respectively, compared to water under similar working situations. Al_2O_3 nanofluids was more preferable in PTC efficiency augmentation compared to Fe_2O_3 for domestic applications.
De los Rios et al. 2018 [158]	Experimental	Nil	Al_2O_3 - water nanofluid	Single phase	Mass flow rate was not specified	The maximum efficiencies obtained later in the year were 57.7% for nanofluid and 46.5% for water at the smallest incident angle.
Allouhi et al. 2018 [159]	Mathematical model/1D	Nil	CuO, Al_2O_3, TiO_2 in Therminol VP-1 nanofluids	Single phase	Mass flow rate was in the range of 0.5 - 2 kg/s	The nanofluid enhanced slightly the PTC thermal efficiency. The CuO-based nanofluid achieved about 9.05% peak exergy efficiency. The maximum daily thermal energy gain was 1.46% when using 5% of Al_2O_3 in a base fluid.
Alsaady et al. 2018 [160]	Experimental	Nil	Ferrofluids (magnetic nanofluids) Fe_2O_3 in water nanofluid	Single phase	Mass flow rate was 0.02 kg/s	The PTC efficiency increased 25% higher than the classical PTC with the existence of the external magnetic field. Nanofluids improved the outlet temperatures and PTC system efficiencies.
Tagle-Salazar et al. 2018 [161]	Mathematical & Experimental	Nil	Al_2O_3 in water nanofluid	Single phase	Volume flow rate was 7.53 gpm	An average prediction error was observed in the outlet temperature of less than 1% and around 10%-15% for the thermal efficiency. The thermal behavior was enhanced even though the collector was a nonevacuated receiver with high thermal losses as compared to an evacuated receiver.
Kumar et al. 2018 [162]	Experimental	Nil	TiO_2 - water nanofluid	Single phase	Not specified	The outlet temperature increased with increases in nanofluid concentration. Fins were utilised to enlarge the surface area so that heat transfer rate was also increased.

Bellos et al., 2020 [163]	Numerical	Nil	Cu/Syltherm 800	Single phase	The mass flow rate was in the range of 25 – 300 L/min	The results revealed that the bare tube has the maximum enhancements and higher thermal losses and nanofluids enhanced its effectiveness. The optimum augmentation were obtained for receivers with no coating.
Minea and El-Maghlany 2018 [164]	Numerical	Nil	Cu-MgO/ Ag-MgO/ GO-CO_3O_4 Al_2O_3-Cu in water	Single phase	Re number was in the range of 100 - 2000	The Cu-MgO hybrid at 2% volume fraction provided the highest increase in average Nu number with high-pressure drop penalty. The Ag-MgO-water hybrid nanofluid at 2% volume fraction offered the maximum efficiency of the solar collector.
Bellos et al. 2018 [166]	Numerical	Nil	(Cu, CuO, Fe_2O_3, TiO_2, Al_2O_3 and SiO_2) in Syltherm 800	Single phase	Volumetric flow rate was in the range of 50-300 L/min	The Cu was the good nanoparticle choice followed by CuO, Fe_2O_3, TiO_2, Al_2O_3 and SiO_2, respectively. Lower flow rates, higher inlet temperatures and nanoparticle concentrations provided higher augmentation with no impact of different solar irradiation levels.
Ekiciler et al. 2020 [167]	Numerical	Nil	Ag-ZnO, Ag-TiO_2, Ag-MgO, in Syltherm 800	Single phase	Re number was in the range of 10000 - 80000	Heat transfer augmented with the increase of Reynolds number and nanoparticle volume fraction. The most efficient working fluid for the PTC receiver was Ag-MgO/Syltherm oil hybrid nanofluid.

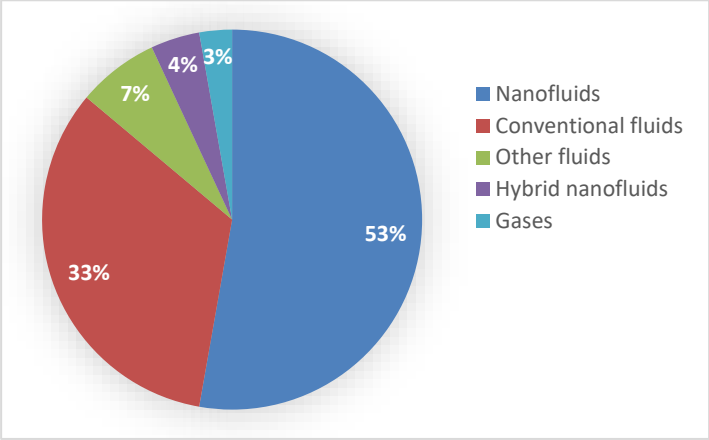

Figure 2.66 Research efforts on PTC with different working fluids.

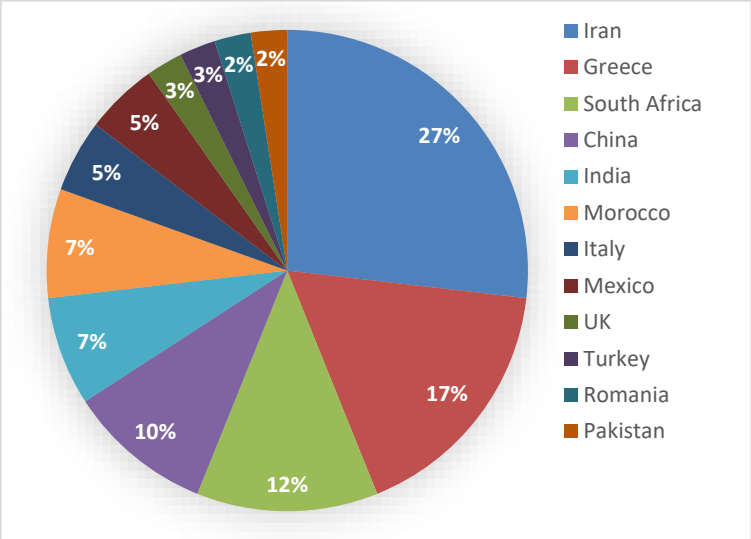

Figure 2.67 Research efforts on PTC enhancement using nanofluids around the globe.

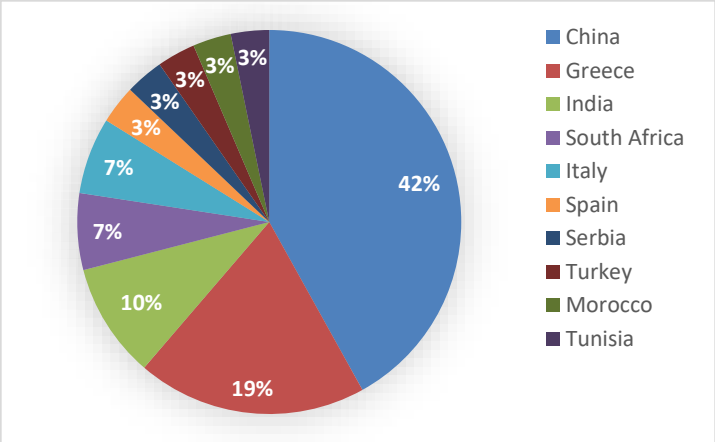

Figure 2.68 Research efforts on PTC using conventional fluids around the globe.

2.7.3 Hybrid Nanofluids

Recently, binary nanofluids terminology has been presented by suspending two kinds of nanoparticles in a base liquid (for example water, ethylene glycol or mixes of these two liquids). Binary nanofluids research began in 2013 and, their research advancement is still in progress. Uses of binary nanofluids in sustainable power sources, particularly in sun-oriented collectors are incredibly low referenced in the literature and there are extremely constrained specialized information accessible on the use of binary nanofluids in PTC. Subsequently, the utilisation of binary nanofluids acquire and more consideration. The binary nanofluid is a homogenous blend, which exhibits novel physical and chemical properties and distinctive thermal and hydraulic properties, that makes it amazingly a promising answer for better thermal qualities, contrasted to mono nanofluid because of synergetic impacts (Minea et al., 2018) [164]; (Sidik et al., 2016) [165].

In the literature, there are exceptionally uncommon examinations with binary nanofluids execution in sun-oriented collectors as can be seen beneath in the accompanying sections.

Menbari et al. (2017) [128] designed an experimental apparatus to investigate the thermal effectiveness of binary nanofluids in direct absorption solar parabolic trough collectors (DASPTCs) and to evaluate the factors involved in their optimal stability. For this purpose, two dissimilar nanoparticles, i.e. CuO and c-Al_2O_3 were chosen to prepare a binary nanofluid. The outcomes demonstrated that the stability and thermal properties of binary nanofluids unequivocally rely upon pH, surfactant mass fraction, and sonication time. It was noticed that the thermal characteristics and aggregation of the synthesised nanofluid were highest and lowest, respectively, under optimal stability conditions. The experiments revealed that the thermal effectiveness significantly enhanced with the rise of nanoparticle concentration and nanofluid mass flowrate. The results indicated that the thermal effectiveness of DAPTSC containing a mixture of two different nanoparticles scattered in water is more prominent than its partner scattered in a water-EG blend. This is mainly because EG can be progressively used for wide temperature range compared with water-EG blend which suffers from higher freezing and bubbling temperatures.

Bellos et al. (2018) [166] investigated the utilisation of single and binary nanofluids with Syltherm 800 in LS-2 PTC module by using a thermal analysis with the aid of EES as shown in Figure 2.69a. The study covered various nanofluid types as 3% Al_2O_3/Oil, 3% TiO_2/Oil and 1.5% Al_2O_3-1.5% TiO_2/Oil, 300 to 650 K of inlet temperature and 150 L/min of mass flowrate. The thermal efficiency enhanced with 0.74% using binary nanofluid, while it was 0.341% and 0.340% using TiO_2 and Al_2O_3 nanofluids respectively. The thermal efficiency enhanced up to 0.7% and 1.8% for single and binary nanofluids, respectively. The Nusselt number enhancement is found 121.7%, 23.8% and 23.4% for hybrid n1anofluid, TiO_2 nanofluid and Al_2O_3 nanofluid, respectively. The binary nanofluid show to be more effective multiple times in improving the thermal effectiveness than the single nanofluids as appeared in Figure 2.69b.

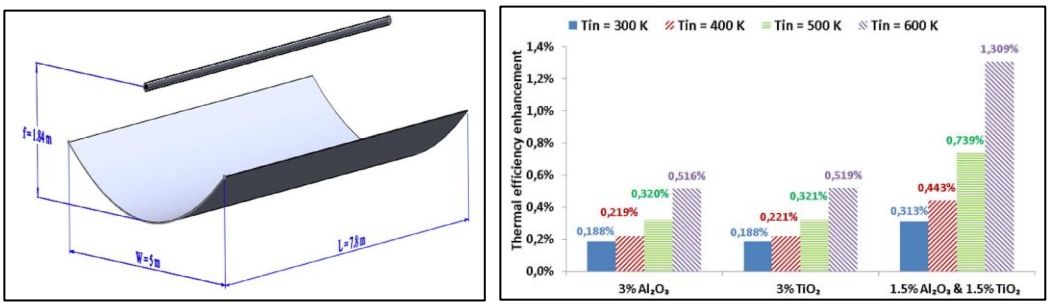

(a) (b)

Figure 2.69 (a) The LS-2 PTC examined module, (b) Thermal efficiency for various nanofluids Bellos et al. (2018) [166] (License Number: 4620041224384).

Minea and El-Maghlany (2018) [164] reviewed the expansion of nanofluids research endeavors in solar frameworks application and to reveal the significance of utilising binary nanofluids in PTC. It was shown that the highest increase in Nu number was noticed for 2% Cu-MgO binary nanofluid, and the thermal efficiency was maximum using 2% Ag-MgO-water binary nanofluid. The water-based binary nanofluid provides acceptable thermal augmentation with less pressure loss penalty. Nevertheless, the addition of nanoparticles to 60EG:40W is not recommended due to high-pressure drop penalty. It was inferred that binary nanofluids are excellent candidates for solar energy applications, even if the studies in the literature are limited at this moment.

Ekiciler et al. (2020) [167] studied numerically 3D thermohydraulic features of binary nanofluids in a PTC's receiver tube. They used three different types of fluids namely Ag-ZnO, Ag-TiO_2, and Ag-MgO and all dispersed in Syltherm 800. The Reynolds number was in the range of 10,000 and 80,000 using nonuniform heat flux boundary condition. It was found that the thermal and flow fields are superior for all binary nanofluids compared with the Syltherm 800. The PTC's thermal efficiency declined with Reynolds number increment and risen with the nanoparticle concentration. It was concluded that Ag-MgO/Syltherm 800 was highly effective fluid compared with other examined fluids at nanoparticle concentration of 4% as shown in Figure 2.70.

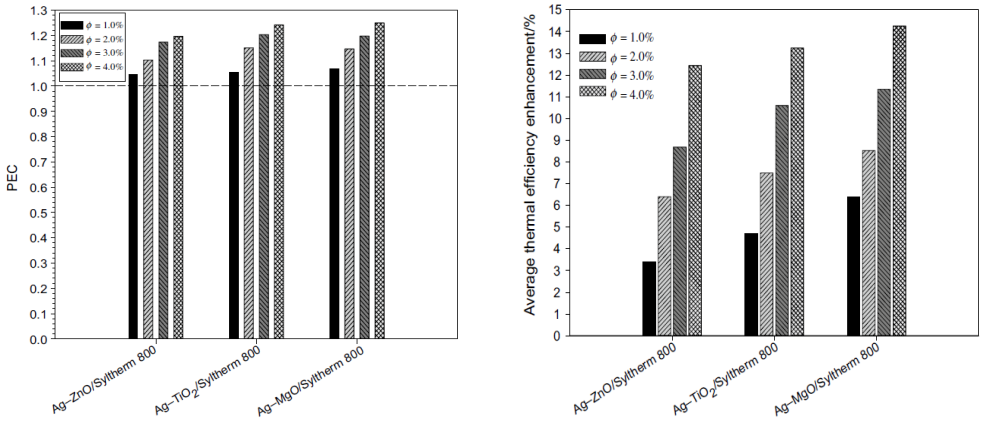

(a) (b)

Figure 2.70 (a) PEC variation, (b) thermal efficiency increment of PTC receiver tube for various binary fluids Ekiciler et al. (2020) [167] (License Number: 4920041356414).

2.7.4 Other Studies/Techniques on PTC

There are other few numerical research articles carried out by few researchers on thermal augmentation using various kinds of fluids and gases in PTC, which are comprehensively summarised below, in the following sections.

Bellos et al. (2016) [168] examined an energetic and exergetic comparison of various gases in a commercial PTC as shown in Figure 2.71a using EES. Air, nitrogen, carbon

dioxide, helium, neon and argon were used. The results affirmed that helium, for inlet temperature up to 700 K, is the best working fluid, while CO_2 is the most appropriate solution for higher temperature levels. Air and nitrogen have similar performances, which are acceptable for utilization in real systems. Argon is the lowest efficiency and it is not suitable for operation in parabolic collectors. Neon performs well up to 380 K and beyond this value has low performance. The optimum exergetic efficiency achieved with helium operating to 640 K inlet temperature as shown in Figure 2.71b. It was found that helium is the gas with the lower pressure drop (about 3 kPa) and for this reason has a high exergetic efficiency. It was proved that the use of alternative working fluids, as helium and carbon dioxide, could lead to higher exergetic output, compared with air, especially at higher temperature levels. This result establishes the use of these gases in many industrial applications and in power generation plants.

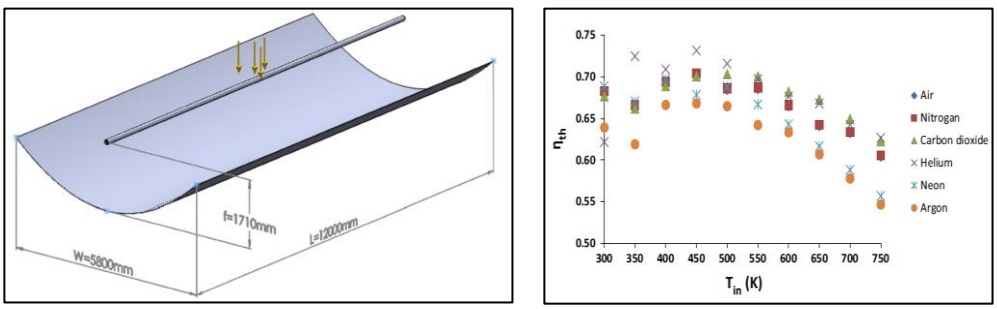

(a) (b)

Figure 2.71 (a) The examined LS-2 PTC module, (b) Thermal efficiency versus inlet temperature for various gases Bellos et al. (2016) [168] (License Number: 4620070074627).

In another study, Bellos et al. (2017) [169] continued their research and investigated the utilisation of supercritical CO_2 in PTC as shown in Figure 2.72a for various operating conditions. The results revealed that 0.5 kg/s is the optimum mass flowrate for maximising the exergetic effectiveness in low-temperature levels and 2.5 kg/s to be the optimum at higher temperatures. The exergetic analysis proved that low-pressure levels in the supercritical region (80 bar) are optimum for low temperatures (up to 550 K) and higher-pressure levels (200 bar) are suitable for temperatures levels over 650 K. The suggested efficiency map of the PTC is shown in Figure 2.72b, which reveals that the optimum

operating region is from 500 K to 800 K. The maximum exergetic efficiency is found 45.3% for inlet temperature 750 K, pressure 200 bar and mass flow rate 2.5 kg/s. The outcomes of this work could be utilised for the best possible design of sun-based power planted dependent on supercritical CO_2.

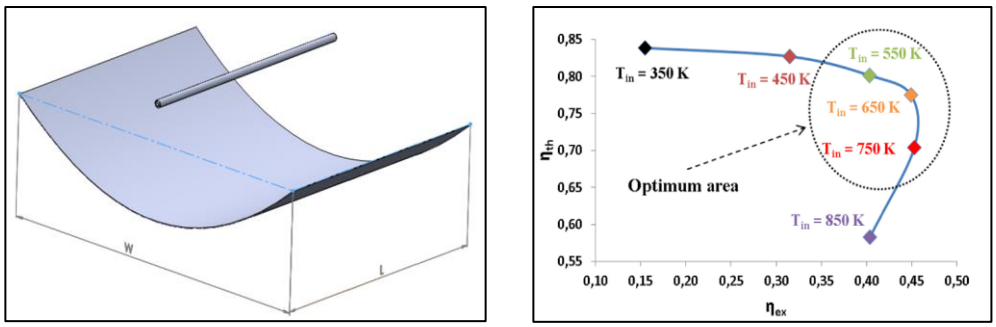

(a) (b)

Figure 2.72 (a) The examined module of LS-2 PTC, (b) Efficiency map of the PTC Bellos et al. (2017) [169] (License Number: 4620070282047).

2.8 Discussion on Heat Transfer Enhancement Methods

In this review, PTC types have been tested for working with different types and shapes of passive techniques, and conventional fluids, nanofluids and hybrid nanofluids. Many nanofluids types have been used such as Al_2O_3, Cu, CuO, TiO_2, Fe_2O_3, and MWCNT. The majority of investigators have used nanofluids with water and oil as base fluids in their mathematical, experimental and numerical studies. High number of practical research used water-based nanofluids, with relatively small number of studies used thermal oils as base fluids. However, the numerical investigations incorporate both base fluids (water and oil). More importantly, the majority of the experimental and numerical studies have assumed the nanofluids as a homogenous mixture and a single-phase model is applied to simulate the nanofluids.

The general trend of the review outcomes shows that the mathematical thermal models of PTC found a maximum thermal effectiveness is equal to 62.5%. The usage of nanofluids along with the thermal models has revealed that there is a small enhancement in heat gain (+0.3 W/m) and thermal efficiency (+0.03%). It is also noticed that the usage of nanofluids

would only provide slight differences for the power loss and the thermal efficiency while the main advantage is lower the pumping power. It is advised that high working temperatures were increasingly reasonable for utilising nanofluids and produce higher relative additions of energy conveyed. The exergetic efficiency improvement was higher priority than the energetic efficiency.

Additionally, the usage of conventional fluids numerically enhances the PTC's thermal performance by more than 20-30%. There is a critical deviation in the discovered outcomes in view of the distinction in the followed approaches among the investigations. In this way, it is fascinating to examine and condense the major results for each technique utilised. It is revealed that the conventional fluids (therminol oil or Syltherm oil) have better PTC thermal effectiveness and a lower pressure loss than other molten salt fluids. Besides that, the entropy generation rate decrease was increased when the fluid inlet temperature and the concentration ratio increased and when the rim angle decreased. The usage of molten salt in PTC increased the CTD of the absorber with DNI rising and decreased when higher inlet temperature and inlet velocity used. The numerical outcomes indicate that the non-uniform solar flux significantly affects the CTD of absorber while it has a small impact on the thermal effectiveness.

It was seen that the absorber tube's material plays a critical factor on the PTC structural effectiveness. It is discovered that the adjustment in absorber tube's material, for instance steel, and copper, aluminum, bimetallic and tetralayered negligibly affects the heat transferred to the HTF, yet it significantly affects the twisting because of thermal expansion just as because of self-weight. It is found that a tetra-layered which had a lower weight and improved temperature profile and provides a reduction in the optimum deflection by 45-49% when contrasted with steel.

Interestingly the numerical results found that it is not appropriate to utilise the experimental correlations for forced convection or traditional mixed convention to carry out thermal design and prediction for PTC. Additionally, the free convective combined with laminar forced convective increased the thermal effectiveness by more than 10%

when the Grashof number is greater than a threshold value. The combined flow and thermal features vary with the solar elevation angle where the thermal deterioration occurs at Richardson number greater than 12.8 (Li et al., 2015) [120]. It was found numerically that the receiver works very well when the fluid's inlet temperature was less than 150 °C (with an efficiency sacrifice within 4%), and particularly in the range of 100-120 °C (with an efficiency sacrifice within 1.5%). Several strategies were suggested to be effective including using non-selective coating material instead of the selective one for the absorber, reducing the outer fluid's velocity and lowering the emissivity of the inner glass tube in specific conditions (Fan et al., 2018) [127].

Furthermore, the usage of nanofluids in numerical studies dramatically augment the PTC's thermal effectiveness. There was a critical deviation in the enhancement rate due to the distinction in the followed approaches among the investigations utilising CFD, FVM, FEM, EES, and OpenFoam. Thus, it is important to highlight and summarise the main results for every method used. Most of the numerical outcomes of a PTC receiver with the use of nanofluids exhibit high thermal and thermodynamic effectiveness by up to 8% compared with a similar conventional-based fluid collector. It is pointed out using CFD models that the heat transfer coefficients present an ascending pattern with Reynolds number increment. The heat transfer improvement has an immediate association with the nanoparticle volume fraction though it has an opposite association with the operational temperature. The results further portray that there is a specific Reynolds number value past which the utilisation of nanofluids turns out to be thermodynamically bothersome at a given inlet temperature.

Generally, the enhancement percentage varied for different researchers as they used different operating and boundary conditions in their studies. For instance, the thermal effectiveness and the thermal efficiency increased up to 38% and 15%, respectively, as indicated by (Mwesigye et al., 2015) [136]. However, the thermal efficiency increased by 12.5% and the entropy generation rates reduced as the nanoparticle concentration changed from 0% to 6% (Mwesigye et al., 2016) [80]. Moreover, the changes of the maximum temperature in the absorber with DNI, inlet temperature, and inlet velocity are remarkably

reduced (Wang et al., 2016) [143]. The utilisation of Al_2O_3-water and CuO-water nanofluids at ϕ=3% provided enhancement in heat transfer up to 28% and 35%, respectively, as observed by (Ghasemi and Ahangar, 2016) [144]. Moreover, the utilisation of oil-based nanofluids and molten salt-based nanofluid boosted the thermal efficiency up to 0.76%, and 0.26%, respectively. The utilisation of Syltherm 800-CuO and molten salt-CuO boosted the Nusselt number up to 40% and 13%, respectively, according to (Bellos et al., 2016) [81]. It was noticed that Au, TiO_2, ZnO, and Al_2O_3 nanofluids exhibited minimal improvements at lower concentrations, contrasted to the utilisation of water. While, there was no advantage with respect to water when the concentration of nanoparticles increased (Coccia et al., 2016) [146]. The maximum augmentation in PTC's thermal effectiveness was recorded for silver nanoparticles which reach 36% rise in heat transfer and 21% decrease in overall heat loss coefficient (Basbous et al., 2016) [141]. Other types of nanofluids such as silver-Therminol, copper-Therminol and Al_2O_3-Therminol show increase in the thermal efficiency by 13.9%, 12.5% and 7.2%, respectively, when the proportion ratio is 113 (Mwesigye et al., 2017) [148]. In contrast, the thermal enhancement is proved approximately to be 50% utilising nanofluids and it is greater at high temperature values. The thermal efficiency increased up to 1.26% and 1.13% with the use of CuO and Al_2O_3, respectively when the concentration ratio is maximised and the flow rate is relatively low (Bellos et al., 2017) [150]. Moreover, the efficiency enhancement for horizontal and rotated reflectors was 14.3% and 12.4%, respectively, when 5% of Al_2O_3 was added to the base synthetic oil (Khakrah et al., 2017) [151].

Furthermore, the usage of carbon nanotubes in the vacuumed glass absorber tube increased the efficiency and temperature to 74.9% and 338.3 K respectively. The carbon nanotubes exhibited optimum values of volume fraction and thermal efficiency at 0.5, and 80.7%, respectively, whereas for nanosilica it is 0.4 and 70.9%, respectively, (Kasaeian et al., 2017) [152]. The usage of SWCNTs significantly improved the thermal effectiveness with little rise in the thermal efficiency. While the thermal effectiveness, thermal efficiency boosted up to 234%, and 4.4%, respectively, with entropy generation decrease of 70% using volume fraction of 2.5% (Mwesigye et al., 2018) [49]. Furthermore, the

utilisation of nanofluids with oil-based and molten salt-based provides thermal efficiency boost up to 0.76% and 0.26%, respectively (Bellos al., 2018) [154]. Moreover, the increase in thermal effectiveness with CuO nanofluid is more than with Al_2O_3 and SiC nanoparticles (Marefati et al., 2018) [156]. However, the CuO nanoparticle exhibited a peak exergy efficiency of 9.05% and the maximum daily gain of thermal energy delivered was 1.46% with the use of 5% Al_2O_3 (Allouhi et al., 2018) [159].

From the experimental perspectives, the literature survey revealed that there is a need of extra experimental investigations on the usage of conventional fluids and nanofluids in PTC systems. However, these experimental studies have also confirmed the PTC's thermal effectiveness boost. These studies have also confirmed that the PTC's thermal effectiveness relies on various factors. For instance, the experimental optical efficiency is equal to 82%, while the thermal efficiency is around 64%, and it can still be improved by using a flat absorber as a piece of a cavity receiver and by covering the absorber tube with a low thermal emittance based on (Bortolato et al., 2016) [121]. In addition, the energy and exergy efficiencies along with the exergy rate varied, for the cloudy and sunny days, between 19.72%, 8.51% and 0.08 to 36.1%, 11.72% and 0.12, respectively (Chafie et al., 2018). The PTC's efficiency diminishes when the working fluid exit temperature increases (Kumar and Kumar 2018) [126].

Furthermore, the experimental studies using nanofluids have also shown higher enhancement of PTC systems contrasted to classical fluids. The experimental results have revealed that the PTC's thermal efficiency could be enhanced by using higher nanoparticle volume fraction and nanofluid flow rate. The PTC's thermal efficiency of nanofluids strongly replies on the incident angle, where it is maximum at the lowest angle. For instance, the nanofluid causes the solar thermal efficiency increased by 7% and the thermal factor enhancement by 32% (Chaudhari et al., 2015) [139]. This is also supported by the results of (Kasaeian et al., 2015) [140], which show that the vacuumed tube thermal efficiency is 11% higher than the bare tube efficiency. This is also further confirmed by (Subramani et al., 2018) [153] results as the maximum thermal efficiency boost using TiO_2 nanoparticle was 8.66% higher than water. The energy factor was 9.5% higher than that

of water. In addition, the maximum efficiencies were 13% and 11% higher using Al_2O_3 and Fe_2O_3 nanoparticles, respectively, compared to water under similar working situations (Rehan et al., 2018) [157]. The maximum thermal efficiencies varied between 52.4 - 57.7% using 3% of nanoparticles and 40.8 - 46.5% using water (De los Rios et al., 2018) [158]. The PTC's efficiency increased to more than 25% with the existence of external magnetic field, than the classical PTC (Alsaady et al., 2018) [160].

It can be observed from the above results that the PTCs based nanofluid spread the most extensive piece of the literature. There was an extraordinary assortment of experimental and numerical examinations utilised diverse nanofluids and different ordinary fluids. The experimental studies demonstrate that there are significant improvements of about 11% with mean thermal proficiency. The numerical examinations give lower values of thermal improvements contrasted with the experimental contemplates. More explicitly, the CFD investigations demonstrate a thermal efficiency improvement of 7%, whereas the thermal models give an improvement of 1%. These various qualities demonstrate that the CFD and the thermal models utilise various strategies/suppositions, which are related to nanofluids. This urges the requirement for multilateral investigations for PTC frameworks, which incorporate both practical and theoretical examinations at the same operating conditions so comparable results could be obtained with high accuracy.

It is worth noting to mention that there is only one numerical study done by (Kaloudis et al., 2016) [145] on modelling the nanoparticles in two-phase flow in PTC framework. It is noticed that the existence of nanoparticles also enhanced the PTC's overall thermal effectiveness. With 10% boost in the thermal efficiency using 4% of Al_2O_3 nanoparticle. Thus, there is also a high need for more experimental and numerical investigations to be carried out for PTC systems at the same operating conditions using two-phase models.

It is also worth mentioning that there are only few numerical studies performed on the usage of hybrid nanofluids in PTC. These studies revealed that the binary nanofluid and single nanofluid produced up to 1.8% and 0.7% in thermal efficiency boost, respectively, (Bellos et al., 2018) [155]. They also stated that the PTC's efficiency increased while Re

number increased and the maximum efficiency was obtained using 2% of Ag-MgO-water binary nanofluid (Minea and El-Maghlany, 2018) [164]. Thus, there is also a high urge for more experimental and numerical investigations to be carried out using various types of hybrid nanofluids to examine their efficacy on the PTC thermal, hydraulic and exergetic performance.

Another aspect of this literature review is the usage of passive techniques for improving the PTC system performance. The numerical studies of PTC using passive techniques cover most extensive piece of the available literature because of the recent development in computers, programming languages and experimental techniques. It thus makes it easier for the researchers to conduct various computational studies under different geometrical and operational conditions. There is an incredible assortment of numerical studies using conventional fluids and nanofluids associated with different types of passive techniques. Most of the numerical results show improved PTC's thermal effectiveness with the use of passive technique by different percentage compared with a plain collector. They also stated that the passive techniques greatly reduced the Q_{loss}, T_{max} and circumferential temperature difference. In fact, various passive technique geometries and different fluids used by various researchers are the main reasons for the changes in thermal efficiency and performance. Many researchers have used the twisted tape insert as it can remarkably enhance the consistency of PTC tube wall's temperature profile. It can also enhance the heat transfer effectively with increasing the friction factor especially when using tight-fit twisted tape. Researchers have also found that the geometrical parameters of the passive technique such as length, thickness, width, depth, distance, have a remarkable influence on the PTC's thermal and hydraulic effectiveness. The advantages of passive technique are to unify the temperature profile and to reduce the maximum temperature on the absorber's tube under certain operational conditions (flow and geometrical parameters, etc) which consequently diminish the thermal deformation and boost the endurance of the PTC receiver.

For instance, the consideration of permeable inserts in a PTC receiver using Therminol-VP improved the thermal effectiveness around 17.5% with a pressure loss of 2 kPa (Reddy

et al., 2008) [58], (Kumar and Reddy, 2009) [59], (Kumar and Reddy 2012) [61]. There was a 3% improvement of the collector efficiency using helical internal fins with Syltherm 800 oil. This outcome proposed an improvement of 2%, with a decline in the maintenance cost (Munoz and Abanades, 2011) [60]. The thermal loss of the PTC using unilateral longitudinal vortex generators with oil syltherm-800 reduces by 1.35-12.1% to that of the smooth PTC. The PTC has greater overall thermal effectiveness than that of the smooth PTC (Cheng et al., 2012) [62]. The PTC pipe without helical internal fins suffers from higher temperature gradient (around 20 K) compared with the pipes with helical fins (Aldali et al., 2013) [64]. The maximum CTD on the external surface of receiver's pipe decreased by 45%, which extraordinarily reduced the thermal deformation (Wang et al., 2013) [65]. The PTC's thermal efficiency was remarkably improved using porous two segmental rings (Ghasemi et al., 2013) [66], perforated louvered twisted tape (LTT) (Ghadirijafarbeigloo et al., 2013) [67], dimples receiver contrasted to that with protrusions or fins (Huang et al., 2015) [75], and the introduction of wire coils (Diwan and Soni, 2015) [79]. The modified thermal efficiency increased between 1.2% to 8% for a PTC equipped with perforated plate insert using sytherm-800 (Mwesigye et al., 2014) [71]. It is also significantly improved with the use of nanofluid (Al_2O_3-synthetic oil) up to 15% (Mwesigye et al., 2015) [74]. There was considerable increase, using wall-detached twisted tape inserts, in thermal efficiency up to 10%, thermal effectiveness of 169%, decline in CTD to 68% and entropy generation rate reduction of about 58% compared with a plain absorber tube (Mwesigye et al., 2016) [80]. The usage of asymmetric outward convex corrugated tube as receiver can provide thermal effectiveness of 148% and maximum thermal deformation of 26.8% (Fuqiang et al., 2016) [83]. The concentric and eccentric pipe inserts with molten salt can remarkably enhance the thermal effectiveness around 1.11~1.64 than a PTC without inserts (Chang et al., 2017) [86].

Furthermore, the PTC absorber tube equipped with internal fins boosted the thermal efficiency and thermal effectiveness factor by 1.27% and 1.483 respectively (Bellos et al. 2017) [91]. The PTC receiver tube equipped with pin fin arrays inserting increased the Nusselt number and the thermal effectiveness factor by 9% and 12% respectively (Xiangtao et al., 2017) [95]. Very recently, the PTC receiver tube equipped with flow

inserts having star shape boosted the thermal, exergy and overall efficiencies by 1% (Bellos et al. 2018) [98]. The utilisation of internal rectangular finned tube fins alone and CuO-oil nanofluid alone provided 1.1% and 0.76% improvement in thermal effectiveness and the combination of both techniques provided 1.54% improvement (Bellos et al. 2018) [99]. The usage of S-curved sinusoidal tube receiver with synthetic oil increased the maximum performance about 135%. The converging-diverging PTC absorber tube provided the highest exergetic improvement of 0.65% and 0.73% using oil and Al_2O_3-oil nanofluid, respectively, compared with other absorber geometries (longitudinal finned absorber, twisted tape tube) (Okonkwo et al. 2018) [102]. The oblique delta-winglet twisted tape insert increased the thermal and exergy efficiencies by 12.05% and 4.95%, respectively. The serrated twisted tape inserts, among all other insert types (square cut, oblique delta-winglet, alternate clockwise and counter-clockwise), increased the thermal and exergy efficiencies by 13.63 % and 15.40 % respectively under the same conditions (Rawani et al. 2018) [103].

It is interesting to highlight in this literature review that diverse scientists in various flow characteristics (i.e. laminar and turbulent flows) also experimentally investigated the thermohydraulic performance of PTC. The PTC performance was found different for both flows, as it was more compelling than laminar flow and it is associated with high-pressure loss. Apart from cross-section configuration, investigations were conducted on twisted tape inserts, coiled insert, fins, ribs, corrugated tube, porous disc, metal foam, and high augmentation was found with these techniques due to high surface to volume ratio. The previous studies also portrayed that high thermal effectiveness is related with these enhancement techniques. The production of swirl stream utilising inserts tapes with different geometries is helpful to increase the Nusselt number. The thermohydraulic performance also relies on the passive technique's geometry. A lot of adjustment on straightforward and sophisticated tapes was made by researchers and discovered enhancements in their outcomes. However, the experimental studies using passive techniques-based PTCs were little compared with the numerical studies mentioned above because of the cost associated with constructing PTC systems with its instrumentations. There is a variety of these studies using conventional fluids and nanofluids. Most of these

studies have stated that, for example, the enhancement efficiency is 135%-205% over plain absorber/receiver of PTC with twisted tape inserts utilising silver-water nanofluid (Waghole et al., 2014) [69].

Moreover, the absorber filled with metal foam has a positive effect on the collector efficiency due to thermal conductivity enhancement compared with applying copper foam inside absorber (Jamal-Abad et al., 2017) [90]. The water was the most appropriate working fluid compared with air, and Therminol VP-1, in corrugated spiral cavity receiver as it can proficiently work at lower temperatures, while the thermal oil is the best at higher temperatures. The exergetic examination indicated that the air and thermal oil is are the best decision in low and high temperature values, respectively (Pavlovic et al., 2017) [124].

In addition, the optimum value of various passive technique parameters such as twist angle, depth of wing cut ratio, space ratio, depth ratio, width ratio, pitch ratio etc. are also evaluated in each study. It can be observed that for different studies there was different overall enhancement ratio with different factors studied. Experimentally, receivers equipped with twisted tape inserts geometries show high thermal performance compared with coiled, porous disc, internal fins, metal foam, and corrugated spiral receivers. It can likewise be noticed that the total improvement is much better at higher Reynolds number values which is associated with higher pressure drop.

It can also be observed, that there was 2-3% improvement in the useful output (heating, cooling or electricity) and these outcomes demonstrate that the utilisation of nanofluids can be used successfully in genuine PTC frameworks. Nonetheless, this moderately little improvement can increase the monetary status of the framework and build its yearly yield with good annual revenue. Additionally, the utilisation of nanofluids can diminish the heat exchange surface regions and consequently decreases the collecting region and minimises the land usage to install the PTC frameworks. Besides, the utilisation of nanofluids can diminish the CO_2 discharges in the process of heat generation or power generation.

Another important aspect of this literature review is the usage of various kinds of gases in numerical studies of PTC systems. It also improved the exergetic performance of the PTC systems by high amount. There is a variation in the found outcomes because of the difference in the operational conditions used in every study. For instance, the optimum exergetic efficiency is 45.3% achieved with helium. However, it is 25.62% for operation with air, while for therminol VP-1 is 31.67% for 500K and 100 L/min (Bellos et al., 2016) [168]. It can thus be seen from this very little literature of PTC system operated with gases that there is a need for further experimental research to be conducted to check the applicability of using different types of gases in PTC systems.

It can also be noticed from this literature review for PTC-based binary nanofluids that there are just few experimental studies, and thermal effectiveness improvement of 13% was observed. It is clear that there is a requirement for increasingly experimental studies for PTC utilising various kinds of binary nanofluids. The outcomes demonstrate that the exergetic augmentation with the utilisation of binary nanofluids is significant and thus the utilisation of PTC-based binary nanofluid for power generation is suggested and promising.

It can also be inferred that the high thermal and exergetic efficiency improvements in the practical and theoretical studies demonstrate that the nanofluids and binary nanofluids are fluids of the future. In any case, there is a requirement for building up measures for performing appropriate investigations with nanofluids. Also, the specialists need to consider that the frameworks must be tried under the equivalent working conditions and to give high accentuation in the best possible assurance of the optical efficiency for each situation. Additionally, the thermophysical properties of each fluid used need to be experimentally quantified and not just depending on theoretical equations that are available in the open literature to estimate these properties.

2.9 Conclusions

This chapter surveys the approaches used (mathematical, experimental, and numerical) on thermal augmentation techniques of PTC systems. There are levels of popularity of giving higher thermal rate and lower pressure loss in PTC frameworks. The utilisation of modified surfaces such as discs, fins, wire coil, twisted tape or any surface modifications can augment the heat transfer with its surface area as it causes high turbulence intensity, and strong secondary flows. Moreover, there important parameters need to be taken into consideration for improving the thermal effectiveness of PTC frameworks and one of them is the choice of the working fluids type with various operating temperatures. Another vital aspect is the thermal energetic and exergetic analyses to identify the thermal and exergetic efficiencies of PTC frameworks. In this chapter, the thermal effectiveness augmentation with conventional fluids, single nanofluids and binary nanofluids as well as gases additionally featured, along with the nanofluids benefits are obviously portrayed. Additionally, the difficulties about the utilisation of these fluids in this solar research area are likewise examined. The major findings from this current chapter are outlined below:

- The utilisation of inserts gives comparable outcomes in the thermal effectiveness augmentation of the PTC framework. Notwithstanding, this strategy presents points of interest contrasted with the utilisation of inner fins or nanofluids as it tends to be applied in the current PTC without alterations which have many working difficulties.
- The use of fins with high number produces to larger effectiveness, however; it is recommended that the location of fins must be in PTC's lower part. The fins located at the PTC's upper part did not provide remarkable improvement in the PTC performance.
- The wavy-tape insert is more viable and appropriate to be utilised more effective and applicable in PTC when the system is operated at a relatively lower flow rate as the merits of wavy PTC slowly diminished as the fluid mass flow rate increased due to the high increment of flow resistance.
- Utilising nanofluid in PTC has several advantages and causes augmenting the thermal field, thusly diminishing the size of cylinders and heat exchangers. Consequently, they diminish the thermal stress and the receiver's deformation. However, these benefits can

be obtained with some modifications (for example, materials, framework design, and capital cost) on the PTC framework.

- The results revealed that with expanded nanofluid volume fraction proportions, receiver thermal execution debases, for both PTC heat loss and CTD expanding, particularly at low stream rates.
- The metallic (Cu, SiC) nanoparticles enhance heat transfer incredibly than different nanoparticles (C, Al_2O_3). It is found that combining both mechanisms (fins and nanofluid) provides excellent heat transfer and greater thermo-hydraulic performance.
- The PTC investigations using nanofluids are the majority in the available literature. The experimental examinations demonstrate significant enhancement near 11-13%, while the theoretical investigations provide lower value. The CFD models produce thermal effectiveness of 8%, while the thermal analyses provide improvements of 1-2%.
- The copper is a suitable option to be utilised as PTC's absorber pipe material in terms of thermal strain and deformation.
- The results clearly indicated that the nanofluids have higher thermal effectiveness than classical fluids. These augmentations are responsively small because of the thermal losses associated with PTCs, however, these augmentations can make the PTCs an increasingly feasible and good energy innovation.
- It is proved that the use of alternative working fluids, as helium and carbon dioxide, can lead to higher exergetic output, compared with air, especially in higher temperature levels. This result establishes the use of these gases in many industrial applications and in power generation plants.

2.10 Challenges and Research Gap

It could be seen from the literature review that nanofluids offer a few alluring and helpful properties that can enhance the exhibition of PTC frameworks. Specifically, thermal conductivity improvement found in various nanofluids has urged numerous scientists to assess their performance in PTC frameworks as found in Table 2.4. The consequences of a few examinations are displayed in Table 2.4, which can affirm that the expansion of

little amounts of nanoparticles can remarkably enhance the properties of working liquids. In any case, investigations have additionally recognised various components (i.e., particle clustering, agglomeration and precipitation) that block the long-term stability, the possibility of the nanofluids in real applications and suitability of nanofluids for practical use in sun-oriented thermal applications.

The long-term stability of nanoparticles suspensions is one of the significant issues for both applied and practical investigations. Planning strategy is a fundamental job in the final nanofluid product quality. It is commonly to add surfactants or added substances to the nanofluid in order to influence its surface science, diminish the surface tension occurs in the liquid, enhance the nanoparticle suspension in a liquid and it would eventually augment the overall properties of the nanofluid. For instance, expanding convergences of surfactants will increase nanofluid consistency and produce larger pressure loss through the PTC framework. This will cause higher pumping power to circulate the nanofluid fluid, which is deemed a significant issue and must be investigated in details. Subsequently, there is a requirement for appropriate computation of the extra pumping power. Thus, it is suggested that the correct criteria to assess both the thermal augmentation and the higher pumping work are made using the exergy and overall efficiency.

Besides, factors, for example, evolving thermo-physical properties with temperature, with temperature, particle size variation, changing particle volume fraction and photo-thermal degradation all require further investigations. For instance, expanding the volume fraction of added substances will expand the nanofluids density and viscosity, which will have higher-pressure loss through the PTC framework, which requires a higher pumping power to flow the working liquid. A regular measurement of surfactant amount can significantly influence the consistency and stability as well as the thermal properties of the nanofluids. Thus, obtaining stable nanofluids with high-volume fraction is the most challenging steps for future investigation.

Another challenge associated with the increment of surfactants amount in the preparation

process of nanofluids at high temperature levels is the added surfactants may be decomposed causing detrimental effects. It is imperative to evaluate the nanofluid quality before it's applied in any application and this is dependent on the used technique rules in order to standardise the experimental outcomes from various research groups. Along these lines, top to bottom hypothetical and experimental examinations are expected to help the exact and systematic comprehension of parameters affecting the nanofluids performance. The need to a detailed clarification to the errors associated with the experimental outcomes is necessary along with providing exact combination and portrayal of nanofluids following a standardised methodology. There is also a need to look more into nanofluid's material science to analyse some confusions about the controlling parameters responsible for heat transfer enhancement.

It can be inferred from the above literature survey that the majority of investigations until date are mostly centered on nanofluids with water as base fluid than oil. Therefore, extra investigations on nanofluids with oil is fundamental to examine their impact on PTC frameworks carefully. More consumption tests are essential to evaluate the impacts of long-term nanofluid runs in PTC frameworks. The nanofluids stability ought to be examined for different PTC frameworks utilising, for example, functionalized nanoparticles. Another important issue is that there is a need for more research on the usage of nanofluids or hybrid nanofluids in PTC systems to check their efficacy.

In addition, the majority of the investigations have centered their attention on PTC systems either with or without passive techniques, whereas very little investigations are reported showing PTC systems using hybrid nanofluids. Mono and binary nanoparticles can be utilised with aqueous and oil as base fluids to examine PTC systems performance. Additionally, environmental impact, exergetic and life cycle analyses should be done in order to evaluate the reasonability of utilising binary nanofluids in PTC frameworks and other solar systems.

There are some research gaps that can be highlighted from the present review which require additional research as follows:

- The development of new heat transfer fluids needs to be intensified and a consistent theory is urgently required to execute new thermal fluids in real solar energy applications.
- Another important topic to be addressed is the report of the thermophysical properties of hybrid nanofluids, as well as to propose solid correlations to estimate the properties of these new heat transfer fluids.
- In solar energy applications, fluid flow is generally in the laminar regime. Therefore, numerical endeavors are considerably required to fully understand the behavior of hybrid nanofluids in turbulent flows.
- The development of new PTC using passive technique with different shapes such as conical and wavy combined with hybrid nanofluids are also needed to distinguish their effects on the PTC overall performance. The performance enhancements of the incredible sunlight-based field will demonstrate the real improvement, and this will be a critical step for the foundation and commercialisation of nanofluid/binary nanofluids based solar frameworks.

References

[1] Romero M., Martınez D., Zarza E. Terrestrial solar thermal power plants: on the verge of commercialization. *In: 4th int conf on sol power from space* (2004).

[2] CSP technologies, 2018 Retrieved from https://hub.globalccsinstitute.com/publications/concentrating-solar-power-india/21-csp-technologies Accessed 10 July 2018

[3] Kalogirou, S. A. Solar thermal collectors and applications. *Progress in Energy and Combustion Science* (2004), *30*, 231–295.

[4] Jebasingh, V. K., Joselin Herbert, G. M.. A review of solar parabolic trough collector. *Renewable and Sustainable Energy Reviews* (2016), *54*, 1085–1091.

[5] Yilmaz, I. H., Mwesigye, A.. Modeling, simulation and performance analysis of parabolic trough solar collectors: A comprehensive review. *Applied Energy* (2018), *225*, 135–174.

[6] Tian, Y., Zhao, C. Y.. A review of solar collectors and thermal energy storage in solar thermal applications. *Appl Energy* (2013), *104*, 538–553.

[7] Thirugnanasambandam, M., Iniyan, S., Goic, R. A review of solar thermal technologies. *Renew. Sustain. Energy Rev.* (2010), *14*, 312–322.

[8] Sukhatme, K., Sukhatme, S. P. Solar Energy-Principles of Thermal Collection and Storage; Tata McGraw-Hill Education: New Delhi, India.

[9] Rabl, A. (1976). Optical and thermal properties of compound parabolic collectors. *Sol. Energy* (1996), *18*, 497–511.

[10] Zhang, H. L., Baeyens, J., Degreve, J., Caceres, G. Concentrated solar power plants: A review and design methodology. *Renew. Sustain. Energy Rev.* (2013), *22*, 466–481.

[11] Kainth, M., Sharma, V. K. Latest evolutions in flat plate solar collectors technology. *Int. J. Mech. Eng.* (2014), *1*, 7–11.

[12] Hellstrom, B., Adsten, M., Nostell, P., Karlsson, B., Wackelgard, E. The impact of optical and thermal properties on the performance of flat plate solar collectors. *Renew. Energy* (2003), *28*, 331–344.

[13] Konttinen, P., Lund, P. D., Kilpi, R. J. Mechanically manufactured selective solar absorber surfaces. *Sol. Energy Mater. Sol. Cells* (2003), *79*, 273–283.

[14] Vasiliev, L. L. Heat pipes in modern heat exchangers. *Appl. Therm. Eng.* (2005), *25*, 1-19.

[15] Alghoul, M. A., Sulaiman, M. Y., Azmi, B. Z., Wahab, M. A. Review of materials for solar thermal collectors. *Anti Corros. Methods Mater.* (2005), *52*, 199–206.

[16] Al-Madani, H.. The performance of a cylindrical solar water heater. *Renew. Energy* (2006), *31*, 1751–1763.

[17] Minardi, J. E., Chuang, H. N. Performance of a “black” liquid flat-plate solar collector. *Sol. Energy* (1975), *17*, 179-183.

[18] Grasse, W., Hertlein, H., Winter, C. J., Braun, G. Thermal solar power plants experience. *In Solar Power Plants; Springer: Berlin/Heidelberg, Germany* (1991).

[19] Lee, D. W., Sharma, A. Thermal performances of the active and passive water heating systems based on annual operation. *Sol. Energy* (2007), *81*, 207–215.

[20] Eastop, T. D., McConkey, A. Applied Thermodynamics for Engineering Technologists; Longman: London, UK, 1977.

[21] Gouthamraj, K., Rani, K., Satyanarayana, G. Design and analysis of rooftop linear fresnel reflector solar concentrator. *Int. J. Eng. Innov. Technol.* (2013), *2*, 66–69.

[22] Bakos, G. C. Design and construction of a two-axis Sun tracking system for parabolic trough collector (PTC) efficiency improvement *Renew. Energy* (2006), *31*, 2411–2421.

[23] Kalogirou, S. A. A detailed thermal model of a parabolic trough collector receiver. *Energy* (2012), *48*(1), 298–306.

[24] Nixon, J. D., Dey, P. K., Davies, P. A. Which is the best solar thermal collection technology for electricity generation in north-west India? Evaluation of options using the analytical hierarchy process. *Energy* (2010), *35*, 5230–5240.

[25] Wei, X. D., Lu, Z. W., Wang, Z. F., Yu, W. X., Zhang, H. X., Yao, Z. H. A new method for the design of the heliostat field layout for solar tower power plant. *Renew. Energy* (2010), *35*, 1970–1975.

[26] Behar, O., Khellaf, A., Mohammedi, K. A review on central receiver solar thermal power plants. *Renew. Sustain. Energy Rev.* (2013), *23*, 12–39.

[27] Sureshkumar, R., Mohideen, S. T., Nethaji, N. Heat transfer characteristics of nanofluids in heat pipes: A review. *Renew. Sustain. Energy Rev.* (2013), *20*, 397–410.

[28] Duncan, A. B., Peterson, G. P. Review of micro-scale heat transfer. *Appl. Mech. Rev.* (1994), *47*, 397–428.

[29] Das, S. K., Choi, S. U. S., Patel, H. P. Heat transfer in nanofluids: A review. *Heat Transf. Eng.* (2006), *27*, 3–19.

[30] Godson, L., Raja, B., Mohan, L. D., Wongwises, S. Experimental investigation on the thermal conductivity and viscosity of silver-deionized water nanofluid. *Exp. Heat Transf.* (2010), *23*, 317–332.

[31] Saidur, R., Leong, K. Y., Mohammed, H. A. A review on applications and challenges of nanofluids. *Renew Sust Energy Reviews* (2011), *15*(3), 1646–1668.

[32] Hwang, Y., Lee, J. K., Lee, C. H., Jung, Y. M., Cheong, S. I., Lee, C. G., Ku, B. C., Jang, S. P. Stability and thermal conductivity characteristics of nanofluids. *Thermochim. Acta* (2007), *455*, 70–74.

[33] Shou, C. H., Luo, Z. Y., Wang, T., Cai, J. C., Zhao, J. F., Ni, M. J., Cen, K. F. Research on the application of nano-fluids into the solar photoelectric utilization. *Shanghai Electr. Power* (2009), *16*, 8–12.

[34] Perry, R. H., Green, D. W. Perry's Chemical Engineers' Handbook, 7th ed.; McGraw-Hill, Inc.: New York, NY, USA (1997).

[35] Kim, S. H., Choi, S. R., Kim, D. Thermal conductivity of metal-oxide nanofluids: Particle size dependence and effect of laser irradiation *J. Heat Transf. Trans. ASME* (2007), *129*, 298–307.

[36] Dean, J. A. Lange's Handbook of Chemistry, 14th ed.; McGraw-Hill, Inc.: New York, NY, USA (1992).

[37] Fernandez-Garcı´a, A., Zarza, E., Valenzuela, L., Pe´rez, M. Parabolic-trough solar collectors and their applications. *Renewable and Sustainable Energy Reviews* (2010), *14*, 1695–1721.

[38] Price, H., Lupfert, E., Kearney, D., Zarza, E., Cohen, G., Gee, R. Advances in parabolic trough solar power technology. *J Solar Energy Eng* (2002), *124*, 109–125.

[39] Yilmaz, I. H., Söylemez, M. S. Transient simulation of solar assisted wheat cooking by parabolic trough collector. *J Global Eng Stud* (2016), *3*, 93–106.

[40] Internationbal Energy Agency, 2018 Retrieved from https://hub.globalccsinstitute.com/publications/concentrating-solar-power-india/21-csp-technologies Accessed 10 July 2018

[41] Behar, O., Khellaf, A., Mohammedi, K. A novel parabolic trough solar collector model–Validation with experimental data and comparison to Engineering Equation Solver (EES). *Energy Convers Manage* (2015), *106*, 268–281.

[42] Yilmaz, I. H. Optimization of an integral flat plate collector-storage system for domestic solar water heating in Adana. *Anad Univ J Sci Technol A - Appl Sci Eng* (2018), *19*, 165–176.

[43] Duffie, J. A., Beckman, W. A. Solar engineering of thermal processes, 2nd ed. John Wiley & Sons (1991).

[44] Gaul, H., Rabl, A. Incidence-angle modifier and average optical efficiency of parabolic trough collectors. *J Sol Energy Eng* (1980); *102*, 16–21.

[45] Xu, C., Chen, Z., Li, M., Zhang, P., Ji, X., Luo, X. Research on the compensation of the end loss effect for parabolic trough solar collectors. *Appl Energy* (2014), *115*, 128–139.

[46] Edenburn, M. W. Performance analysis of a cylindrical parabolic focusing collector and comparison with experimental results. *Sol Energy* (1976), *18*, 437–444.

[47] Guven, H., Bannerot, R. Derivation of universal error parameters for comprehensive optical analysis of parabolic troughs. *J Sol Energy Eng* (1986), *108*, 275–281.

[48] Mokheimer, E. M., Dabwan, Y. N., Habib, M. A., Said, S. A., Al-Sulaiman, F. A. Techno-economic performance analysis of parabolic trough collector in Dhahran, Saudi Arabia *Energy Convers Manage* (2014), *86*, 622–633.

[49] Mwesigye, A., Yılmaz, I. H., Meyer, J. P. Numerical analysis of the thermal and thermodynamic performance of a parabolic trough solar collector using SWCNTs-Therminol VP-1 nanofluid. *Renewable Energy* (2018), *119*, 844-862.

[50] Herwig, H., Kock, F. Direct and indirect methods of calculating entropy generation rates in turbulent convective heat transfer problems. *J Heat Mass Transfer* (2007), *43*, 207-215.

[51] Bejan, A. Entropy generation minimization: the method of thermodynamic optimization of finite-size systems and finite-time processes. CRC Press (1996).

[52] Amani, E., Nobari, M. R. H. A numerical investigation of entropy generation in the entrance region of curved pipes at constant wall temperature. *J Energy* (2011), *38*(11), 1-10.

[53] Hojjat, M., Etemad, S. G., Bagheri, R., Thibault, J. Turbulent forced convection heat transfer of non-Newtonian nanofluids. *Exp Therm Fluid Sci* (2011), *35*, 1351–1356

[54] Geyer, P. E., Fletcher, D. F., Haynes, B. S. Laminar flow and heat transfer in a periodic trapezoidal channel with semi-circular cross section. *Int J Heat Mass Transf* (2007), *50*, 3471–3480.

[55] Dewan, A., Mahanta, P., Sumithra Raju, K., Suresh Kumar, P. Review of passive heat transfer augmentation techniques. *Proc IMechE Part A: J Power Energy* (2004), *218*, 509–527.

[56] Hsieh, S. S., Huang, I. W. Heat transfer and pressure drop of laminar flow in horizontal tubes with/without longitudinal inserts *J Heat Transf (ASME)* (2000), *122*, 465–475.

[57] Reddy, K. S., Satyanarayana, G. V. Numerical study of porous finned receiver for solar parabolic trough concentrator. *Engineering Applications of Computational Fluid Mechanics* (2008), *2*(2), 72–184.

[58] Reddy, K. S., Kumar, K. R., Satyanarayana, G. V. Numerical investigation of energy-efficient receiver for solar parabolic trough concentrator. *Heat Transfer Engineering* (2008), *29* (11), 961–972.

[59] Kumar, K. R., Reddy, K. S. Thermal analysis of solar parabolic trough with porous disc receiver *Applied Energy* (2009), *86*, 1804–1812.

[60] Muñoz, J., Abánades, A. Analysis of internal helically finned tubes for parabolic trough design by CFD tools. *Applied Energy* (2011), *88*, 4139–4149.

[61] Kumar, K. R., Reddy, K. S. Effect of porous disc receiver configurations on performance of solar parabolic trough concentrator. *Heat Mass Transfer* (2012), *48*, 555–571.

[62] Cheng, Z. D., He, Y. L., Cui, F. Q. Numerical study of heat transfer enhancement by unilateral longitudinal vortex generators inside parabolic trough solar receivers. *International Journal of Heat and Mass Transfer* (2012), *55*, 5631–5641.

[63] Islam, M., Karim, A., Saha, A. C., Miller, S., Prasad, K. D., Yarlagadda, V. Three dimensional simulation of a parabolic trough concentrator thermal collector. *Proceedings of the 50th annual conference, Australian Solar Energy Society (Australian Solar Council),* (2012) *Swinburne University of Technology, Melbourne, Australia.*

[64] Aldali, Y., Muneer, T., Henderson, D. Solar absorber tube analysis: thermal simulation using CFD. *International Journal of Low-Carbon Technologies* (2013), *8*, 14–19.

[65] Wang, P., Liu, D.Y., Xu, C. Numerical study of heat transfer enhancement in the receiver tube of direct steam generation with parabolic trough by inserting metal foams. *Applied Energy* (2013), *102*, 449–460.

[66] Ghasemi, S. E., Ranjbar, A. A., Ramiar, A. Three-dimensional numerical analysis of heat transfer characteristics of solar parabolic collector with two segmental rings. *Journal of mathematics and computer Science* (2013), *7*, 89 - 100.

[67] Ghadirijafarbeigloo, S., Zamzamian, A. H., Yaghoubi, M. 3-D numerical simulation of heat transfer and turbulent flow in a receiver tube of solar parabolic trough concentrator with louvered twisted-tape inserts. *Energy Procedia* (2014), *49*, 373 – 380.

[68] Too, Y. C. S., Benito, R. Enhancing heat transfer in air tubular absorbers for concentrated solar thermal applications, Applied Thermal Engineering (2013); 50 (1), 1076-1083.

[69] Waghole, D. R., Warkhedkar, R. M., Kulkarni, V. S., Shrivastva, R. K. Experimental Investigations on Heat Transfer and Friction Factor of Silver Nanofliud in Absorber/Receiver of Parabolic Trough Collector with Twisted Tape Inserts. *Energy Procedia* (2014), *45*, 558 – 567.

[70] Song, X., Dong, G., Gao, F., Diao, X., Zheng, L., Zhou, F. A numerical study of parabolic trough receiver with nonuniform heat flux and helical screw-tape inserts. *Energy* (2014), *77*, 771-782.

[71] Mwesigye, A., Bello-Ochende, T., Meyer, J. P. Heat transfer and thermodynamic performance of a parabolic trough receiver with centrally placed perforated plate inserts. *Applied Energy* (2014), *136*, 989–1003.

[72] Mwesigye, A., Bello-Ochende, T., Meyer, J. P. Multi-objective and thermodynamic optimisation of a parabolic trough receiver with perforated plate inserts. *Applied Thermal Engineering* (2015), *77*, 42-56.

[73] Syed Jafar, K., Sivaraman, B. Thermal performance of solar parabolic trough collector using nanofluids and the absorber with nail twisted tapes inserts. *International Energy* (2014), *14*, 189-198.

[74] Mwesigye, A., Huan, Z. Thermal and thermodynamics performance of a parabolic trough receiver with Syltherm 800-Al_2O_3 nanofluid as the heat transfer fluid. *Energy Procedia* (2015), *75*, 394 – 402.

[75] Huang, Z., Yu, G. L.,Li, Z. Y., Tao, W. Q. Numerical study on heat transfer enhancement in a receiver tube of parabolic trough solar collector with dimples, protrusions and helical fins. *Energy Procedia* (2015), *69*, 1306 – 1316.

[76] Chang, C., Xu, C., Wu, Z. Y., Li, X., Zhang, Q. Q., Wang, Z. F. Heat transfer enhancement and performance of solar thermal absorber tubes with circumferentially non-uniform heat flux. *Energy Procedia* (2015), *69*, 320 – 327.

[77] Lu, J., Ding, J., Yu, T., Shen, X. Enhanced heat transfer performances of molten salt receiver with spirally grooved pipe. *Applied Thermal Engineering* (2015), *88*, 491- 498.

[78] Reddy, K. S., Kumar, K. R., Ajay, C. S. Experimental investigation of porous disc enhanced receiver for solar parabolic trough collector. *Renewable Energy* (2015), *77*, 308-319.

[79] Diwan, K., Soni, M. S. Heat transfer enhancement in absorber tube of parabolic trough concentrators using wire-coils inserts. *Universal Journal of Mechanical Engineering* (2015), *3*(3), 107-112.

[80] Mwesigye, A., Bello-Ochende, T., Meyer, J. P. Heat transfer and entropy generation in a parabolic trough receiver with wall-detached twisted tape inserts. *International Journal of Thermal Sciences* (2016), *99*, 238-257.

[81] Bellos, E., Tzivanidis, C., Antonopoulos, K. A., Daniil, I. The use of gas working fluids in parabolic trough collectors – An energetic and exergetic analysis. *Applied Thermal Engineering* (2016), *109*, 1–14.

[82] ZhangJing, Z., Yang, X., Yaling, H. Thermal analysis of a solar parabolic trough receiver tube with porous insert optimized by coupling genetic algorithm and CFD. *Science China Technological Sciences* (2016), *59* (10), 1475-1485.

[83] Fuqiang, W., Qingzhi, L., Huaizhi, H., Jianyu, T. Parabolic trough receiver with corrugated tube for improving heat transfer and thermal deformation characteristics. *Applied Energy* (2016), *164*, 411–424.

[84] Jaramillo, O. A., Borunda, M., Velazquez-Lucho, K. M., Robles, M. Parabolic trough solar collector for low enthalpy processes: An analysis of the efficiency enhancement by using twisted tape inserts. *Renewable Energy* (2016), *93*, 125-141.

[85] Benabderrahmane, A., Aminallah, M., Laouedj, S., Benazza, A., Solano, J. P. (2016). Heat transfer enhancement in a parabolic trough solar receiver using longitudinal fins and nanofluids. *Journal of Thermal Science*, *25* (5), 410-417.

[86] Chang, C., Peng, X., Nie, B., Leng, G., Li, C., Hao, Y., She, X. Heat transfer enhancement of a molten salt parabolic trough solar receiver with concentric and eccentric pipe inserts. *Energy Procedia* (2017); (142), 624–629.

[87] Ghasemi, S. E., Ranjbar, A. A. Numerical thermal study on effect of porous rings on performance of solar parabolic trough collector. *Applied Thermal Engineering* (2017), *118*, 807–816.

[88] Bortolato, M., Dugaria, S., Del Col, D. Experimental study of a parabolic trough solar collector with flat bar-and-plate absorber during direct steam generation. *Energy* (2016), *116*, 1039-1050.

[89] Rawani, A., Sharma, S. P., Singh, K. D. P. Enhancement in performance of parabolic trough collector with serrated twisted-tape inserts. *International Journal of Thermodynamics* (2017), *20* (2), 111-119.

[90] Jamal-Abad, M. T., Saedodin, S., Aminy, M. Experimental investigation on a solar parabolic trough collector for absorber tube filled with porous media. *Renewable Energy* (2017), *107*, 156-163.

[91] Bellos, E., Tzivanidis, C., Tsimpoukis, D. Multi-criteria evaluation of parabolic trough collector with internally finned absorbers. *Applied Energy* (2017), *205*, 540–561.

[92] Bellos, E., Tzivanidis, C., Daniil, I., Antonopoulos, K. A. The impact of internal longitudinal fins in parabolic trough collectors operating with gases. *Energy Conversion and Management* (2017), *135*, 35–54.

[93] Bellos, E., Tzivanidis, C., Daniil, I. Energetic and exergetic investigation of a parabolic trough collector with internal fins operating with carbon dioxide. *Int J Energy Environ Eng* (2017), *8*, 109–122.

[94] Zhu, X., Zhu, L., Zhao, J. Wavy-tape insert designed for managing highly concentrated solar energy on absorber tube of parabolic trough receiver. *Energy* (2017), *141*, 1146 -1155.

[95] Xiangtao, G., Fuqiang, W., Haiyan, W., Jianyu, T., Qingzhi, L., Huaizhi, H. Heat transfer enhancement analysis of tube receiver for parabolic trough solar collector with pin fin arrays inserting. *Solar Energy* (2017), *144*, 185–202.

[96] Huang, Z., Li, Z. Y., Yu, G. L., Tao, W. Q. Numerical investigations on fully-developed mixed turbulent convection in dimpled parabolic trough receiver tubes. *Applied Thermal Engineering* (2017), *114*, 1287–1299.

[97] Chang, C., Sciacovelli, A., Wu, Z., Li, X., Li, Y., Zhao, M., Deng, J., Wang, Z., Ding, Y. Enhanced heat transfer in a parabolic trough solar receiver by inserting rods and using molten salt as heat transfer fluid. *Applied Energy* (2018), *220*, 337–350.

[98] Bellos, E., Tzivanidis, C., Tsimpoukis, D. Thermal, hydraulic and exergetic evaluation of a parabolic trough collector operating with thermal oil and molten salt based nanofluids. *Energy Conversion and Management* (2018), *156*, 388–402.

[99] Bellos, E., Tzivanidis, C., Tsimpoukis, D. Optimum number of internal fins in parabolic trough collectors. *Applied Thermal Engineering* (2018), *137*, 669–677.

[100] Bitam, E., Demagh, Y., Hachicha, A. A., Benmoussa, H., Kabar, Y. Numerical investigation of a novel sinusoidal tube receiver for parabolic trough technology. *Applied Energy* (2018), *218*, 494–510.

[101] Tripathy, A. K., Ray, S., Sahoo, S. S., Chakrabarty, S. Structural analysis of absorber tube used in parabolic trough solar collector and effect of materials on its bending: A computational study. *Solar Energy* (2018), *163*, 471–485.

[102] Okonkwo, E. C., Abid, M., Ratlamwala, T. A. H. Effects of synthetic oil nanofluids and absorber geometries on the exergetic performance of the parabolic trough collector. *Int J Energy Res.* (2018), 1-16.

[103] Rawani, A., Sharma, S. P., Singh, K. D. P. Comparative performance analysis of different Twisted tape inserts in the absorber tube Of parabolic trough collector. *International Journal of Mechanical and Production Engineering Research and Development* (2018), *8*(1), 643-656.

[104] Benabderrahmane A., Benazza A., Hussein A. K. Heat transfer enhancement analysis of tube receiver for parabolic trough solar collector with central corrugated insert, *J. Heat Transfer*, (2020); 142(6): 062001.

[105] Khan, M. S., Yan, M., Ali, H. M., Amber, K. P., Bashir, M. A., Akbar, & Javed, S. Comparative performance assessment of different absorber tube geometries for parabolic trough solar collector using nanofluid. *Journal of Thermal Analysis and Calorimetry Volume* (2020), *142*, 2227–2241.

[106] Cheng, Z. D., He, Y. L., Xiao, J., Tao, Y. B., Xu, R. J. Three-dimensional numerical study of heat transfer characteristics in the receiver tube of parabolic trough solar collector. *International Communications in Heat and Mass Transfer* (2010), *37*, 782–787.

[107] Tao, Y. B., He, Y. L. Numerical study on coupled fluid flow and heat transfer process in parabolic trough solar collector tube. *Solar Energy* (2010), *84*, 1863–1872.

[108] He, Y. L., Xiao, J., Cheng, Z. D., Tao, Y. B. A MCRT and FVM coupled simulation method for energy conversion process in parabolic trough solar collector. *Renewable Energy* (2011), *36*, 976-985.

[109] Cheng, Z. D., He, Y. L., Cui, F.Q., Xu, R. J., Tao, Y. B. Numerical simulation of a parabolic trough solar collector with nonuniform solar flux conditions by coupling FVM and MCRT method. *Solar Energy* (2012), *86*, 1770–1784.

[110] Hachicha, A. A., Rodríguez, I., Capdevila, R., Oliva, A. Heat transfer analysis and numerical simulation of a parabolic trough solar collector. *Applied Energy* (2013), *111*, 581–592.

[111] Mwesigye, A., Bello-Ochende, T., Meyer, J. P. Numerical investigation of entropy generation in a parabolic trough receiver at different concentration ratios. *Energy* (2013), *53*, 114-127.

[112] Mwesigye, A., Bello-Ochende, T., Meyer, J. P. Minimum entropy generation due to heat transfer and fluid friction in a parabolic trough receiver with non-uniform heat flux at different rim angles and concentration ratios. *Energy* (2014), *73*, 606-617.

[113] Chang, C., Li, X., Zhang, Q. Q. Experimental and numerical study of the heat transfer characteristics in solar thermal absorber tubes with circumferentially non-uniform heat flux. *Energy Procedia* (2014), *49*, 305 – 313.

[114] Wang, Y., Liu, Q., Lei, J., Jin, H. A three-dimensional simulation of a parabolic trough solar collector system using molten salt as heat transfer fluid. *Applied Thermal Engineering* (2014), *70*, 462-476.

[115] Wu, Z., Li, S., Yuan, G., Lei, D., Wang, Z. Three-dimensional numerical study of heat transfer characteristics of parabolic trough receiver. *Applied Energy* (2014), *113*, 902–911.

[116] Cheng, Z. D., He, Y. L., Cui, F. Q., Du, B. C., Zheng, Z. J., Xu, Y. Comparative and sensitive analysis for parabolic trough solar collectors with a detailed Monte Carlo ray-tracing optical model. *Applied Energy* (2014), *115*, 559–572.

[117] Wang, Y. L., Q., Lei, J., Jin, H. Performance analysis of a parabolic trough solar collector with non-uniform solar flux conditions. *International Journal of Heat and Mass Transfer* (2015), *82*, 236–249.

[118] Tzivanidis, C., Bellos, E., Korres, D., Antonopoulos, K. A., Mitsopoulos, G. Thermal and optical efficiency investigation of a parabolic trough collector. *Case Studies in Thermal Engineering* (2015), *6*, 226–237.

[119] Li, Z. Y., Huang, Z., Tao, W. Q. Three-dimensional numerical study on turbulent mixed convection in parabolic trough solar receiver tube. *Energy Procedia* (2015), *75*, 462 – 466.

[120] Li, Z. Y., Huang, Z., Tao, W. Q. Three-dimensional numerical study on fully-developed mixed laminar convection in parabolic trough solar receiver tube. *Energy* (2016), *113*, 1288-1303.

[121] Bortolato, M., Dugaria, S., Agresti, F., Barison, S., Fedele, L., Sani, E., Del Col, D. Investigation of a single wall carbon nanohorn-based nanofluid in a fullscale

direct absorption parabolic trough solar collector. *Energy Conversion and Management* (2017), *150*, 693–703.

[122] Bellos, E., Tzivanidis, C., Antonopoulos, K. A. A detailed working fluid investigation for solar parabolic trough collectors. *Applied Thermal Engineering* (2017), *114*, 374–386.

[123] Bellos, E., Tzivanidis, C., Tsimpoukis, D. Thermal enhancement of parabolic trough collector with internally finned absorbers. *Solar Energy* (2017), *157*, 514–531.

[124] Pavlovic, S., Daabo, A. M., Bellos, E., Stefanovi, V., Mahmoud, S., Al-Dadah, R. K. Experimental and numerical investigation on the optical and thermal performance of solar parabolic dish and corrugated spiral cavity receiver. *Journal of Cleaner Production* (2017), *150*, 75-92.

[125] Chafie, M., Ben Aissa, M. F., Guizani, A. Energetic end exergetic performance of a parabolic trough collector receiver: An experimental study. *Journal of Cleaner Production* (2018); (171), 285-296.

[126] Kumar, D., Kumar, S. Thermal performance of the solar parabolic trough collector at different flow rates: an experimental study. *International Journal of Ambient Energy* (2018), *39* (1), 93–102.

[127] Fan, M., Liang, H., You, S., Zhang, H., Zheng, W., Xia, J. Heat transfer analysis of a new volumetric based receiver for parabolic trough solar collector. *Energy* (2018), *142*, 920-931.

[128] Menbari, A., Alemrajabi, A. A., Rezaei, A. (2017). Experimental investigation of thermal performance for direct absorption solar parabolic trough collector (DASPTC) based on binary nanofluids. *Experimental Thermal and Fluid Science* (2017), *80*, 218–227.

[129] Choi, S. U. S. Enhancing thermal conductivity of fluids with nanoparticles, in: D.A. Siginer, H.P. Wang (Eds.). *Developments and Applications of Non-Newtonian Flows, in: FED, vol. 231/MD, vol. 66, ASME, New York*, (1995); 99–103.

[130] Khullar, V., Tyagi, H., Phelan, P. E., Otanicar, T. P., Singh, H., Taylor, R. A. Solar energy harvesting using nanofluids-based concentrating solar collector. *Journal of*

Nanotechnology in Engineering and Medicine (2012), *3*, 031003-031001 - 031003-031009.

[131] Kasaeian, A. B., Sokhansefat, T., Abbaspour, M. J., Sokhansefat, M. Numerical study of heat transfer enhancement by using Al_2O_3/Synthetic oil nanofluid in a parabolic trough collector tube. *World Academy of Science, Engineering and Technology* (2012), *69*, 1154-1159.

[132] de Risi, A., Milanese, M., Laforgia, D. Modelling and optimization of transparent parabolic trough collector based on gas-phase nanofluids *Renewable Energy* (2013), *58*, 134-139.

[133] Sokhansefat, T., Kasaeian, A.B., Kowsary, F. Heat transfer enhancement in parabolic trough collector tube using Al_2O_3/synthetic oil nanofluid. *Renewable and Sustainable Energy Reviews* (2014), *33*, 636–644.

[134] Ghasemi, S. E., Mehdizadeh Ahangar, GH. R. Numerical analysis of performance of solar parabolic trough collector with Cu-Water nanofluid. *International Journal of Nano Dimension* (2014), *5* (3), 233-240.

[135] Sunil, K., Kundan, L., Sumeet, S. Performance evaluation of a nanofluid based parabolic solar collector– an experimental study. *International Journal of Mechanical And Production Engineering* (2014), *2*(10), 61-67.

[136] Mwesigye, A., Huan, Z., Meyer, J. P. Thermodynamic optimisation of the performance of a parabolic trough receiver using synthetic oil–Al_2O_3 nanofluid. *Applied Energy* (2015), *156*, 398–412.

[137] Mwesigye, A., Huan, Z., Meyer, J. P. Thermal performance of a receiver tube for a high concentration ratio parabolic trough system and potential for improved performance with syltherm800-CuO nanofluid. *Proceedings of the ASME 2015 International Mechanical Engineering Congress & Exposition IMECE2015, Houston, Texas, USA.*

[138] Zadeh, P. M., Sokhansefat, T., Kasaeian, A. B., Kowsary, F., Akbarzadeh, A. Hybrid optimization algorithm for thermal analysis in a solar parabolic trough collector based on nanofluid. *Energy* (2015), *82*, 857-864.

[139] Chaudhari, K. S., Walke, P. V., Wankhede, U. S., Shelke, R. S. An Experimental investigation of a nanofluid (Al_2O_3+H_2O) based parabolic trough solar collectors. *British Journal of Applied Science & Technology* (2015), *9*(6), 551-557.

[140] Kasaeian, A., Daviran, S., Azarian, R. D., Rashidi, A. Performance evaluation and nanofluid using capability study of a solar parabolic trough collector. *Energy Conversion and Management* (2015), *89*, 368–375.

[141] Basbous, N., Taqi, M., Janan, M. A. Thermal Performances Analysis of a Parabolic Trough Solar Collector Using Different Nanofluids. *IEEE* (2016), 1-5.

[142] Mwesigye, A., Huan, Z., Meyer, J. P. Thermal performance and entropy generation analysis of a high concentration ratio parabolic trough solar collector with Cu-Therminol VP-1 nanofluid. *Energy Conversion and Management* (2016), *120*, 449–465.

[143] Wang, Y., Xu, J., Liu, Q., Chen, Y., Liu, H. Performance analysis of a parabolic trough solar collector using Al_2O_3/synthetic oil nanofluid. *Applied Thermal Engineering* (2016), *107*, 469–478.

[144] Ghasemi, S. E., Ranjbar, A. A. Thermal performance analysis of solar parabolic trough collector using nanofluid as working fluid: A CFD modelling study. *Journal of Molecular Liquids* (2016), *222*, 159–166.

[145] Kaloudis, E., Papanicolaou, E., Belessiotis, V. Numerical simulations of a parabolic trough solar collector with nanofluid using a two-phase model. *Renewable Energy* (2016), *97*, 218-229.

[146] Coccia, G., Di Nicola, G., Colla, L., Fedele, L., Scattolini, M. Adoption of nanofluids in low-enthalpy parabolic trough solar collectors: Numerical simulation of the yearly yield. *Energy Conversion and Management* (2016), *118*, 306–319.

[147] Ferraroa, V., Settino, J., Cucumo, M. A., Kaliakatsos, D. Parabolic trough system operating with nanofluids: comparison with the conventional working fluids and influence on the system performance. *Energy Procedia* (2016), *101*, 782 – 789.

[148] Mwesigye, A., Meyer, J. P. Optimal thermal and thermodynamic performance of a solar parabolic trough receiver with different nanofluids and at different concentration ratios. *Applied Energy* (2017), *193*, 393-413.

[149] Ghasemi, S. E., Ranjbar, A. A. Effect of using nanofluids on efficiency of parabolic trough collectors in solar thermal electric power plants. *International Journal of Hydrogen Energy* (2017), *42*, 21626 -21634.

[150] Bellos, E., Tzivanidis, C. Parametric investigation of nanofluids utilization in parabolic trough collectors. *Thermal Science and Engineering Progress* (2017), *2*, 71–79.

[151] Khakrah, H., Shamloo, A., Hannani, S. K. Determination of parabolic trough solar collector efficiency using nanofluid: A comprehensive numerical study. *Journal of Solar Energy Engineering* (2017), *139*, 051006-051001- 051006-051011.

[152] Kasaeian, A., Daneshazarian, R., Pourfayaz, F. Comparative study of different nanofluids applied in a trough collector with glass-glass absorber tube. *Journal of Molecular Liquids* (2017), *234*, 315–323.

[153] Subramani, J., Nagarajan, P.K., Mahian, O., Sathyamurthy, R. Efficiency and heat transfer improvements in a parabolic trough solar collector using TiO_2 nanofluids under turbulent flow regime. *Renewable Energy* (2018), *119*, 19-31.

[154] Bellos, E., Tzivanidis, C. Thermal efficiency enhancement of nanofluid-based parabolic trough collectors. *Journal of Thermal Analysis and Calorimetry* (2018), *1*, 1-12.

[155] Bellos, E., Tzivanidis, C., Tsimpoukis, D. Enhancing the performance of parabolic trough collectors using nanofluids and turbulators. *Renewable and Sustainable Energy Reviews* (2018), *91*, 358–375.

[156] Marefati, M., Mehrpooya, M., Shafii, M. B. Optical and thermal analysis of a parabolic trough solar collector for production of thermal energy in different climates in Iran with comparison between the conventional nanofluids. *Journal of Cleaner Production* (2018), *175*, 294-313.

[157] Rehan, M. A., Ali, M., Sheikh, N. A., Khalil, M. S., Chaudhary, G. Q., Ur Rashid, T., Shehryar, M. Experimental performance analysis of low concentration ratio solar parabolic trough collectors with nanofluids in winter conditions. *Renewable Energy* (2018), *118*, 742-751.

[158] De los Rios, M. S. B., Rivera-Solorio, C. I., García-Cuellar, A. J. Thermal performance of a parabolic trough linear collector using Al_2O_3/H_2O nanofluids. *Renewable Energy* (2018), *122*, 665-673.

[159] Allouhi, A., Benzakour Amine, M., Saidur, R., Kousksou, T., Jamil, A. Energy and exergy analyses of a parabolic trough collector operated with nanofluids for medium and high temperature applications. *Energy Conversion and Management* (2018), *155*, 201–217.

[160] Alsaady, M., Fu, R., Yan, Y., Liu, Z., Wu S., Boukhanouf, R. An Experimental investigation on the effect of ferrofluids on the efficiency of novel parabolic trough solar collector under laminar flow conditions. *Heat Transfer Engineering* (2018), *1*(1), 1-9.

[161] Tagle-Salazar, P. D., Nigam, K. D. P., Rivera-Solorio, C. I. Heat transfer model for thermal performance analysis of parabolic trough solar collectors using nanofluids. *Renewable Energy* (2018), *125* 334-343.

[162] Kumar, M. K., Yuvaraj, G., Balaji, D., Pravinraj, R., Shanmugasundaram, P. Influence of nanofluid and receiver modification in solar parabolic trough collector performance. *IOP Conf. Series: Materials Science and Engineering* (2018), *310*, 012140.

[163] Bellos, E., Tzivanidis, C., & Said, Z. A systematic parametric thermal analysis of nanofluid-based parabolic trough solar collectors. *Sustainable Energy Technologies and Assessments* (2020), *39*, 100714.

[164] Minea, A. A., El-Maghlany, W. M. Influence of hybrid nanofluids on the performance of parabolic trough collectors in solar thermal systems: Recent findings and numerical comparison. *Renewable Energy* (2018), *120*, 350-364.

[165] Sidik, N. A. C., Adamu, I. M., Jamil, M. M., Kefayati, G. H. R., Mamat, R., Najafi, G. Recent progress on hybrid nanofluids in heat transfer applications: a comprehensive review. *Int Commun Heat Mass Transfer* (2016), *75*, 68–79.

[166] Bellos, E., Tzivanidis, C. Thermal analysis of parabolic trough collector operating with mono and hybrid nanofluids. *Sustainable Energy Technologies and Assessments* (2018), *26*, 105–115.

[167] Ekiciler, R., Arslan, K., Turgut, O., Kurşun, B. Effect of hybrid nanofluid on heat transfer performance of parabolic trough solar collector receiver, *Journal of Thermal Analysis and Calorimetry* (2021), 143, 1637–1654.

[168] Bellos, E., Tzivanidis, C., Antonopoulos, K. A., Daniil, I. The use of gas working fluids in parabolic trough collectors – An energetic and exergetic analysis. *Applied Thermal Engineering (2016), 109*, 1–14.

[169] Bellos, E., Tzivanidis, C. Parametric investigation of supercritical carbon dioxide utilization in parabolic trough collectors. *Applied Thermal Engineering* (2017), *127* 736–747.

Chapter 3 Research Methodology and Numerical Techniques

3.1 Introduction

Experimental techniques require considerable financial investment such as equipment procurement, infrastructure construction, resources dedication, hiring and training of staff. Numerical modeling reduces dramatically the costs, time, risks involved in running the repeated experiments. Computational Fluid Dynamics (CFD) is one of the many numerical techniques used for simulating fluid flow [1] and the tools used in this thesis. CFD allows computer-based simulations and subsequent analysis of fluid systems by solving conversation equations for mass, energy, and momentum using numerical methods. Moreover, computational techniques, possess the powers to provide information regarding the flow anywhere in the selected domain without interfering with the flow itself and can lead to better understanding of the flow and heat transfer aspects in PTSC systems.

Many researchers are utilising CFD techniques to gain insight of various phenomena taking place within the PTSC system to improve its performance or to provide valuable information for the design process. Moreover, many research groups have shifted their focus to CFD making it widely used tool in the field of solar energy. The advantage of CFD too over the traditional experimental methods lies in the built-in flexibility to change operating conditions, fluid properties, and geometric parameters of the flow channel. For instance, geometric parameters of the flow channel can be varied using an appropriate CFD software, does not need the physical construction of the modified channel, to investigate the effects on parameters of interest. Similarly, fluid properties and operating conditions can be varied to investigate their impact on the parameters of interest without experimentations. Another important and interesting feature of the CFD is that the data can be reported anywhere in the computational domain at any time during the simulation without obstructing the flow itself.

In this thesis, basic data are generated by using Computational Fluid Dynamics (CFD) tools. It is therefore necessary to understand the basic concepts behind CFD. This chapter covers the fundamental concepts of CFD and it also explains the partial differential equations, describing the fluid flow, are converted to algebraic equations for numerical solution.

3.2 Basic Elements of a CFD Code

Fluid flow problems are tackled in every CFD code by means of numerical algorithms. The access to the solving powers of those algorithms is provided by means of user-friendly interfaces in CFD codes. Those interfaces are used to provide problem specific input data and are used to examine the results. Following are the three major elements of every CFD code [1]:

3.2.1 Pre-processor

Function of a pre-processor is to provide flow problem inputs to CFD program by means of user-friendly interface and to convert the input provided in a form suitable to be used by the solver. At the stage of pre-processing following user activities are involved [1]:

- Defining computational domain, i.e. geometry creation of specific region of interest.
- Grid generation or meshing, by dividing the main computational domain into a number of smaller and non-overlapping sub-domains by means of a grid of cells. This yield small control volumes or elements.
- Selecting chemical and physical phenomena that are needed to be modelled.
- Defining fluid properties
- Defining or specifying appropriate boundary conditions at the cells coinciding with domain boundary.

In CFD the solution of the flow problem is defined at nodes inside each cell. The accuracy of the solution depends on the number of cells in the grid. Generally speaking, solution will be more accurate for grids involving larger number of cells.

The accuracy of the solution along with the computational cost (in terms of necessary computer hardware and computational time) both largely depends on the grid fineness. To reduce the computational cost without having an adverse impact on the accuracy of the solution often non-uniform grids are used. These grids are finer in the regions where the variations are higher from point to point and coarser in the area where the variations are on a relatively lower side. To date no CFD commercial code is equipped with robust self-adapting meshing capabilities, although efforts are being made in this direction. Hence, it solely relies on the CFD user to develop an optimal grid, which provides a suitable compromise between the solution accuracy and computational cost. In an industrial CFD project more than 50% of the total time is devoted to the computational domain generation and its meshing [1]. Most of the modern CFD codes either provides CAD-style interface or provides the facility to import data from other pre-processors.

3.2.2 Solver

Commercially available CFD codes use different numerical solution techniques. For instance, CFD codes including ANSYS FLUENT, CFX, PHOENICS and STAR-CD make use of finite volume method to solve the fluid flow problems. Generally, the numerical algorithm follows the three steps:

- Governing equations of fluid flow are integrated over all the finite control volumes of the domain.
- The resulting integral equations are converted to a system of algebraic equations, this step is also referred to as discretization.
- An iterative method is employed to solve the algebraic equations.

Control volume integration results in the conversation of relevant properties for each finite size cell. The most interesting aspect of finite volume method is that clear linkage between the numerical algorithm and physical conversation principles making it conveniently understandable by engineers and in this regard provides it superiority over other methods including finite element and spectral methods. Following equation represents conversation of a flow variable φ within a finite control volume:

$$\begin{pmatrix} Rate\ of\ change \\ of\ \emptyset \\ in\ control\ volume \\ w.r.t\ time \end{pmatrix} = \begin{pmatrix} Net\ rate\ of\ incresae \\ of\ \emptyset \\ due\ to\ convection\ into \\ the\ control\ volume \end{pmatrix} + \begin{pmatrix} Net\ rate\ of\ incresae \\ of\ \emptyset \\ due\ to\ diffusion\ into \\ the\ control\ volume \end{pmatrix} + \begin{pmatrix} Net\ rate\ of\ creation \\ of\ \emptyset \\ inside\ control\ volume \end{pmatrix} \quad (3.1)$$

CFD codes are equipped with discretization techniques for the treatment of relevant transport phenomena (convection/or diffusion), source term (generation or destruction of ∅) and for the rate of change with time. The underlying physical phenomena are quite complex and non-linear in nature and thus needs an iterative approach for the solution. The approach employed by ANSYS FLUENT for that matter is described in detail in section 3.4.1.

3.2.3 Post-processor

Most of the leading commercial CFD packages are equipped with powerful data visualization and export tools, for instance:

- Display of domain geometry and grid. The facility of generating different surfaces at different areas of interest.
- Plotting vectors at various surfaces of interest.
- Contour plots
- Two-dimensional and three-dimensional surface plots.
- Particle tracking
- Manipulate the view (rotate, translate, scale, etc..).
- Animation for dynamic result display
- Data export facility to analyse the generated data outside the code

The reliability of the fluid flow problem results generated by the CFD codes depend on the proper embedment of physical laws and also on the skills of the user. The important decisions that the user has to make at an early stage is whether to model a flow domain in 2D or 3D, to include or exclude the effect of ambient temperature, assume constant density for the working fluid or incorporate the effect of pressure variations on the fluid density etc. The appropriateness of assumptions made by the user at this stage (to simplify the model) partly determines the quality of the results generated by the code.

To have successful simulation results defining the appropriate domain geometry and optimal grid generation are also important tasks for the user at the input stage. The usual criteria for successful results are convergence and grid independence. It has been established earlier that the solution of the fluid flow problem using CFD codes is iterative in nature, which means that for a converged solution the residuals (measure of overall conversation of flow properties) should be very small. The grid independent solution can be obtained by successive refinement of an initially coarse grid till the point when the key results do not change with further grid refinement.

3.3 Transport Equations

A set of equations derived from mass, momentum and energy balances are used to describe transport processes. These equations are generally known as Navier-Stokes equations. These equations are partial differential equations (PDE) and have analytical solution for simple cases only. Numerical methods are employed to solve Navier-Stokes equations for general flows which involve complex geometries and boundary conditions. CFD technique is employed for numerical solution of PDE of continuity, momentum, energy and species transport. The following equation represents general form of transport equation for any property $\emptyset$ [1]:

$$\frac{\partial(\rho\,\emptyset)}{\partial t} + div\,(\rho\,\emptyset\,\mathbf{v}) = div\,(\Gamma_{\emptyset}\,gard\,\emptyset) + S_{\emptyset} \qquad (3.2)$$

In the above equation $\emptyset$ represents any transported quantity which could be a scalar, a vector or a second order tensor. $\mathbf{v}$ and $\Gamma_{\emptyset}$ are the velocity vector and the diffusion coefficient of $\emptyset$. The term $S_{\emptyset}$ represents generation or consumption of $\emptyset$ by a source or a sink respectively. The first term in the above equation represents accumulation of $\emptyset$, second and third terms represent transport of $\emptyset$ due to convection (due to fluid velocity) and diffusion respectively. The above equation can be represented in a differential manner with $\boldsymbol{\nabla}$ operator as:

$$\frac{\partial(\rho\,\emptyset)}{\partial t} + \boldsymbol{\nabla}.(\rho\,\emptyset\,\mathbf{v}) = \boldsymbol{\nabla}.(\Gamma_{\emptyset}\,\boldsymbol{\nabla}\,\emptyset) + S_{\emptyset} \tag{3.3}$$

As it is evident from the literature review that for fluid flow and heat transfer in a PTSC, there is significant effect of gravity and density variation on the solution obtained by CFD simulations [2], [3]. Hence, for that reason variable density was employed for all the simulations carried out in this thesis and the gravitational effect was also considered. Moreover, the working fluid was assumed to be Newtonian and having variable properties as function of temperature.

In most of real-life cases, flow through a PTSC do fall in the Reynolds number category which is below the transition to turbulent flow regime [4]. However, in these types of geometries arrangements of unsteady flow conditions are not common. It can be concluded from the above discussion that steady and unsteady flow conditions through a PTSC modules can be simulated by solving the transport equations with the need of incorporating a turbulence model.

For contact density fluids, continuity equation is defined as [1]:

$$\boldsymbol{\nabla}.\mathbf{v} = 0 \tag{3.4}$$

For incompressible Newtonian fluid neglecting the gravitational effects, momentum transport equation is defined as [5]:

$$\frac{\partial(\rho\,\mathbf{v})}{\partial t} + \boldsymbol{\nabla}.(\rho\,\mathbf{v}\,\mathbf{v}) = -\nabla\,\mathrm{P} + \nabla.[\mu\,(\nabla\,\mathbf{v} + \nabla\,\mathbf{v}^{\boldsymbol{T}})] + \mathbf{F} \tag{3.5}$$

In the above equations **v,** ρ, P, μ, t and **F** represents the velocity vector, density, pressure, dynamic viscosity, time, and external body forces vector respectively.

The species transport equation is defined as [6]:

$$\frac{\partial(\rho\,Y)}{\partial t} + \boldsymbol{\nabla}.(\rho\,Y\,\mathbf{v}) = \boldsymbol{\nabla}.(\rho\,D\,\boldsymbol{\nabla}\,Y) + S \tag{3.6}$$

In the above equations Y**,** D, and S represent the mass fraction of the species, mass diffusivity and source of the species in the fluid respectively.

The above equations are valid at every point in the fluid flow field and require problem specific boundary conditions for solution. The set of PDEs can be solved by a number of available methods including finite element, finite volume, finite difference and spectral methods [1]. Basic philosophy of every numerical method involves transformation of the PDEs to a system of algebraic equations which are later solved by numerical methods. Most of the CFD codes, including FLUENT, use finite volume method [1], [5] for the solution of PDEs. Steps followed by the numerical algorithm in case of finite volume method are explained in section 3.2.2.

In order to simulate fluid flow of an incompressible Newtonian fluid, the governing equations for steady and three-dimensional flow in a cylindrical coordinate acquire the following form [6], [7]:

Continuity equation:

$$\frac{1}{r}\frac{\partial}{\partial\theta}(\rho_{eff}\,u) + \frac{1}{r}\frac{\partial}{\partial r}(\rho_{eff}\,rv) + \frac{1}{r}\frac{\partial}{\partial Z}(\rho_{eff}\,w) = 0 \tag{3.7}$$

θ- Momentum equation:

$$\frac{1}{r}\frac{\partial}{\partial\theta}\left(\rho_{eff}\,uu\right) + \frac{1}{r}\frac{\partial}{\partial r}\left(\rho_{eff}\,rvu\right) + \frac{\partial}{\partial Z}\left(\rho_{eff}\,wu\right) + \frac{1}{r}\left(\rho_{eff}\,uv\right) = -\frac{1}{r}\frac{\partial P}{\partial\theta} +$$
$$\frac{1}{r^2}\frac{\partial}{\partial\theta}\left(\mu_{eff}\,\frac{\partial u}{\partial\theta}\right) + \frac{\partial}{\partial r}\left(\frac{\mu_{eff}}{r}\,\frac{\partial(ru)}{\partial r}\right) + \frac{2\mu_{eff}}{r^2}\,\frac{\partial v}{\partial\theta} + \rho_{eff}\,g\,\beta_{eff}(T_w - T)\sin\theta \tag{3.8}$$

r - Momentum equation:

$$\frac{1}{r}\frac{\partial}{\partial\theta}\left(\rho_{eff}\, uv\right) + \frac{1}{r}\frac{\partial}{\partial r}\left(\rho_{eff}\, rvv\right) + \frac{\partial}{\partial Z}\left(\rho_{eff}\, wv\right) - \frac{1}{r}\left(\rho_{eff}\, u^2\right) = -\frac{1}{r}\frac{\partial P}{\partial r} + \frac{1}{r^2}\frac{\partial}{\partial\theta}\left(\mu_{eff}\,\frac{\partial v}{\partial\theta}\right) + \frac{\partial}{\partial r}\left(\frac{\mu_{eff}}{r}\,\frac{\partial(rv)}{\partial r}\right) - \frac{2\mu_{eff}}{r^2}\,\frac{\partial u}{\partial\theta} - \rho_{eff}\, g\, \beta_{eff}(T_w - T)\cos\theta \qquad (3.9)$$

Z- Momentum equation:

$$\frac{1}{r}\frac{\partial}{\partial\theta}\left(\rho_{eff}\, uw\right) + \frac{1}{r}\frac{\partial}{\partial r}\left(\rho_{eff}\, rvw\right) + \frac{\partial}{\partial Z}\left(\rho_{eff}\, w^2\right) = -\frac{\partial P}{\partial Z} + \frac{1}{r^2}\frac{\partial}{\partial\theta}\left(\mu_{eff}\,\frac{\partial w}{\partial\theta}\right) + \frac{1}{r}\,\frac{\partial}{\partial r}\left(r\,\mu_{eff}\,\frac{\partial w}{\partial r}\right) \qquad (3.10)$$

Energy equation:

$$\frac{1}{r}\frac{\partial}{\partial\theta}\left(\rho_{eff}\, u\, T\right) + \frac{1}{r}\frac{\partial}{\partial r}\left(\rho_{eff}\, r\, v\, T\right) + \frac{\partial}{\partial Z}\left(\rho_{eff}\, w\, T\right) = \frac{1}{r^2}\frac{\partial}{\partial\theta}\left(\frac{k_{eff}}{C_{p_{eff}}}\frac{\partial T}{\partial\theta}\right) + \frac{1}{r}\,\frac{\partial}{\partial r}\left(r\,\frac{k_{eff}}{C_{p_{eff}}}\,\frac{\partial T}{\partial r}\right) \qquad (3.11)$$

In the above equations u, v, and w represents the θ, r, Z components of velocity.

3.4 Finite Volume Method Employed by ANSYS FLUENT

As already mentioned ANSYS FLUENT is used as the CFD tool to simulate flow through a PTSC in this thesis and it employs finite volume method for the solution of Navier-Stokes equation [5]. This section addresses application of finite volume method employed by ANSYS FLUENT in particular, for solution of fluid flow problems. The aim of this section is to provide an overview of the methodology followed by ANSYS FLUENT for discretization of transport equations.

General transport equation (3.3) for a scalar $\emptyset$ can be integrated over a control volume (V) as:

$$\int_V \frac{\partial(\rho\,\emptyset)}{\partial t}\, dV + \int_V \nabla.(\rho\,\emptyset\,\mathbf{v})\, dV = \int_V \nabla.(\Gamma_\emptyset\,\nabla\,\emptyset)\, dV + \int_V S_\emptyset\, dV \qquad (3.12)$$

According to Gauss's divergence theorem, volume integral of divergence of a vector over a control volume is equal to the surface integral of that particular vector over the area enclosing the control volume [8]. In the light of Gauss's theorem second and third terms of the above equation acquire the following form:

$$\int_V \nabla.(\rho\, \emptyset\, \mathbf{v})\, dV = \oint (\rho\, \emptyset\, \mathbf{v})\, d\boldsymbol{A} \tag{3.13}$$

$$\int_V \nabla.(\Gamma_\emptyset\, \nabla\, \emptyset)\, dV = \oint (\Gamma_\emptyset\, \nabla\, \emptyset)\, d\boldsymbol{A} \tag{3.14}$$

Equation (3.1) can be re-written in the following form:

$$\int_V \frac{\partial(\rho\, \emptyset)}{\partial t}\, dV + \oint (\rho\, \emptyset\, \mathbf{v})\, d\boldsymbol{A} = \oint (\Gamma_\emptyset\, \nabla\, \emptyset)\, d\boldsymbol{A} + \int_V S_\emptyset\, dV \tag{3.15}$$

Above equation holds good for every control volume or cell present in the flow domain under finite volume method. Each term in the above equation needs to be discretised to convert the set of PDFs to a system to algebraic equations.

A triangular control volume or cell, in two-dimensional form is presented in Figure 3.1.

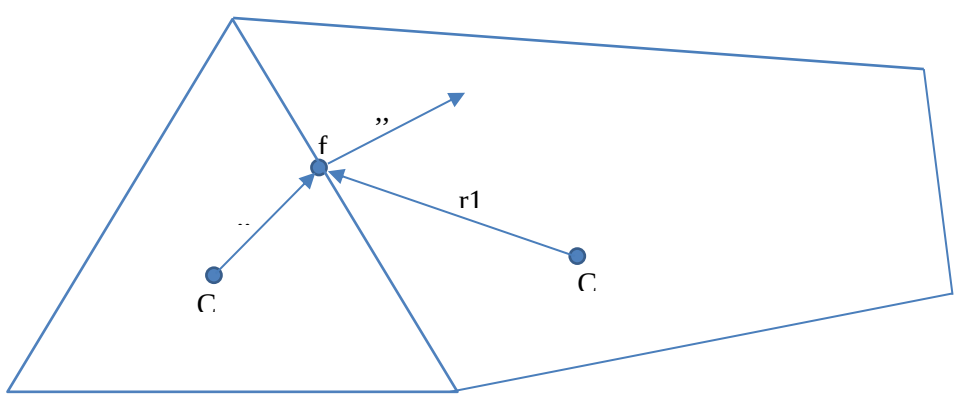

Figure 3.1 Control volume used to illustrate Discretization of a transport equation [5].

Discretization of equation (3.15) on a given cell can yield to the following expression [5]:

$$\frac{\partial(\rho\,\emptyset)}{\partial t}\,V + \sum_{f}^{N\,faces}\left(\rho_f\,\emptyset_f\,\mathbf{v}_{\boldsymbol{f}}\right).A_f = \sum_{f}^{N\,faces}\left(\Gamma_\emptyset\,\boldsymbol{\nabla}\,\emptyset_f\right).A_f + \mathrm{S}_\emptyset\,V \qquad (3.16)$$

In the above equation:

N_{faces}	= Number of faces enclosing the cell
$\emptyset_f$	= value of $\emptyset$ convected through face f
$\left(\rho_f\ \mathbf{v}_{\boldsymbol{f}}\right).A_f$	= Mass flux through the face
A_f	= Area of face f
$\boldsymbol{\nabla}\,\emptyset_f$	= Gradient of $\emptyset$ at face f
V	= Cell volume

The temporal discretization of the first term in the above equation is discussed separately in section 3.4.3. In ANSYS FLUENT, the value of $\emptyset$ and its diffusion coefficients are stored at cell centers. This results in a co-located or non-staggered grid layout because values of all the variables (pressure, velocity components, Reynolds stress components, and all scalars) are stored at the centre of the control volume or cell. Since both velocity and pressure values are stored at the same location (cell centre) which leads to the "checkerboard" pressure field [1], [5]. To prevent checker boarding of pressure ANSYS FLUENT employs a procedure similar to one proposed by Rhie and Chow [9] to find face value of velocity (value of velocity at face between cells C0 and C1 in Figure 3.1) required in equation (3.16).

The equations presented above, in addition to the transport of a scalar $\emptyset$, are also valid for Cartesian components of vectors or elements of a higher order tensor which are scalars.

3.4.1 Solving the Linear System

In the previous section, the discretized scalar equation (3.16) contains unknown scalar variable $\emptyset$ at the cell center, also the values are unknown at the neighboring cells. This equation will be non-linear with respect to these variables. The following equation represents a linearized form of the equation (3.16) [5]:

$$a_p \emptyset = \sum_{nb} a_{nb}\, \emptyset_{nb} + b \qquad (3.17)$$

In the above expression, a_p and a_{nb} represents the linearized coefficients for $\emptyset$ and $\emptyset_{nb}$ respectively and the subscript 'nb' stands for the neighbor cells. The number of neighbor cells for each particular cell depends on the topology of the mesh and apart from the boundary cells, typically equal to number of faces that enclose the particular cell.

For each cell present in the mesh similar equation can be written which results in a set of algebraic equations. ANSYS FLUENT employs a point implicit linear equation solver (Gauss-Seidel) along with an algebraic multigrid (AMG) method to solve the linear system of the scalar equations.

3.4.2 Spatial Discretization

Discrete values of the scalar $\emptyset$, are stored by ANSYS FLUENT, at the cell center of the cells, for instance at C0 and C1 in Figure 3.1. Whereas the face values $\emptyset_f$ required by the convective terms in equation 3.16 are interpolated from the cell center values by employing an upwind scheme.

The term Unwinding means that the face value $\emptyset_f$is obtained from the quantities in the cell upstream or upwind relative to the normal velocity. In ANSYS FLUENT different upstream are present, for example, first-order upwind, second-order, power law, QUICK (Quadratic Upstream Interpolation for Convection Kinetics), etc. The user has the choice to select from those upwind schemes depending on the problem complexity and experience.

In this thesis QUICK and Power Law upwind schemes are used to discretize the momentum and energy equations respectively and are discussed in Chapters 4, 5, and 6 along with the governing equation for the flow through a PTSC absorber tube. The diffusion terms in equation (3.16) are central-differenced and always second-order accurate [5].

3.4.3 Temporal Discretization

In case of transient simulations, the governing equations have to be discretized in both time and space. For time-dependent equations, spatial discretization is the same as that for steady-state cases. But for temporal discretization, every term involved in the differential equation has to be integrated over a time step Δt.

Time evolution of a variable $\emptyset$ is represented by the following generic expression [5]:

$$\frac{\partial \emptyset}{\partial t} = F(\emptyset) \tag{3.18}$$

In the above expression, the function F incorporates any spatial discretization. Considering the time derivative is discretized using backward differences, first-order accurate temporal discretization is presented as:

$$\frac{\emptyset^{n+1} - \emptyset^{n}}{\Delta t} = F(\emptyset) \tag{3.19}$$

And the second-order temporal discretization can be represented as [5]:

$$\frac{3\,\emptyset^{n+1} - 4\,\emptyset^{n} + \emptyset^{n-1}}{2\,\Delta t} = F(\emptyset) \tag{3.20}$$

In the above equations:

n	=	value at the current time level, t
$n+1$	=	value at the next time level, $t + \Delta t$
$n-1$	=	value at the current time level, $t - \Delta t$
$\emptyset$	=	A scalar quantity

For pressure-based solver ANSYS LUENT provides only the choice of using Implicit time integration to evaluate $F(\emptyset)$ at future time level as:

$$\frac{\emptyset^{n+1} - \emptyset^{n}}{\Delta t} = F(\emptyset^{n+1}) \tag{3.21}$$

Where $\emptyset^{n+1}$ in a particular cell is related to $\emptyset^{n+1}$ in the neighbouring cell through $F(\emptyset^{n+1})$ as:

$$\emptyset^{n+1} = \emptyset^{n} + \Delta t\, F(\emptyset^{n+1}) \tag{3.22}$$

The above implicit equation can be iteratively solved at each time step before moving to the next time step. The beauty of the above equation is that it is unconditionally stable with respect to the size of the time step.

3.5 Programming Procedure

In this thesis, mainly the Design Modeler is used as a pre-processor to develop a new 3D models of different shapes of PTSC systems along with a Monte carlo ray tracing (MCRT) algorithm to model the nonuniform solar radiation. ANSYS FLUENT is used as a solver, which allows importing the meshed computational domain developed by the design modeler. After reading the mesh file in FLUENT physical model, nanofluids/hybrid nanofluids and material properties are defined in FLUENT. Boundary conditions that were earlier defined in the design modeler cane be varied (or kept same) to describe the nature of the problem in FLUENT. These user inputs along with the grid information are stored in a case file. A case file is a record of all the information provided to the solver (FLUENT) pertaining to a specific fluid flow problem. All the calculation performed by FLUENT and post processing activities can be saved in a data file.

In this thesis, the information generated by ANSYS FLUENT is compared with the experimental and numerical studies. Since the geometries of the smooth PTSCs absorber tubes are identical to those considered in this thesis, therefore, qualitative comparison of results obtained from this work is made with the experimental and numerical studies involving closely matching PTSC absorber tubes configurations. Among the variables

considered for comparison are outlet temperature, circumferential temperature difference, Nusselt number, friction factor and thermal efficiency.

References

[1] Versteeg, H. K., Malalasekera, W. An Introduction to Computational Fluid Dynamics: The finite volume method. Prentice Hall; 2007.

[2] Li, Z. Y., Huang, Z., Tao, W. Q. Three-dimensional numerical study on fully-developed mixed laminar convection in parabolic trough solar receiver tube. Energy (2016), 113:1288–303.

[3] Huang, Z., Li, Z. Y., Yu, G. L., Tao, W.Q. Numerical investigations on fully-developed mixed turbulent convection in dimpled parabolic trough receiver tubes. Appl Therm Eng (2017), 114:1287–1299.

[4] Ghadirijafarbeigloo, S., Zamzamian, A. H., Yaghoubi M. 3-D numerical simulation of heat transfer and turbulent flow in a receiver tube of solar parabolic trough concentrator with louvered twisted-tape inserts. Energy Procedia (2014), 49:373 – 380.

[5] ANSYS Theory Guide. ANSYS® Academic Research, Release 19.5, ANSYS FLUENT, Theory Guide, ANSYS, Inc. 2019.

[6] Bird, R. B., Stewart, W. E., Lighfoot F. Transport Phenomena. Newyork: John & Sons; 1960.

[7] Sokhansefat, T., Kasaeian, A. B., Kowsary, F. Heat transfer enhancement in parabolic trough collector tube using Al_2O_3/synthetic oil nanofluid. Renew Sustain Energy Rev (2014), 33:636–644.

[8] Chen, W. D., De kee, D., Kaloni, P.N. Advanced Mathematics for Engineering and Science. World Scientific Pub Co. Inc.; 2003.

[9] Rhie, C., Chow, W. Numerical study of turbulent flow past an airfoil with trailing edge separation. AIAA J (1983), 21:1525–32.

Chapter 3

Every reasonable effort has been made to acknowledge the owners of copyright material. I would be pleased to hear from any copyright owner who has been omitted or incorrectly acknowledged.

Chapter 4 Two-Phase Forced Convection of Nanofluids Flow in Circular Tubes using Convergent and Divergent Conical Rings Inserts

Abstract

Numerical investigations are conducted using finite volume method to study the thermal and hydraulic characteristics of turbulent forced convection of nanofluid flow in a circular tube equipped with conical ring inserts. Four nanofluids with different types of nanoparticles, Al_2O_3, CuO, SiO_2, and ZnO with 1- 4% volume fraction and particle diameters from 20 -50 nm in base fluid (water) are tested. Two different approaches for simulating nanofluids viz., a single-phase and two-phase mixture are implemented. The effects of Reynolds number (2000-10000) and conical rings type (convergent and divergent) are studied to test the heat transfer enhancement. The results revealed that the highest performance enhancement criteria based on the same pumping power is provided by the divergent ring inserts with 365%. Amongst the four tested nanofluids, those with SiO_2 particles have achieved the highest heat transfer enhancement in terms of Nusselt number and the friction factor. The Nusselt number was enhanced with the increase of the particle volume fraction and Reynolds number, and with the decrease of nanoparticle diameter. It is found that the comparison of calculated results for different models with the experimental and numerical values shows that the two-phase mixture model is more precise than the single-phase model.

The content of this chapter has been published in International Communications in Heat and Mass Transfer **(Q1, IF=5.683).**

Chapter 4

4.1 Introduction

The technology of enhanced heat transfer has received strong attention over the recent years. Heat transfer augmentation techniques can be applied mainly in the design of more compact heat exchangers found in various industries, especially refrigeration, automotive and chemical processes. Hence, there have been continuous attempts to have smaller, cost-effective and more energy efficient heat exchangers. One of the best methods to achieve this is the use of passive method of heat transfer enhancement, which involves surface geometry modification to represent the appropriate field to generate a local turbulent flow to increase the heat transfer areas. Employing different insert shapes on the inner surface of circular tubes has been one of the passive techniques, which were investigated by many researchers.

Numerous types of tube inserts have been developed to date. Promvonge and Eiamsa-ard [1] carried out an experimental investigation to assess turbulent forced convection heat transfer and friction loss behaviors for air flow through a circular tube fitted with conical nozzles and swirl generator. It was found that as the conical-nozzle pitch ratio decreases and the Reynolds number increases, the value of Nusselt number increases significantly. However, the friction factor was found to be decreased with higher Reynolds number and higher pitch ratio values. Promvonge [2] investigated experimentally the effects of the conical ring turbulator inserts on the heat transfer rate and friction loss behavior of airflow in a round tube. Conical rings with three different diameter ratios of the ring to tube diameter (d/D = 0.5 to 0.7) were tested. The rings were arranged with three different arrangements (converging conical ring, diverging conical ring, and converging-diverging conical ring). The enhancement efficiency of the diverging conical ring was found to be the highest compared to those of the converging and converging-diverging arrays for all similar diameter ratios.

Bhuiya et al. [3] studied experimentally the turbulent heat transfer augmentation and friction factor characteristics in a circular tube fitted with twisted wire brush inserts. The results showed that the heat transfer performance obtained for the tube with twisted

wire brush inserts of different wire densities increased by 1.1 to 1.85 compared to the plain tube values. Akhavan-Behabadi et al. [4] carried out an experimental study on the heat transfer enhancement and pressure drop characteristics in the presence of twisted tape inserts, during flow boiling of R-134a, inside a horizontal evaporator. When the twist ratio was reduced from 15 to 6 the average heat transfer coefficient ratio increased by 24% for the mass velocity of 136 kg/s.m^2, while the pressure drop enhanced for smaller twist ratios. Murugesan et al. [5] analyzed experimentally the effect of V-cut twisted tape insert with twist ratios of 2 to 6 on the thermal-hydraulic characteristics of water flow in a circular tube. It was inferred that the arrangements with higher depth ratio and lower width ratio provide high heat transfer and friction factor. The influence of different types of twisted tapes inserts placed separately at different clearances from the tube wall on heat transfer and friction factor was experimentally investigated by Bas and Ozceyhan [6]. It was found that the typical twist provides more heat transfer enhancement than separately placed types at the same twist ratios. Nevertheless, the heat transfer enhancement is nearly the same for different clearance ratios.

Gunes et al. [7] presented an experimental examination of heat transfer and pressure drop in a tube with coiled wire inserts placed separately from the tube wall in turbulent flow regime. Results showed that heat transfer, the overall enhancement efficiency and friction factor increase with decreasing of pitch ratio and the clearance from the tube wall. Fan et al. [8] investigated numerically the characteristics of heat transfer, flow resistance, and overall thermo-hydraulic performance of steady three-dimensional turbulent airflow in a circular tube fitted with backward arrangement louvered strip inserts. It was found that higher heat transfer enhancement can be obtained for the arrangement with smaller pitch and higher slant angle of louvered strip.

The conventional heat transfer fluids such as water, engine oil and ethylene glycol, do not satisfy the necessity of a great heat transfer with high efficiency because they have low thermal conductivities. So, the investigators turning to the solids with high thermal conductivities and methods to mix these materials with base working fluids such as the ones aforementioned. The composite material in nanoscale mixed with base fluid to

produce medium is termed as "nanofluid" to enhance the heat transfer properties. Nanofluids have the potential to reduce thermal resistances, and the industrial groups that would benefit from such improved heat transfer fluids are quite varied. They include transportation, electronics, medical, food, and manufacturing of many types.

Several studies [9-12] have revealed the great thermal transport characteristics of nanofluids. Suresh et al. [13] performed an experimental study on the convective heat transfer augmentation of Al_2O_3-water nanofluid in circular tube fitted with spiraled rod inserts. According to the results, the use of both Al_2O_3-water nanofluid increased

the Nusselt number by 18%, as compared with distilled water. Mohammed et al. [14] numerically investigated the thermal and hydraulic characteristics of turbulent forced convective nanofluids flow in a circular double pipe heat exchanger placed with louvered strip inserts. It was noticed that the louvered strip with backward arrangement led to better overall performance evaluation criteria than that of forward arrangement for all slant angles and pitches.

Conical ring is another type of tube inserts used for heat transfer augmentation. The effects of the geometrical parameters such as pitch and diameter, as well as the arrangement of conical rings have been numerically and experimentally investigated. Despite of the substantial increase of the flow resistance, the enhancement efficiency of conical rings could exceed unity [15-16]. Fan et al. [17] studied numerically the characteristics of heat transfer rate, flow resistance, and overall thermo-hydraulic performance of turbulent flow in a circular tube fitted with conical strip inserts. The value of performance evaluation criterion (PEC) lies in the range of 1.67-2.06, which demonstrates that the conical strip insert has a very good thermo-hydraulic performance.

Liu et al. [18] carried out numerical simulations on the flow structures and heat transfer enhancement of laminar flow in a heat exchanger tube fitted with multiple conical strips inserts. Stereoscopic particle image velocimetry (SPIV) measurements on the flow structures were also conducted to verify the numerical results. It is found that both the

heat transfer rate and flow resistance increase with the increasing number of conical strips, central angle and the decreasing pitch, and they both increase first and then decrease with the increase of slant angle. Sheikholeslami et al. [19] investigated the effect of typical and perforated conical ring turbulators on hydrothermal behavior of air to water double pipe heat exchanger. Two arrays (Direct Conical Ring (DCR) array and Reverse Conical Ring (RCR) array) were considered. The results indicated that the Nusselt number reduces with the increase of open area ratio and pitch ratio while it augments with the increase of Reynolds number.

Anvari et al. [20, 21] performed an experimental investigation on forced transient convective heat transfer performance of water flow in a horizontal tube equipped with conical ring inserts. It was observed that the Nusselt number increases with increasing the Reynolds number. Furthermore, the diverging arrangement increased the Nusselt number more than the converging arrangement, which was associated with higher pressure drop penalty. Promvonge and Eiamsa-ard [22] investigated experimentally the heat transfer, friction factor and enhancement efficiency characteristics in a circular tube fitted with conical-ring turbulators and a twisted-tape swirl generator placed at the core of the conical-ring. Eiamsa-ard and Promvonge [23] investigated turbulent channel flow over periodic grooves. Air as the tested fluid was passed through both enhancement devices in a Reynolds number range of 6000 to 26,000. The results revealed that the tube fitted with the conical-ring and twisted-tape provides Nusselt number values of around 4 to 10% and enhancement efficiency of 4 to 8% higher than that with the conical-ring alone. Sripattanapipat et al. [24] investigated numerically the use of V-shaped hexagonal conical rings (VHCR) in a heat exchanger tube. The numerical results revealed that the VHCR insert leads to much higher heat transfer than the typical CR/HCR insert or the smooth tube alone and also provides lower friction factor.

Fan et al. [25] and You et al. [26] investigated numerically the thermo-hydraulic performance of turbulent and laminar flows in conical strip inserts. The numerical results indicated that larger strip size, smaller strip-wall gap and smaller strip pitch can effectively enhance the heat transfer rate, but also increase the flow resistance. Moreover, it was

shown that the Nusselt number and friction factor are sensitive to the geometry angle, while the most sensitive factor of PEC value is the strip pitch.

By a review of relevant research articles having investigated so far, and to the best of authors' knowledge, there is no numerical study published on turbulent convective nanofluid flow in circular tubes having conical rings inserts using two-phase mixture model; so the scarcity of study in this subject is felt strongly and this has motivated the present study. The aim of this article is to explore nanoparticle distribution by employing single phase and two-phase mixture models, which examines turbulent flow with the effects of different nanofluid (Al_2O_3, ZnO, CuO and SiO_2), different volume fraction (0-4%) and different particle diameters (20-50 nm). The effects of insert shape and nanofluid model on various parameters of interest such as Nusselt number, friction factor coefficient and performance evaluation criterion (PEC) for turbulent forced convective in inserted tubes are investigated in the present work.

4.2 Numerical Model

4.2.1 Physical Model

The schematic diagram of the tube equipped with conical rings is shown in Figure 4.1. As shown, the geometry consists of two different conical ring inserts namely, Convergent Ring (CR) insert and Divergent Ring (DR) insert. The inserted tube is seen to have four conical ring inserts and internal diameter of D=138 mm. The length of test section is L_{ts}=1100 mm, with the entrance length of L_{ent}= 3312 mm to ensure a fully developed flow in the test section. The exit section has a length of L_{exit} = 1246 mm which is used in case of occurring adverse pressure effects only to prevent the reverse flow through the computational domain. The left side of the tube is subjected to uniform inlet velocity based on the Reynolds number ranging from 2500-9500 and the exit side of the tube is subjected to pressure outlet. The test section is subjected to a uniform heat flux of 1500 W/m^2. It is assumed that the incoming fluid flow through the total length of tube is steady and turbulent to many words mixed here and make this bit clearer at temperature of T_{in}=300 K.

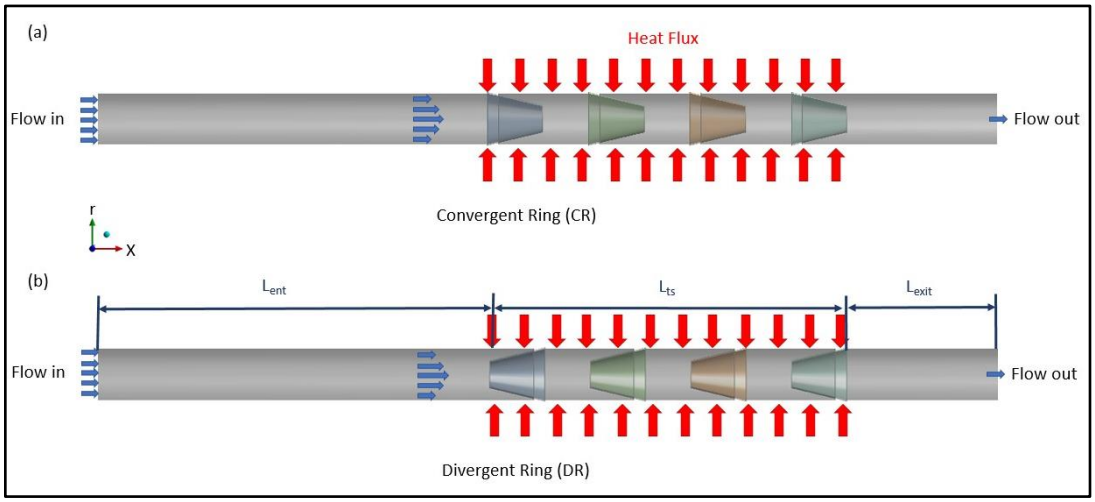

Figure 4.1 Schematic diagram of the physical model: (a) CR inserts and (b) DR inserts.

4.2.2 Governing Equations

4.2.2.1 Single-Phase Model

Several assumptions were made on the operating conditions of the inserted tube such as: (i) the inserted tube operates under steady-state conditions; (ii) the fluid is incompressible and remains in single phase along the tube; (iii) the properties of the fluid and tube material are temperature dependent; (iv) constant heat flux is applied at the test section wall.

The governing equations for flow and heat transfer in the inserted tube can be written as [27]:

Continuity Equation:

$$\frac{\partial}{\partial x_i}(\rho u_i) = 0 \tag{4.1}$$

Momentum equation:

$$\frac{\partial}{\partial x_i}(\rho u_i u_j) = -\frac{\partial P}{\partial x_i} + \frac{\partial}{\partial x_j}\left[\mu\left(\frac{\partial u_i}{\partial x_j} + \frac{\partial u_j}{\partial x_i}\right)\right] + \frac{\partial}{\partial x_j}(-\rho\overline{\acute{u}_i\acute{u}_j}) \tag{4.2}$$

Energy equation:

$$\frac{\partial}{\partial x_i}(\rho u_i T) = \frac{\partial}{\partial x_j}[(\Gamma + \Gamma_t)\frac{\partial T}{\partial x_j}] \tag{4.3}$$

Where Γ and Γ_t are molecular thermal diffusivity and turbulent thermal diffusivity, respectively and are given by:

$$\Gamma = \frac{\mu}{\mathrm{Pr}}, \quad \text{and} \quad \Gamma_t = \frac{\mu_t}{Pr_t}, \tag{4.4}$$

The k-ε turbulence model was chosen for modeling Reynolds stresses $(-\rho\overline{u'_\iota u'_\jmath})$ in Eq. (4.2), which is explained in the next section. The Boussinesq hypothesis is used to relate Reynolds stresses to the mean velocity gradient:

$$\left(-\rho\overline{u'_\iota u'_\jmath}\right) = \mu_t\left(\frac{\partial u_i}{\partial x_j} + \frac{\partial u_j}{\partial x_i}\right) \tag{4.5}$$

In this model, the turbulence viscosity is given as:

$$\mu_t = \rho C_\mu \frac{k^2}{\varepsilon} \tag{4.6}$$

The modeled equation of the turbulent kinetic energy (TKE), k is written as:

$$\frac{\partial}{\partial x_i}(\rho k u_i) = \frac{\partial}{\partial x_j}\left[\left(\mu + \frac{\mu_t}{\sigma_k}\right)\frac{\partial k}{\partial x_j}\right] + G_k - \rho\varepsilon \tag{4.7}$$

Similarly the dissipation rate of TKE, ε, is given by:

$$\frac{\partial}{\partial x_i}(\rho\varepsilon u_i) = \frac{\partial}{\partial x_j}\left[\left(\mu + \frac{\mu_t}{\sigma_\varepsilon}\right)\frac{\partial \varepsilon}{\partial x_j}\right] + C_{1\varepsilon}\frac{\varepsilon}{k}G_k - C_{2\varepsilon}\rho\frac{\varepsilon^2}{k} \tag{4.8}$$

Where G_k is the rate of generation of the TKE while $\rho\varepsilon$ is its destruction rate.

G_k is given by:

$$G_k = -\rho\overline{u'_\iota u'_\jmath}\frac{\partial u_j}{\partial x_i} \tag{4.9}$$

$C_\mu = 0.09$, $C_{1\varepsilon} = 1.44$, $C_{2\varepsilon} = 1.92$, $\sigma_k = 1.0$, $\sigma_\varepsilon = 1.3$ and $Pr_t = 0.9$ are chosen to be empirical constants [27] in the turbulence transport equations.

4.2.2.2 Two-Phase Model

The mixture model, based on a single fluid two-phase approach, is employed in the simulation by assuming that the coupling between phases is strong, and particles closely follow the flow. The two-phases are assumed to be interpenetrating, meaning that each phase has its own velocity vector field, and within any control volume there is a volume fraction of primary phase and also a volume fraction of the secondary phase. Instead of utilizing the governing equations of each phase separately, the continuity, momentum and energy equations for the mixture are employed. The mixture model is used to investigate the hydraulic and thermal behaviors of the nanofluid inside a circular tube having conical ring inserts with uniform heating at the wall boundary. The nanofluid flow is considered

incompressible and steady state and the viscous dissipation is neglected. Therefore, the dimensional steady state mean condition equations for continuity, momentum, energy and volume fraction of nanoparticles for two-phase mixture model are expressed as follows [28]:

Continuity equation:

$$\nabla.(\rho_m V_m) = 0$$

(4.10)

Momentum equation:

$$\nabla.(\rho_m V_m V_m) = -\nabla p_m + \nabla.[\tau - \tau_t] + \nabla.\left(\sum_{k=1}^{n} \Phi_k \rho_k V_{dr,k} V_{dr,k}\right) \quad (4.11)$$

Energy equation:

$$\nabla.\left(\sum_{k=1}^{n} \Phi_k \rho_k V_k C_{p,k} T\right) = \nabla.(\lambda_m \nabla T) \quad (4.12)$$

Volume fraction of nanoparticles:

$$\nabla.\left(\Phi_p \rho_p V_m\right) = -\nabla.\left(\Phi_p \rho_p V_{dr,p}\right) \quad (4.13)$$

Where V denotes velocity, Φ_k and $V_{dr,k}$ represent the volume fraction and drift velocity for the secondary phase k, i.e. the nanoparticles in the present study. The subscripts p, f, m represent nanoparticles, base fluid, and mixture, respectively. The mixture density, viscosity, thermal conductivity, mass average velocity along the drift velocity of nanoparticles are defined as follows:

$$\rho_m = \sum_{k=1}^{n} \Phi_k \rho_k \quad (4.14)$$

$$\mu_m = \sum_{k=1}^{n} \Phi_k \mu_k \quad (4.15)$$

$$\lambda_m = \sum_{k=1}^{n} \Phi_k \lambda_k \quad (4.16)$$

$$V_m = \frac{\sum_{k=1}^{n} \Phi_k \rho_k V_k}{\rho_m} \quad (4.17)$$

$$V_{dr,k} = V_k - V_m \quad (4.18)$$

The τ and τ_t are defined as follows:

$$\tau = \mu_m \nabla V_m \quad (4.19)$$

$$\tau_t = -\sum_{k=1}^{n} \Phi_k \rho_k \overline{\upsilon_k \upsilon_k} \quad (4.20)$$

The slip velocity (relative velocity) is defined as the velocity of a secondary phase (p) relative to the velocity of the primary phase (f) which is proposed by Manninen et al. [29] is presented in the following equation:

$$V_{pf} = V_p - V_f = \frac{\rho_p d_p^2}{18\,\mu_f\, f_{drag}} \frac{(\rho_p - \rho_m)}{\rho_p} \left(g - (V_m \,.\, \nabla) V_m\right) \tag{4.21}$$

The drift velocity is related to the relative velocity

$$V_{dr,p} = V_{pf} - \sum_{k=1}^{n} \frac{\Phi_k\, \rho_k V_k}{\rho_m} \tag{4.22}$$

The relative velocity is determined as proposed by Manninen et al. [29] while the drag function f_{drag} is proposed by Schiller and Naumann [30] as:

$$f_{drag} = \begin{cases} 1 + 0.15\, Re_p^{0.687} & for\ \ Re_p \le 1000 \\ 0.0183\, Re_p & for\ \ Re_p > 1000 \end{cases} \tag{4.23}$$

Where $Re_p = \frac{V_m\, d_p}{\nu_m}$ and the acceleration (a) can be calculated from:

$$a = g - \left(V_m . \nabla\right) V_m \tag{4.24}$$

The key controlling parameters are the average Nusselt number, the Reynolds number, the friction factor and the performance evaluation criteria index are dimensionless parameters which are calculated, respectively, as follows [31]:

$$Nu_{av} = \frac{h\, D_h}{\mathrm{k}} \tag{4.25}$$

Where k and h are the thermal conductivity and average heat transfer coefficient, respectively.

The Reynolds number is defined as:

$$Re = \frac{\rho u_m D_h}{\mu} \tag{4.26}$$

Where u_m is the mean velocity of fluid over the cross section. The hydraulic diameter of tube (D_h) defines as:

$$D_h = \frac{4A}{P_h} \tag{4.27}$$

Where A is the cross-sectional area and P_h is the wetted perimeter of the cross-sectional area.

The friction factor for fully developed flow is expressed as follows:

$$f = \frac{2}{(L/D_h)} \frac{\Delta P}{\rho\, u_m{}^2} \tag{4.28}$$

Where ΔP is the pressure difference between inlet and outlet:

$$\Delta P = P_{av,inlet} - P_{av,outlet} \tag{4.29}$$

Where $P_{av,inlet}$ and $P_{av,outlet}$ are the inlet and outlet average pressure, respectively.

The performance evaluation criterion (PEC) is used to evaluate the heat transfer enhancement of the inserted tube and it is calculated using the predicted average Nusselt numbers and friction factor as follows:

$$PEC = \left(\frac{Nu}{Nu_0}\right) / (\frac{f}{f_0})^{1/3} \tag{4.30}$$

Where Nu and Nu_0 are the average Nusselt numbers for the inserted and smooth tube, respectively.

4.3 Details of Modeling Work

4.3.1 Grid Independence Test

A grid independence test was performed for the tubes with CR and DR inserts using water as a working fluid to analyze the effects of grid sizes on the results. A non-uniform structured grid is applied for the inserted tube with more cells near the rings and near the walls. To provide solution in viscous sub-layer, the grid adoption for y+ = 1 at adjacent wall region has been taken into account in the mesh generation as shown in Figure 4.2 for both conical rings shapes (CR inserts and DR inserts). The grid independence test is firstly done for the tube with CR inserts depending on the convergence of average Nusselt number as shown in Figure 4.3a. Five number of cells are considered, which are 813247 cells, 1024742 cells, 1234652 cells, 1487437 and 1683279 cells. The grid size of 1487437 cells is selected as the best size for the tube with CR inserts. Similarly, Figure 4.3b shows the grid independence test was then done for the same tube when equipped with DR inserts. By comparing the grid size of 655626 cells, 723960 cells, 925632 cells, 1108063 cells and 1378523 cells, the grid size of 1108063 cells is adopted as the best size for the tube with DR inserts, in terms of both the computational time and accuracy.

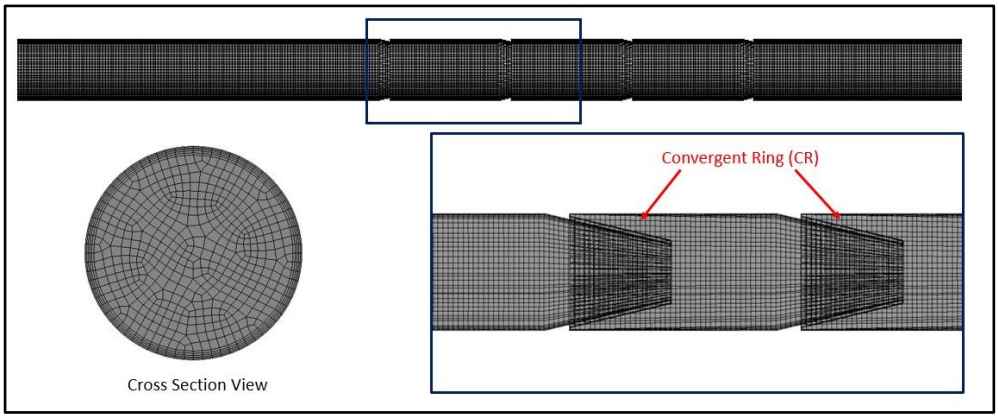

(a)

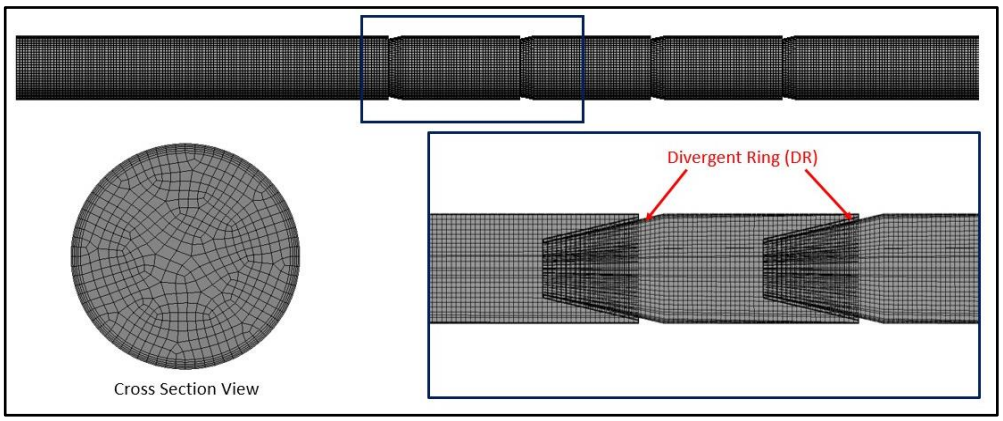

(b)

Figure 4.2 The mesh topology of full geometry, lateral view, and cross-sectional view for PTC tube equipped with conical rings, (a) CR inserts, and (b) DR inserts.

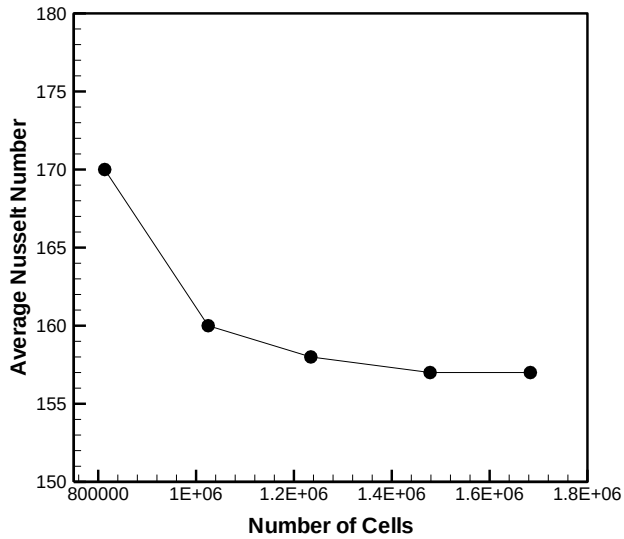

(a)

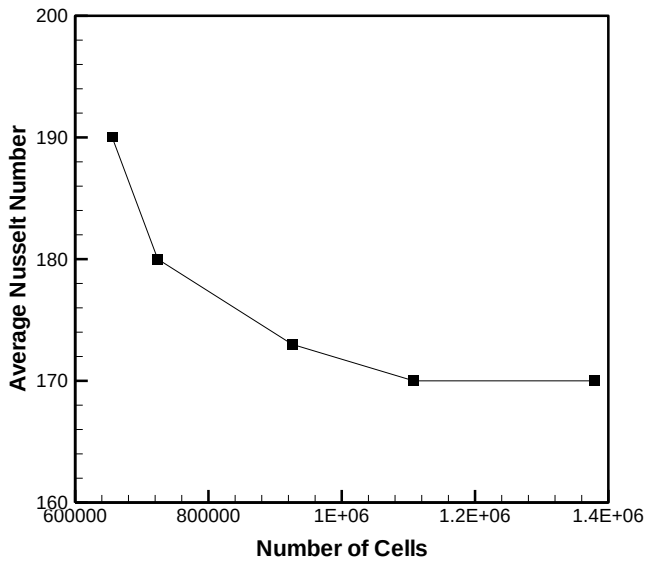

(b)

Figure 4.3 Grid independence test for tubes with (a) CR inserts and (b) DR inserts.

4.3.2 Model Validation

The model validation was done based on the geometry and boundary conditions which were used by Anvari et al. [20, 21]. They performed experimental investigation for the heat transfer enhancement of forced convection of turbulent flow through the tube with

two different inserts (CR inserts and DR inserts). The comparison of the present results in terms of average Nusselt number with the results of Anvari et al. [20, 21] shows a similar trend with maximum deviation of less than 2.48 % as shown in Figure 4.4. This discrepancy could be due to the experimental conditions used in their experiments which might differ from the numerical assumptions. For the sake of further validating the present model, the average Nusselt number and friction factor obtained from the present smooth tube for turbulent flow are also compared with the correlations of Dittus-Boelter and Gnielinski- Petukhov respectively [32], as shown in Figure 4.5.

Correlation of Dittus–Boelter is:

$$Nu = 0.024 Re^{0.8} Pr^{0.4} \tag{4.31}$$

Correlation of Blasius is:

$f = 0.316\ Re^{-0.25}$ for $3000 \leq Re \leq 20000$

Correlation of Gnielinski and Petukhov is:

$$Nu = \frac{f/8(Re-1000)Pr}{1+12.7(f/8)^{1/2}(Pr^{2/3}-1)} \tag{4.32}$$

With $f = (0.79 \log_{10} Re - 1.64)^{-2}$ for $3000 \leq Re \leq 5 \times 10^6$

Figure 4.4 shows that the present results fall between the accepted ranges within maximum deviation of 2.31% and 1.48% for the average Nusselt number and friction factor respectively for smooth tubes.

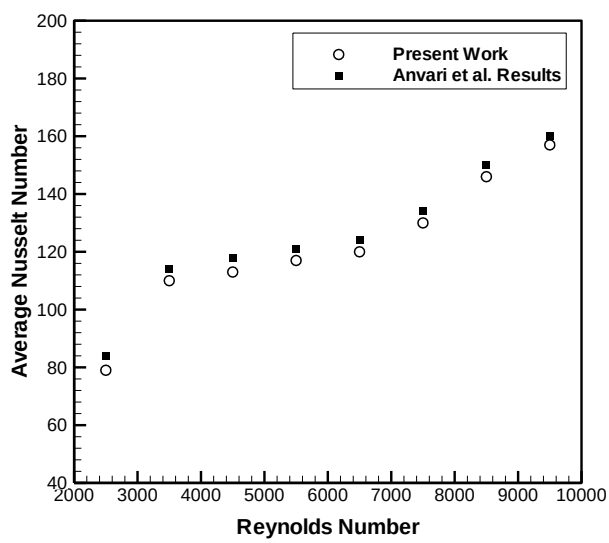

(a)

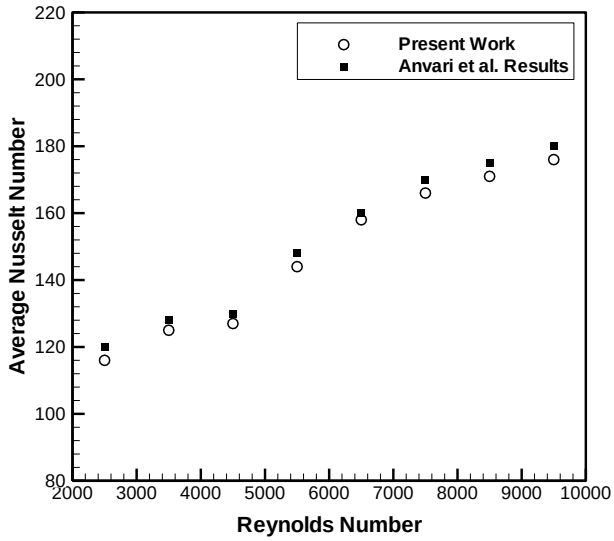

(b)

Figure 4.4 Comparison of the present results with the results of Anvari et al. [21, 22], (a) tubes with CR inserts, (b) tubes with DR inserts.

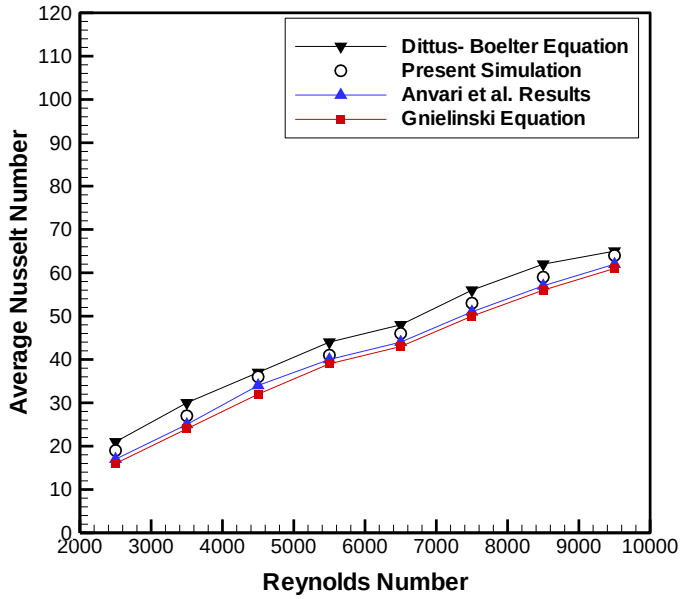

(a)

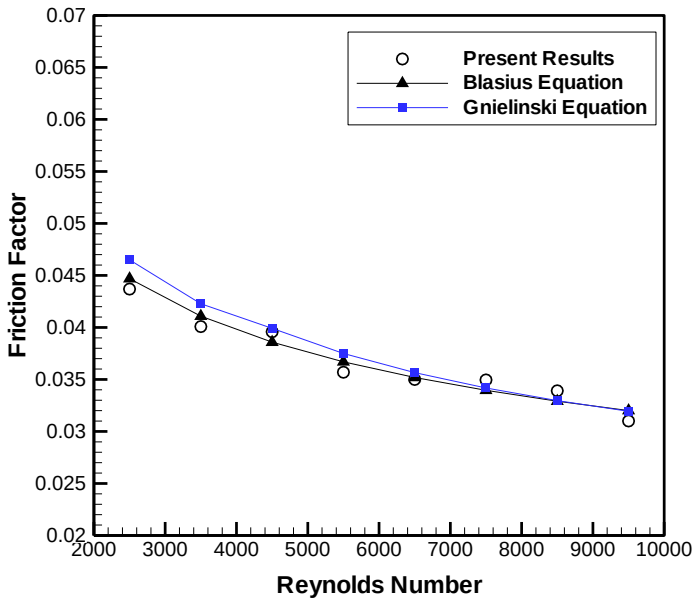

(b)

Figure 4.5 Verification of the present results of (a) average Nusselt number, (b) friction factor for smooth tube with the Anvari et al. results [21, 22] and other available correlations.

4.4 Modelling Approach

A numerical steady-state simulation of the flow field through two-dimensional inserted tube is considered to examine and solve the complex fluid flow and heat transfer model. The control volume approach was used to solve the system of classical single-phase governing equations and convert them to algebraic equations that can be solved linearly. The standard k–ε turbulence model was selected. The numerical computations were performed by solving the governing conservations along with the boundary conditions using the finite volume method (FVM). The diffusion term in the momentum and energy equations was approximated by first-order central difference which gives a stable solution.

In addition, a first-order upwind differencing scheme was adopted to discretize the convection terms. The numerical model was developed in the physical domain, and dimensionless parameters were calculated from the computed velocity and temperature

distributions. Pressure-velocity was coupled employing SIMPLE algorithm [33]. It is essentially a guess and correct procedure for calculation of the pressure field. In general, for this algorithm, the discretization of momentum equation for entire domain under assumption of a known pressure distribution is used to determine the velocity components. The pressure is updated using the continuity equation. Although the continuity equation does not contain any pressure, it can be transformed easily into a pressure correction equation [34]. The convergence criterion was considered 10^{-5} for all variables. A non-uniform structured grid was applied for the inserted tube and the grids were fine enough near the walls ($y^+ \leq 1$) with enhanced wall treatment to provide solution in viscous sub-layer over the range of considered Reynolds numbers.

4.5 Thermophysical Properties of Water and Nanofluids

The effects of the temperature on the thermo-physical properties are considered in the study. Both theoretical and experimental equations for effect of the temperature on the thermo-physical properties are available in the literature [35, 36]. Although empirical correlations may have bitter accuracy their validity are limited for a small range of concentration. Moreover, it was shown that the deviation between experimental and theoretical correlation is minimal [36]. Therefore, in the present results, the thermophysical properties (ρ, C_p, k and μ) of water and nanofluid are calculated as a function of the absolute temperature and volume fraction based on the theoretical equations [35] which gives these physical properties as a fourth order polynomial of temperature as follows:

$$\rho, C_p, k \text{ or } \mu = AT^4 + BT^3 + CT^2 + DT \quad + E \tag{4.33}$$

Where the coefficients A, B, C, D and E are different for each property and depend on the volume fraction as given by [35] and the temperature used was in the range of 300 K to 320 K.

The thermophysical properties of nanofluid with spherical nanoparticle are calculated using the following equations:

The effective density ρ_{nf} and specific heat $(C_P)_{nf}$ of the nanofluid at the reference temperature (T_{in}) are determined by the following equations [37]:

Density of nanofluid is estimated using the following equation:

$$\rho_{nf} = (1-\phi)\rho_{bf} + \phi\rho_{np} \tag{4.34}$$

Heat capacity is estimated using the following equation:

$$\left(C_p\right)_{nf} = \left[(1-\phi)\left(\rho C_p\right)_{bf} + \phi\left(\rho C_p\right)_{np}\right]/\rho_{nf} \tag{4.35}$$

Effective thermal conductivity is estimated using the following equation:

$$k_{eff} = k_{static} + k_{Brownian} \tag{4.36}$$

$$k_{static} = k_{bf}\left[\frac{(k_{np}+2k_{bf})-2\phi(k_{bf}-k_{np})}{(k_{np}+2k_{bf})+\phi(k_{bf}-k_{np})}\right] \tag{4.37}$$

$$k_{brownian} = 5\times 10^4\beta\phi\rho_{bf}C_{P,bf}\sqrt{\frac{KT}{\rho_{np}d_{np}}}f(T,\phi) \tag{4.38}$$

Where K is the Boltzmann constant ($K = 1.3807\times 10^{-23}\,J/K$) and β represents the fraction of liquid volume which travels with particle and T is the temperature (*K*).

Values of β for different particles are listed in Table 4.1 [38].

Table 4.1 The values of (β) for different nanoparticles types [37-38].

Type of particles	**β**	**Concentration (%)**	**Temperature (K)**
Al_2O_3	$8.4407\,(100\,\phi)^{-1.07304}$	$1\% \le \phi \le 10\%$	$298\,K \le T \le 363\,K$
CuO	$9.881\,(100\,\phi)^{-0.9446}$	$1\% \le \phi \le 6\%$	$298\,K \le T \le 363\,K$
SiO_2	$1.9526\,(100\,\phi)^{-1.4594}$	$1\% \le \phi \le 10\%$	$298\,K \le T \le 363\,K$
ZnO	$8.4407\,(100\,\phi)^{-1.07304}$	$1\% \le \phi \le 7\%$	$298\,K \le T \le 363\,K$

$f(T,\phi)$ function can be obtained using:

$$f(T,\phi) = (2.8217\times 10^{-2}\phi + 3.917\times 10^{-3})\left(\frac{T}{T_0}\right) + (-3.0669\times 10^{-2}\,\phi - 3.3.91123\times 10^{-3}) \tag{4.39}$$

For 1% ≤ ϕ ≤ 4% and 300 K <T <325 K, $T_0 = 293$ K

Effective dynamic viscosity is calculated by the following expression:

$$\mu_{eff} = \mu_{bf} \times \frac{1}{(1-34.87\,(d_{np}/d_f)^{-0.3} \times \phi^{1.03})} \tag{4.40}$$

Base fluid equivalent diameter is estimated using following expression:

$$d_f = \left[\frac{6M}{N\pi\rho_{bf}}\right]^{1/3} \tag{4.41}$$

Some of the thermophysical properties of water and different types of nanoparticles is given in Table 4.2.

Table 4.2 The thermophysical properties of water and different types of nanoparticles at T=300 K [37-38].

Thermophysical properties	**Water**	**Al_2O_3**	**CuO**	**SiO_2**	**ZnO**
ρ (*kg/m*^{3})	998.2	3970	6500	2200	5600
Cp (*J/kg.K*)	4182	765	535.6	703	495.2
k (*W/m.K*)	0.6	40	20	1.2	13
μ (*Ns/m*^{2})	0.001003	-	-	-	-

4.6 Results and Discussion

The effects of inserts shape (convergent and divergent rings), different nanofluids types with its parameters such as volume fraction and diameter of nanoparticles and Reynolds number as well as nanofluid model (single-phase and two-phase mixture model) on the thermal and flow fields are analyzed and discussed in this section.

4.6.1 Effect of Different Conical Inserts

In this section, the effect of different conical inserts fitted in two arrangements is considered to examine their influence on the thermal and flow fields. The computed

average Nusselt numbers distribution with Reynolds numbers for conical rings and smooth tube are presented in Figure 4.6a. It can be seen that as Reynolds number increases, the average Nusselt number also increases almost linearly. The large

Reynolds number is attributed to the higher velocity which can lead to disturb the flow and thus, the heat transfer is strengthened. The modified tubes flows gave higher values of Nusselt number than that for the smooth tube flow due to the induction of high recirculation flow and periodic interruption of boundary layer created by the rings, leading to higher temperature gradients. It is found that the tube with DR insert configuration represents the highest average Nusselt number for all ranges of Reynolds number. On the other hand, as expected, applying conical rings in tubes causes a significant increase in friction factor leading to higher pressure drop as well, in comparison with the smooth tube.

Figure 4.6b shows the variation of friction factor along the tube over the investigated Reynolds number which indicates that the tube with DR inserts yields to greater value of friction factor as compared with CR inserts. It is obvious that the friction factor decreases gradually for all of the configurations with the increase of Reynolds number. The PEC is used to evaluate the heat transfer enhancement at the same pumping power for water flowing through horizontal modified tube with different shapes and geometrical parameters. Figure 4.6c depicts the PECs calculated for the tube with CR and DR inserts. The results indicate that the PECs for the tubes decrease with increasing Reynolds number, which means that there is an optimum Reynolds number is corresponding to the maximum PEC for each type of geometry. The optimum Reynolds number is related to Re=2500 for all tested geometries. The PEC of tube with DR and CR inserts are found to be about 3.65 and 2.8 respectively, at the lowest value of Reynolds number.

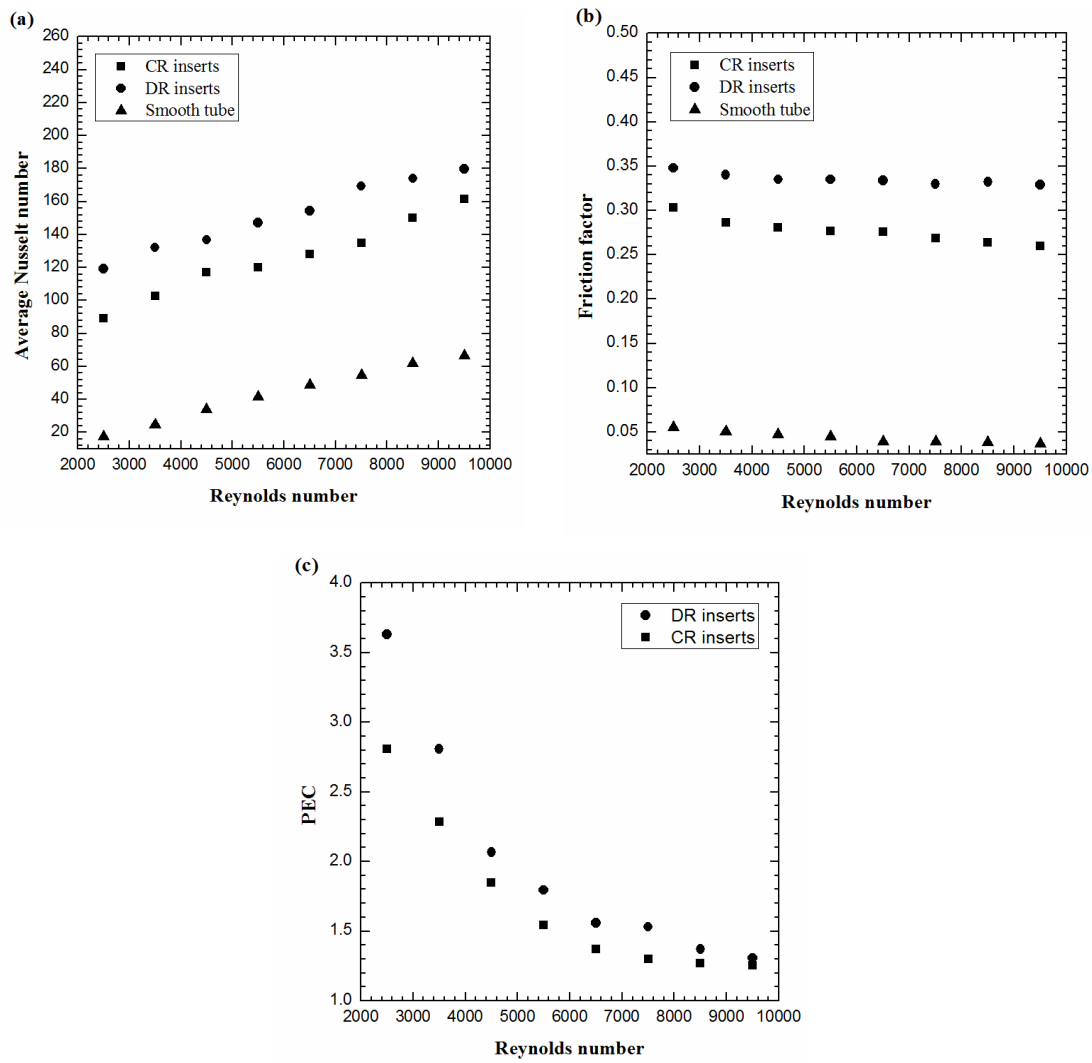

Figure 4.6 The effect of conical ring inserts at different Reynolds numbers on (a) Nusselt number, (b) friction factor, and (c) PEC.

4.6.2 Effect of Different Nanoparticles

Nanofluids are produced from a suspension of nanoparticles with specified volume fraction in a certain base fluid such as water. Use of high thermal conductivity metallic nanoparticles increases the thermal conductivity of such mixtures, thus enhancing their overall energy transport capability. Therefore, research is underway to apply nanofluids in environments where higher heat flux is encountered and the conventional fluid is not

capable of achieving the desired heat transfer rate. In this section, the effects of using four different nanoparticles (Al_2O_3, ZnO, CuO and SiO_2) with 20 nm nanoparticle diameter and volume fraction of 4% on heat transfer and fluid flow characteristics in a tube with CR inserts are discussed. The average Nusselt number profile for different nanofluid types, compared with the results obtained in the case with water in the plain tube are plotted in Figure 4.7a. The results indicate that all the types of nanofluids provide higher average Nusselt number values than the pure water. It is clear that the nanofluid with SiO_2 nanoparticles has the highest average Nusselt number, followed by the Al_2O_3, ZnO and CuO respectively. One of the reasons is related to highest thermal conductivity of the SiO_2 nanofluid, compared to the other nanofluids. On the other hand, the fluid velocity plays an important role on the heat transfer in case of forced convection. Due to the lowest density of colloidal mixture of water-SiO_2, it has the highest average velocity in comparison with other nanofluids and this is resulted in the highest heat transfer coefficient. It can be noticed that at lower Reynolds number the Nusselt number reduces considerably because of higher bulk mean temperature and lower viscosity.

The variation of the friction factor for different nanofluids with Reynolds number is presented in Figure 4.7b. It is observed that the friction factor decreases with the increase of Reynolds number for different nanofluid types. The small variations of friction factor for all types of nanofluids mean that the one with highest Nusselt number must represent the best performance in thermal and hydraulic behavior.

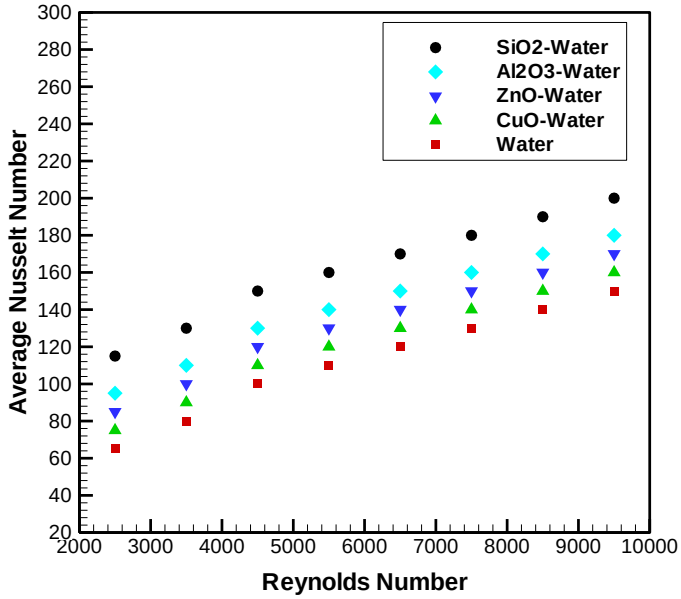

(a)

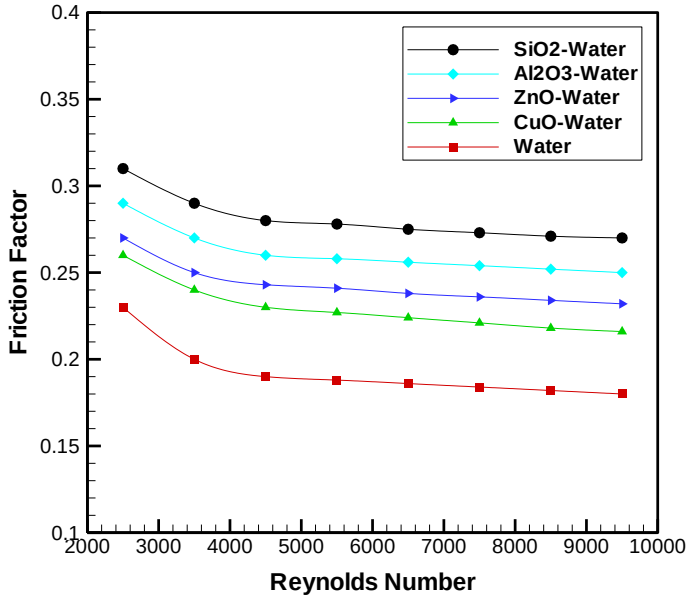

(b)

Figure 4.7 The effect of different nanoparticles at different Reynolds numbers on (a) average Nusselt number and (b) friction factor.

4.6.3 Effects of Nanoparticle Volume Fraction and Size

The comparison study among the four types of nanofluids in the previous section showed that the nanofluid with SiO_2 nanoparticles has the highest Nusselt number. Thus, it is used through the geometry for further numerical analysis. The effect of SiO_2-water nanofluid with 20 nm nanoparticle diameter and volume fractions of 0, 1, 2, 3 and 4% on the heat transfer enhancement in the terms of average Nusselt number is plotted in Figure 4.8a. The results indicate that the average Nusselt number of SiO_2-water nanofluid increases with increasing particle volume concentration. According to Eq. (4.36), nanofluids with higher particle concentration have higher static and dynamic thermal conductivities, which in turn increase the average Nusselt number. It is also clear that when the particle volume fraction increases, the Nusselt number also increases sharply for a certain Reynolds number and nanoparticle diameter. This is due to the incremental change of Prandtl number and thermal conductivity of nanoparticles and to the large energy exchange process resulting from the chaotic movement of nanoparticles. That also means that the momentum diffusivity is dominant with increasing volume fraction of nanoparticle in the nanofluid.

Figure 4.8b depicts the influence of different particles size (20 nm, 30 nm and 50 nm) on average Nusselt number for volume fraction of 4%. As seen for SiO_2-water nanofluid, decreasing particles diameter leads to higher Nusselt number. This is due to aggregation of nanoparticles, increasing relative surface area and stronger Brownian motion at smaller nanoparticles diameters, which leads to higher thermal conductivity of nanofluids. The Brownian motion plays a key role in thermal conductivity enhancement and with decreasing the particles size, the effect of Brownian motion increases due to improvement of micro-convection around nanoparticles. Furthermore, the thermal energy transfer is dependent on surface area. Hence, with decreasing particles size, the specific area of nanoparticles increases which results in enhancement in thermal conductivity.

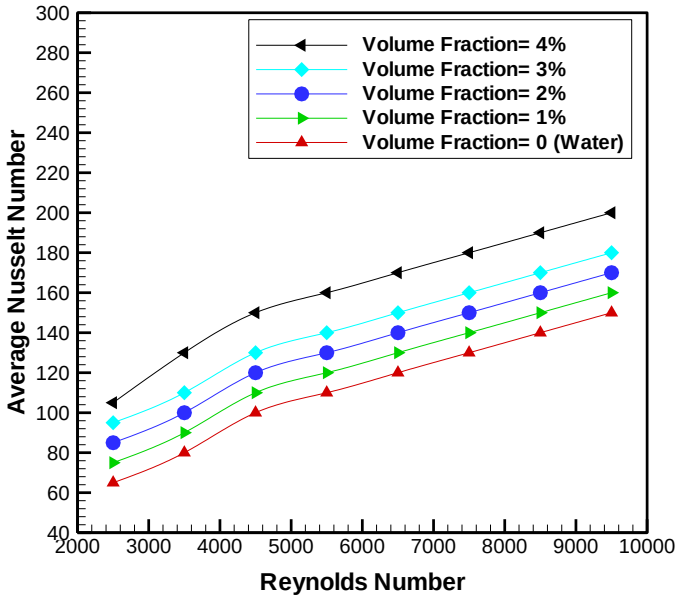

(a)

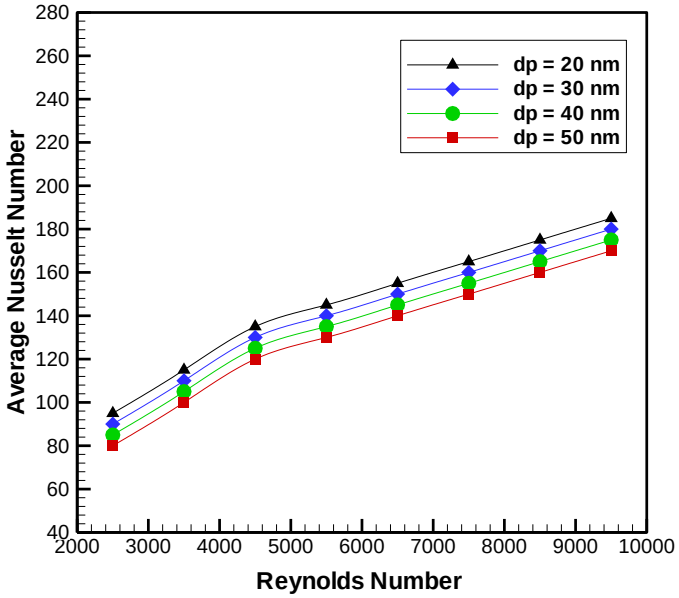

(b)

Figure 4.8 Variation of the average Nusselt number versus Reynolds number for (a) Different values of SiO_2-nanoparticles volume fractions at d_p=20 nm, (b) Different SiO_2 nanoparticle diameters at $\phi = 4\%$.

The isotherms are plotted in Figure 4.9 at different Reynolds numbers for SiO_2-water nanoparticles with particles diameter of 20 nm and volume fraction of 4% flowing in a tube fitted with CR rings. This figure shows the temperature map in the tube for Reynolds number of 2500, 5500 and 9500, respectively. In regions behind the nozzles walls, vortices are generated which appears to interrupt the boundary layers and consequently increase the Nusselt number in those regions. Figure 4.10 illustrates the velocity magnitude, temperature and pressure contours for a tube fitted with DR rings at Reynolds number of 9500. The streamlines show clearly the macro-vortex behind the rings increases its dimension with the increase of Reynolds number, so there is an enhancement of the turbulent mixing and heat exchange.

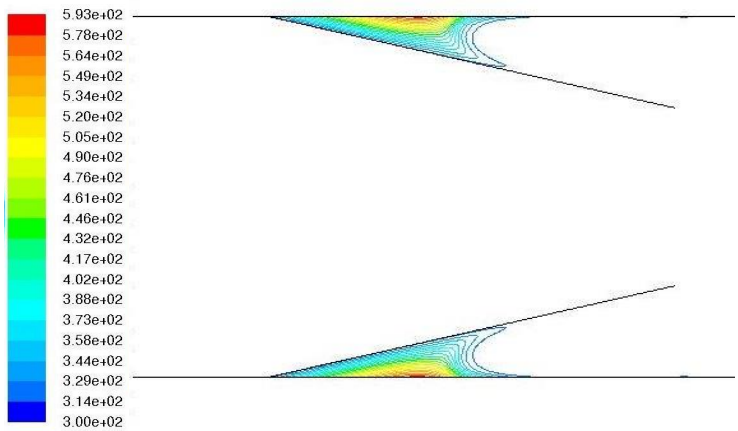

Re = 2500

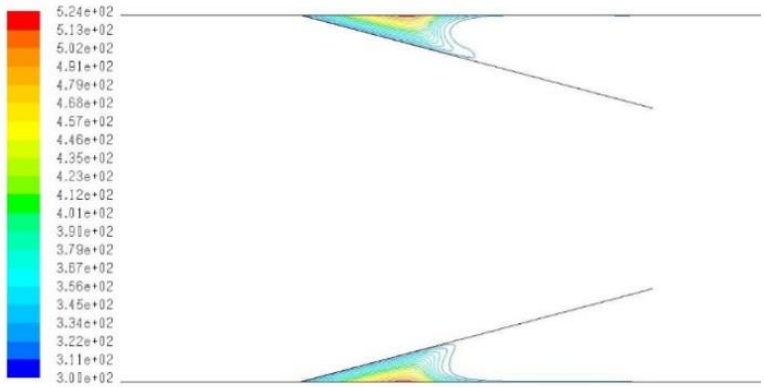

Re = 5000

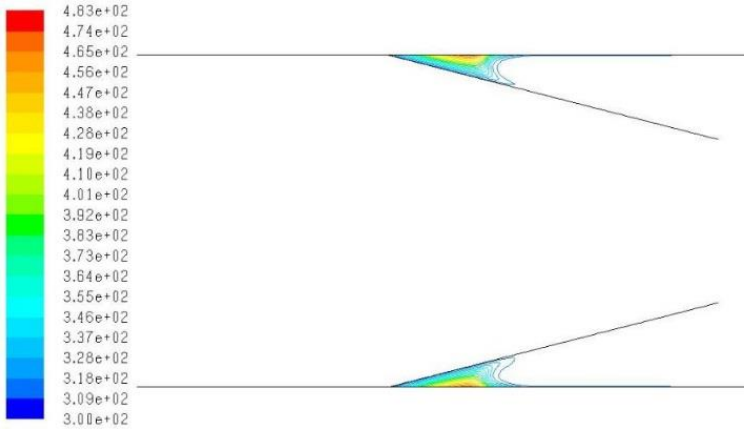

Re = 9500

Figure 4.9 Isotherms for different Reynolds numbers for SiO_2-water nanofluid flowing in a tube fitted with CR rings

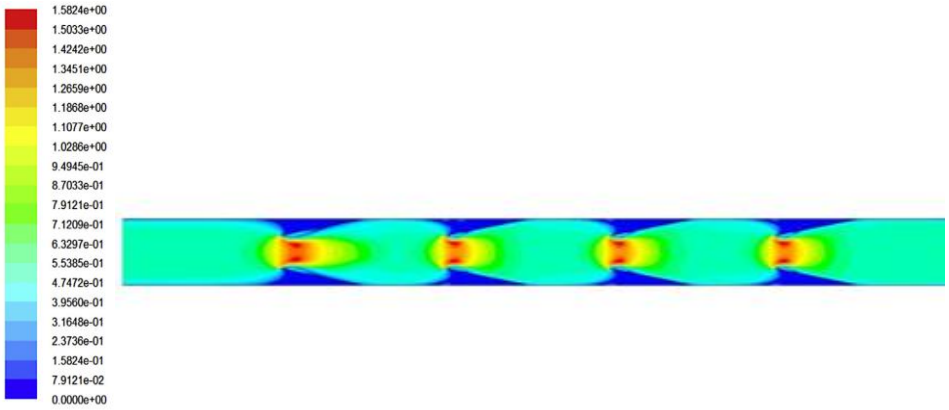

(a)

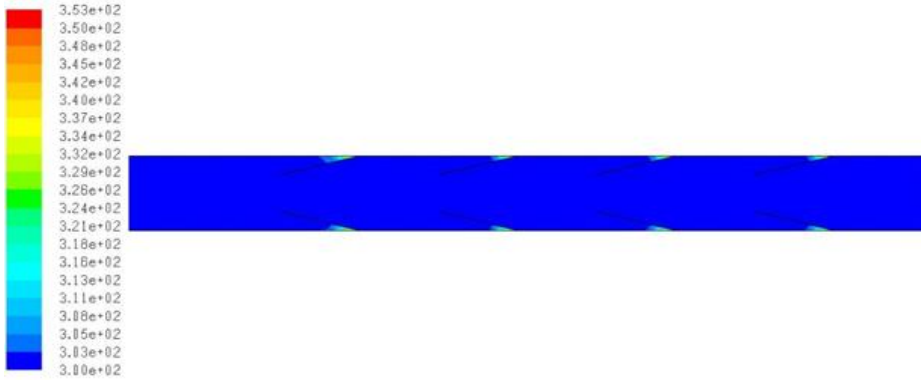

(b)

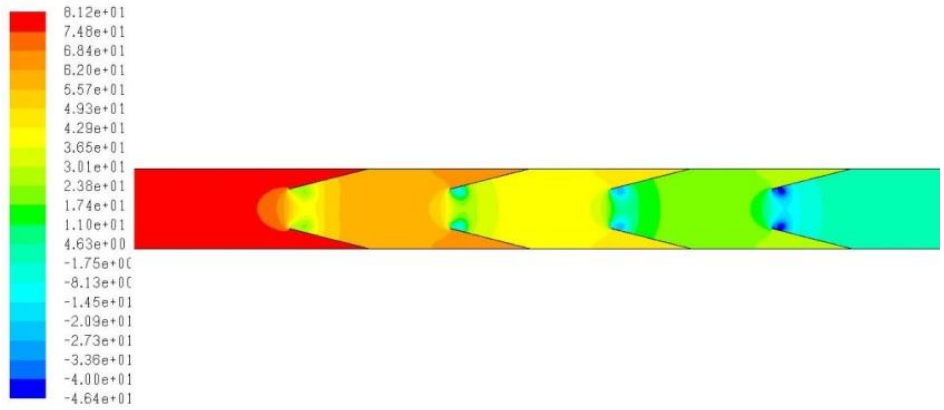

(c)

Figure 4.10 The (a) velocity, (b) temperature, and (c) pressure contours for DR ring at Re= 9500 and SiO_2-water nanofluid.

4.6.4 Effect of Single and Two-phase Mixture Models

In this section the two-phase mixture model is used to study the turbulent nanofluid flow characteristics in an inserted tube with conical rings. The two-phase model provides the possibility of understanding the functions of both the fluid phase and the solid particles in the heat transfer process. The comparison of the previous numerical studies with the experimental proved that, the mixture model is more precise and this encourages considering the mixture model in this study. The two-phases are assumed to be inter-penetrating meaning that each phase has its own velocity vector field, and within any control volume there is a volume fraction of primary phase and also a volume fraction of the secondary phase [28].

The presented results are compared with results of single-phase model to show the difference between them. In this part the distilled water is used to represent the fluid phase and the SiO_2 nanoparticles considered with 4% volume concentration used to represent the solid phase. The nanoparticles diameter was chosen to be 20 nm and the base fluid flow Reynolds numbers were 2500-9500. The DR arrangement is adopted, while all other parameters are kept constant.

The results of average Nusselt number and friction factor are presented for both single-

and two-phase using mixture models. Comparison of single-phase and two-phase models revealed similar trends (see Figure 4.11). The results show that for both parameters namely average Nusselt number and friction factor, the two-phase model is more precise than that of the single-phase model with maximum deviation of 8 to 10% as shown in Figure 4.11. Thus, it is inferred that the two-phase model could be used to test new nanofluids, since it captures the information on both particles and base fluid.

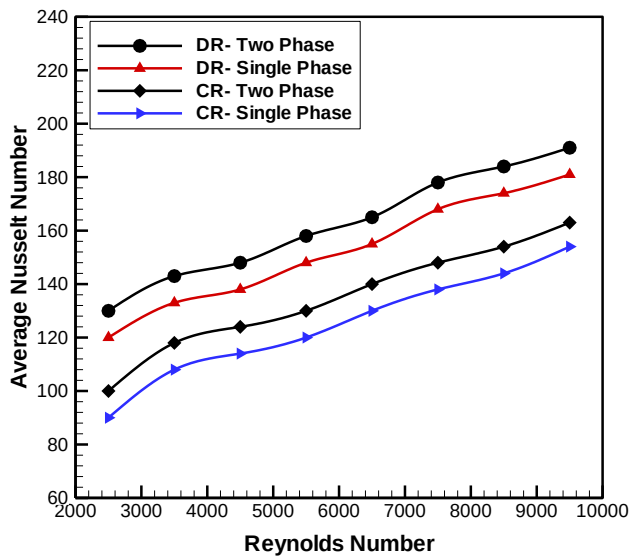

(a)

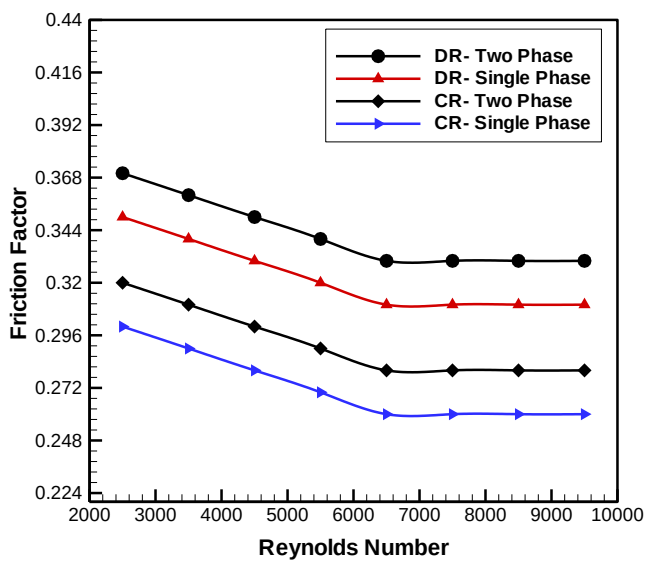

(b)

Figure 4.11 The effect of single and two-phase models using SiO_2-water nanofluid on (a) variation of average Nusselt number, (b) variation of friction factor versus Reynolds number at volume fraction ϕ = 1% and d_p=20 nm.

4.7 Conclusions

The main goal of the current study was to investigate the turbulent forced convection of nanofluid flow in inserted tubes numerically. Finite volume method was used to solve the governing equations with appropriate boundary conditions. The effects of different nanoparticle parameters on heat transfer enhancement at different Reynolds numbers (2000-10000) were analyzed. In order to demonstrate the validity and also precision of the model and the numerical procedure, comparison with the previously published traditional expressions was done. Nusselt numbers from the present numerical analysis for forced convection flow are compared with the equations given by Dittus-Boelter and Gnielinski formulas. The agreement of results with the results published by other numerical works was also illustrated. Two different approaches for simulating nanofluids, which are a single-phase and two-phase mixture models were implemented for the first time to study such a flow field. The following conclusions can be drawn as follows:

- The results show that the DR inserts provide higher value of heat transfer augmentation, pressure drop and PEC index in comparison with CR inserts. It is found that the insertion of conical rings has enhanced the Nusselt number for the DR arrangement up to 365%, and for the CR arrangement up to 280%.
- Nanofluid with SiO_2 particle achieved the highest Nusselt number and it was followed by Al_2O_3, ZnO and CuO respectively, while the pure water gave the lowest values. The heat transfer in terms of Nusselt number improved well for the higher particle volume fraction (4%) and the lower particle diameter (20 nm).
- It is found that there was no considerable increase in the friction factor noticed when using different types of nanofluids. The average Nusselt number increases with increasing Reynolds number, while friction factor represents reverse trend for both water and nanofluids.
- Most importantly, the comparison of calculated results for different models shows that the two-phase mixture model is more precise than the single-phase model.
- Generally, these numerical results can be seen as a useful vision onto forced convection heat transfer and fluid flow characteristics inside a circular tube fitted

with conical rings with different arrangements filled with different nanofluids. The results from the present work are of practical significance for industries aiming for heat transfer enhancement techniques and make their heat transfer equipment operations more effective.

References

[1] P. Promvonge, S. Eiamsa-ard, Heat transfer enhancement in a tube with combined conical-nozzle inserts and swirl generator, Energy Conversion and Management, 47 (18) (2006): 2867-2882.

[2] P. Promvonge, Heat transfer behaviors in round tube with conical ring inserts, Energy Conversion and Management, 49 (1) (2008): 8-15.

[3] M. M. K. Bhuiya, M. S. U. Chowdhury, M. Islam, J.U. Ahamed, M.J.H. Khan, M.R.I. Sarker, M. Saha, Heat transfer performance evaluation for turbulent flow through a tube with twisted wire brush inserts, International Communications in Heat and Mass Transfer, 39 (10) (2012): 1505-1512.

[4] M. Akhavan-Behabadi, R. Kumar, A. Mohammadpour, M. Jamali-Asthiani, Effect of twisted tape insert on heat transfer and pressure drop in horizontal evaporators for the flow of R-134a, International Journal of Refrigeration, 32 (5) (2009): 922-930.

[5] P. Murugesan, K. Mayilsamy, S. Suresh, P. Srinivasan, Heat transfer and pressure drop characteristics in a circular tube fitted with and without V-cut twisted tape insert, International Communications in Heat and Mass Transfer, 38 (3) (2011): 329-334.

[6] H. Bas, V. Ozceyhan, Heat transfer enhancement in a tube with twisted tape inserts placed separately from the tube wall, Experimental Thermal and Fluid Science, 41 (2012): 51-58.

[7] S. Gunes, V. Ozceyhan, O. Buyukalaca, Heat transfer enhancement in a tube with equilateral triangle cross sectioned coiled wire inserts, Experimental Thermal and Fluid Science, 34 (6) (2010): 684-691.

[8] A. Fan, J. Deng, A. Nakayama, W. Liu, Parametric study on turbulent heat transfer and flow characteristics in a circular tube fitted with louvered strip inserts, International Journal of Heat and Mass Transfer, 55 (19) (2012): 5205-5213.

[9] H. A. Mohammed, G. Bhaskaran, N. Shuaib, R. Saidur, Heat transfer and fluid flow characteristics in microchannels heat exchanger using nanofluids: a review, Renewable and Sustainable Energy Reviews, 15 (3) (2011): 1502-1512.

[10] K. Narrein, H. A. Mohammed, Influence of nanofluids and rotation on helically coiled tube heat exchanger performance, Thermochimica Acta, 564 (2013): 13-23.

[11] K.V. Sharma, L.S. Sundar, P.K. Sarma, Estimation of heat transfer coefficient and friction factor in the transition flow with low volume concentration of Al_2O_3 nanofluid flowing in a circular tube and with twisted tape insert, International Communications in Heat and Mass Transfer, 36 (5) (2009): 503-507.

[12] L. S. Sundar, K.V. Sharma, Turbulent heat transfer and friction factor of Al_2O_3 Nanofluid in circular tube with twisted tape inserts, International Journal of Heat and Mass Transfer, 53 (7–8) (2010): 1409-1416.

[13] S. Suresh, P. Selvakumar, M. Chandrasekar, V.S. Raman, Experimental studies on heat transfer and friction factor characteristics of Al_2O_3/water nanofluid under turbulent flow with spiraled rod inserts, Chemical Engineering and Processing: Process Intensification, 53 (2012): 24-30.

[14] H. A. Mohammed, H. A. Hasan, M. A. Wahid, Heat transfer enhancement of nanofluids in a double pipe heat exchanger with louvered strip inserts, International Communications in Heat and Mass Transfer, 40 (2013): 36-46.

[15] K. Yakut, B. Sahin, Flow-induced vibration analysis of conical rings used for heat transfer enhancement in heat exchangers, Applied Energy 78 (2004): 273-288.

[16] K. Yakut, B. Sahin, C. Celik, S. Canbazoglu, Performance and flow-induced vibration characteristics for conical-ring turbulators, Applied Energy 79 (2004): 65-76.

[17] A. Fan, J. Deng, J. Guo, W. Liu, A numerical study on thermo-hydraulic characteristics of turbulent flow in a circular tube fitted with conical strip inserts, Applied Thermal Engineering 31 (2011): 2819-2828.

[18] P. Liu, N. Zheng, F. Shan, Z. Liu, W. Liu, An experimental and numerical study on the laminar heat transfer and flow characteristics of a circular tube fitted with multiple conical strips inserts, International Journal of Heat and Mass Transfer 117 (2018): 691–709

[19] M. Sheikholeslami, D. D. Ganji, M. Gorji-Bandpy, Experimental and numerical analysis for effects of using conical ring on turbulent flow and heat transfer in a double pipe air to water heat exchanger, Applied Thermal Engineering 100 (2016): 805–819.

[20] A. R. Anvari, R. Lotfi, A. M. Rashidi, S. Sattari, Experimental research on heat transfer of water in tubes with conical ring inserts in transient regime, International Communications in Heat and Mass Transfer 38 (2011): 668–671.

[21] A. R. Anvari, K. Javaherdeh, M. Emami-Meibodi, A. M. Rashidi, Numerical and experimental investigation of heat transfer behavior in a round tube with the special conical ring inserts, Energy Conversion and Management, 88 (2014): 214-217.

[22] P. Promvonge, S. Eiamsa-ard, Heat transfer behaviors in a tube with combined conical-ring and twisted-tape insert, International Communications in Heat and Mass Transfer 34 (2007): 849-859.

[23] S. Eiamsa-ard, P. Promvonge, Numerical study on heat transfer of turbulent channel flow over periodic grooves, International Communications in Heat and Mass Transfer, 35 (7) (2008): 844-852.

[24] S. Sripattanapipat, S. Tamna, N. Jayranaiwachira, P. Promvonge, Numerical heat transfer investigation in a heat exchanger tube with hexagonal conical-ring inserts, Energy Procedia 100 (2016): 522-525.

[25] A. W. Fan, J. J. Deng, J. Guo, W. Liu, A numerical study on thermo-hydraulic characteristics of turbulent flow in a circular tube fitted with conical strip inserts, Applied Thermal Engineering 31 (2011): 2819-2828.

[26] Y. You, A. Fan, W. Liu, S. Huang, Thermo-hydraulic characteristics of laminar flow in an enhanced tube with conical strip inserts, International Journal of Thermal Sciences 61 (2012): 28-37.

[27] R. Lotfi, Y. Saboohi, A. M. Rashidi, Numerical study of forced convective heat transfer of Nanofluids: Comparison of different approaches. International Communications Heat and Mass Transfer 37 (1) (2010): 74-78.

[28] O. Ghaffari, A. Behzadmehr, H. Ajam, Turbulent mixed convection of a nanofluid in a horizontal curved tube using a two-phase approach, International Communications in Heat and Mass Transfer 37 (2010): 1551–1558.

[29] M. Manninen, V. Taivassalo, S. Kallio, On the mixture model for multiphase flow, *Finland: Technical Research Centre of Finland (1996)*.

[30] L. Schiller, A. Naumann, A drag coefficient correlation, *Vdi Zeitung* 77 (1935): 318-320.

[31] B.E. Launder, D.B. Spalding, Lectures in mathematical models of turbulence, (1972).

[32] F. Incropera, P.D. Dewitt, Introduction to Heat Transfer, fifth ed., John Wiley & Sons Inc, New York, 2006.

[33] S. V. Patankar, Numerical heat transfer and fluid flow, Taylor & Francis Group, 1980.

[34] J. D. Anderson, Computational fluid dynamics, McGraw-Hill New York, 1995.

[35] J. S. Jayakumar, S.M. Mahajani, J.C. Mandal, P.K. Vijayan, R. Bhoi, Experimental and CFD estimation of heat transfer in helically coiled heat exchangers, Chem. Eng. Res. Des. 86 (3) (2008): 221-232.

[36] C. T. Nguyen, F. Desgranges, N. Galanis, G. Roy, T. Maré, S. Boucher, H. Angue Mintsa, Viscosity data for Al_2O_3-water nanofluid–hysteresis: is heat transfer enhancement using nanofluids reliable?, International Journal Thermal Sciences 47 (2008): 103-111.

[37] R. S. Vajjha, D.K. Das, Experimental determination of thermal conductivity of three nanofluids and development of new correlations, International Journal of Heat and Mass Transfer, 52(21–22) (2009): 4675-4682.

[38] R. S. Vajjha, D. K. Das, D. P. Kulkarni, Development of new correlations for convective heat transfer and friction factor in turbulent regime for nanofluids, International Journal of Heat and Mass Transfer, 53 (21) (2010): 4607-4618.

Chapter 5 Heat Transfer Augmentation of Parabolic Trough Solar Collector Receiver's Tube using Hybrid Nanofluids and Conical Turbulators

Abstract

Parabolic Trough Solar Collector (PTSC) is one of the most popular and an effective device that converts solar radiation into a heat or useful energy. However, it suffers from high temperature gradient and low thermal efficiency. The solution for this problem is to use new advanced coolants (hybrid nanofluids) in order to enhance PTSC's thermal efficiency. A numerical analysis on the thermo-hydraulic performance of a PTSC receiver's tube equipped with conical turbulators is presented. The Navier-Stokes equations are solved using Finite Volume Method (FVM) coupled with Monte Carlo Ray Tracing (MCRT) method. The flow and thermal characteristics as well as entropy generation of the PTSC's receiver tube are investigated for three hybrid nanofluids (Ag-SWCNT, Ag-MWCNT, and Ag-MgO) having a mixing ratio of (50:50) dispersed in Syltherm oil 800, Reynolds number (5000 to 100000) and fluid inlet temperatures (400 to 650K). The conical turbulators effectively augmented the thermal performance by 233.4% utilising Ag-SWCNT/Syltherm oil instead of pure Syltherm oil. The performance evaluation criterion is found to be in the range of 0.9-1.82. The thermal and exergetic efficiencies increased by 11.5% and 18.2%, respectively. The maximum decrement in the entropy generation rate and entropy generation ratio are 42.7% and 33.7%.

The content of this chapter has been published in Journal of the Taiwan Institute of Chemical Engineers, 2021 **(Q1, IF=5.876).**

Chapter 5

5.1 Introduction

5.1.1 Research Background and Motivation

Solar energy exploitation is considered one of the foremost encouraging solutions for solving the current energy management and environmental problems such as global warming, fossil fuel depletion, and rapidly increasing energy demand [1-2]. There are various technologies being used for harnessing energy from assorted renewable energies. Solar concentrating technologies are mainly available in five types: (i) Solar power tower (SPT), (ii) Parabolic dish collector (PDC), (iii) Linear Fresnel reflector (LFR), (iv) Enclosed trough (ET), and (v) Parabolic trough solar collector (PTSC). The PTSC is one of the most popular and the most proven solar concentration technique [3-4]. The PTSC utilises its linear focus receiver to change over the solar beam radiation into thermal energy. The parabolic trough receiver (PTR) is one of the major parts of a PTSC system, which has a paramount role on the plant's overall performance. The PTRs can viably deliver heat at high temperature up to 400°C.

PTSCs suffer from the high circumferential temperature gradient, which is caused by the nonuniform heat flux generated from the concentrated solar radiation. Moreover, it was suggested to use high concentration ratios and diminish the number of drives and associations in order to reduce the cost of PTSC production, which in turn leads to a higher circumferential temperature gradient and high overall temperature in the PTR. Thus, these serious operational conditions of high circumferential temperature gradient in the PTR would have unfavorable impacts on the PTR's effectiveness and durability. The high temperature can lead to degradation of the heat transfer fluid and remarkably boost the heat loss and thus diminishing the energetic efficiency of the PTSC. On the other hand, it can create a huge thermal stress, which might twist the tube and break the glass envelope and thus reducing the lifetime of the PTSC. In order to solve the above-mentioned problems, passive and active thermal augmentation strategies have been widely utilised to enhance PTSCs thermal performance for industrial processes. Passive techniques have been commonly used in the open literature as they are preferable and utilise surface alterations across the flow such as tape inserts or fins or particle addition such as gas

bubbles, solid particles, and liquid droplets. It was found that both techniques are very useful in augmenting the thermal performance of PTSC frameworks.

5.1.2 Adopted Literature Review on PTSC Heat Transfer Augmentation

Extensive experimental and numerical research has been conducted on the thermal enhancement using various strategies (different types of passive techniques), which is thoroughly investigated and summarised in the next paragraphs. The PTSC's performance with different porous shapes (square, triangular, trapezoidal and circular) was numerically studied with water and therminol oil by Reddy et al. [5]. The PTSC's efficiency remarkably improved with the usage of trapezoidal porous fin receiver and the heat transfer was 13.8% augmented with 1.7 kPa pressure drop losses. Waghole et al. [6] determined experimentally, using silver nanoparticles, the thermal and flow fields data in a PTSC absorber tube with and without twisted tape inserts. Their experiments show that the Nu number, friction factor and enhancement efficiency were 1.25-2.1 times, 1.0-1.75 times and 135%-205%, respectively, over a smooth PTSC tube. Jafar and Sivaraman [7] investigated experimentally the impact of using nail twisted tape (NTT) and Al_2O_3/water nanofluid in a PTSC receiver. It was concluded that the NTT absorber with nanofluids remarkably enhanced the PTSC thermal effectiveness with a slight increment of friction factor due to high swirl flow.

Bellos et al. [8] utilised a dimpled with sine geometry PTSC absorber tube utilising thermal oil, thermal oil-Al_2O_3 nanofluid and pressurized water. The outcomes revealed a remarkable boost in both thermal efficiency and thermal performance of 10%, 169%, respectively, and decrement in the circumferential temperature up to 68% over a plain receiver pipe. In addition, the thermal oil-Al_2O_3 nanofluid produced 4.25% improvement of the mean efficiency while 6.34% was produced by the use of pressurized water. Benabderrahmane et al. [9] investigated numerically the thermal effectiveness of a PTSC equipped with longitudinal fins inserts (LFI) and various types of nanofluids. It was found that the metallic nanoparticles significantly enhanced the heat transfer than other nanoparticle types. Zhu et al. [10] used CFD to study the flow and thermal fields inside

an absorber tube of a PTSC fitted with wavy-tape insert utilising Syltherm-800. The wavy-tape produced a performance evaluation index more than 2.11 and heat loss reduction by 17.5-33.1% with an entropy generation rate reduction by 30.2-81.8%.

Xiangtao et al. [11] used pin fin arrays insert (PFAI) in a PTSC receiver tube to enhance the thermal effectiveness. The thermal effectiveness factor and the Nusselt number increased up to 12.0% and 9.0% respectively with the unitisation of PFAI. Huang et al. [12] studied numerically a 3D turbulent mixed heat transfer in dimpled tubes of PTSC tube. The outcomes revealed that the deep dimples (d/Di = 0.875) performed much better than the shallow dimples (d/Di = 0.125) at similar Grashof number. Bellos and Tzivanidis [13] and Bellos et al. [14] used a star shape insert and investigated the internal fins best number and location in a PTSC for enhancing its thermal performance. The results revealed that the Nusselt number enhancement is up to 60% with thermal losses decrement up to 14%. It was concluded that the internal fins should be located in the absorber tube's lower part where the heat flux is highly concentrated.

Bitam et al. [15] conducted a 3D numerical model to investigate the thermal effectiveness in a PTSC having a S-curved/sinusoidal tube receiver using synthetic oil. It was noticed that the maximum performance evaluation criterion is about 135%. Okonkwo et al. [16] used three insert kinds in a PTSC absorber tube such as longitudinal fins, twisted tape, and converging-diverging tube with Therminol VP-1 and Al_2O_3-oil nanofluids. The outcomes have shown that the converging-diverging geometry achieved thermal efficiency of 65.95% and exergetic efficiency of 38.24%. Khan et al. [17] compared numerically the energetic and exergetic performance of twisted tape insert and longitudinal fins inside an absorber tube of a PTSC with Al_2O_3/water nanofluid utilising Engineering Equation Software (EES). The outcomes revealed that the twisted tape insert has the highest thermal efficiency of 72.26%, compared to a tube with internal fins (72.10%), and plain tube (71.09%).

It can be seen from the above literarure review section that the passive technique with different configurations are appropriate methods for enhancing the thermal effectiveness

inside a PTSC receiver tube as it decreased the Q_{loss}, T_{max} and reduce the thermal strain and it has remarkably enhanced the consistency of temperature distribution of the tube wall. It was also pointed out that the utilisation of passive techniques would decrease the absorber's circumferential temperature range and this would in turns decrease the failure danger caused by the thermal stresses. It was observed that about 15% maximum decrement in the temperature range could be achieved with passive technqiue associated absorber tube compared to a smooth absorber tube.

Recently, PTSC technology has been widely applied in concentrating power plants, hydrogen production or other industrial processes with high temperature requirement. In any case, the huge temperature gradient is the basic explanation of instigating the thermal twisting and harm of PTSC. Accordingly, numerous scientists have embraced the strategy for heat transfer enhancement to diminish the temperature gradient by utilising diverse operating liquids. Nanofluids are considered the fluids of future and the second option of thermal augmentation in PTSC frameworks. Nanofluids have received an extensive research attention in the past decade because they have a great potential to augment the thermal performance in a PTSC. Nanofluids are additionally called as extraordinary coolant liquids because of their high capacity to assimilate heat more than any customary liquids, so they can diminish the size of frameworks and boost its efficiency. The utilisation of these nanoparticles prompts higher thermal conductivity and subsequently higher heat transfer rate to the working liquid in a PTSC framework. Higher heat transfer rate prompts a lower temperature in the PTSC frameworks and to bring down heat losses, the way that prompts higher thermal effectiveness. Therefore, the utilisation of nanofluids with different types and concentrations is considered among the most effective working liquids in PTSC frameworks as indicated by the literatures, which have been summarised below in the following paragraphs.

Kasaeian et al. [18] studied numerically mixed convective turbulent flow of Al_2O_3-oil nanofluid in a PTSC pipe. de Risi et al. [19] tested Cu-water nanofluid numerically in a PTSC to examine its thermal performance. Sunil et al. [20] investigated experimentally the PTSC performance using SiO_2-H_2O based nanofluid. Zadeh et al. [21] used genetic

algorithm (GA) optimisation method and sequential quadratic programming (SQP) of a PTSC absorber tube subjected to a non-uniform heat flux (NUHF) using Al_2O_3/synthetic oil. Chaudhari et al. [22] investigated experimentally using Al_2O_3-water on the thermal effectiveness of a PTSC. The outcomes revealed that the Nu number has direct reliance on the nanofluid's volume fraction. The heat transfer decreased by increasing the operational temperature at a given mass flowrate. The optimum thermal efficiency increased as the nanoparticle's volume flow rate increased. Mwesigye and Huan [23] and Mwesigye et al. [24] used synthetic oil-Al_2O_3 nanofluid and Syltherm800-CuO nanofluid to examine its efficacy in a PTSC having high concentration ratio of 113 utilising the entropy generation minimisation technique. The outcomes show that the utilisation of nanofluids remarkably enhanced the receiver's thermal effectiveness up to 7.6%.

Kasaeian et al. [25] used multi walled carbon nanotube (MWCNT)/oil nanofluid with 0.2-0.3% volume fraction in a vacuumed copper absorber tube. Basbous et al. [26] utilised ultrafine particles Al_2O_3, Cu, CuO and Ag dispersed in Syltherm 800 to examine numerically the thermal effectiveness of a PTSC framework. Mwesigye et al. [27] presented numerically the thermodynamic effectiveness of a PTSC using Cu-Therminol VP-1 nanofluid. Wang et al. [28] implemented a combined optical-thermal-stress simulation model based on FEM to examine the Al_2O_3/synthetic oil nanofluid on a PTSC thermal effectiveness. Ghasemi and Ranjbar [29] simulated numerically forced convective turbulent nanofluids using (CuO and Al_2O_3 nanofluids) flow in a solar PTSC receiver. The outcomes revealed that the thermal efficiency boosted by 12.5% and the entropy generation rates reduced significantly as the nanoparticle volume fraction increased.

Coccia et al. [30] analysed numerically the yearly yield assessment of a low-enthalpy PTSC using six water-based nanofluids: Fe_2O_3, SiO_2, TiO_2, ZnO, Al_2O_3, and Au. The results show that small improvements are associated with Au, TiO_2, ZnO, and Al_2O_3 nanofluids at low volume fractions compared with water. Ferraro et al. [31] analysed using thermal analysis model the behaviour of a PTSC operating with Al_2O_3 in synthetic oil nanofluids. It was observed that there were only slight differences in the power loss and efficiency, while the main advantage is represented by lowering the pumping power.

Mwesigye and Meyer [32] investigated the PTSC's thermal and thermodynamic effectiveness utilising Cu-Therminol, Ag-Therminol and Al_2O_3-Therminol nanofluids. It was found that the thermal efficiency increased by 13.9%, 12.5% and 7.2% for Ag-Therminol, Cu-Therminol and Al_2O_3-Therminol, respectively, at a concentration ratio of 113. Bellos and Tzivanidis [33] investigated the use of Al_2O_3 and CuO suspended in Syltherm 800 oil nanofluids in a PTSC using comprehensive thermal model constructed utilising Engineering Equation Software (EES). The results found that the nanofluids with high concentration and low flow rates provided higher enhancement, which would be paramount criteria to select nanofluids in PTSC frameworks.

Khakrah et al. [34] performed a comprehensive numerical study of Al_2O_3/synthetic oil nanofluid in a PTSC receiver tube. The outcomes show that the efficiency augmentation was 14.3% when using 5% volume fraction of Al_2O_3-synthetic oil nanofluid. Kasaeian et al. [35] presented new forms of PTSC with three different receivers made of glass: a bare tube, non-evacuated tube, and a vacuumed tube. The influences of using MWCNT and nanosilica suspended in ethylene glycol nanofluids and the properties of the absorber tube on the PTSC's thermal effectiveness were investigated. The carbon nanotubes exhibited maximum values of volume fraction and thermal efficiency at 0.5, and 80.7%, respectively, and it was 0.4 and 70.9%, respectively, for nanosilica.

Mwesigye et al. [36] investigated numerically using energy and exergy analyses the PTSC's thermal effectiveness using SWCNTs-Therminol® VP-1 nanofluid. Subramani et al. [37] investigated experimentally the performance of TiO_2/water nanofluids in a PTSC under turbulent flow regime. Bellos and Tzivanidis [38] used different types of nanoparticles such as Cu, CuO, Fe_2O_3, TiO_2, Al_2O_3 and SiO_2 dispersed in Syltherm 800 and tested numerically in a PTSC system using EES. Bellos et al. [39] examined the addition of CuO nanoparticles in Syltherm 800 and in nitrate molten salt and tested its efficacy on a PTSC thermal performance. The results revealed that the thermal effectiveness was augmented using nanofluids compared with base-fluid. They suggested a new index, which considered the heat transfer, the fluid's properties and the flow rate for the assessment of the thermal performance enhancement. Marefati et al. [40] analysed

the optical and thermal analyses of PTSC using various nanofluids (CuO, Al_2O_3, and SiC) for four cities of Iran with different weather conditions. It was found that the thermal effectiveness using CuO nanofluid is higher than other nanofluids. Rehan et al. [41] evaluated the experimental effectiveness of a locally developed PTSC system utilising Al_2O_3/H_2O and Fe_2O_3/H_2O for domestic heating applications. The results revealed that Al_2O_3 nanofluids were preferable in the efficiency enhancement compared to Fe_2O_3. Rios De los et al. [42] investigated experimentally the impact of Al_2O_3-water nanofluid on the PTSC thermal effectiveness. The PTSC's outlet temperatures were higher using nanofluids than those when using water even when the solar radiation value was very small. Allouhia et al. [43] proposed a 1D- mathematical model to study the influence of various nanoparticles (Al_2O_3, CuO, and TiO_2) in a PTSC system. The exergy efficiency, for base fluid, ranged between 3.05% to 8.5%, whereas it was significantly enhanced to 9.05% for CuO nanofluid. Alsaady et al. [44] used Fe_3O_4 ferrofluids experimentally to test its efficacy on the thermal effectiveness of a small-scale PTSC. The outcomes revealed that the thermal efficiency increased by 16% and 25% with the utilisation of ferrofluids without and with external magnetic field compared to base fluid, respectively. Tagle-Salazar et al. [45] presented a thermal mathematical model and an experimental work of PTSC for heating applications using alumina-water nanofluid with the aid of EES. It was inferred that the thermal behaviour of the nonevacuated receiver remarkably enhanced with high thermal losses contrasted to an evacuated receiver. Kumar et al. [46] studied experimentally PTSC with a modified absorber tube with copper fins and using TiO_2 nanofluid. The results revealed that the usage of fins increased the thermal effectiveness and the outlet temperature increased with the increases in nanofluid concentration. Recently, Bellos et al. [47] studied mathematically the thermal augmentation using (Cu/Syltherm 800) nanofluid in a PTSC. Three PTSC receiver's tube were utilised in the analysis; evacuated, non-evacuated and bare with no cover. The optimum augmentation for bare tube, nonevacuated tube and evacuated tube was found to be 7.16%, 4.87% and 4.06%, respectively, when using cermet coating. Very recently, there have been few studies examined the enhancement of PTSC absorber tube using different types of nanofluids and various passive techniques [48-52].

5.1.3 Research Novelty and Objectives

It can be obviously noticed from the above literature that various kinds of nanofluids have been implemented in PTSC frameworks. Nonetheless, there are yet other nanoparticle kinds such carbon nanotubes that can be commendable of examination because of their outstanding thermophysical properties. Furthermore, in spite of the majority of studies have focused on the thermal effectiveness of PTSCs using nanofluids, the investigations on the thermal and thermodynamic effectiveness utilising hybrid nanofluids are still scarce in the open literature. Thus, this study aims to fulfil the existing gap and presents a 3D numerical model to examine the flow and thermal fields in a PTSC geometry equipped with central conical turbulators under turbulent hybrid nanofluids flow conditions. Various hybrid nanofluid kinds namely Ag-SWCNT, Ag-MWCNT and Ag-MgO having a mixing ratio of (50:50) dispersed in Syltherm oil were applied with various volume fractions in the range of 1-2%. The PTSC's absorber tube is exposed to a nonuniform heat flux distribution utilising the Monte Carlo Ray Tracing (MCRT) method. The numerical thermal and hydrodynamic performance data are compared with the smooth tube results and other relevant available data. Furthermore, the thermodynamic irreversibilities and exergetic efficiency of the enhanced PTSC framework utilising hybrid nanofluids were also examined in order to identify the overall efficacy of these hybrid nanofluids.

5.2 Numerical Method

5.2.1 Physical Model

PTSCs are low-weight and relatively cheap frameworks that convey high temperatures with a higher efficiency. The PTSC shown in Figure 5.1 a receiver consists of two coaxial tubes and a metal tube called an absorber covered with a glass envelope to diminish the heat losses. The space between them is considered as a very low vacuum pressure about 0.0103 Pa (rarefied air) in order to avoid the heat loss by the natural convection. The working fluid circulates through the absorber tube, which is in this work a hybrid nanofluid with different types (Ag-SWCNT, Ag-MWCNT and Ag-MgO) having a mixing ratio of (50:50) dispersed in Syltherm oil. In this work, the materials utilised for the absorber and the glass tube are, respectively, steel and borosilicate glass. It is aimed to

augment the heat transfer performance, and reduce the PTSC's temperature gradient. The PTSC's absorber tube fitted by a central conical insert, is proposed as an enhanced absorber tube of PTSC and its geometrical factors are given in Table 5.1. Meanwhile, the geometrical dimensions of the conical turbulator are also illustrated in Figure 5.1c, where it shows the conical turbulator start and end diameters, the turbulator length, and the distance between two successive conical turbulators, respectively. There were in total 124 conical turbulators in the full computational domain. The heat transfer modes of the present study are also illustrated in Figure 5.2.

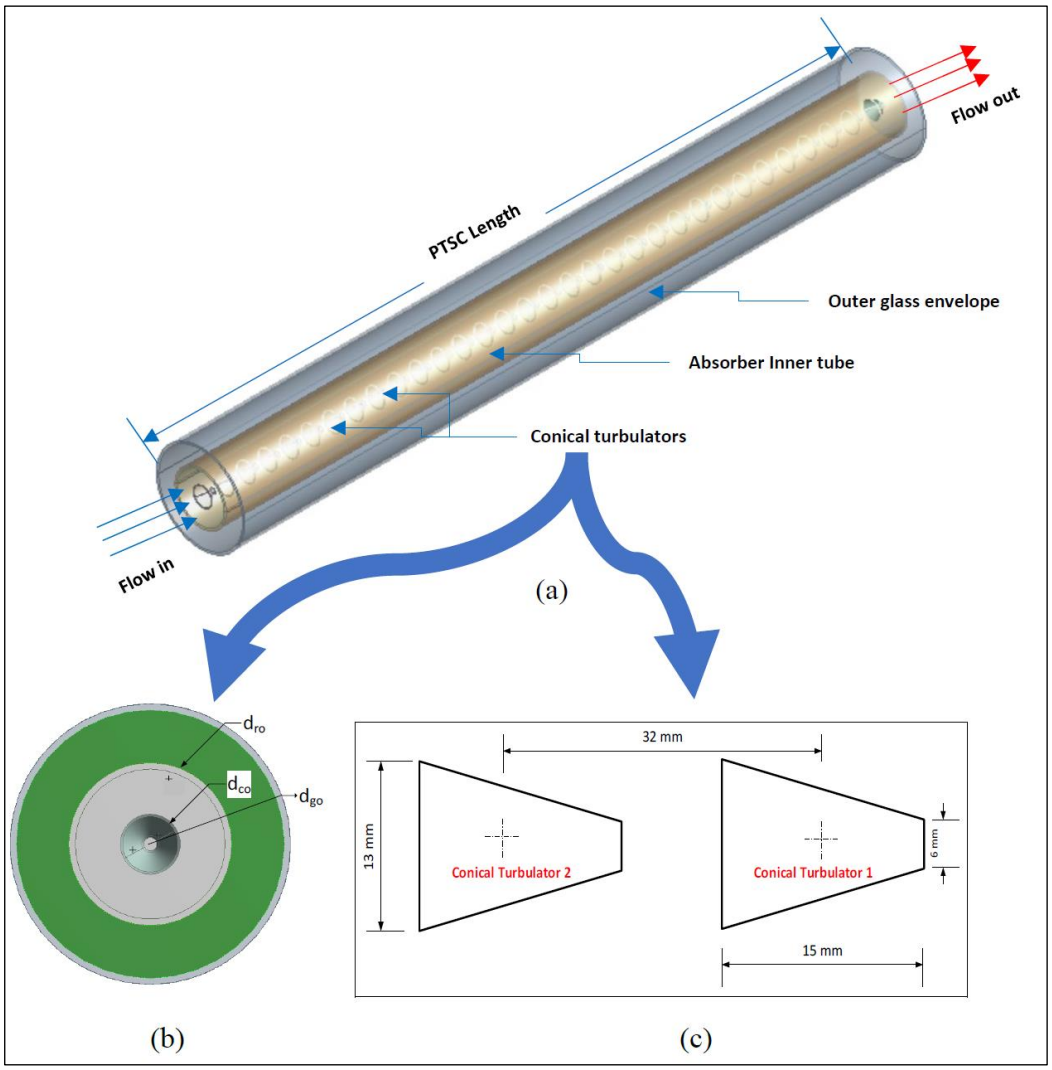

Figure 5.1 PTSC tube used in this study, (a) Full lateral view with conical turbulators, (b) Full cross-sectional view, and (c) conical turbulators dimensions.

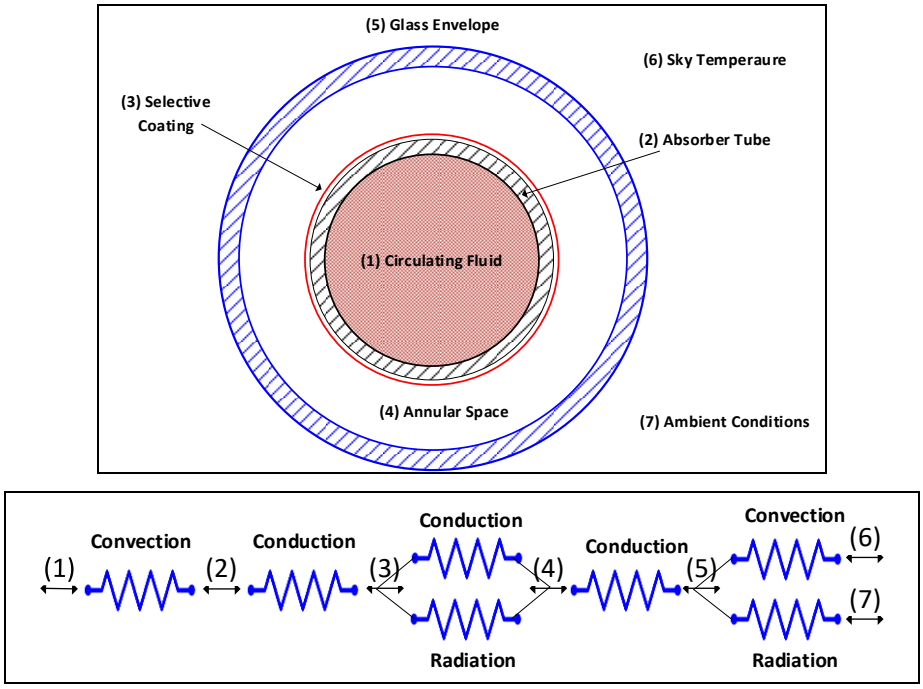

Figure 5.2 PTSC's Cross-sectional view and the associated thermal resistances.

Table 5.1 The dimensions of the PTSC's receiver tube with a conical turbulator.

Dimension	Value (mm)
Absorber tube length	4096
Absorber inner tube inside diameter (d_{ri})	70
Absorber inner tube outside diameter (d_{ro})	76
Glass outer tube inside diameter (d_{gi})	125
Glass outer tube outside diameter (d_{go})	131
Conical turbulator start diameter (d_{ci})	6
Conical turbulator end diameter (d_{co})	13
Length of conical turbulator	15
Pitch between two conical turbulators	32

5.2.2 Governing Equations

The Navier-Stokes equations (NSE) which govern the flow and thermal fields were used to model the PTSC's absorber tube as shown below [53]. The following assumptions were considered for modelling the PTSC tube: (i) PTSC tube works under steady-state conditions; (ii) incompressible fluid and single-phase was used; (iii) the fluid and tube material properties vary with temperature; and (iv) heat flux is constant at the absorber's inner upper half surface and it is nonuniform heat flux at the absorber's inner lower half surface.

Continuity:

$$\frac{\partial(\rho\bar{u}_{i)}}{\partial x_i} = 0 \tag{5.1}$$

Momentum:

$$\frac{\partial}{\partial x_j}\left(\rho\bar{u}_i\bar{u}_j\right) = -\frac{\partial\bar{P}}{\partial x_i} + \frac{\partial}{\partial x_j}\left[\mu\left(\frac{\partial\bar{u}_i}{\partial x_j} + \frac{\partial\bar{u}_j}{\partial x_i}\right) - \frac{2}{3}\mu\frac{\partial\bar{u}_i}{\partial x_i}\,\delta_{ij} - \left(\rho\overline{\acute{u}_\iota\acute{u}_\jmath}\right)\right] \tag{5.2}$$

Energy:

$$\frac{\partial}{\partial x_j}\left(\rho\bar{u}_j C_p\bar{T}\right) = \frac{\partial}{\partial x_j}\left(k\frac{\partial\bar{T}}{\partial x_j} + \frac{\mu_t}{\sigma_{ht}}\frac{\partial(C_p\bar{T})}{\partial x_j}\right) + \bar{u}_j\frac{\partial\bar{P}}{\partial x_j} + \left[\mu\left(\frac{\partial\bar{u}_i}{\partial x_j} + \frac{\partial\bar{u}_j}{\partial x_i}\right) - \frac{2}{3}\mu\frac{\partial\bar{u}_i}{\partial x_i}\,\delta_{ij} - \left(\rho\overline{\acute{u}_\iota\acute{u}_\jmath}\right)\right]\frac{\partial\bar{u}_i}{\partial x_j} \tag{5.3}$$

For modelling the Reynolds stresses $(-\rho\overline{u'_\iota u'_\jmath})$ in Eq. (5.2), k-ε turbulence model was selected for this purpose. In equations 5.2 and 5.3, $\bar{u}_i$ and $\bar{u}_j$ are the time-averaged velocity components in the i-and j- directions respectively. $\bar{T}$ and $\bar{P}$ are the time-averaged temperature and pressure, respectively. The eddy viscosity model was utilised to calculate the Reynolds stresses components in the RANS equations, which uses the Boussinesq approximation to interconnect the stress and strain as [53]:

$$\left(-\rho\overline{u'_\iota u'_\jmath}\right) = \mu_t\left(\frac{\partial u_i}{\partial x_j} + \frac{\partial u_j}{\partial x_i}\right) - \frac{2}{3}\left(\rho\,k + \mu_t\frac{\partial u_k}{\partial x_k} + \frac{\partial\bar{u}_j}{\partial x_i}\right)\,\delta_{ij} \tag{5.4}$$

The turbulence viscosity is calculated by:

$$\mu_t = \rho\,C_\mu\frac{k^2}{\varepsilon} \tag{5.5}$$

The turbulent kinetic energy (TKE) per unit mass, k is expressed as:

$$TKE = \frac{1}{2}\left(\overline{\acute{u}^2} + \overline{\acute{v}^2} + \overline{\acute{w}^2}\right) \tag{5.6}$$

The dissipation rate of TKE, ε, is given by:

$$\frac{\partial}{\partial x_i}(\rho\varepsilon u_i) = \frac{\partial}{\partial x_j}\left[\left(\mu + \frac{\mu_t}{\sigma_\varepsilon}\right)\frac{\partial \varepsilon}{\partial x_j}\right] + C_{1\varepsilon}\frac{\varepsilon}{k}G_k - C_{2\varepsilon}\rho\frac{\varepsilon^2}{k} \tag{5.7}$$

Where G_k is the TKE rate of generation, while $\rho\varepsilon$ is its destruction rate.

G_k is given by:

$$G_k = -\rho\overline{u'_\iota u'_J}\frac{\partial u_j}{\partial x_i} \tag{5.8}$$

Where the empirical constants are $C_\mu = 0.09, C_{1\varepsilon} = 1.44, C_{2\varepsilon} = 1.92$, $\sigma_k = 1.0$, $\sigma_\varepsilon = 1.3$ and $Pr_t = 0.9$ in the turbulence transport equations.

The discrete ordinates radiation model equation is [53]:

$$\frac{dI(\boldsymbol{r},\boldsymbol{s})}{ds} + (a + \sigma_s)\, I(\boldsymbol{r},\boldsymbol{s}) = a\, n^2\frac{\sigma T^4}{\pi} + \frac{\sigma_s}{4\pi}\int_0^{4\pi} I\,(\boldsymbol{r},\acute{\boldsymbol{s}})\Phi\,(\boldsymbol{s},\acute{\boldsymbol{s}})\, d\Omega \tag{5.9}$$

where $\vec{\boldsymbol{r}}$ is the position vector, $\vec{\boldsymbol{s}}$ is the direction vector, $\acute{\vec{\boldsymbol{s}}}$ is the scattering direction vector, s is the path length, $\boldsymbol{a}$ is the absorption coefficient, n is the refractive index, σ is the Stefan-Boltzmann constant, σ_s is the scattering coefficient, I is the radiation intensity, which depends on position $\vec{\boldsymbol{r}}$ and direction $\vec{\boldsymbol{s}}$, T is the local temperature, Φ is the phase function, and $\acute{\Omega}$ is the solid angle.

5.2.3 Boundary Conditions

The PTSC's absorber tube cross-section and the relevant thermal circuit are shown in Figure 5.2. The thermal process in this study is sophisticated as it involves three heat transfer mechanisms: conduction, convection and radiation. The PTSC's absorber tube outer surface received a direct and concentrated solar radiation and then it is absorbed by a selective coating and eventually converted into a heat. The absorber's inner upper half surface is exposed to a uniform heat flux boundary condition. The absorber's inner lower half surface is exposed to a nonuniform heat flux (concentrated solar radiation) boundary condition. This distribution was obtained by using the Monte Carlo Ray Tracing (MCRT) method. The results of the local concentration ratio (LCR= q_w/DNI) profile are presented in Figure 5.3a, where the direct normal irradiance (DNI) of 1000 W/m^2 was implemented. It is noticed that the heat flux profile is approximately symmetrical, and it is nonuniform in the circumferential direction. The heat flux profile on the PTSC's absorber tube external surface is also shown in Figure 5.3b.

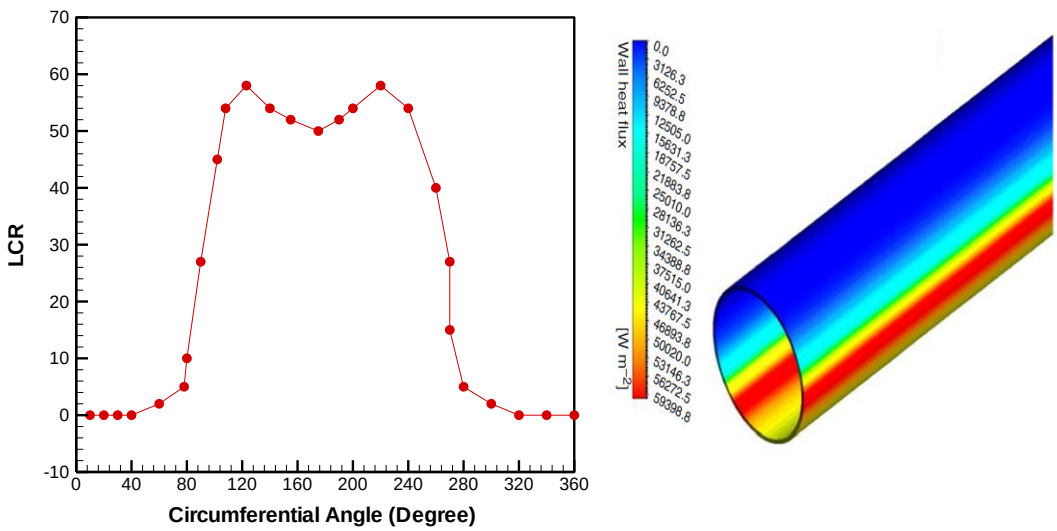

(a) (b)

Figure 5.3 (a) Variation of LCR with the circumferential angle on a cross-section of PTSC's absorber tube, (b) Heat flux profile along the absorber tube external surface.

The majority of the heat is imposed on the absorber tube's outer wall is conducted to the inner wall and then carried away by the circulating hybrid nanofluid through heat convection. The absorber tube was made of stainless steel (32H) having a thermal conductivity of 25 W/m.K. The Syltherm-800 has properties of temperature-dependent, it is along with a hybrid nanofluid are applied as the circulating fluid inside the absorber tube. The inlet of the absorber tube is set to inlet velocity based on Reynolds number in the range of 5000 to 100000 and inlet temperature in the range of 400 to 650K. The PTSC's absorber tube inner wall and the conical turbulators surface are considered as no-slip boundary conditions.

The rest of heat is transmitted to the glass cover's inner surface by radiation and conduction modes when there is a small amount of gas in the annular gap. The discrete ordinates (DO) radiation mode was utilised to model the radiation heat transfer through the annular gap as presented in Eq.5.9. The number of bands in the DO model was assumed three and the wavelength intervals values were taken as the default values as

suggested by ANSYS Theory Guide [53]. Cermet was used as the selective coating on the tube's outer wall whose emissivity is also deemed temperature-dependent and it is calculated using the following equation [54]:

$$\varepsilon = 0.062 + 2 \times 10^{-7} T^2 \quad (5.10)$$

Where T is the absorber tube's outer temperature in Kelvin. The glass envelope is considered a gray-body and the glass inner wall's emissivity is assumed to be 1.

The heat, which is converted from the outer surface of the absorber tube to the inner surface of the glass envelope, is conducted to the glass envelope's outer surface and then carried away to the surroundings via convection and radiation mechanisms. The glass envelope is made of Pyrex, which is made of borosilicate glass having a thermal conductivity of 1.2 W/m.K. The external surface of the glass envelope is exposed to a combined boundary condition (that involves convection and radiation). The Stefan-Boltzmann law was utilised to calculate the net heat flux produced by the radiation mode. The external emissivity of the external surface of the glass envelope is assumed to be 0.89. The convection heat transfer coefficient, sky temperature and emissivity for heat transfer by radiation are calculated by the following correlations [55] and [56]:

$$h_w = 4 \; v_w^{0.58} d_{go}^{-0.42} \quad (5.11)$$

$$T_{sky} = 0.0552 \, T_{amb}^{1.5} \quad (5.12)$$

$$\varepsilon_{sky} = 0.711 + 0.56 \left(\frac{T_{dp} - 273.15}{100}\right) + 0.73 \left(\frac{T_{dp} - 273.15}{100}\right)^2 \quad (5.13)$$

Where v_w is the wind velocity (2 m/s utilised in this study), d_{go} is the glass cover outer diameter, T_{amb} is the surrounding temperature (assumed 300 K in this study), and T_{dp} is the dew point temperature.

5.2.4 Data Acquisition

The following parameters utilised in this study such as average Nusselt number, Reynolds number, friction factor and performance evaluation criteria index are presented in this section [57]:

The friction factor is evaluated based on pressure drop as:

$$f = \frac{2}{(L/d_{ri})} \frac{\Delta P}{\rho\, u_m{}^2} \tag{5.14}$$

Where ΔP, ρ, d_{ri}, u_m, and L are the pressure drop, hybrid nanofluid density, the absorber tube's inner diameter, the mean velocity in the absorber tube and the length of the tube, respectively.

The average heat transfer coefficient (h) and average Nusselt number (Nu) are calculated using the following equations:

$$h = \frac{q''}{(T_{ri} - T_b)} \tag{5.15}$$

Where T_{ri}, and T_b are the average temperature of the inner wall's of the absorber tube and the bulk temperature of the fluid given as (T_{inlet}+T_{outlet}/2), respectively.

$$Nu_{av} = \frac{h\, d_{ri}}{\mathrm{k}} \tag{5.16}$$

The flow Reynolds number is calculated as:

$$Re = \frac{\rho\, u_m\, d_{ri}}{\mu} \tag{5.17}$$

Where k is the thermal conductivity of the fluid and $u_m$is the mean velocity.

The difference between the maximum temperature and minimum temperature of the absorber tube is called the circumferential temperature gradient:

$$\Delta T = T_{abs.max} - T_{abs.min} \tag{5.18}$$

The thermal efficiency of the PTSC's tube is defined as:

$$\eta_{th} = \frac{\dot{Q}_u - P_p/\eta_{el}}{A_a\, I_b} \tag{5.19}$$

In the above equation, $\dot{Q}_u = \dot{m}\, C_p(T_{outlet} - T_{inlet})$ is the heat transfer rate, $P_p = \dot{V}\, \Delta P$ is the pumping power, A_a is the collector's aperture area, I_b is the incident solar radiation and η_{el} is the electrical efficiency of the power block and assumed 32.7% [58]. It can be seen from Eq. (5.19), that the increment in pumping work demand is deducted from the heat transfer rate, which means that the enhanced and non-enhanced absorber tubes could be compared. For this deduction, the pumping work demand is changed over to a similar structure as the heat transfer rate by dividing it with the electrical efficiency.

The performance evaluation criterion (PEC) displays the thermal and hydraulic effectiveness of thermal management frameworks. In this work, it is calculated based on the fluid used (PEC_1) and based on the passive technique used (PEC_2) as given by:

$$PEC_1 = \left(\frac{Nu_{hnf}}{Nu_f}\right) / \left(\frac{f_{hnf}}{f_f}\right)^{1/3} \tag{5.20}$$

$$PEC_2 = \left(\frac{Nu_c}{Nu_o}\right) / \left(\frac{f_c}{f_o}\right)^{1/3} \tag{5.21}$$

Where the subscripts hnf, f, c and o refer to hybrid nanofluids, base fluid (Syltherm oil), PTSC with conical turbulators, and PTSC without turbulators respectively.

The entropy generation comes from irreversibilities of heat transfer $\left(S_{gen}^{H}\right)$ and fluid friction $\left(S_{gen}^{F}\right)$ and its formula is given:

$$\left(S_{gen}^{T}\right) = \left(S_{gen}^{F}\right) + \left(S_{gen}^{H}\right) \tag{5.22}$$

The entropy generation caused by irreversibility of fluid friction is calculated by:

$$\left(S_{gen}^{F}\right) = S_{PROD,VD} + S_{PROD,TD} \tag{5.23}$$

Where $S_{PROD,VD}$ is the direct dissipation entropy production and $S_{PROD,TD}$ is the indirect (turbulent) dissipation entropy production

$$S_{PROD,VD} = \frac{\mu}{T}\left(\frac{\partial u_i}{\partial x_j} + \frac{\partial u_j}{\partial x_i}\right)\frac{\partial u_i}{\partial x_j} \tag{5.24}$$

$$S_{PROD,TD} = \frac{\rho\varepsilon}{T} \tag{5.25}$$

The entropy generation caused by irreversibility of heat transfer is calculated by:

$$\left(S_{gen}^{H}\right) = S_{PROD,T} + S_{gen,TG} \tag{5.26}$$

Where $S_{PROD,T}$ is the heat transfer entropy production using mean temperatures and $S_{gen,TG}$ is the heat transfer entropy production using fluctuating temperatures.

Where $S_{PROD,T} = \frac{k}{T^2}\,(\nabla T)^2$ (5.27)

$$S_{gen,TG} = \frac{\alpha_t}{\alpha}\,\frac{k}{T^2}(\nabla T)^2 \tag{5.28}$$

Where α and α_t are the thermal diffusivities, and k is the fluid's thermal conductivity.

The entropy generation rates caused by fluid friction and heat transfer irreversibilities are first calculated for each control volume, then the total entropy generation rate over the whole computational domain was calculated by integrating them over the entire volume V by:

$$\left(S_{gen}^{T}\right) = \iiint_V \; S_{gen} \, dV \tag{5.29}$$

The Bejan number, presents the irreversibility caused by heat transfer to total entropy generation, is described as:

$$Be = \frac{\left(S_{gen}^{H}\right)}{\left(S_{gen}^{T}\right)} \tag{5.30}$$

The irreversibility of heat transfer is predominant when Be = 1, and the irreversibility of fluid friction is prevailing when Be = 0 as described by Amani et al. [59].

The entropy generation ratio (Ns), presents the total entropy generation of PTSC having conical turbulators to the total entropy generation of smooth PTSC, is described as:

$$Ns = \frac{\left(S_{gen}^{T}\right)_c}{\left(S_{gen}^{T}\right)_0} \tag{5.31}$$

The exergetic effectiveness can be assessed using the pressure losses and the thermal contribution to PTSC produced from the incident solar radiation, which can be calculated by Mwesigye et al. [36]:

$$\eta_{exr} = \frac{Ex_u}{Ex_a} = \frac{\dot{m}C_{p,f}\left[(T_{out}-T_{in})-T_{amb}\ln\left(\frac{T_{out}}{T_{in}}\right)\right]}{A_a\, I_b\left[1+\frac{1}{3}\left(\frac{T_{amb}}{T_s}\right)^4-\frac{4}{3}\left(\frac{T_{amb}}{T_s}\right)\right]} \tag{5.32}$$

Where T_{amb} is the ambient temperature, which is considered 300K in this work, and T_s is the sun's surface temperature, which is considered 5800K in this work.

5.2.5 Numerical Method

All the governing equations are numerically solved with the aid of commercial computational fluid dynamics software (ANSYS-FLUENT). These equations are discretised by using the finite volume method (FVM). The convective terms in momentum and energy equations, the convective terms in equations of turbulence models (k-epsilon and k-Omega SST) and discrete ordinates radiation model are discretised by utilising the second-order upwind scheme. The SIMPLE algorithm is applied for decoupling the velocity and pressure solution. The pressure is discretised by the scheme of PRESTO. The enhanced wall treatment method is implemented with lower values of y+ to ensure capturing the high resolution of gradients in the regions near the tube wall as recommended [53]. The solution is deemed converged when the residual values are less

than 10^{-8} for all other variables.

5.2.6 Grid Sensitivity

In order to justify the accuracy as well as the stability of the numerical results, extensive calculations have been made to determine the total number of grid points that generate array results that will be appropriate to determine the flux and thermal fields. The mesh topology generated for the whole geometry for the PTSC with conical turbulators is shown in Figure 5.4. It is clearly seen that for the CFD simulations of the fluid domain, tetrahedral elements with highly refined grids in the regions near the PTSC inner wall are employed. Whilst, for the CFD simulations of the PTSC tube outer wall, vacuum and glass tube domains, structured hexahedral mesh is employed. Table 5.2 presents the evolution of the average Nusselt number, friction factor, average temperature and maximum temperature of the PTSC's tube inner wall at Re number of 10^4 and an inlet temperature of 400K. It appears from the results that the grid model 2 of 702791elements is adequately dense and is adopted in the current study because the maximum deviation was less than 1% for all tested parameters, which means that the number of grids does not influence the results, but the solution takes more time for converging.

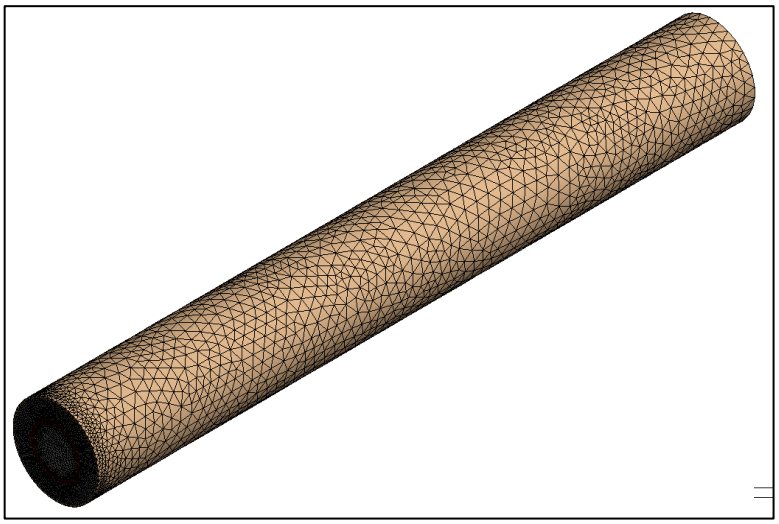

(a)

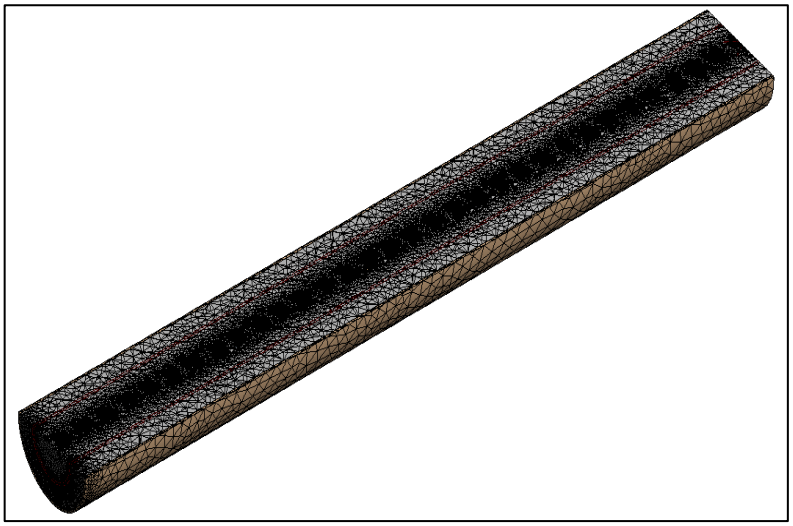

(b)

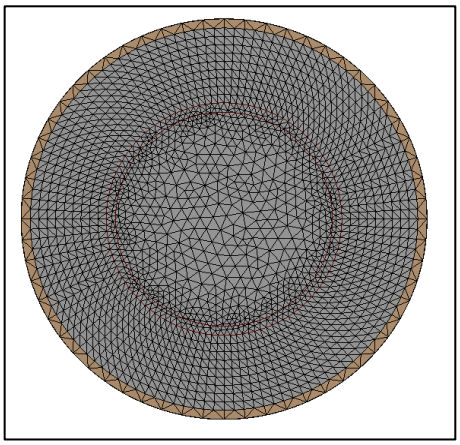

(c)

Figure 5.4 The mesh topology for a PTSC tube equipped with conical turbulators, (a) Full geometry, (b) Lateral view, (c) Cross-sectional view.

Table 5.2 Mesh checking test for Re=10^4 and inlet temperature of 400 K.

Grid model	***Grid number***	**Nu number**	**Friction factor**	**$T_{w,\,ave}$ (°C)**	**$T_{w,\,max}$ (°C)**
1	483912	220.123	0.302134	257.613	363.67
2	702791	222.754	0.305713	258.719	362.15
3	1250856	222.984	0.309237	258.035	361.03

5.2.7 Model Validation

The model's results were verified in terms of average Nusselt number and friction factor with the available correlations data [57] and it shows same pattern with a maximum deviation of less than 5.1% as shown in Figures 5.5-5.6.

Correlation of Dittus-Boelter is:

$$Nu = 0.023\, Re^{0.8} Pr^{0.4} \tag{5.33}$$

Correlation of Filoneko is:

$$f = (1.82 \log_{10} Re - 1.64)^{-2} \tag{5.34}$$

Correlations of Gnielinski and Petukhov are given as:

$$Nu = \frac{f/8(Re-1000)Pr}{1.07+12.7(f/8)^{1/2}(Pr^{2/3}-1)} \tag{5.35}$$

$$f = (0.79 \log_{10} Re - 1.64)^{-2} \tag{5.36}$$

Figures 5.5-5.6 show that the average Nusselt number and friction factor results are within the acceptable ranges with a deviation of 3.2% and 1.82% respectively for smooth tubes. The results are also compared using different turbulent models (k-epsilon and k-Omega SST) as presented in Figure 5.5. The results revealed that the estimations by using k-Omega SST model are much better than the k-epsilon model as it matched well with the experimental correlations with a maximum deviation of 4.1% and 5.3% for Nusselt number and friction factor, respectively.

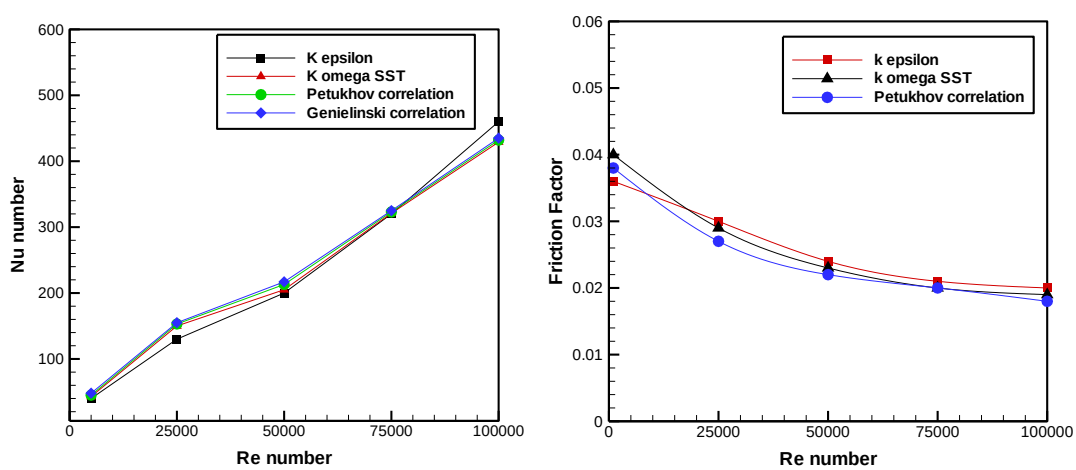

(a) (b)

Figure 5.5 Comparison of the present results with the available empirical correlations data, (a) Nusselt number, (b) Friction factor.

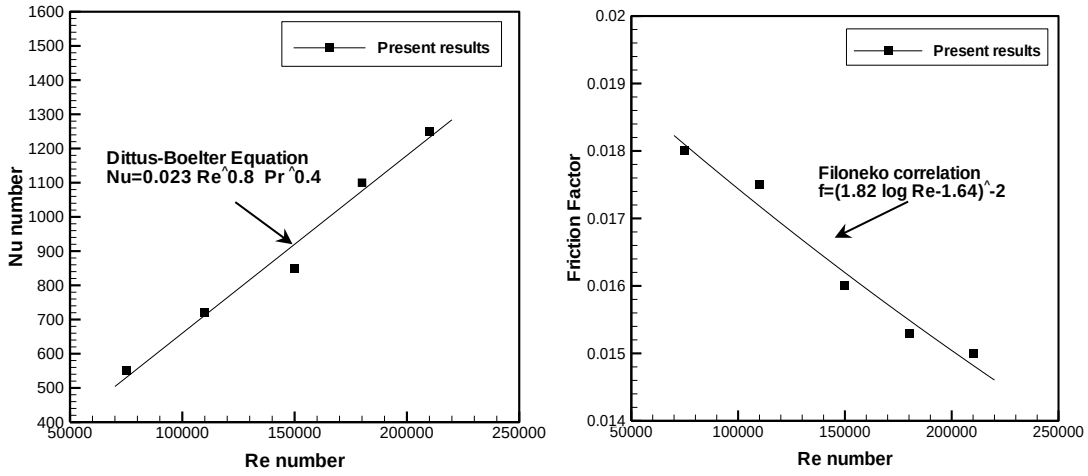

(a) (b)

Figure 5.6 Comparison of the present results with the available empirical correlations data, (a) Nusselt number, (b) Friction factor.

Figure 5.7 shows the comparison of the present numerical results with the experimental data of Amina et al. [59] of a receiver tube with longitudinal fins inserts. The results show a good agreement between the two studies with relative deviations of 2.4% for Nusselt number ratios and 4.6% for friction factor ratios. In addition, the temperature difference and the thermal efficiency of a smooth receiver are compared with the experimental data of Dudley [60] to verify the calculations of the present numerical model as shown in Table 5.3. It is noticed that a good agreement was also obtained with deviations less than ±3.2% for the temperature difference and ±1.2% for the thermal efficiency. Therefore, the current numerical model is valid and provides reliable results.

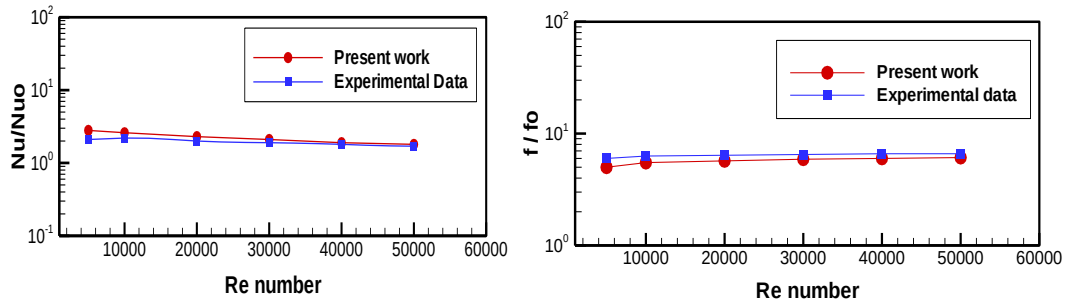

(a) (b)

Figure 5.7 Comparison of the present results with the available experimental data of Amina et al. [59] (a) Nu/Nu_o, (b) f/f_o.

Table 5.3 Comparison of temperature difference and thermal efficiency of the present work with Dudley's results [60].

Case number	**1**	**2**	**3**	**4**
DNI (W/m^2)	880.6	903.2	933.7	982.3
Wind speed (m/s)	2.9	4.2	2.6	2.5
Air temperature (°C)	27.5	31.1	21.2	24.3
Flow rate (L/min)	55.6	56.3	47.7	49.1
T_{inlet} (°C)	299	355.9	102.2	197.5
ΔT (°C) (Experiments)	18.2	18.5	21.8	22.02
ΔT (°C) (Present work)	**17.92**	**18.4**	**21.6**	**22.32**
Thermal Efficiency (Experiments)	68.92	63.83	72.51	70.17
Thermal Efficiency (Present work)	**67.66**	**64.53**	**71.32**	**70.29**

5.2.8 Base-fluid and Hybrid Nanofluids Thermophysical Properties

The working medium utilised in this study as a base fluid was Syltherm800 [61]. Three nanoparticle kinds were suspended in the base fluid (Ag-MgO, Ag-SWCNT, and Ag-MWCNT) having a mixing ratio of (50:50). The effective properties of the resultant hybrid nanofluid (Ag-MgO/ Syltherm800, Ag-SWCNT/ Syltherm800, and Ag-MWCNT/ Syltherm 800) mixture substantially rely upon the properties of the individual component of the mixture. In this work, carbon nanotubes have been chosen because they possess extraordinary thermal and physical characteristics and widespread in optics, nanotechnology, electronics and other applications relevant to material science. These classified as single (SWCNTs) and multi-walled carbon nanotubes (MWCNTs). Their composition is of huge interest due to its unique thermal and mechanical characteristics. Accordingly, based on the available literature, any nanoparticle has higher thermal conductivity, would have higher thermal performance. For instance, SWCNTs and MWCNTs have remarkably higher thermal conductivities than other nanoparticles and they are supposed to provide higher thermal properties and thus higher thermal effectiveness. In this work, the Syltherm800 oil thermo-physical properties are considered

temperature-dependent using polynomials equations [61]. The relevant equations are presented in Table 5.4 for dynamic viscosity, thermal conductivity, specific heat capacity, and density. Table 5.5 shows the thermophysical properties values of Syltherm-800 and different nanoparticles used in this study.

Table 5.4 Thermophysical properties equations of Syltherm-800 [61].

Properties	$a + bT + cT^2 + dT^3 + eT^4$				
	a	**b**	**c**	**d**	**e**
Dynamic Viscosity, Pa.s	8.4866×10^{-2}	-5.5412×10^{-4}	1.3882×10^{-6}	-1.5660×10^{-9}	6.672×10^{-13}
Thermal conductivity, W/m.K	1.9002×10^{-1}	-1.8752×10^{-4}	-5.7534×10^{-10}	—	—
Specific heat capacity, J/kg.K	1.1078×10^{3}	1.7080	—	—	—
Density, kg/m^3	1.1057×10^{3}	-4.1535×10^{-1}	-6.0616×10^{-4}	—	—

Table 5.5 Properties of Syltherm-800 and different nanoparticles used in this study [62], [63], [64], [65].

Materials	***ρ (kg/m³)***	***κ (W/m.K)***	***μ (Pa.s)***	***C_p (J/kg.K)***
Syltherm-800	747.2	0.0961	0.00084	1962
Ag	10500	426.77	—	236
MgO	3580	69.036	—	921
SWCNT	2600	6600	—	425
MWCNT	1600	3000	—	796

The effective density (ρ_{nf}) and specific heat ($C_{P_{nf}}$) of the nanofluid at the reference temperature (T_{in}) are determined by utilising the following equations [66], [67]:

Density of single nanofluid is estimated using the following equation:

$$\rho_{eff} = (1-\phi)\rho_f + \phi\rho_{hnp} \tag{5.37}$$

Heat capacity of single nanofluid is estimated using the following equation:

$$(\rho C_p)_{eff} = \left[(1-\phi)(\rho C_p)_f + \phi(\rho C_p)_{hnp}\right] \tag{5.38}$$

The effective thermal conductivity for Ag-MgO is estimated using the following equation [68], which is valid for $0 \leq \phi \leq 3\%$

$$k_{eff} = k_f \left[\frac{0.1747 \times 10^5 + \phi}{0.1747 \times 10^5 - 0.1498 \times 10^6\phi + 0.1117 \times 10^7\phi^2 + 0.1997 \times 10^8\phi^3}\right] \tag{5.39}$$

The thermal conductivity of carbon nanotubes is calculated using the following equations which are based on the accurate model developed and validated by [69] and [70]:

$$\frac{k_{eff}}{k_f} = \frac{3+\phi\beta_x+\beta_z}{3-\phi\beta_x} \tag{5.40}$$

Where $\beta_x = \frac{2\,(k_{11}^c - k_f)}{k_{11}^c + k_f}$ (5.41)

$$\beta_z = \frac{k_{33}^c}{k_f - 1} \tag{5.42}$$

In Eqs. (5.40-5.42), ϕ is the volume fraction, k_{11}^c and k_{33}^c portray the equivalent thermal conductivities along the transverse and longitudinal axes of a composite unit cell, respectively. These terms are expressed as follows:

$$k_{11}^c = \frac{k_c}{1+\frac{2\,a_k k_c}{d_{CNT} k_f}} \tag{5.43}$$

$$k_{33}^c = \frac{k_c}{1+\frac{2\,a_k\,k_c}{L_{CNT} k_f}} \tag{5.44}$$

In Eqs. (5.43-5.44), d_{CNT}, L_{CNT}, k_c, k_f, a_k, and R_K are the diameter of nanotubes, length of the nanotubes, the thermal conductivity of nanotubes and the thermal conductivity of the base fluid, constant, the interface thermal resistance (R_K = 8×10^{-8} m^2.K/W), respectively, [69] and [70].

$$a_k = R_K\, k_f \tag{5.45}$$

The effective dynamic viscosity for Ag-MgO is estimated using the following equation [68], which is valid for $0 \leq \phi \leq 2\%$

$$\mu_{eff} = \mu_f\left(1 + 32.795\,\phi - 7214\,\phi^2 + 714600\,\phi^3 - 0.1941 \times 10^8 \phi^4\right) \tag{5.46}$$

The effective dynamic viscosity for SWCNT and MWCNT is calculated by using the following expression [71]:

$$\mu_{eff} = \frac{\mu_f}{(1-34.87\,(d_{hnp}/d_f)^{-0.3}\,\phi^{1.03})} \tag{5.47}$$

The equivalent diameter of the base fluid is estimated by:

$$d_f = \left[\frac{6\,M}{N\,\pi\,\rho_f}\right]^{1/3} \tag{5.48}$$

The ϕ, ρ_{hnp}, $C_{p_{hnp}}$, and k_{hnp} for hybrid nanofluids are obtained from the following equations [72]:

$$\phi = \phi_{p1} + \phi_{p2} \tag{5.49}$$

$$\rho_{hnp} = \frac{\rho_{p1}\phi_{p1} + \rho_{p2}\phi_{p2}}{\phi} \tag{5.50}$$

$$C_{p_{hnp}} = \frac{C_{p_{p1}}\phi_{p1} + C_{p_{p2}}\phi_{p2}}{\phi} \tag{5.51}$$

$$k_{hnp} = \frac{k_{p1}\phi_{p1} + k_{p2}\phi_{p2}}{\phi} \tag{5.52}$$

5.3 Results and Discussion

The impacts of nanofluids type, nanoparticles concentration, fluid inlet temperature and Reynolds number in the range of 5000 to 100000 were studied for nanoparticle diameter of 50 nm with spherical shape for all cases examined. The results of the thermohydraulic assessment, entropy reduction and exergetic efficiency of PTSC equipped with conical turbulators are analysed and interpreted in this section.

5.3.1 Thermal Assessment

The heat transfer assessment has been conducted in this subsection for various hybrid nanofluid types, different fluid inlet temperatures and different nanoparticle concentrations. This is performed because the properties of the working fluid (hybrid

nanofluid in this case) have strong dependence on temperature, and accordingly the fluid inlet temperature has a remarkable impact on the thermal and hydraulic performance. Figure 5.8(a)-(c) shows the absorber's tube outlet temperature distribution versus Re number for different hybrid nanofluid types, different fluid inlet temperatures and different nanoparticle concentrations, respectively. It can also be observed from Figure 5.8(a) that the Syltherm oil has the highest outlet temperature of the absorber's tube. Whilst, the hybrid nanofluid of Ag-SWCNT has the lowest outlet temperature, because of its exceptional thermophysical properties which makes it very promising coolant in PTSC frameworks. This is followed by Ag-MWCNT and then Ag-MgO, which have moderate

temperature variation. Figure 5.8(b) displays that the outlet temperature of the absorber's tube was highest at an inlet temperature of 650K, while it has the lowest values at an inlet temperature of 400K. Figure 5.8(c) shows that the outlet temperature of the absorber's tube diminishes with the increment of the nanoparticle concentration. The results revealed that the Syltherm oil with (ϕ=0%) has the highest outlet temperature, while the hybrid nanofluid of Ag-SWCNT with (ϕ=2%) has the lowest outlet temperature, which makes it an alternative coolant in PTSC frameworks. These results can be interpreted as follows: the conical turbulators direct the cold fluid in the absorbers' tube core region to encroach the inner wall of the absorber tube that has the high-heat flux region to take away the heat from the tube's wall drastically. Consequently, remarkable decrease in the absorber's outlet temperatures can be achieved particularly at low Re numbers. It is worth noting that the absorber's outlet temperatures are decreased by approximately 36-210K for all the cases examined in this work.

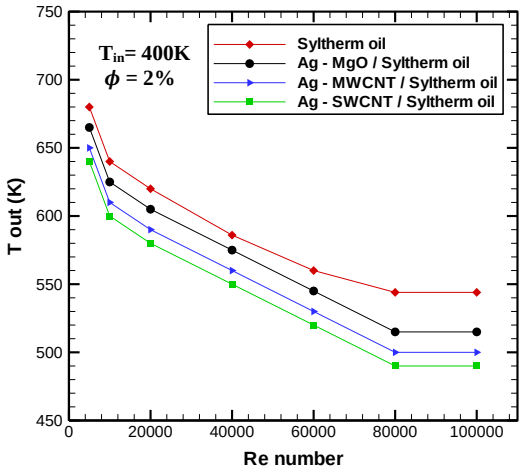

(a)

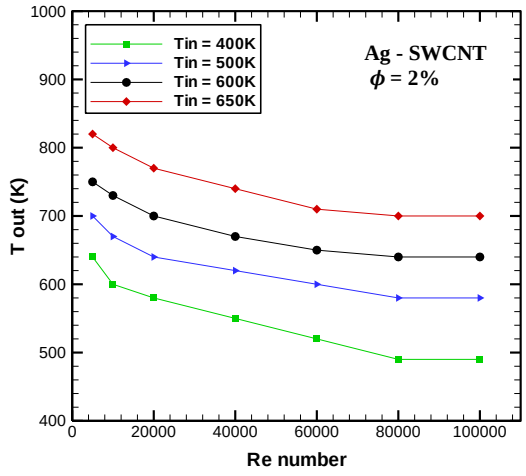

(b)

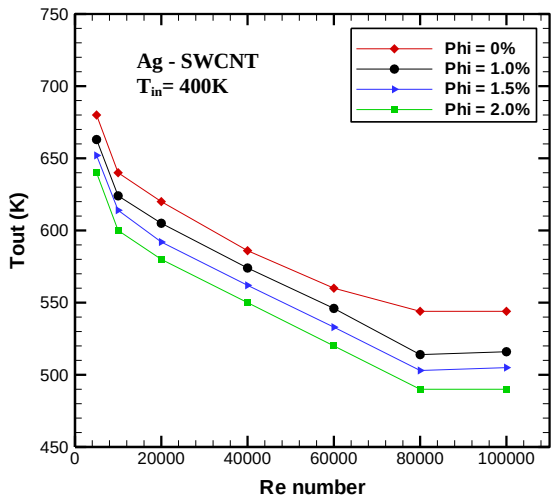

(c)

Figure 5.8 The absorber's tube outlet temperature variation versus Re number for various, (a) hybrid nanofluid types, (b) inlet fluid temperatures, (c) nanoparticle concentrations.

The absorber's tube temperature gradient versus Re number for various hybrid nanofluid types, various inlet fluid temperatures, and various nanoparticle concentrations is presented in Figure 5.9(a)-(c). It can be noticed that the absorber's tube temperature gradient follows the outlet temperature pattern as presented in Figure 5.8. Figure 5.9(a)-(c) portrays that the Syltherm oil, fluid inlet temperature of 650K and nanoparticle concentration of (ϕ=0%) have the highest values. While, the hybrid nanofluid of Ag-SWCNT, fluid inlet temperature of 400K and nanoparticle concentration of (ϕ=2%) have the lowest values. These results can be interpreted as follows: the conical turbulators direct the cold fluid in the absorbers' tube core region to encroach the inner wall of the absorber tube that has the high-heat flux region to take away the heat from the tube's wall drastically. Consequently, remarkable decrease in the absorber's tube temperature gradient can be achieved particularly at low Re numbers. It is worth noting that the absorber's tube temperature gradients are reduced by 30-170K for all cases examined.

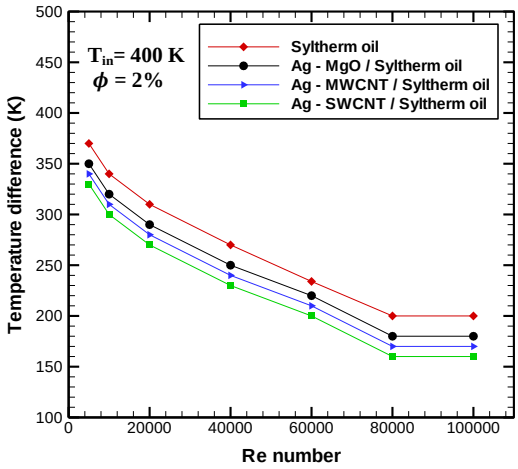

(a)

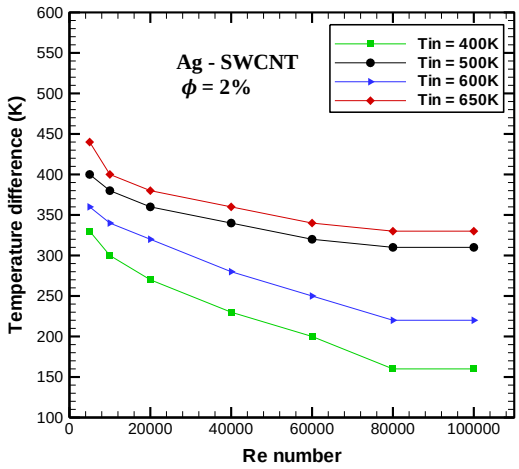

(b)

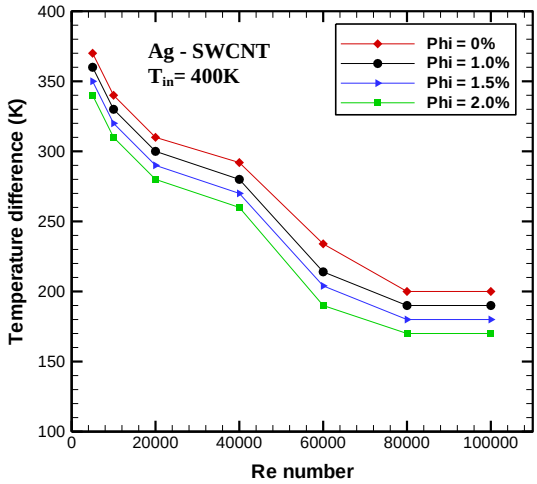

(c)

Figure 5.9 The absorber's tube temperature gradient versus Re number for various, (a) hybrid nanofluid types, (b) inlet fluid temperatures, (c) nanoparticle concentrations.

The isotherms (temperature contours) at the absorber's outlet for various hybrid nanofluid types at different nanoparticle concentrations and Re numbers are shown in Figure 5.10. It is noticed that the temperature profile of Syltherm oil displays the highest values compared to other hybrid nanofluid types, which show the lowest. The isotherms also reveal that the temperature profile of the fluid and the absorber's wall becomes uniform when the Re number and nanoparticle concentration increase. The results show

that Ag-SWCNT/Syltherm oil hybrid nanofluid exhibits the lowest temperature distribution which makes it a good alterative working fluid in terms of reducing the deformation of the absorber tube.

Syltherm Oil (ϕ = 0%)		 Re = 20000 Re = 100000	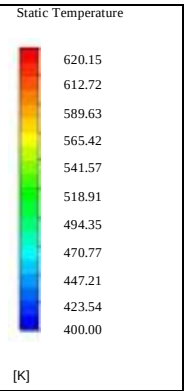
Ag – MgO / Syltherm oil	**(ϕ = 1.0%)**	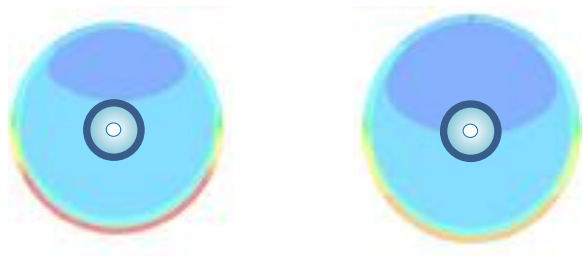 Re = 20000 Re = 100000	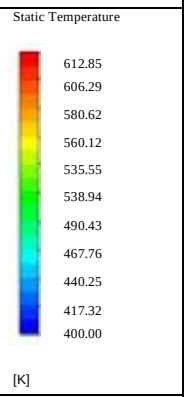
	(ϕ = 2.0%)	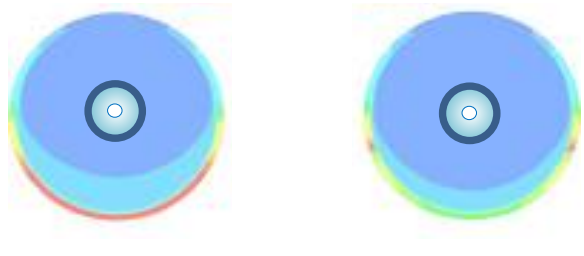 Re = 20000 Re = 100000	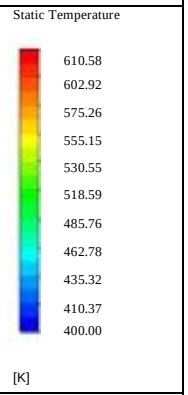
Ag – MWCNT/ Syltherm oil	**(ϕ = 1.0%)**	 Re = 20000 Re = 100000	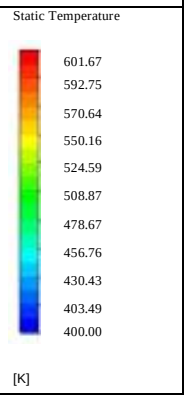

	(ϕ = 2.0%)		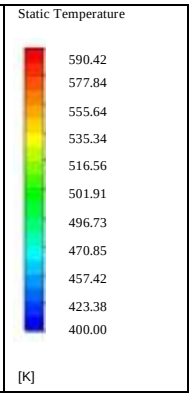
Ag – SWCNT/ Syltherm oil	**(ϕ = 1.0%)**	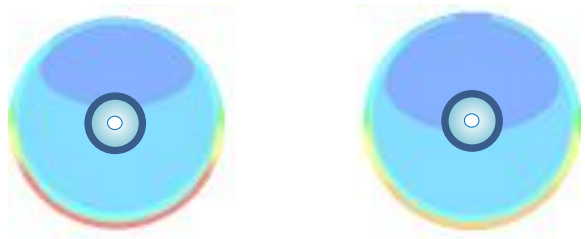	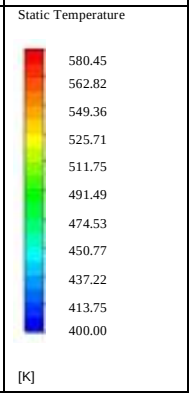
	(ϕ = 2.0%)		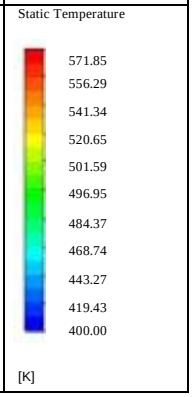

Figure 5.10 The temperature contours (isotherms) at the absorber's outlet for various hybrid nanofluid types at various nanoparticle concentrations and Re numbers.

The average Nusselt number profile versus Re number for various hybrid nanofluid types, various inlet fluid temperatures, and various nanoparticle concentrations is plotted in Figure 5.11(a)-(c). The outcomes reveal that all hybrid nanofluids types produce higher average Nusselt number values when Re number increases because of the high forced convection domination on the heat transfer process. It is clear from Figure 5.11(a) that the

nanofluid with Ag-SWCNT/Syltherm oil hybrid nanofluid has the highest average Nusselt number, followed by Ag-MWCNT/Syltherm oil, Ag-MgO/Syltherm oil, and pure Syltherm oil, respectively. This is because of Ag-SWCNT hybrid nanofluid has the highest thermal conductivity and lowest density (i.e. highest average velocity), which both contributed to its high thermal performance compared to other hybrid nanofluids. Figure 5.11(b)-(c) reveal that the fluid inlet temperature of 650K and nanoparticle concentration of (ϕ=2%) have the highest Nusselt number values. While, the fluid inlet temperature of 400K and nanoparticle concentration of (ϕ=0%) have the lowest values. This is anticipated as at higher fluid inlet temperatures, the hybrid nanofluid is less dense and less viscous and thus it can move the heat energy more viably. Furthermore, the Nusselt number is enhanced as the nanoparticle volume fraction and Re number increase. This is mainly due to the increased thermal conductivity of the resulting hybrid nanofluid even at low concentrations [69]. It is worth noting that the Nusselt number improvement is in the range of 8.2-233.4% for all the parameters and for all cases examined in this work.

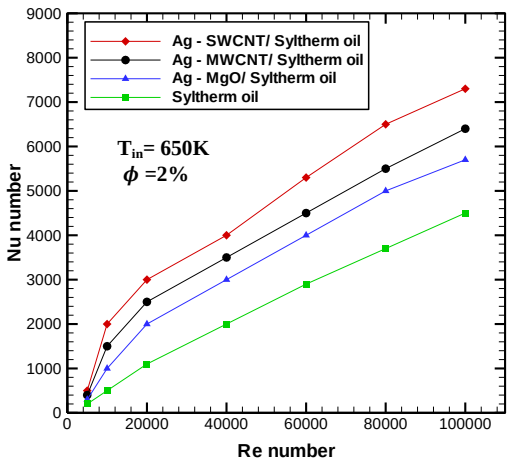

(a)

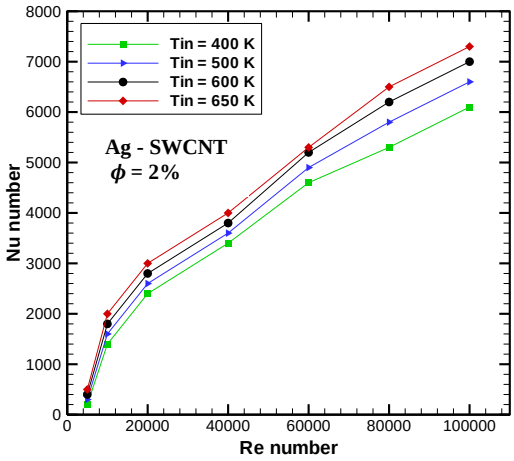

(b)

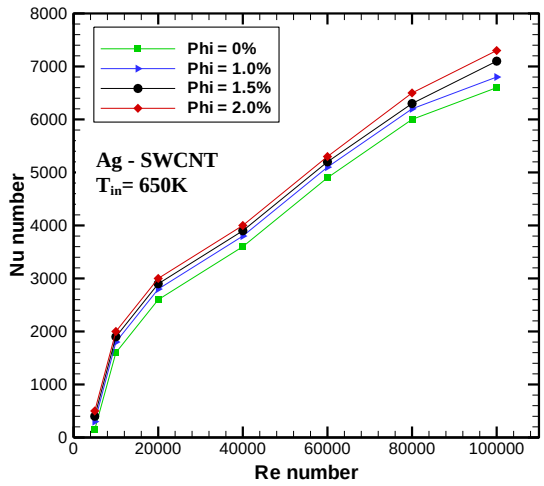

(c)

Figure 5.11 The Nu number variation versus Re number for various, (a) hybrid nanofluid types, (b) inlet fluid temperatures, (c) nanoparticle concentrations.

5.3.2 Hydraulic Assessment

The variation of the friction factor for various hybrid nanofluid types, various inlet fluid temperatures, and various nanoparticle concentrations is plotted in Figure 5.12(a)-(c). It is observed that the friction factor rises with the increment of Re number and nanoparticle volume fraction. The results indicate that all hybrid nanofluids types provide higher friction factor values when Re number increases because of the increased viscosity and density of the resulting hybrid nanofluids. It is found from Figure 5.12(a) that at T_{in}=650K and ϕ=2% the hybrid nanofluid with Ag-MgO nanoparticles has the lowest friction factor, followed by Ag-MWCNT, and Ag-SWCNT respectively while pure Syltherm oil shows the lest values compared to all hybrid nanofluid types. This is because of the highest viscosity effect of all hybrid nanofluid and lowest density (i.e. highest average velocity) compared to Syltherm oil, which both contributed to the high-pressure drop penalty. Figure 5.11(b)-(c) reveal that the fluid inlet temperature of 400K and nanoparticle concentration of (ϕ=2%) have the highest friction factor values while the fluid inlet temperature of 400K and nanoparticle concentration of (ϕ=0%) have the lowest values. It should be mentioned that the conical turbulators make disturbance in the fluid, which causes a remarkable boost in the flow resistance contrasted to the plain PTSC. It is

worth noting that the friction factor increase is about 9.1-31.4% for all the parameters examined in this work. The results of the friction factor together with Nusselt number results need to be studied further by calculating the thermal performance evaluation criterion, to identify the thermal enhancement percentage using hybrid nanofluids and conical turbulators, which will be presented in the next subsection.

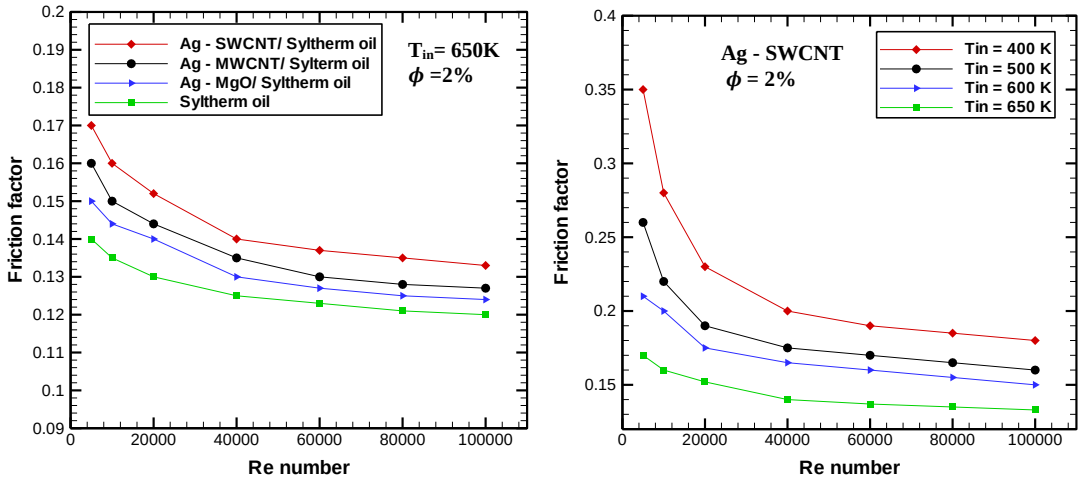

(a) (b)

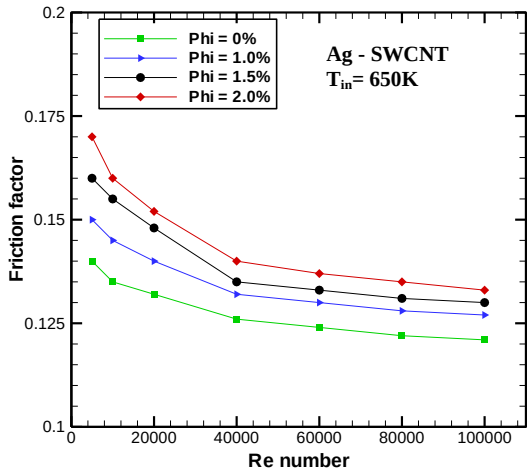

(c)

Figure 5.12 The friction factor variation versus Re number for various, (a) hybrid nanofluid types, (b) inlet fluid temperatures, (c) nanoparticle concentrations.

The variation of the pumping power for various hybrid nanofluid types, various inlet fluid temperatures, and various nanoparticle concentrations is plotted in Figure 5.13(a)-(c). It is observed that the pumping power demand increases with the increment of Re number and nanoparticle volume fraction as well as with the decrease of inlet fluid temperature. The outcomes indicate that all hybrid nanofluids types provide higher pumping work demand values compared to base fluid (Syltherm oil) because of the increased viscosities and densities of these hybrid nanofluids. It is found from Figure 5.13(a) that at T_{in}=650K and ϕ=2% the hybrid nanofluid with Ag-MgO nanoparticles has the highest pumping power, followed by Ag-SWCNT, and Ag-MWCNT respectively while pure Syltherm oil shows the least values compared to other hybrid nanofluid types. Figure 5.13(b)-(c) reveal that the fluid inlet temperature of 650K and nanoparticle concentration of (ϕ=0%) have the lowest pumping power. This shows that the pumping demand work is minimum at higher inlet fluid temperature at a given Re number. This is typically genuine at specific mass flow rates and specific Re numbers. This case is anticipated, as at lower temperatures, the hybrid nanofluid becomes denser and more viscous which demands substantial amount of power to transport inside the receiver tube. For instance, the pumping power rose up to approximately 23.4-35.4% as the nanoparticle concentration increased from 1-2%.

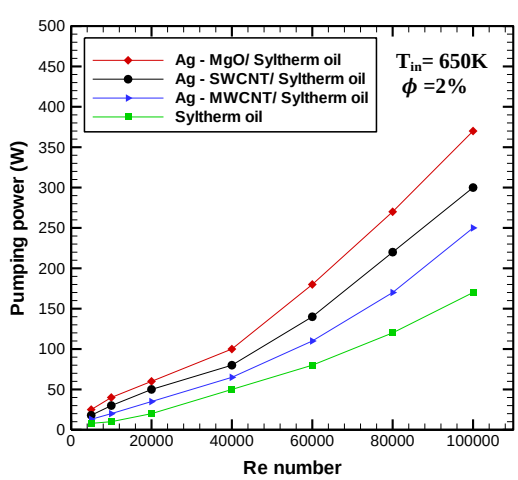

(a)

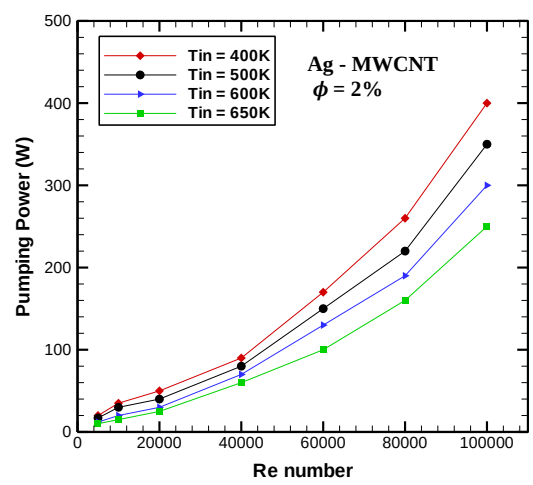

(b)

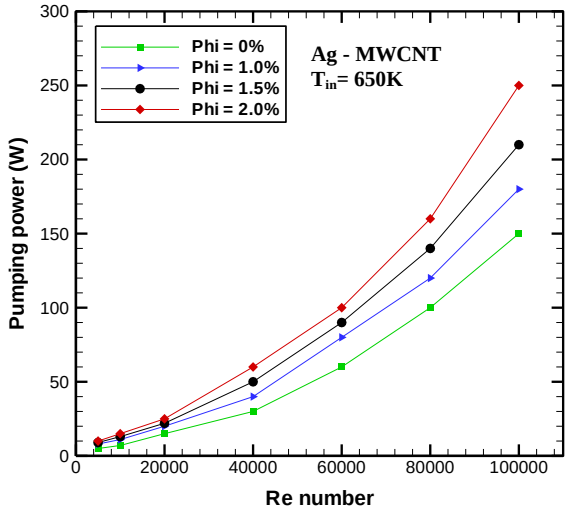

(c)

Figure 5.13 The pumping power variation versus Re number for various, (a) hybrid nanofluid types, (b) inlet fluid temperatures, (c) nanoparticle concentrations.

5.3.3 Thermohydraulic Assessment

The PEC used to evaluate the heat transfer enhancement at similar pumping work demand for different hybrid nanofluids flowing through a PTSC tube having conical turbulators is depicted in Figure 5.14(a)-(c). The PEC values calculated for PTSC tube with and without nanofluids called (PEC1) and its values calculated for PTSC tube equipped with and without conical turbulators is called (PEC2). It was mentioned in the previous sections that hybrid nanofluids augment the thermal and flow fields. Thus, the PEC values need to be estimated to assess which one is dominant on the thermal process either the heat transfer or the pressure drop penalty. Figure 5.14(a) indicates that at T_{in}=650K and ϕ=2% all hybrid nanofluids provides higher PEC values at lower Re numbers and it decreases gradually as Re number rises. This is because of the substantial decrement in the heat losses at low Re numbers. The results revealed that hybrid nanofluid of Ag-SWCNT provides the highest PEC value in the range of 0.9-1.82 followed by Ag-MWCNT and Ag-MgO respectively. It is noticed that the PEC decreases as the inlet fluid temperature increases as shown in Figure 5.14(b). The PEC is observed to rise with the increment of

the nanoparticle volume fraction as shown in Figure 5.14(c). For example, the increase in PEC value at Re = 40000 for 1%, 1.5% and 2% nanoparticle volume fraction of Ag-SWCNT hybrid nanofluid is 7.5%, 13.1% and 16.7%, respectively.

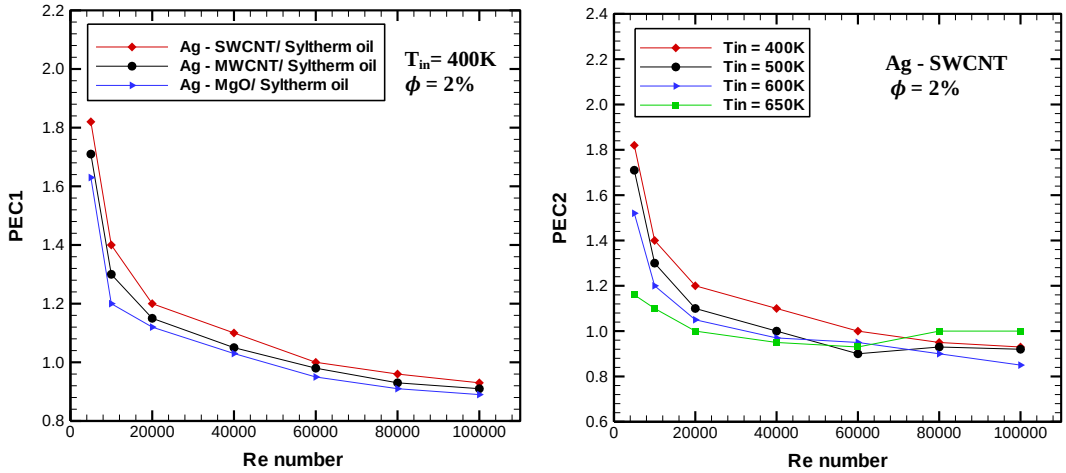

(a)

(b)

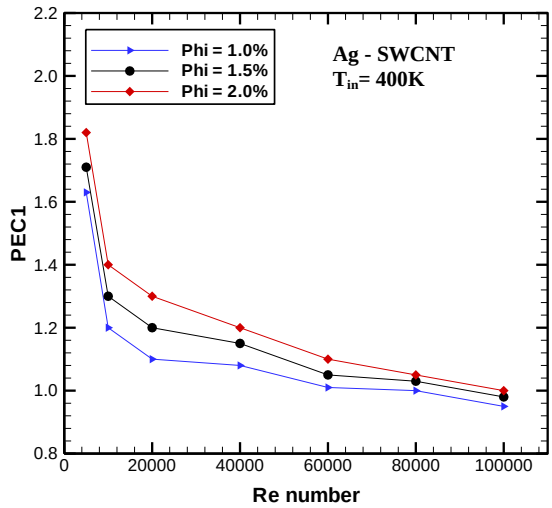

(c)

Figure 5.14 The performance criterion evaluation variation versus Re number for various, (a) hybrid nanofluid types, (b) inlet fluid temperatures, (c) nanoparticle concentrations.

The PTSC's thermal efficiency deems the performance augmentation due to the enhanced heat transfer at the penalty of thermal losses and pumping work demand. Figure 5.15(a)-(c) shows the thermal efficiency versus Re number for various hybrid nanofluid types, various inlet fluid temperatures, and various nanoparticle concentrations. It is generally observed that thermal efficiency rises up to a specific value and then it starts to diminish with the increase of Re number. This is due to the increment of pumping power as Re number increases which gets remarkably higher than the useful heat gain. Additionally, it is due to the decrement in the absorber's tube temperature with thermal augmentation and consequently the decrement of absorber's thermal losses as reported by Mwesigye et al. [27]. It is found from Figure 5.15(a) that the highest thermal efficiency is prevailed for hybrid nanofluid of Ag-SWCNT and the lowest was for hybrid nanofluid of Ag-MgO. For instance, hybrid nanofluid of Ag-SWCNT/Syltherm oil is increased the thermal efficiency up to 11.5% with reasonable friction factor as shown in Figure 5.15(a). This indicates that this hybrid nanofluid can be utilised and to be the best-suited working fluid among other fluids examined in this study in PTSC frameworks. The thermal efficiency variation with different inlet fluid temperatures at a specific volume fraction of 2% is plotted in Figure 5.15(b). It is noticed that the thermal efficiency has higher values at low inlet fluid temperatures because of the low absorber's temperature and thus lower thermal losses. It is worth noting that rising the inlet fluid temperature refers to higher absorber's tube temperature, which increases the thermal losses of the absorber's tube, because of the radiation mode, which occurs from the high temperature medium (absorber's tube) to the low temperature medium (the surroundings). Besides that, as the hybrid nanofluid is dense and more viscous at low temperatures, the thermal efficiency rises to a highest value and then it starts to diminish due to the boosted pumping work demand as Re number increases. The thermal efficiency rises as the nanoparticle volume fraction rises as shown in Figure 5.15(c). For example, if hybrid nanofluid of Ag-SWCNT is to be used at Re= 60000 with 1%, 1.5% and 2% nanoparticle concentration instead of base fluid (Syltherm oil in this case), there would be an increment in the thermal efficiency of 3.2%, 4.7% and 6.2%, respectively.

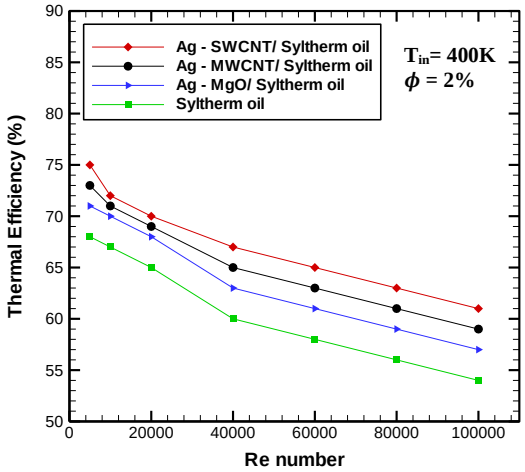

(a)

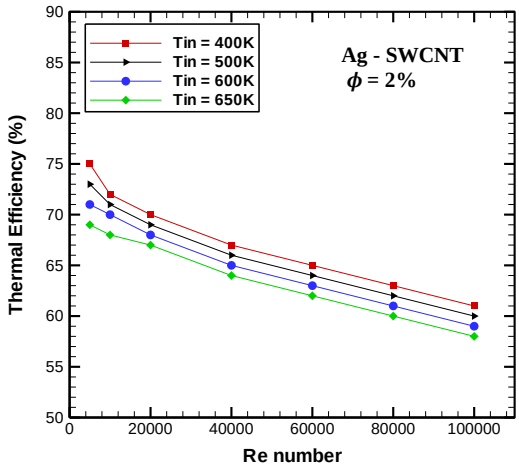

(b)

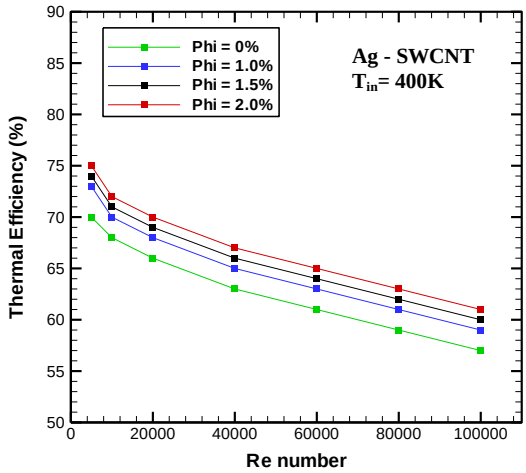

(c)

Figure 5.15 The Thermal efficiency variation versus Re number for various, (a) hybrid nanofluid types, (b) inlet fluid temperatures, (c) nanoparticle concentrations.

5.3.4 Entropy Generation and Exergetic Efficiency

The thermodynamic effectiveness of the conical turbulators is evaluated by conducting entropy and exergetic analyses. The estimation of how much entropy being generated in thermal management frameworks such as PTSCs and the attempts of reducing the thermal and flow irreversibilities are effective methods of enhancing the thermodynamic effectiveness of these frameworks. In addition, the exergetic efficiency was evaluated as

an indication of the exergetic performance and its results will be discussed and interpreted at the end of this section.

The entropy generation rate distribution because of heat transfer, fluid friction and the total entropy generation rate versus Re number for various hybrid nanofluid types at T_{in}=650K and ϕ=2% are plotted in Figure 5.16(a)-(c). It is noticed from Figure 5.16(a) that the entropy generation because of heat transfer (S_{gen}^{H}) decreases as Re number increases and becomes relatively steady. While, it shows that opposite pattern for the entropy generation because of fluid friction (S_{gen}^{F}) as shown in Figure 5.16(b). The outcomes illustrated in Figure 5.16(c) reveal that the total entropy generation rate (S_{gen}^{T}) decreases as Re numbers increases and then it increases at higher Re number. This implies that, at lower Re number, the entropy generation because of heat transfer dominates the irreversibility source. Besides that, at high Re numbers, the entropy generated because of heat transfer decreases and the entropy generated because of fluid friction significantly rises and ultimately dominates the irreversibility source. It is observed from Figure 5.16(a)-(c) that the hybrid nanofluid of Ag-SWCNT has the lowest value of (S_{gen}^{H}), (S_{gen}^{F}) and (S_{gen}^{T}) compared to other hybrid nanofluids considered in this study. While, the base fluid (Syltherm oil) exhibits the highest value of (S_{gen}^{H}), (S_{gen}^{F}) and (S_{gen}^{T}). It is important to highlight that the maximum reduction of the total entropy generation rate obtained in this work for different hybrid nanofluid types is about 43.8%.

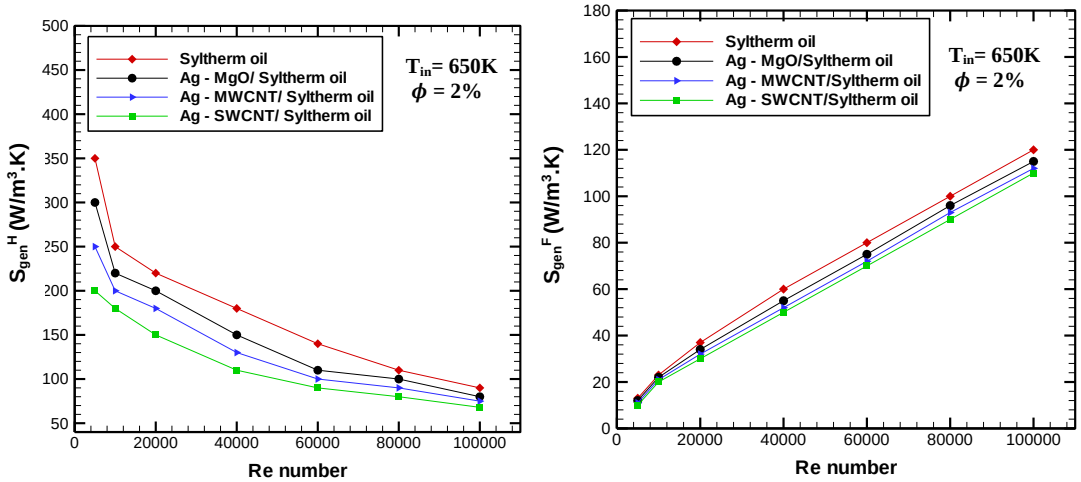

(a) (b)

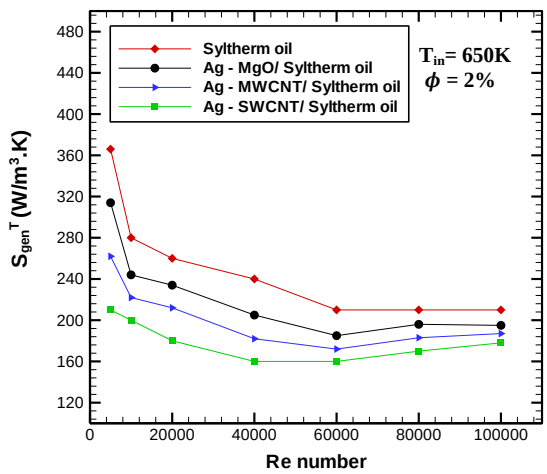

(c)

Figure 5.16 The entropy generation rate variation versus Re number for various hybrid nanofluid types, (a) entropy generation because of heat transfer, (b) entropy generation because of fluid friction, (c) total entropy generation.

The variation of (S_{gen}^{H}), (S_{gen}^{F}) and (S_{gen}^{T}) versus Re number for various inlet fluid temperatures for Ag-SWCNT hybrid nanofluid and ϕ=2% is plotted in Figure 5.17(a)-(c). It can be seen from Figure 5.17 that the (S_{gen}^{H}), and (S_{gen}^{T}) have the same patterns as mentioned in the previous section where both decrease as Re number increases and become approximately steady. While, the (S_{gen}^{F}) shows that opposite pattern as it increases as Re number increases. The results shown in Figure 5.17(a)-(c) reveal that higher (S_{gen}^{T}) rates are anticipated at low inlet fluid temperatures. This implies that, at low inlet fluid temperature, the thermal performance is low which leads to augment the thermal irreversibilities, and the flow irreversibilities are also higher because of the high viscosity and density of the hybrid nanofluid used. In addition, as the inlet fluid temperature rises, the properties of the hybrid nanofluid would be changed and led to enhanced thermal performance and less fluid friction as the fluid becomes less dense and less viscous (i.e. less fluid friction irreversibilities). It is observed from Figure 5.17(a)-(c) that the hybrid nanofluid of Ag-SWCNT with an inlet fluid temperature of 650K has the lowest value of (S_{gen}^{H}), (S_{gen}^{F}) and (S_{gen}^{T}) compared to an inlet fluid temperature of 400K which exhibits the highest value of (S_{gen}^{H}), (S_{gen}^{F}) and (S_{gen}^{T}). It is paramount to highlight that the

maximum reduction of the total entropy generation rate obtained in this work for different inlet fluid temperatures is about 37.5%.

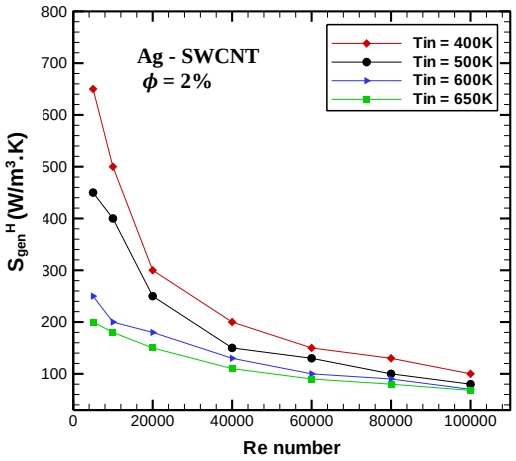

(a)

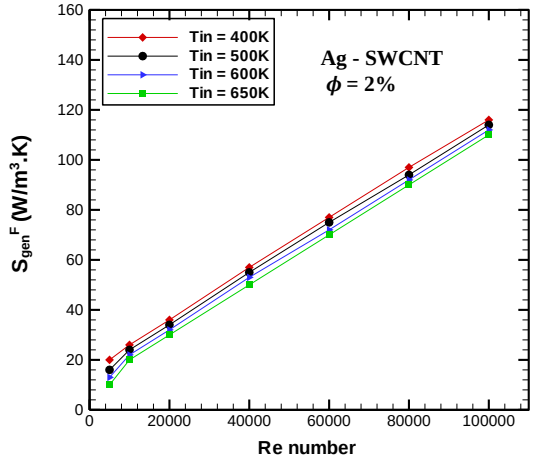

(b)

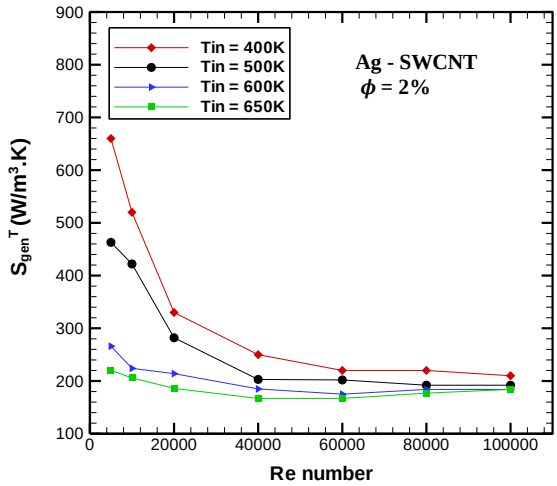

(c)

Figure 5.17 The entropy generation rate variation versus Re number for various inlet fluid temperatures, (a) entropy generation because of heat transfer, (b) entropy generation because of fluid friction, (c) total entropy generation.

The variation of (S_{gen}^{H}), (S_{gen}^{F}) and (S_{gen}^{T}) versus Re number for various nanoparticle volume fractions of Ag-SWCNT hybrid nanofluid at T_{in}=650K is plotted in Figure 5.18(a)-(c). It can be seen from Figure 5.18 that the (S_{gen}^{H}), (S_{gen}^{F}) and (S_{gen}^{T}) follow the same trend as previously mentioned. It is observed that (S_{gen}^{H}), (S_{gen}^{F}) and

(S_{gen}^{T}) show significant decrease as the nanoparticle concentration rises at a specific Re number. This is because of the decreased thermal irreversibility and increased flow irreversibility as Re number and nanoparticle volume fraction increase. It is observed from Figure 5.18(a)-(c) that the hybrid nanofluid of Ag-SWCNT with volume fraction of 2% has the lowest value of (S_{gen}^{H}), (S_{gen}^{F}) and (S_{gen}^{T}) compared with other volume fractions considered in this study. While, the base fluid (Syltherm oil) with volume fraction of 0% exhibits the highest value of (S_{gen}^{H}), (S_{gen}^{F}) and (S_{gen}^{T}). It is worthy to highlight that the maximum reduction of the total entropy generation rate obtained in this work for different nanoparticle volume fractions is about 42.7%. This is anticipated as the thermal effectiveness was much greater and thus remarkably diminished the finite temperature differences. Remarkable minimization in the total entropy generation rate is obtainable at lower Re number values of less than 65000.

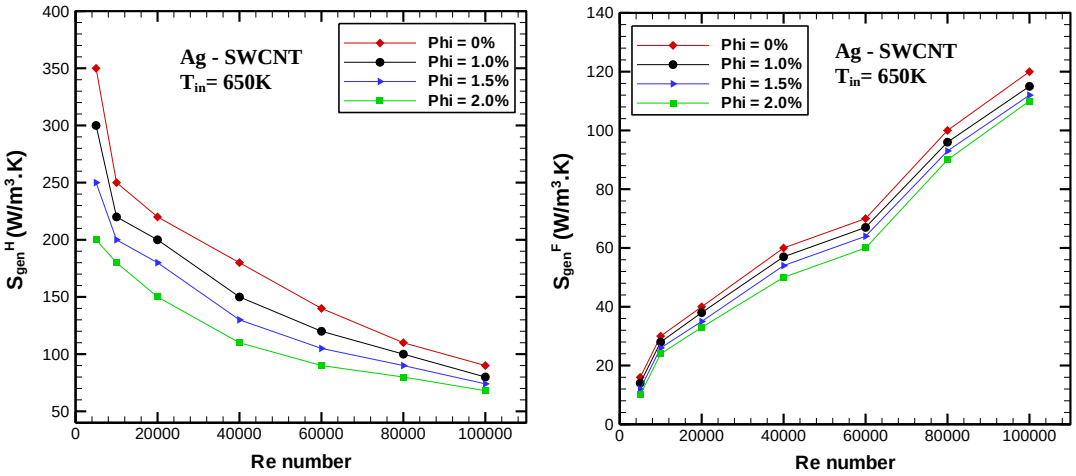

(a) (b)

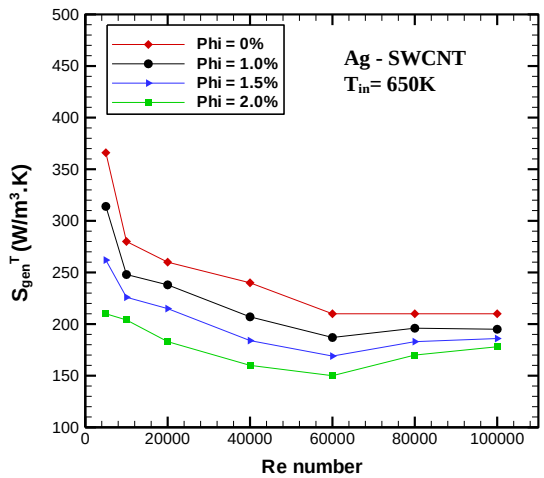

(c)

Figure 5.18 The entropy generation rate variation versus Re number for various nanoparticle concentrations, (a) entropy generation because of heat transfer, (b) entropy generation because of fluid friction, (c) total entropy generation.

The contribution of each irreversibility (heat transfer and fluid friction) to the total entropy generation rate is expressed utilising the Bejan number (Be). It is the entropy generation rate because of thermal irreversibility divided by the total entropy generation rate. The Bejan number distribution versus Re number for various hybrid nanofluid types, various inlet fluid temperatures, and various nanoparticle concentrations is plotted in Figure 5.19(a)-(c). It can be noticed from Figure 5.19(a) that the Be number of hybrid nanofluid of Ag-SWCNT is the lowest among other hybrid nanofluids used in this study. It is also observed that the fluid inlet temperature of 650K has the lowest value of Be number among other fluid inlet temperatures examined in this work as shown in Figure 5.19(b). This is anticipated as at low temperatures the thermal irreversibility would be greater when the finite temperature difference is higher due to the weak thermal performance. Nonetheless, at higher inlet temperatures the Be number is seen to be lower due to the higher finite temperature differences and lower mass flow rate needed to achieve the required Re number which is contrasted to low inlet temperature cases. Furthermore, at low inlet fluid temperature, the high fluid friction irreversibility is contributed to the Be number reduction. It is noticed from Figure 5.19(c) that the Be

number remarkably diminishes as the nanoparticle volume fraction rises at a specific Re number. This is because of the decreased thermal irreversibility and the boosted flow irreversibility as Re number and nanoparticle volume fraction increase. It is worth noting that that the hybrid nanofluid of Ag-SWCNT with volume fraction of 2% has the lowest value of Be number compared to Syltherm oil which has the highest value. It is worth noting that the maximum reduction in the Bejan number obtained in this work for different parameters is about 57.2%.

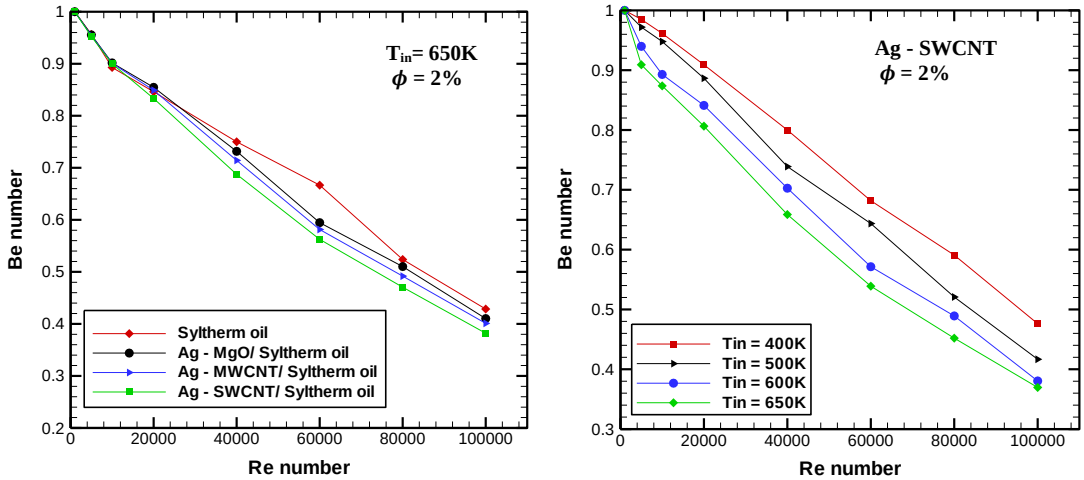

(a) (b)

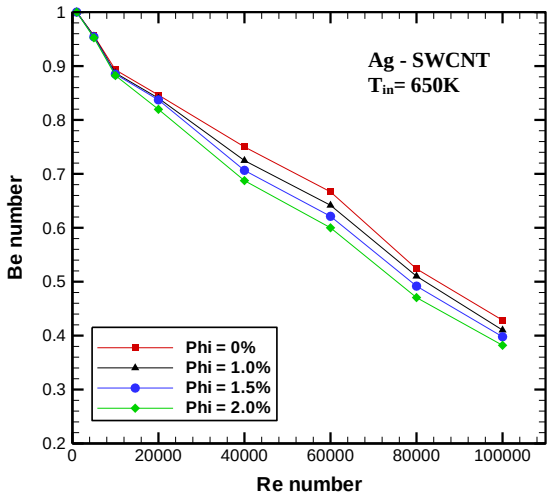

(c)

Figure 5.19 The Bejan number variation versus Re number for various, (a) hybrid nanofluid types, (b) inlet fluid temperatures, (c) nanoparticle concentrations.

Figure 5.20(a)-(c) shows the entropy generation ratio (N_s) variation versus Re number for various hybrid nanofluid types, various inlet fluid temperatures, and various nanoparticle concentrations. N_s indicates the conical turbulators can augment the thermodynamic performance when its values are less than 1. It is noticed from Figure 5.20 that N_s results reveal identical patterns to the total entropy generation rate and it is lower than 1 for all cases and lower than those of the corresponding plain PTSC. It can be obviously noticed from Figure 5.20(a) that the N_s value of each hybrid nanofluid is lower than the plain PTSC and the N_s value of Ag-SWCNT is the lowest among other hybrid nanofluids used in this study. Figure 5.20(b) portrays that, at lower Re number, the N_s value of each inlet fluid temperature considered in this study is lower than the smooth PTSC. In addition, at higher Re number, the N_s results reveal that there is a Reynolds number (Re= 65000) beyond which the N_s value becomes more than 1. Thus, it is recommended that the Re number should be less than Re= 65000 to make sure that the N_s value of the PTSC with conical turbulators becomes less than that of the smooth PTSC. Figure 5.20(c) shows that the N_s value of each nanoparticle volume fraction of Ag-SWCNT hybrid nanofluid is lower than the smooth PTSC. For instance, if hybrid nanofluid of Ag-SWCNT is to be used at Re= 40000 with 1%, 1.5% and 2% nanoparticle concentration instead of base fluid (Syltherm oil in this case), there would be a reduction in the N_s value of 13.8%, 23.4% and 33.4%, respectively.

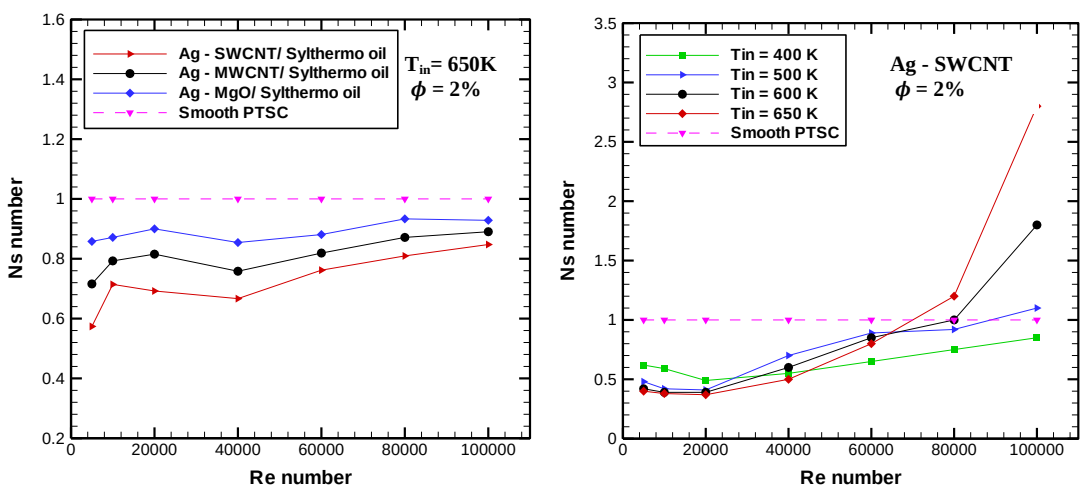

(a) (b)

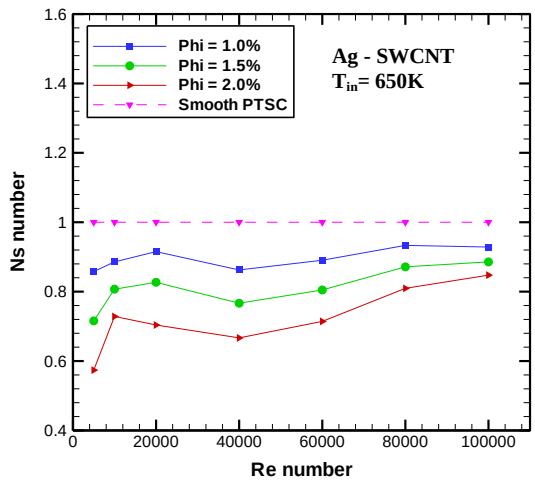

(c)

Figure 5.20 The entropy generation ratio variation versus Re number for various, (a) hybrid nanofluid types, (b) inlet fluid temperatures, (c) nanoparticle concentrations.

The variation of exergetic efficiency versus Re number for various hybrid nanofluid types, various inlet fluid temperatures, and various nanoparticle concentrations is plotted in Figure 5.21(a)-(c). It is noticed from Figure 5.21(a) that the exergetic efficiency decreases gradually as Re number increases and becomes relatively steady. It is observed that the hybrid nanofluid of Ag-SWCNT has the highest exergetic efficiency compared to other hybrid nanofluids considered in this study. While, the base fluid (Syltherm oil) has the lowest exergetic efficiency value. Figure 5.21(b) indicates that the exergetic efficiency remarkably rises as the fluid inlet temperature rises. It can be noticed that, at lower inlet temperatures, the exergetic efficiency declines as Re number rises due to the high irreversibilities and lower thermal losses. This implies continuous decrement of the available energy and thus the exergetic efficiency. Nevertheless, at high inlet temperatures, the situation is different as the irreversibilities are lower, the thermal losses are higher, and they rise as Re number rises. This increases the available energy and reduces the irreversibilities. As Re number rises further, the irreversibilities due to fluid friction rise and cause a decline in the exergetic efficiency. The value of this decline of the exergetic efficiency is based on the nanoparticle concentration utilised. The maximum

exergetic efficiency achieved at an inlet fluid temperature of 650K is 46% and the lowest value was around 20% at an inlet temperature of 400K. Figure 5.21(c) shows that the exergetic efficiency at different nanoparticle volume fractions of Ag-SWCNT hybrid nanofluid at T_{in}= 560K increases with the increase of the nanoparticle concentrations. However, the impact of nanoparticle volume fraction on the exergetic efficiency is not significant particularly for the hybrid nanofluids. It is essential to highlight that the maximum augmentation in the exergetic efficiency obtained in this work is about 18.2%.

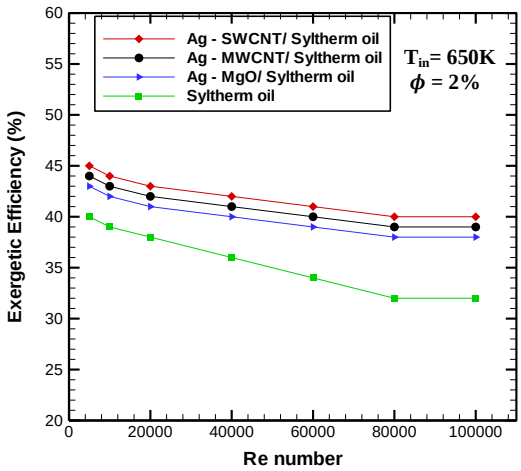

(a)

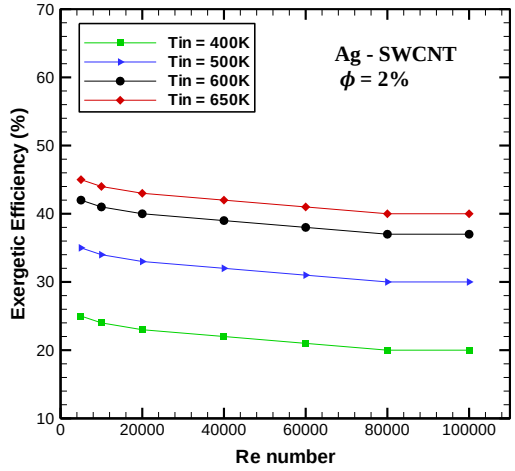

(b)

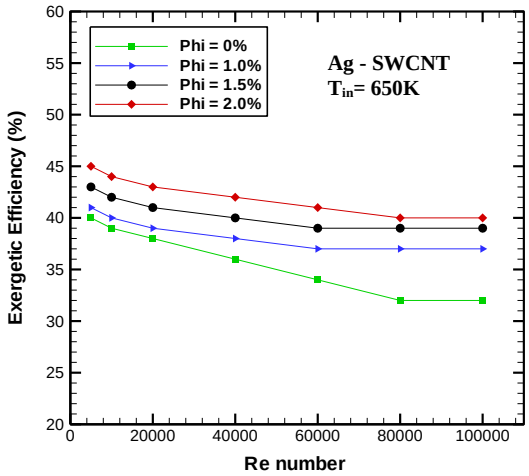

(c)

Figure 5.21 The exergetic efficiency variation versus Re number for various, (a) hybrid nanofluid types, (b) inlet fluid temperatures, (c) nanoparticle concentrations.

5.3.5 Overall Assessment

The overall performance assessment of the proposed design of a PTSC equipped with conical turbulators using various types of hybrid nanofluids compared to smooth PTSC is plotted in Figure 5.22(a)-(c). The overall performance assessment is expressed in terms of Nu/Nu_o, f/f_o and PEC versus Re number for different relevant studies available from the literature of longitudinal fins and nanofluids [9], pin-fin arrays inserts [11], centrally placed perforated plate inserts [54], wall-detached twisted tape inserts [72], unilateral longitudinal vortex generator [73], helical screw-tape inserts [74], asymmetric outward convex corrugated tube [75], and conical strip inserts [76]. These relevant studies have mostly developed their numerical models using FVM and commercial software. This is a paramount procedure to ensure that the overall performance of the proposed PTSC of conical turbulators is within the acceptable ranges. It is noticed from Figure 5.22(a)-(c) that the current PTSC configuration has high overall performance at low Reynolds number and it declines as Re number rises. It can also be observed that the current results are higher than other turbulators types. This affirms that the PTSC fitted with conical turbulators can significantly augment the thermal and hydraulic performance and it is performed well than other PTSC equipped with other insert types.

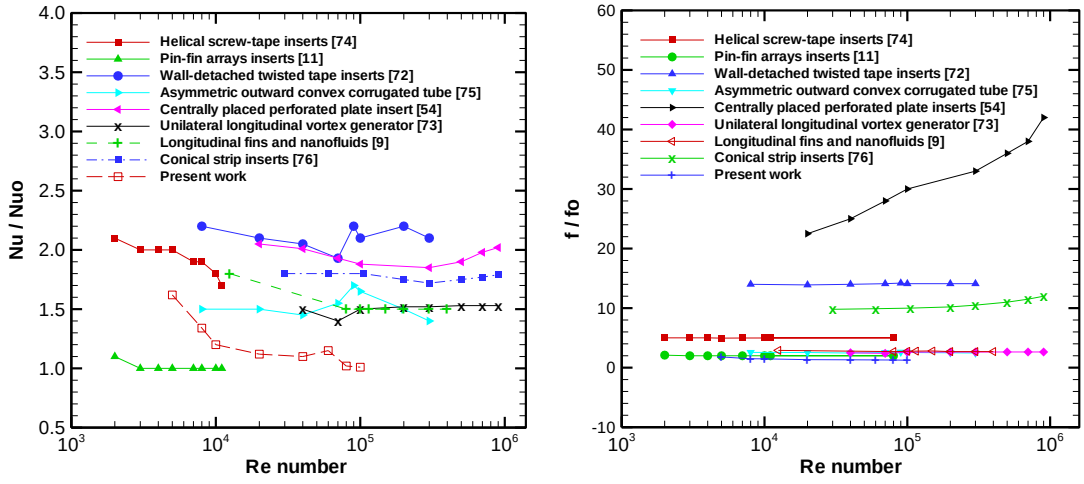

(a) (b)

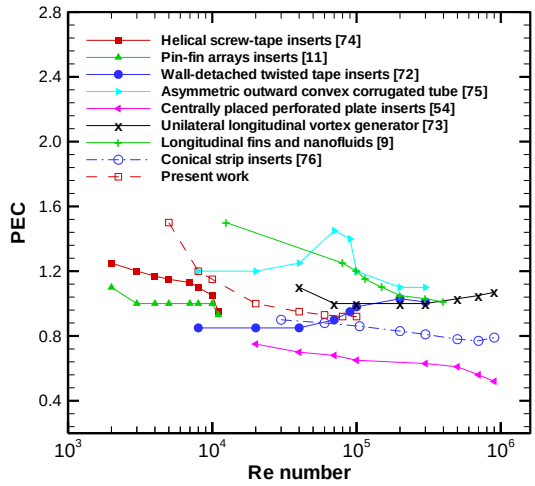

(c)

Figure 5.22 Comparison of the present results with other relevant studies, (a) Nu/Nu_o, (b) f/f_o, (c) PEC versus Re number at T_{in}= 600K.

5.4 Conclusions

The impact of using various hybrid nanofluid kinds, namely (Ag-SWCNT/Syltherm oil, Ag-MWCNT/Syltherm oil, and Ag-MgO/Syltherm oil) at various nanoparticle volume fractions (ϕ = 1.0-2.0%) flowing in a three-dimensional PTSC model equipped with conical turbulators is numerically investigated. The thermohydraulic performance along with the exergy and entropy assessment under turbulent flow conditions (Re number in the range of 5000 to 100000) is comprehensively carried out. The following findings of this research can be drawn:

- High augmentation in heat transfer inside a PTSC framework was produced with the utilisation of different hybrid nanofluid types. It is noticed that Nu number is improved by approximately 233.4%, 150%, and 66.7% when utilising Ag-SWCNT/Syltherm oil, Ag-MWCNT/Syltherm oil, and Ag-MgO/Syltherm oil hybrid nanofluids, respectively, at 2.0% concentration instead of Syltherm oil.
- The pumping power increased with the utilisation of hybrid nanofluids. It is observed that Ag-SWCNT/Syltherm oil hybrid nanofluid has the highest pumping power, while Ag-MgO/Syltherm oil has the lowest value. Furthermore, the pumping power

rose up to approximately 23.4-35.4% as the nanoparticle concentration increased from 1-2%.

- The maximum decrement in the absorber's outlet temperature and the temperature gradient was approximately 28.1% and 38.3%, respectively, particularly at low Re number.
- Thermal performance of hybrid nanofluids is noticed to be superior compared to base fluid as the PEC value of PTSC equipped with conical turbulators is in the range of 0.9-1.82.
- The thermal efficiency of the PTSC has remarkably enhanced with the utilisation of hybrid nanofluids. The maximum boost in the thermal efficiency was 11.5% using Ag-SWCNT/Syltherm oil hybrid nanofluid.
- The maximum decrement in the entropy generation rate and the entropy generation ratio were approximately 42.7% and 33.7%, respectively, particularly at low Re number. This was achieved because of the remarkable boost of thermal performance and the decrement in the finite temperature difference.
- At specific parameters, there was a Re number (Re= 65000) beyond which the entropy generation rate became higher than 1 and the entropy generation ratio became higher than the smooth PTSC.
- The exergetic efficiency of the conical turbulators PTSC has prominently improved with the utilisation of hybrid nanofluids at low Re numbers. The maximum augmentation in the exergetic efficiency was about 18.2%.

Therefore, with conical turbulators and hybrid nanofluids, there is a high potential for enhancing the PTSC's absorber tube thermal effectiveness. The results of this research could also be exploited as an initiative for further developments in PTSC industry.

References

[1] Hussein A. K. Applications of Nanotechnology to Improve the Performance of Solar Collectors-Recent Advances and Overview. Renew Sustain Energy Rev 2016; 62: 767–792.

[2] Kumaresan G., Santosh R., Velraj R., Sudhakar P. Experimental and numerical studies of thermal performance enhancement in the receiver part of solar parabolic trough collectors. Renew Sustain Energy Rev 2017; 77: 1363–74.

[3] Hafez A., Eltwab A. M., ElKousy H. S., Afifi A. O., AbdElhamid A. A., A Z AG. Design analysis of solar parabolic trough thermal collectors. Renew Sustain Energy Rev 2018; 82: 1215–60.

[4] Yang S., Ordonez J. C., Sensoy T. S. Dynamic 3D volume element model of a parabolic trough solar collector for simulation and optimization. Appl Energy 2018; 217: 509–26.

[5] Reddy K. S., Kumar K. R., Ajay C. S. Experimental investigation of porous disc enhanced receiver for solar parabolic trough collector. Renew Energy 2015; 77: 308–19.

[6] Waghole D. R., Warkhedkar R. M., Kulkarni V. S., Shrivastva R. K. Experimental Investigations on Heat Transfer and Friction Factor of Silver Nanofliud in Absorber/Receiver of Parabolic Trough Collector with Twisted Tape Inserts. Energy Procedia 2014; 45: 558 – 567.

[7] Jafar K. S., Sivaraman B. Thermal performance of solar parabolic trough collector using nanofluids and the absorber with nail twisted tapes inserts. Int Energy 2014; 14: 189–98.

[8] Bellos E., Tzivanidis C., Antonopoulos K. A., Gkinis G. Thermal enhancement of solar parabolic trough collectors by using nanofluids and converging-diverging absorber tube. Renew Energy 2016; 94: 213–22.

[9] Benabderrahmane A., Aminallah M., Laouedj S., Benazza A., Solano J. P. Heat transfer enhancement in a parabolic trough solar receiver using longitudinal fins and nanofluids. J Therm Sci 2016; 25: 410–7.

[10] Zhu X., Zhu L., Zhao J. Wavy-tape insert designed for managing highly concentrated solar energy on absorber tube of parabolic trough receiver. Energy 2017; 141: 1146–55.

[11] Xiangtao G., Fuqiang W., Haiyan W., Jianyu T., Qingzhi L., Huaizhi H. Heat transfer enhancement analysis of tube receiver for parabolic trough solar collector with pin fin arrays inserting. Sol Energy 2017; 144: 185–202.

[12] Huang Z., Li Z.Y., Yu G. L., Tao W. Q. Numerical investigations on fully-developed mixed turbulent convection in dimpled parabolic trough receiver tubes. Appl Therm Eng 2017; 114: 1287–1299.

[13] Bellos E., Tzivanidis C. Investigation of a star flow insert in a parabolic trough solar collector. Appl Energy 2018; 224: 86–102.

[14] Bellos E., Tzivanidis C., Tsimpoukis D. Optimum number of internal fins in parabolic trough collectors. Appl Therm Eng 2018; 137: 669–677.

[15] Bitam E., Demagh Y., Hachicha A. A., Benmoussa H., Kabar Y. Numerical investigation of a novel sinusoidal tube receiver for parabolic trough technology. Appl Energy 2018; 218: 494–510.

[16] Okonkwo E. C., Abid M., Ratlamwala T. A. H. Effects of synthetic oil nanofluids and absorber geometries on the exergetic performance of the parabolic trough collector. Int J Energy Res 2018: 1–16.

[17] Khan M. S., Yan M., Ali H. M., Amber K. P., Bashir M. A., Akbar, et al. Comparative performance assessment of different absorber tube geometries for parabolic trough solar collector using nanofluid. J Therm Anal Calorim Vol 2020; 142: 2227–2241.

[18] Kasaeian A. B., Sokhansefat T., Abbaspour M. J., Sokhansefat M. Numerical study of heat transfer enhancement by using Al_2O_3/synthetic oil nanofluid in a parabolic trough collector tube. World Acad Sci Eng Technol 2012; 69: 1154–9.

[19] Ghasemi S. E., Ahangar G. R. M. Numerical analysis of performance of solar parabolic trough collector with Cu-Water nanofluid. Int J Nano Dimens 2014; 5: 233–40.

[20] Sunil K., Kundan L., Sumeet S. Performance evaluation of a nanofluid based parabolic solar collector – an experimental study. Int J Mech Prod Eng 2014; 2: 61–7.

[21] Zadeh P. M., Sokhansefat T., Kasaeian A. B., Kowsary F., Akbarzadeh A. Hybrid optimization algorithm for thermal analysis in a solar parabolic trough collector based on nanofluid. Energy 2015; 82: 857–64.

[22] Chaudhari K. S., Walke P. V., Wankhede US, Shelke RS. An experimental investigation of a nanofluid (Al_2O_3+H_2O) based parabolic trough solar collectors. Br J Appl Sci Technol 2015; 9: 551–7.

[23] Mwesigye A., Huan Z. Thermal and thermodynamics performance of a parabolic trough receiver with Syltherm 800-Al_2O_3 nanofluid as the heat transfer fluid. Energy Procedia 2015; 75: 394 – 402.

[24] Mwesigye A, Huan Z., Meyer J. P. Thermal performance of a receiver tube for a high concentration ratio parabolic trough system and potential for improved performance with syltherm800-CuO nanofluid. Proc ASME 2015 Int Mech Eng Congr Expo IMECE2015, Houston, Texas, USA 2015.

[25] Kasaeian, Daviran S., Azarian R.D , Rashidi A. Performance evaluation and nanofluid using capability study of a solar parabolic trough collector. Energy Convers Manag 2015; 89: 368–375.

[26] Basbous N., Taqi M., Janan M. A. Thermal performances analysis of a parabolic trough solar collector using different nanofluids. IEEE 2016:1–5.

[27] Mwesigye A., Huan Z., Meyer J. P. Thermal performance and entropy generation analysis of a high concentration ratio parabolic trough solar collector with Cu-Therminol VP-1 nanofluid. Energy Convers Manag 2016; 120: 449–465.

[28] Wang, Xu J., Liu Q., Chen Y., Liu H. Performance analysis of a parabolic trough solar collector using Al_2O_3/synthetic oil nanofluid. Appl Therm Eng 2016; 107: 469–478.

[29] Ghasemi S. E., Ranjbar A. A. Thermal performance analysis of solar parabolic trough collector using nanofluid as working fluid: A CFD modelling study. J Mol Liq 2016; 222: 159–166.

[30] Coccia G., Di Nicola G.., Colla L., Fedele L., Scattolini M. Adoption of nanofluids in low-enthalpy parabolic trough solar collectors: Numerical simulation of the yearly yield. Energy Convers Manag 2016; 118: 306–319.

[31] Ferraro V., Settino J., Cucumo M. A., Kaliakatsos D. Parabolic trough system operating with nanofluids: comparison with the conventional working fluids and influence on the system performance. Energy Procedia 2016; 101:782 – 789.

[32] Mwesigye A., Meyer J. P. Optimal thermal and thermodynamic performance of a solar parabolic trough receiver with different nanofluids and at different concentration ratios. Appl Energy 2017; 193: 393–413.

[33] Bellos E., Tzivanidis C. Parametric investigation of nanofluids utilization in parabolic trough collectors. Therm Sci Eng Prog 2017; 2: 71–79.

[34] Khakrah H., Shamloo A., Hannani S. K. Determination of parabolic trough solar collector efficiency using nanofluid: A comprehensive numerical study. J Sol Energy Eng 2017; 139: 51006–11.

[35] Kasaeian A., Daneshazarian R., Pourfayaz F. Comparative study of different nanofluids applied in a trough collector with glass-glass absorber tube. J Mol Liq 2017; 234: 315–323.

[36] Mwesigye A., Yılmaz I. H., Meyer J. P. Numerical analysis of the thermal and thermodynamic performance of a parabolic trough solar collector using SWCNTs-Therminol VP-1 nanofluid. Renew Energy 2018; 119: 844–62.

[37] Subramani J., Nagarajan P. K., Mahian O., Sathyamurthy R. Efficiency and heat transfer improvements in a parabolic trough solar collector using TiO_2 nanofluids under turbulent flow regime. Renew Energy 2018; 119: 19–31.

[38] Bellos E., Tzivanidis C. Thermal efficiency enhancement of nanofluid-based parabolic trough collectors. J Therm Anal Calorim 2018; 1: 1–12.

[39] Bellos E., Tzivanidis C., Tsimpoukis D. Thermal, hydraulic and exergetic evaluation of a parabolic trough collector operating with thermal oil and molten salt based nanofluids. Energy Convers Manag 2018; 156: 388–402.

[40] Marefati M., Mehrpooya M., Shafii M. B. Optical and thermal analysis of a parabolic trough solar collector for production of thermal energy in different climates in Iran with comparison between the conventional nanofluids. J Clean

Prod 2018; 175: 294–313.

[41] Rehan M. A., Ali M., Sheikh N. A., Khalil M. S., Chaudhary G. Q., Ur Rashid T., et al. Experimental performance analysis of low concentration ratio solar parabolic trough collectors with nanofluids in winter conditions. Renew Energy 2018; 118: 742–51.

[42] Rios, De los M. S. B, Rivera-Solorio C. .I, García-Cuellar A. J. Thermal performance of a parabolic trough linear collector using Al_2O_3/H_2O nanofluids. Renew Energy 2018; 122: 665–73.

[43] Allouhia A., Amine M. B., Saidur R., Kousksou T., Jamil A. Energy and exergy analyses of a parabolic trough collector operated with nanofluids for medium and high temperature applications. Energy Convers Manag 2018; 155: 201–217.

[44] Alsaady M., Fu R., Yan Y., Liu Z., Wu S., Boukhanouf R. An experimental investigation on the effect of ferrofluids on the efficiency of novel parabolic trough solar collector under laminar flow conditions. Heat Transf Eng 2018; 1: 1–9.

[45] Tagle-Salazar P. D., Nigam K. D. P., Rivera-Solorio C. I. Heat transfer model for thermal performance analysis of parabolic trough solar collectors using nanofluids. Renew Energy 2018; 125: 334–43.

[46] Kumar M. K., Yuvaraj G., Balaji D., Pravinraj R., Shanmugasundaram P. Influence of nanofluid and receiver modification in solar parabolic trough collector performance. IOP Conf Ser Mater Sci Eng 2018; 310: 12140.

[47] Bellos E., Tzivanidis C., Said Z. A systematic parametric thermal analysis of nanofluid-based parabolic trough solar collectors. Sustain Energy Technol Assessments 2020; 39: 100714.

[48] Al-Rashed A., Alnaqi A., Alsarraf J., Thermo-hydraulic and economic performance of a parabolic trough solar collector equipped with finned rod turbulator and filled with oil-based hybrid nanofluid, Journal of the Taiwan Institute of Chemical Engineers 2021: 1-13.

[49] Fattahi A., The effect of cross-section geometry on the performance of a solar nanofluid heater in a parabolic solar receiver: A comparison study, Journal of the Taiwan Institute of Chemical Engineers 2021: 1-12.

[50] Dehaj M., Rezaeian M., Mousavi D., Shamsi S., Salarmofrad M., Efficiency of the parabolic through solar collector using $NiFe_2O_4$/Water nanofluid and U-tube, Journal of the Taiwan Institute of Chemical Engineers 2021; 120: 136-149.

[51] Khan M., Alsaduni .I, Alluhaidan M., Xia W., Ibrahim M., Evaluating the energy efficiency of a parabolic trough solar collector filled with a hybrid nanofluid by utilizing double fluid system and a novel corrugated absorber tube, Journal of the Taiwan Institute of Chemical Engineers 2021: 1-12.

[52] Fattahi A., On the rotary concentrated solar collector containing twisted ribs and MgO-Ag-water nanofluid, Journal of the Taiwan Institute of Chemical Engineers 2021: 1-12.

[53] ANSYS Theory Guide. ANSYS® Academic Research, Release 19.5, ANSYS FLUENT, Theory Guide, ANSYS, Inc. 2019.

[54] Mwesigye A., Bello-Ochende T., Meyer J. P. Heat transfer and thermodynamic performance of a parabolic trough receiver with centrally placed perforated plate inserts. Appl Energy 2014; 136: 989–1003.

[55] Pandey D. K., Lee R. B., Paden J. Effects of atmospheric emissivity on clear sky temperatures. Atmos Environ 1995; 29: 2201–2204.

[56] Garcıa-Valladares O., Velazquez N. Numerical simulation of parabolic trough solar collectori: improvement using counter flow concentric circular heat exchangers. Int J Heat Mass Transf 2009; 52: 597–609.

[57] Incropera F., Dewitt P. D. Introduction to Heat Transfer, fifth ed., John Wiley & Sons Inc, New York. 2006.

[58] Wirz M., Haselbacher A., Petit J. Potential improvements in the optical and thermal efficiencies of parabolic trough concentrators. Sol Energy 2014; 107(0): 398–414.

[59] Amina B., Miloud A., Samir L., Abdelylah B., Solano J.P. Heat transfer enhancement in a parabolic trough solar receiver using longitudinal fins and nanofluids. J Therm Sci 2016; 25: 410–7.

[60] Dudley E. V., D. K., Kolb J.G. SEGS LS2 solar collector-test results. Rep Sandia Natl Lab 1994;SAN94: 1884.

[61] Dow. SYLTHERM 800 Heat Transfer Fluid: Product Technical Data 2012.

[62] Minea A. Challenges in hybrid nanofluids behavior in turbulent flow: recent research and numerical comparison. Renew Sustain Energy Rev 2017; 71: 426–34.

[63] Sidik N. A. C., Adamu I. M., Jamil M. M., Kefayati G. H. R., Mamat R., Najafi G. Recent progress on hybrid nanofluids in heat transfer applications: a comprehensive review. Int Commun Heat Mass Transf 2016; 75: 68–79.

[64] Nadeem S., Khan U., Hussain S. Model based study of SWCNT and MWCNT thermal conductivities effect on the heat transfer due to the oscillating wall conditions. Int J Hydrog Energy 2017; 42: 28945–28957.

[65] Hussanan A., Khan I., Gorji M. R., Khan W. A. CNTS-water–based nanofluid over a stretching sheet. Bionanoscience 2019; 9: 21–29.

[66] Pak B. C., Cho Y. I. Hydrodynamic and heat transfer study of dispersed fluids with submicron metallic oxide particles. Exp Heat Transf 1998; 11: 151–70.

[67] Tayebi T., Chamkha A. J. Free convection enhancement in an annulus between horizontal confocal elliptical cylinders using hybrid nanofluids. Numer Heat Transf Part Appl 2016; 70: 141–56.

[68] Esfe M. H., Arani A. A. A., Rezaie M., Yan W. M., Karimipour A. Experimental determination of thermal conductivity and dynamic viscosity of Ag–MgO/water hybrid nanofluid. Int Comm Heat Mass Transf 2015; 66: 189–195.

[69] Nan C., Liu G., Lin Y., Li M. Interface effect on thermal conductivity of carbon nanotube composites. Appl Phys Lett 2004; 85: 3549–51.

[70] Choi S. U. S., Zhang Z. G., Yu W. L., Grulke E. A. Anomalous thermal conductivity enhancement in nanotube suspensions. Appl Phys Lett 2001; 79: 2252–4.

[71] Corcione M. Heat transfer features of buoyancy-driven nanofluids inside rectangular enclosures differentially heated at the sidewalls. Int J Therm Sci 2010; 49: 1536–1546.

[72] Mwesigye A., Bello-Ochende T., Meyer J. P. Heat transfer and entropy generation in a parabolic trough receiver with wall-detached twisted tape inserts. Int J Therm Sci 2016; 99: 238–57.

[73] Cheng Z. D., He Y. L., Cui F. Q. Numerical study of heat transfer enhancement by unilateral longitudinal vortex generators inside parabolic trough solar receivers. International Journal of Heat and Mass Transfer 2012; 55: 5631–5641.

[74] Song X., Dong G., Gao F., Diao X., Zheng L., Zhou F. A numerical study of parabolic trough receiver with nonuniform heat flux and helical screw-tape inserts. Energy 2014; 77: 771–82.

[75] Fuqiang W., Xiangtao G., Jianyu T., Huaizhi H., Bingxi L. Heat transfer performance enhancement and thermal strain restrain of tube receiver for parabolic trough solar collector by using asymmetric outward convex corrugated tube. Energy 2016; 114: 275-292.

[76] Liu P., Zheng N., Liu Z., Liu W. Thermal-hydraulic performance and entropy generation analysis of a parabolic trough receiver with conical strip inserts, Energy Conversion and Management 2019; 179: 30–45.

Chapter 6 Thermohydraulic and Thermodynamics Performance of Hybrid Nanofluids based Parabolic Trough Solar Collector equipped with Wavy Promoters

Abstract

This article presents a numerical analysis on the thermohydraulic and thermodynamic performance of a parabolic trough solar collector (PTSC) receiver's tube equipped with wavy promoters. A computational fluid dynamics (CFD) with the aid of finite volume method (FVM) is adopted to examine the flow and thermal features of the PTSC's tube receiver. The Reynolds number in the range of 5000 to 100000 with four fluid inlet temperatures in the range of 400 to 650K are utilised. Three different advanced hybrid nanofluids (Fe_2O_3-GO, Fe_2O_3-SiC and Fe_2O_3-TiO_2) dispersed in Syltherm oil 800 are employed inside the PTSC's receiver tube. The numerical outcomes are verified with the available correlations and with other numerical and experimental data available in the open literature. The numerical outcomes reveal that the utilisation of wavy promoters inside the PTSC's receiver tube can significantly augment the thermal performance, where the average Nusselt number is improved by 150.4% when utilising Fe_2O_3-GO/Syltherm oil hybrid nanofluids at 2.0% concentration instead of Syltherm oil. Furthermore, the maximum reduction in the absorber's average outlet temperature is in the range of 7-31°C. The overall thermal evaluation criterion (PEC) is found to be in the range of 1.24-2.46 using bricks-shaped nanoparticles. The results show that the thermal efficiency increased by 18.51% and the exergetic efficiency increased by 16.21%. The maximum reduction in the entropy generation rate and the entropy generation ratio are about 48.27% and 52.6% respectively. New correlations for Nusselt number, friction factor and thermal efficiency for PTSC tube having wavy promoters using hybrid nanofluids are developed.

The content of this chapter has been published in Renewable Energy, 2022 **(Q1, IF=8.001).**

Chapter 6

6.1 Introduction

6.1.1 Background and Motivation

Harnessing solar energy is considered to be one of the most encouraging solutions for solving the current energy management and environmental issues such as global warming, fossil fuel depletion, and rapidly increasing energy demand (Hussein, 2016) [1] and (Kumaresan et al., 2017) [2]. There are various technologies being used for harnessing energy from assorted renewable energies. Solar concentrating technologies are mainly available in five types: (i) Solar power tower (SPT), (ii) Parabolic dish collector (PDC), (iii) Linear Fresnel reflector (LFR), (iv) Enclosed trough (ET), and (v) Parabolic trough solar collector (PTSC). The PTSC is the most proven solar concentration technique (Hafez et al., 2018) [3] and (Yang et al., 2018) [4]. It uses its linear focus receiver to convert the solar radiation beam into useful thermal energy. The parabolic trough receiver (PTR) is the most significant part of a PTSC system, which has a paramount role on the plant's overall performance. The PTCs can achieve temperatures over 400 ºC; however, this temperature is restricted usually up to 400 ºC by thermal degradation of the heat transfer fluid.

PTSCs suffer from high circumferential temperature gradient, which is caused by the nonuniform heat flux generated from the concentrated solar radiation. The high temperature leads to heat transfer fluid reduction and remarkably boosts the heat loss and thus diminishing the energetic efficiency of the PTSC. On the other hand, the high circumferential temperature gradient causes a large thermal stress, which may bend the tube and break the glass cover and thus reducing the lifetime of the PTSC (Khanna et al., 2013) [5]. In order to solve the above-mentioned problems, passive and active heat transfer augmentation techniques have been widely utilised to enhance PTSCs thermal performance for industrial processes. Passive techniques have been commonly used in the open literature as they are preferable and utilise surface alterations across the flow such as tape promoters or fins or particle addition such as gas bubbles, solid particles, and liquid droplets. It was found that both techniques are very useful in augmenting the thermal performance of PTSC frameworks.

6.1.2 Enhancement Techniques Used in PTSC

Recently, PTSC technology has been widely applied in concentrating power plants, hydrogen production or other industrial processes with high temperature requirement. Accordingly, numerous scientists have embraced the strategy for heat transfer upgrade to diminish the temperature gradient by utilising diverse operating liquids. The regular working liquids utilised in PTSC frameworks, for example, water, thermal oils, molten salts have limitations such as the requirements of high operating temperatures, the sophisticated control strategies and high maintenance cost or high security in the activity. Therefore, nanofluids are considered as the fluids of future and the second option of thermal augmentation in PTSC frameworks. Nanofluids have received an extensive research attention in the past decade because they have a great potential to augment the thermal performance in a PTSC. This is due to their high capacity to assimilate heat more than any customary liquids, so they can diminish the size of frameworks and boost its efficiency (Bellos et al., 2017) [6]. Therefore, the utilisation of nanofluids with different types and concentrations is considered among the most effective working liquids in PTSC frameworks as indicated by the literature summarised below in the following sections. Extensive experimental and numerical notable contributions have been conducted on the thermal enhancement using various strategies (different types of passive techniques and various working fluids), which is thoroughly investigated and summarised in the following Table 6.1 and next paragraphs.

Table 6.1: Literature studies carried out to date on PTSC using various passive techniques.

Reference	Study Type	Passive Technique	Fluid Used	Flow Type	Remarks
(Kumar and Reddy, 2012) [7]	Numerical	Porous finned receiver with different inclinations	Therminol-oil 500 and water	Mass flow rate was in the range of 0.5 - 1 kg/s	The optimum porous disc receiver improved the heat transfer rate and reduced the pumping power losses using therminol oil-55 higher than water as compared to plain receiver.
(Cheng et al., 2012) [8]	Numerical	Unilateral longitudinal vortex generators	Syltherm-800 oil	Turbulent flow Re number was 3.8×10^4 - 7.0×10^5	The thermal loss of the PTR reduced by 1.35-12.1% to that of the smooth PTR. The enhanced heat transfer performance is higher when the Re number is larger at the same inlet temperature.
(Aldali et al., 2013) [9]	Numerical	Helical internal fins	Water	Velocity was in the range	The thermal gradient for the pipe without a helical fin is significantly higher compared with the pipe with

				of 0.257 - 0.354 m/s	helical fins. Aluminium pipe has much lower thermal gradient compared to steel pipe.
(Ghasemi et al., 2013) [10]	Numerical/ CFD	Two segmental rings	Therminol 66	Re number was in the range of 30000 - 250000	The optimum thermal performance was achieved for the case when 'Q' = 0.75d 'the distance between porous two segmental rings' and 'd/D'= 0.6 'inner diameter/inner diameter ratio' respectively.
(Ghadirijafarbeigloo et al., 2013) [11]	Numerical	Perforated louvered twisted tape (PLTT)	Behran thermal oil	Turbulent flow Re number was in the range of 5000 - 25000	PLTT provided a maximum of 150% enhancement for Nusselt number and 210% for friction factor compared to a smooth tube.
(Waghole et al., 2014) [12]	Experimental	Twisted tape inserts	Silver-water Nanofluid	Turbulent flow Re number was in the range of 500 - 6000	The thermal and hydraulic performance of silver nanofluid is higher compared to water in a PTC receiver. The Nusselt number, friction factor and enhancement efficiency were observed to be in the range of 1.25-2.10, 1.0-1.75 and 135-205%, respectively, compared with the plain PTC receiver.
(Song et al., 2014) [13]	Numerical	Helical screw-tape inserts	Downtherm-A	Turbulent flow Re number was in the range of 5000 - 75000	The influence of the transversal angle (β) on the heat flux distribution was found more significant than the longitudinal angle (φ). It is observed that the helical screw-tape inserts remarkably decreased the heat losses and maximum and circumferential temperature differences.
(Mwesigye et al., 2014) [14]	Numerical	Perforated plate insert	Sytherm-800	Turbulent flow Re number was in the range of 1.02×10^4 - 7.38×10^5	The inclusion of perforated plate inserts was shown to enhance the thermodynamic performance and to reduce the temperature gradients of the receiver. The modified thermal efficiency increased between 1.2% and 8%.
(Jafar and Sivaraman, 2014) [15]	Experimental	Nail twisted tapes inserts	Al_2O_3 - water nanofluid	Laminar flow Re number was in the range of 710 - 2130	The insertion of nail twisted tape in an absorber of PTC using nanofluids can greatly enhance its thermal performance and increase its friction factor
(Mwesigye et al., 2015) [16]	Numerical	Perforated plate insert	Al_2O_3- Synthetic oil	Turbulent flow Re number was in the range of 3560 - 1.15×10^6	The thermal performance and the thermal efficiency increased up to 38% and 15% respectively. It was found that high inlet temperatures and low flow rates show remarkable enhancement in the receiver's thermal efficiency.
(Huang et al., 2015) [17]	Numerical	Helical fins, protrusions and dimples	Therminol-VP1	Turbulent flow Re number was in the range of 1×10^4 - 2×10^4	The dimpled receiver tubes have unrivalled thermal performance compared with that having helical fins or protrusions. The dimples with deeper depth, narrower pitch and more numbers in the circumferential direction enhanced the thermal performance while other arrangements shown insignificant effect.

(Lu et al., 2015) [18]	Theoretical	Spirally grooved pipe	Molten salt	Turbulent flow Re number was in the range of 5000 - 15000	The increment of flow velocity and groove height increased the absorption efficiency and decreased the wall temperature. The heat absorption efficiency increased by 0.7%, and the maximum bulk fluid temperature increased to 31.1 °C.
(Reddy et al., 2015) [19]	Experimental work	Porous disc enhanced receiver	Water and oil	Turbulent flow Flow rate was in the range of 100 -1000 L/h	The porous disc enhanced receiver reduced the temperature gradient compared to classical tubular receiver. The performance of PTC with porous disc receiver is much better than other receiver configurations.
(Diwan and Soni, 2015) [20]	Numerical	wire-coils insert	Water	Turbulent flow Mass flow rate was in the range of 0.01388 – 0.099 kg/s	The introduction of wire coils increased the Nusselt number by 104% to 330%. Good thermal performance was obtained when using wire-coils inserts with pitch value from 6 – 8 mm at lower flow rates and using pitch of 8 mm at higher flow rate.
(Mwesigye et al., 2016) [21]	Numerical	Wall-detached twisted tape inserts	Sytherm-800	Turbulent flow Re number was in the range of 10260 - 1353000	There was an increase of thermal performance of 169%, and thermal efficiency up to 10% compared to a plain absorber tube. A 58% decrease in the entropy generation rate was also attained.
(Bellos et al., 2016) [22]	Numerical	Converging-diverging absorber tube	Thermal oil, thermal oil-nanoparticles (Al_2O_3), pressurized water	Turbulent flow Re number was in the range of 4000 - 25000	The utilisation of Al_2O_3-thermal oil nanofluid increased the thermal efficiency by 4.25% while the use of pressurized water by 6.34%. The results showed 4.55% mean efficiency enhancement compared to plain tube. At higher fluid temperature levels, the increase in the efficiency was greater.
(ZhangJing et al., 2016) [23]	Numerical (optimized by Genetic Algorithm (GA)	Porous insert	Water/steam	Turbulent flow Re number was in the range of 50 000- 900 000	The porous insert receiver tube exhibited higher thermal performance than that of the plain receiver. It achieved flawless thermo-hydraulic performance by using similar optimized porous insert, which is difficult to achieve by utilising the plain receiver.
(Fuqiang et al., 2016) [24]	Numerical	Asymmetric outward convex corrugated tube (AOCCT)	Thermal oil-D12	Turbulent flow Re number was in the range of 10×10^3 to 98×10^3	The utilisation of AOCCT improved the thermal performance and decreased the thermal strain effectively. A maximum 148% and 26.8% of overall thermal performance and von-Mises thermal strain respectively were achieved.
(Jaramillo et al., 2016) [25]	Numerical	Twisted tape insert	Water, air	Turbulent flow Re number was in the range of 1389.7 - 8338.03	The thermal and flow fields, and the removal factor increased as both the twist ratio (y/w) and the Reynolds number decreased. These quantities did not present an enhancement when the twist ratio increased.
(Benabderrahmane et al., 2016) [26]	Numerical 3D	Longitudinal rectangular/ triangular fins	Downtherm-A oil with different	Turbulent flow	There was a remarkable thermal enhancement from 1.3 to 1.8 times. The Cu, and SiC nanoparticles

			nanofluids Al_2O_3, Cu, Sic, C and Cu	Re number was in the range of 2.57×10^4 - 2.57×10^5	improved heat transfer significantly than C, and Al_2O_3 nanoparticles. The utilisation of fins and nanofluid provided greater performance.
(Ghasemi and Ranjbar, 2017) [27]	Numerical	Porous rings	Syltherm 800	Turbulent flow Re number was in the range of 30000 - 250000	The heat transfer characteristics enhanced by inserting the porous rings. The decrement in the distance between porous rings and the increment of the inner diameter of the porous rings would increase and decrease the heat transfer, respectively.
(Bellos et al., 2017) [28]	Numerical	Internally finned / evacuated tube absorber	Oil syltherm-800	Turbulent flow mass flowrate was in the range of 50 - 250 L/min	The thermal efficiency improved around 0.82%, the Nusselt number increased 65.8%, whilst the friction factor and the pressure losses were doubled compared to the smooth case.
(Zhu et al., 2017) [29]	Numerical	Wavy-tape insert	Sytherm-800	Turbulent flow The mass flowrate was in the range of 240 -720 L/min	The Nusselt number improved by 261-310%, and the heat loss reduced by 17.5-33.1%, depending on the HTF flow rate.
(Xiangtao et al., 2017) [30]	Numerical/ CFD	Pin fin array absorber	Thermal oil-D12	Re number was in the range of 2000 to 18000	The utilisation of tube receiver with pin fin arrays inserts increased the Nusselt number up to 9% and the thermal performance factor up to 12%.
(Huang et al., 2017) [31]	Numerical	Dimpled receiver	Therminol-VP1	Turbulent flow Re number was 2×10^4	The average Nusselt number and friction factor under non-uniform heat flux (NUHF) were larger than those under UHF. The deep dimples (d/D_i= 0.875) were good performing compared with shallow dimples (d/D_i= 0.125) at similar Grashof number.
(Bellos et al., 2018) [32]	Numerical	Internal rectangular finned tube	CuO in Syltherm 800	Volumetric flow rate was 150 L/min	The utilisation of internal fins and nanofluids exhibit an increment of 1.1% and 0.76% thermal efficiency enhancement, and the combination of both techniques provided 1.54%.
(Bitam et al., 2018) [33]	Numerical/ CFD	S-curved sinusoidal tube receiver	Synthetic oil	Mass flow rate was in the range of 2 - 9.5 kg/s	The Nusselt number and friction factor increased by 45%-63%, less than 40.8%, respectively, which provided 135% maximum PEC. The maximum of 35 K decrement in the circumferential temperature difference resulted in the reduction of thermal stresses and heat losses.
(Okonkwo et al., 2018) [34]	Numerical	Longitudinal finned absorber, twisted tape tube, converging-diverging absorbers	Al_2O_3-Therminol VP-1 nanofluid	Mass flow rate was in the range of 25-200 L/min	The converging-diverging absorber produced the best exergetic enhancement of 0.65% using Therminol VP-1 and 0.73% using Al_2O_3/Therminol VP-1 nanofluid.
(Rawani et al., 2018) [35]	Mathematical	Square cut, Oblique delta-winglet, alternate	Therminol VP-1	Mass flow rate was in the range of	The serrated twisted tape inserts (x=2) produced Nusselt number of 3.56 and 3.19 times over PTC plain absorber. The thermal efficiency enhancement

		clockwise and counter-clockwise, and Serrated twisted tape insert		0.06 – 0.16 kg/s	was 13.63% and the exergy efficiency was 15.40%. The serrated twisted tape provided the lowest entropy generation.
(Benabderrahmane et al., 2020) [36]	Numerical	Corrugated tube insert	Nitrate salt	Turbulent flow, Re number was in the range of 10^4- 10^6	The corrugated insert significantly augment the overall thermal effectiveness by 1.3-2.6. The increment of corrugation's twist ratio and the decrement of pitch between two corrugations increased the thermal performances.
(Khan et al., 2020) [37]	Numerical	Absorber tube with twisted tape insert and longitudinal fins	Al_2O_3/water	Turbulent flow, Re number was in the range of 10^3- $5*10^5$	The absorber tube with twisted tape insert has the highest thermal efficiency of 72.26%, compared to a tube with internal fins (72.10%), and smooth absorber tube (71.09%).

It can be noticed from the aforementioned literature review section that the passive technique with different configurations are appropriate methods for enhancing the thermal effectiveness inside a PTSC receiver tube as it decreases Q_{loss}, T_{max} and reduces the thermal strain and remarkably enhances the consistency of temperature distribution of the tube wall. It was also pointed out that the utilisation of passive techniques would decrease the absorber's circumferential temperature range and this would in turn decrease the failure danger caused by the thermal stresses. It was observed that about 15% maximum decrement in the temperature range could be achieved with passive technique associated absorber tube compared to a smooth absorber tube.

Other studies used different types of nanofluids in PTSC systems such as Cu-Therminol, Ag-Therminol and Al_2O_3-Therminol nanofluids (Mwesigye & Meyer, 2017) [38]; Al_2O_3 and CuO suspended in Syltherm 800 oil (Bellos & Tzivanidis, 2017) [39]; Al_2O_3/synthetic oil nanofluid (Khakrah et al., 2017) [40]; SWCNTs-Therminol® VP-1 nanofluid (Mwesigye et al., 2018) [41]; TiO_2/water nanofluids (Subramani et al., 2018) [42]; Cu, CuO, Fe_2O_3, TiO_2, Al_2O_3 and SiO_2 dispersed in Syltherm 800 (Bellos & Tzivanidis, 2018) [43]; CuO, Al_2O_3, and SiC nanofluids (Marefati et al., 2018) [44]; Al_2O_3, CuO, and TiO_2 (Allouhi et al., 2018) [45]; Fe_3O_4 ferrofluids (Alsaady et al., 2018) [46]; TiO_2 nanofluid (Kumar et al., 2018) [47]. It was found that the thermal efficiency increased by around 14% when using small fraction of nanofluid. Recently, (Bellos et al., 2020) [48] used Cu/Syltherm 800 nanofluid in a PTSC having three shapes: evacuated, non-evacuated and

bare with no cover. The optimum augmentation for bare tube, nonevacuated tube and evacuated tube was found to be 7.16%, 4.87% and 4.06%, respectively, when using cermet coating.

A modern category of nanofluids is the set of ferric/magnetic nanofluids that are produced, in fact, by suspending magnetic nanoparticles in a base fluid. Ferric/magnetic nanofluids, in addition to their great thermal properties, have also important magnetic properties. Due to having magnetic properties alongside flowability, many researchers have been attracted to this class of nanofluids in recent years. Ferric nanofluids can have many applications in different areas such as bioengineering, electronic packing, thermal energy (Aminfar et al., 2013) [49] and (Bahiraei et al., 2016) [50]. In the field of thermal engineering, the ability to control heat transfer process as they cause the velocity gradient to increase near the walls so that the local Nusselt number is enhanced. They can create a pair of vortices, which improve the heat transfer rate and prevent sedimentation of nanoparticles. Some researchers have employed ferric oxide nanofluids as coolant in different heat exchangers such as (Hong et al., 2007) [51] and (Aghabozorg et al., 2016) [52]. They found that the ferric oxide hybrid nanofluid demonstrates greater heat transfer coefficient in comparison with the base fluid.

It can be obviously noticed from the above literature that various kinds of nanofluids have been implemented in PTSC frameworks. However, there are still other nanoparticle categories such as ferric oxide, graphene, silicon and its derivatives that can be commendable of examination due to their outstanding thermophysical properties. Despite the vast majority of studies carried out on the thermal effectiveness of PTSCs using nanofluids, the studies on the thermal and thermodynamic effectiveness utilising hybrid nanofluids are still scarce in the literature. Thus, this study aims to fulfil the existing gap and presents a 3D numerical model to examine the flow and thermal fields in a PTSC geometry equipped with wavy promoters under turbulent hybrid nanofluids flow conditions. Various hybrid nanofluid types including Fe_2O_3-GO, Fe_2O_3-SiC and Fe_2O_3-TiO_2 were applied in various volume fractions in the range of 1-2%. The effect of nanoparticle shapes (spherical, platelets, blades, cylindrical and bricks) on the

thermophysical properties of hybrid nanofluids is also considered. The numerical thermal and hydrodynamic performance data are compared with the smooth tube results and other relevant available data. Furthermore, the thermodynamic irreversibilities and exergetic efficiency of the enhanced PTSC framework utilising hybrid nanofluids was also examined to identify the overall efficacy of hybrid nanofluids. The novelty of the current work lies in the fact that hybrid nanofluids have not been tested as a potential candidate to be used in PTSC frameworks. New correlations for Nusselt number, friction factor and thermal efficiency for PTSC tube having wavy promoters using hybrid nanofluids are also developed in this paper. These correlations can serve as a practical reference for PTSC designers to assess the thermohydraulic performance of their PTSC systems.

6.2 Numerical Method

6.2.1 Physical Model

The PTSC shown in Figure 6.1 receiver consists of two coaxial tubes and a metal tube called an absorber covered with a glass envelope to diminish the heat losses. The space between them is considered as a very high vacuum in order to avoid the heat loss by the natural convection. The working fluid circulates through the absorber tube, which is in this work a hybrid nanofluid with different types (Fe_2O_3-GO, Fe_2O_3-SiC and Fe_2O_3-TiO_2). In this work, the materials utilised for the absorber and the glass tube are, respectively, stainless steel and Pyrex. It is aimed to augment the heat transfer performance, and reduce the PTSC's temperature gradient. The PTSC's absorber tube fitted with wavy promoter with sinusoidal shape is introduced as an enhanced absorber tube of PTSC. The insert waviness is in sinusoidal shape, which has this expression: $W_t = A_t.\sin(2\pi/P_t.z)$. The geometrical parameters of the receiver are given in Table 6.2. Meanwhile, the geometrical dimensions of the wavy promoter are also illustrated in Figure 6.1b, where it shows the width of wavy tape (W_t), amplitude (A_t), and the pitch of waviness (P_t) between two successive waves, respectively. An aluminum material was used for the wavy promotor with a thermal conductivity of 239 W/m.K as it considered an excellent heat and electricity conductor with light weight and high strength properties. The heat transfer modes of the present study with its associated thermal resistances are illustrated in Figure 6.2.

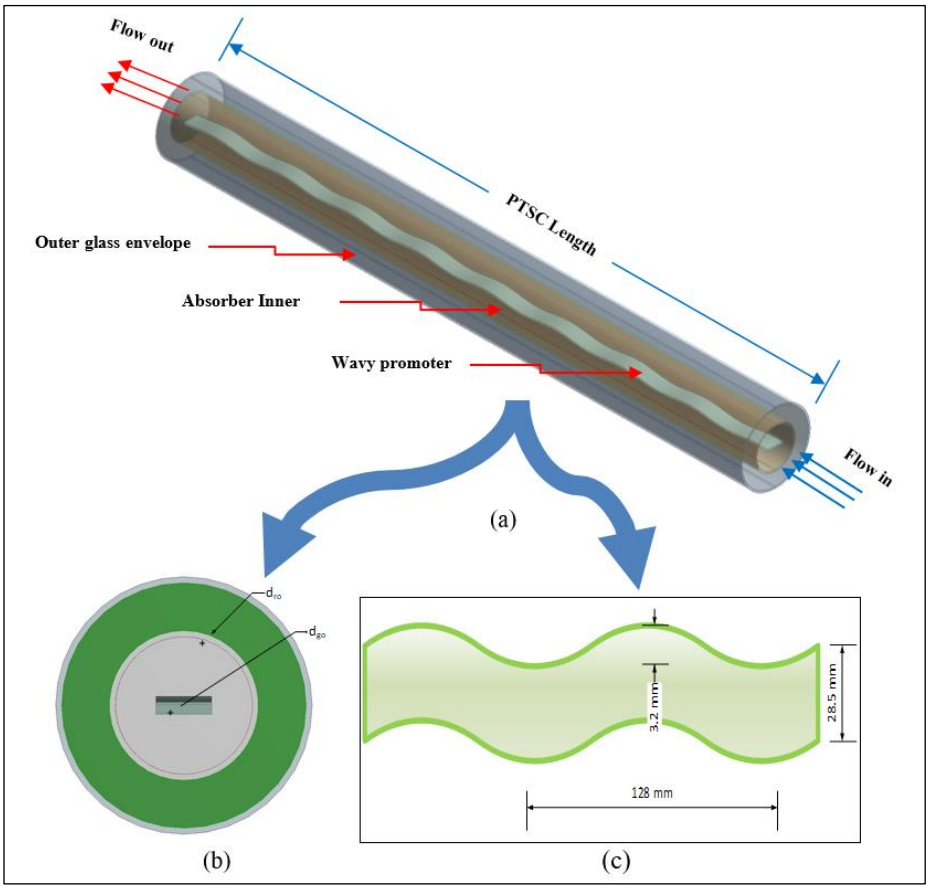

Figure 6.1 PTSC tube used in this study, (a) Full view with wavy promoters, (b) Cross-sectional view of the PTSC with wavy promoters, (c) wavy promoter dimensions.

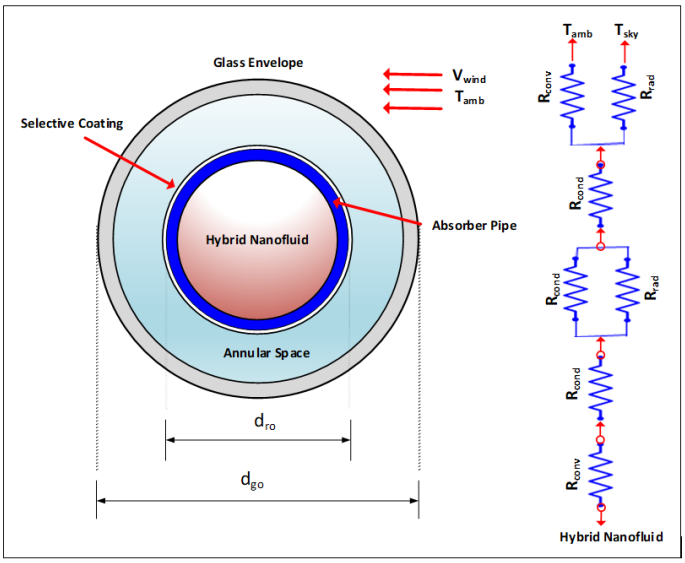

Figure 6.2 PTSC's Cross-sectional view and the associated thermal resistances.

Table 6.2 The dimensions of PTSC's receiver tube with wavy promoter.

Dimension	Value (mm)
Absorber tube length	2096
Absorber inner tube inside diameter (d_{ri})	70
Absorber inner tube thickness (t_r)	3
Glass outer tube inside diameter (d_{gi})	125
Glass outer tube thickness (t_g)	3
Width of wavy insert (W_t)	28.5
Amplitude (A_t)	3.2
Pitch of waviness (P_t)	128

6.2.2 Governing Equations

The Reynolds averaged Navier-Stokes equations (NSE) which govern the flow and thermal fields were used to model the PTSC's absorber tube under turbulent flow conditions [53]. The following assumptions were considered for modelling the PTSC tube: (i) PTSC tube works under steady-state conditions; (ii) incompressible fluid and single-phase was used; (iii) the fluid and tube material properties vary with temperature; and (iv) heat flux is uniform at the absorber's inner upper half surface and it is nonuniform at the absorber's inner lower half surface.

Continuity:

$$\frac{\partial(\rho\bar{u}_i)}{\partial x_i} = 0 \tag{6.1}$$

Momentum:

$$\frac{\partial}{\partial x_j}\left(\rho\bar{u}_i\bar{u}_j\right) = -\frac{\partial\bar{P}}{\partial x_i} + \frac{\partial}{\partial x_j}\left[\mu\left(\frac{\partial\bar{u}_i}{\partial x_j} + \frac{\partial\bar{u}_j}{\partial x_i}\right) - \frac{2}{3}\mu\frac{\partial\bar{u}_i}{\partial x_i}\,\delta_{ij} - \left(\rho\overline{\acute{u}_i\acute{u}_j}\right)\right] \tag{6.2}$$

Energy:

$$\frac{\partial}{\partial x_j}\left(\rho\bar{u}_j C_p\bar{T}\right) = \frac{\partial}{\partial x_j}\left(k\frac{\partial\bar{T}}{\partial x_j} + \frac{\mu_t}{\sigma_{h,t}}\frac{\partial(C_p\bar{T})}{\partial x_j}\right) + \bar{u}_j\frac{\partial\bar{P}}{\partial x_j} + \left[\mu\left(\frac{\partial\bar{u}_i}{\partial x_j} + \frac{\partial\bar{u}_j}{\partial x_i}\right) - \frac{2}{3}\mu\frac{\partial\bar{u}_i}{\partial x_i}\,\delta_{ij} - \left(\rho\overline{\acute{u}_i\acute{u}_j}\right)\right]\frac{\partial\bar{u}_i}{\partial x_j} \tag{6.3}$$

For modelling the Reynolds stresses $(-\rho\overline{u'_\iota u'_\jmath})$ in Eq. (6.2), k-epsilon turbulence model was selected for this purpose. In equations 6.2 and 6.3, $\bar{u}_i$ and $\bar{u}_j$ are the time-averaged velocity components in the i-and j- directions respectively. $\bar{T}$ and $\bar{P}$ are the time-averaged temperature and pressure, respectively. The eddy viscosity model was utilised to calculate the Reynolds stresses components in the RANS equations, which uses the Boussinesq approximation to interconnect the stress and strain as [53]:

$$-\rho\overline{\acute{u}_\iota \acute{u}_\jmath} = \mu_t\left(\frac{\partial \bar{u}_i}{\partial x_j} + \frac{\partial \bar{u}_j}{\partial x_i}\right) - \frac{2}{3}\left(\rho\,\boldsymbol{k} + \mu_t \frac{\partial \bar{u}_k}{\partial x_k}\right)\,\delta_{ij} \tag{6.4}$$

where $\boldsymbol{k}$ is the turbulent kinetic energy per unit mass and it is given by:

$$\boldsymbol{k} = \frac{1}{2}\left(\overline{\acute{u}^2} + \overline{\acute{v}^2} + \overline{\acute{w}^2}\right) \tag{6.5}$$

The transport equations for the turbulent kinetic energy ($\boldsymbol{k}$) and the turbulent dissipation rate (ε) used in the realisable k-epsilon turbulence model are given by:

$$\frac{\partial}{\partial x_j}\left(\rho\boldsymbol{k}\bar{u}_j\right) = \frac{\partial}{\partial x_j}\left[\left(\mu + \frac{\mu_t}{\sigma_{\boldsymbol{k}}}\right)\frac{\partial \boldsymbol{k}}{\partial x_j}\right] + G_k - \rho\varepsilon \tag{6.6}$$

$$\frac{\partial}{\partial x_j}\left(\rho\varepsilon\bar{u}_j\right) = \frac{\partial}{\partial x_j}\left[\left(\mu + \frac{\mu_t}{\sigma_\varepsilon}\right)\frac{\partial \varepsilon}{\partial x_j}\right] + \rho\, C_1 S\, \varepsilon - \rho\, C_2 \frac{\varepsilon^2}{\boldsymbol{k} + \sqrt{\nu\varepsilon}} \tag{6.7}$$

Where G_k is the production of turbulent kinetic energy given by:

$$G_k = -\rho\overline{\acute{u}_\iota \acute{u}_\jmath}\frac{\partial u_j}{\partial x_i} \tag{6.8}$$

From the above equation, the production of turbulent kinetic energy (G_k) can be obtained as:

$$G_k = \mu_t\, S^2 \tag{6.9}$$

The eddy turbulence viscosity is calculated by:

$$\mu_t = \rho\, C_\mu \frac{\boldsymbol{k}^2}{\varepsilon} \tag{6.10}$$

Detailed determination of C_μ is given in [53]. The model constants for the realisable k-epsilon turbulence model are:

$C_1 = \max\left[0.43, \frac{\eta}{\eta+5}\right]$, $\eta = S\frac{\boldsymbol{k}}{\varepsilon}$, $S = \sqrt{2\, S_{ij}S_{ij}}$, $C_2 = 1.9$, $\sigma_{\boldsymbol{k}} = 1.9$, $\sigma_\varepsilon = 1.2$, and S_{ij} represents the rate of linear deformation of a fluid element.

The discrete ordinates radiation model equation is [53]:

$$\frac{dI(\vec{r},\vec{s})}{ds} + (\boldsymbol{a} + \sigma_s)\, I(\vec{r},\vec{s}) = a\, n^2 \frac{\sigma T^4}{\pi} + \frac{\sigma_s}{4\pi}\int_0^{4\pi} I\left(\vec{r},\acute{\vec{s}}\right)\Phi\left(\vec{s},\acute{\vec{s}}\right) d\acute{\Omega} \tag{6.11}$$

where $\vec{\boldsymbol{r}}$ is the position vector, $\vec{\boldsymbol{s}}$ is the direction vector, $\acute{\vec{\boldsymbol{s}}}$ is the scattering direction vector, s is the path length, $\boldsymbol{a}$ is the absorption coefficient, n is the refractive index, σ is the Stefan-Boltzmann constant, σ_s is the scattering coefficient, I is the radiation intensity, which depends on position $\vec{\boldsymbol{r}}$ and direction $\vec{\boldsymbol{s}}$, T is the local temperature, Φ is the phase function, and $\acute{\Omega}$ is the solid angle.

6.2.3 Boundary Conditions

The PTSC's absorber tube outer surface received a direct and concentrated solar radiation and then it is absorbed by a selective cermet coating and eventually converted into a heat. The absorber's inner upper half surface is exposed to a uniform heat flux boundary condition. The absorber's inner lower half surface is exposed to a nonuniform heat flux (concentrated solar radiation) boundary condition. This distribution was obtained from the mathematical expression by the Monte Carlo Ray Tracing (MCRT) method (Mwesigye et al., 2014) [14] as shown in Table 6.3. The direct normal irradiance (DNI) was assumed in this study to be 1000 W/m^2.

Table 6.3: Mathematical expression of the heat flux profile (Mwesigye et al., 2014) [14].

θ Range	$q = a_o + a_1\cos(\omega\theta) + b_1\sin(\omega\theta) + a_2\cos(2\omega\theta) + b_2\sin(2\omega\theta)$					
	$\boldsymbol{\omega}$	$\boldsymbol{a_o}$	$\boldsymbol{a_1}$	$\boldsymbol{b_1}$	$\boldsymbol{a_2}$	$\boldsymbol{b_2}$
$0° \le \theta \le 41.6°$	0	680	0	0	0	0
$41.6° \le \theta \le 88.6°$	5.88×10^{-2}	3.512×10^4	2.547×10^4	-2.425×10^4	-1.464×10^3	-6.71×10^3
$88.6° \le \theta \le 180°$	3.12×10^{-2}	5.616×10^4	-1.129×10^4	1.051×10^4	-4.039×10^3	-1.582×10^3

The majority of the heat is imposed on the absorber tube's outer wall is conducted to the inner wall and then carried away by the circulating hybrid nanofluid through heat convection. The absorber tube was made of stainless steel (32H) with a thermal conductivity of 25 W/m.K. The stainless steel was considered because it offers many advantages such as excellent corrosion resistance, life-cycle costing benefits, high

ductility and strength, non-magnetic, excellent high and low temperature properties, and resistance to unsightly staining. The inlet of the absorber tube is set to inlet velocity based on Reynolds number in the range of 5000 to 100000 and inlet fluid temperature in the range of 400 to 650K. The PTSC's absorber tube inner wall and the wavy promoter's surface are set as no-slip boundary conditions. The rest of heat is transmitted to the glass cover's inner surface by heat radiation and conduction modes when there is a small amount of gas in the annular gap. The discrete ordinates (DO) radiation mode was utilised to model the radiation heat transfer through the annular gap as presented in Eq.6.11. The cermet coating emissivity on the tube's outer wall is deemed temperature-dependent and it is calculated using the following equation (Mwesigye et al., 2014) [14]:

$$\boldsymbol{\varepsilon} = 0.062 + 2 \times 10^{-7}\, T^2 \tag{6.12}$$

where T is the absorber tube's temperature in Kelvin. The glass envelope is considered a gray-body and the glass inner wall's emissivity is assumed to be 1.

The heat, which is transported from the outer surface of the absorber tube to the inner surface of the glass envelope, is conducted to the glass envelope's outer surface and then carried away to the surroundings via convection and radiation mechanisms. The glass envelope is made of Pyrex with a thermal conductivity of 1.2 W/m.K. The external surface of the glass envelope is exposed to a combined boundary condition (that involves convection and radiation). The Stefan-Boltzmann law was utilised to calculate the net heat flux produced by the radiation mode. The external emissivity of the external surface of the glass envelope is assumed to be 0.89. The convection heat transfer coefficient, sky temperature and emissivity for heat transfer by radiation are calculated by the following correlations (Pandey et al., 1995) [54] and (Garcia-Valladares & Velazquez, 2009) [55]:

$$h_w = 4\ v_w^{0.58} d_{go}^{-0.42} \tag{6.13}$$

$$T_{sky} = 0.0552\, T_{amb}^{1.5} \tag{6.14}$$

$$\varepsilon_{sky} = 0.711 + 0.56 \left(\frac{T_{dp}-273.15}{100}\right) + 0.73 \left(\frac{T_{dp}-273.15}{100}\right)^2 \tag{6.15}$$

where v_w is the wind velocity (2 m/s utilised in this study), d_{go} is the glass cover outer diameter, T_{amb} is the surrounding temperature (assumed 300 K in this study), and T_{dp} is the dew point temperature.

6.2.4 Data Acquisition

The following parameters utilised in this study (Incropera & Dewitt, 2006) [56]:

The pressure drop is related to the friction factor according to:

$$\Delta P = f \frac{L}{d_{ri}} \frac{\rho\, u_m{}^2}{2} \tag{6.16}$$

Where f, ρ, d_{ri}, u_m, and L are the friction factor, hybrid nanofluid density, the absorber tube's inner diameter, the mean velocity in the absorber tube and the length of the tube, respectively.

The friction factor is evaluated using the following equation:

$$f = \frac{2\,\tau_w}{\rho\, u_m{}^2} \tag{6.17}$$

where τ_w is the shear stress.

The heat transfer coefficient (h) and Nusselt number (Nu) are calculated as follows:

$$h = \frac{q''}{(T_{ri} - T_b)} \tag{6.18}$$

where T_{ri}, and T_b are the average temperature of the absorber tube's inner wall and the bulk fluid temperature given as (T_{inlet}+T_{outlet}/2), respectively.

$$Nu_{av} = \frac{h\, d_{ri}}{\mathrm{k}} \tag{6.19}$$

where k and h are the thermal conductivity and average heat transfer coefficient, respectively.

The flow Reynolds number is calculated as:

$$Re = \frac{\rho\, u_m\, d_{ri}}{\mu} \tag{6.20}$$

where $u_m$is the mean velocity and d_{ri} is the absorber tube's inner diameter.

The circumferential temperature gradient of the absorber tube is defined as:

$$\Delta T = T_{abs.max} - T_{abs.min} \tag{6.21}$$

The thermal efficiency of the receiver tube is the ratio of the useful energy delivered to the energy of the solar and it is given by:

$$\eta_{th} = \frac{\dot{Q}_u - P_p/\eta_{el}}{A_a\, I_b} \tag{6.22}$$

In the above equation, $\dot{Q}_u = \dot{m}\, C_p(T_{outlet} - T_{inlet})$ is the heat transfer rate, $P_p = \dot{V}\, \Delta P$ is the pumping power, A_a is the collector's aperture area, I_b is the incident solar radiation and η_{el} is the product of typical efficiencies of the power block, the electrical generator, and the heat transfer fluid pump and it was assumed 32.7% (Wirz et al, 2014) [57].

The performance evaluation criterion factor (PEC) is calculated based on the fluid used (PEC_1) and based on the passive technique used (PEC_2) as given by:

$$PEC_1 = \left(\frac{Nu_{hnf}}{Nu_f}\right) / \left(\frac{f_{hnf}}{f_f}\right)^{1/3} \tag{6.23}$$

$$PEC_2 = \left(\frac{Nu_w}{Nu_o}\right) / \left(\frac{f_w}{f_o}\right)^{1/3} \tag{6.24}$$

Where the subscripts hnf, f, w and o refer to hybrid nanofluids, base fluid (Syltherm oil), PTSC with wavy promoters, and PTSC without promoters respectively.

The total entropy generation comes from irreversibilities of heat transfer $\left(S_{gen}^{H}\right)$ and fluid friction $\left(S_{gen}^{F}\right)$ and its formula is given:

$$\left(S_{gen}^{T}\right) = \left(S_{gen}^{F}\right) + \left(S_{gen}^{H}\right) \tag{6.25}$$

The entropy generation caused by irreversibility of fluid friction is calculated by:

$$\left(S_{gen}^{F}\right) = \frac{\mu}{T}\left(\frac{\partial u_i}{\partial x_j} + \frac{\partial u_j}{\partial x_i}\right)\frac{\partial u_i}{\partial x_j} + \frac{\rho\varepsilon}{T} \tag{6.26}$$

The entropy generation due to irreversibility of heat transfer is calculated by:

$$\left(S_{gen}^{H}\right) = \frac{k}{T^2}\,(\nabla T)^2 + \frac{\alpha_t}{\alpha}\,\frac{k}{T^2}\,(\nabla T)^2 \tag{6.27}$$

Where α and α_t are the thermal diffusivities, and k is the fluid's thermal conductivity.

The total entropy generation rates are first calculated for each control volume, then the total entropy generation rate over the whole computational domain was then calculated by integrating them over the entire volume V by:

$$\left(S_{gen}^{T}\right) = \iiint_V S_{gen}\, dV \tag{6.28}$$

The Bejan number, presents the irreversibility caused by heat transfer to the total entropy generation rate, is described as (Paoletti et al., 1989) [58]:

$$Be = \frac{(S_{gen}^{H})}{(S_{gen}^{T})} \tag{6.29}$$

The irreversibility of heat transfer is predominant when Be = 1, and the irreversibility of fluid friction is prevailing when Be = 0.

The entropy generation ratio (Ns), presents the total entropy generation of PTSC having wavy promoters to the total entropy generation of smooth PTSC, is described as:

$$Ns = \frac{(S_{gen}^{T})_{w}}{(S_{gen}^{T})_{0}} \tag{6.30}$$

The exergetic efficiency is described as the ratio of the useful work output of the system to the reversible work output for work-consuming systems and it can be assessed by (Mwesigye et al., 2018) [41]:

$$\eta_{exr} = \frac{Ex_u}{Ex_a} = \frac{\dot{m}C_{p,f}\left[(T_{out}-T_{in})-T_{amb}\ln\left(\frac{T_{out}}{T_{in}}\right)\right]}{A_a\, I_b\left[1+\frac{1}{3}\left(\frac{T_{amb}}{T_s}\right)^4-\frac{4}{3}\left(\frac{T_{amb}}{T_s}\right)\right]} \tag{6.31}$$

where T_{amb} is the ambient temperature, which is considered 300K in this work, and T_s is the sun's surface temperature, which is considered 5800K in this work.

6.2.5 Numerical Method

The commercial computational fluid dynamics software ANSYS FLUENT was utilised to solve the governing equations numerically. These equations are discretised by using the finite volume method (FVM). The convective terms in momentum and energy equations, the convective terms in equations of turbulence models (k-epsilon realizable) and discrete ordinates radiation model are discretised by utilising the second-order upwind scheme. The SIMPLE algorithm is applied for decoupling the velocity and pressure solution. The pressure is discretised by the scheme of PRESTO. The enhanced wall treatment method is implemented with lower values of y+ to ensure capturing the high resolution of gradients in the regions near the tube wall as recommended by [53]. The convergence criteria used in this study are 10^{-6} and 10^{-8} for the continuity equation and for all other variables, respectively.

6.2.6 Grid Optimisation

The mesh topology generated for the whole geometry for the PTSC with wavy promoters is shown in Figure 6.3. It is clearly seen that for the CFD simulations of the fluid domain, tetrahedral elements with highly refined grids in the regions near the PTSC inner wall are employed. Whilst, for the CFD simulations of the PTSC tube outer wall, vacuum and glass tube domains, structured hexahedral mesh is employed. Table 6.4 presents the evolution of the thermal efficiency and entropy generation rate of the PTSC tube inner wall at Re number of 10^4 and an inlet temperature of 500 K. It appears from the results that the grid model of 2339704 elements is adequately dense and is adopted in the current study because the maximum deviation was less than 2% for all tested parameters, which means that the number of grids does not influence the results, but the solution takes more time for converging.

(a)

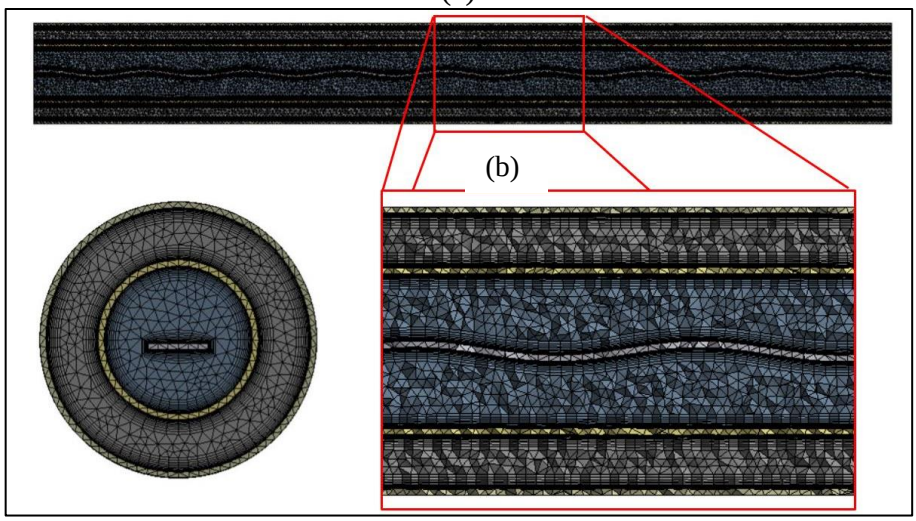

(c)

Figure 6.3 The mesh topology for PTSC tube equipped with wavy promoters, (a) Full geometry, (b) Lateral close-up view, and (c) Cross-sectional view.

Table 6.4: Mesh independence study for Re=10^4 and inlet temperature of 500 K.

Number of elements	Thermal efficiency (η%)	Entropy generation rate (S_{gen} (W/m.K))	η error %	S_{gen} error %
883741	61.03	0.281	-----	-----
1362436	62.08	0.273	1.73	2.94
2339704	62.83	0.268	1.21	1.87
2986426	62.93	0.265	0.16	1.14

6.2.7 Model Verification

The model's results were first validated in terms of average Nusselt number and friction factor with the available correlations data (Incropera & Dewitt, 2006) [56] using smooth PTSC receiver's tube. The results show same pattern with a maximum deviation of less than 5.1% as presented in Figures 6.4-6.5.

Correlation of Dittus-Boelter is:

$$Nu = 0.023\, Re^{0.8} Pr^{0.4} \tag{6.32}$$

Correlation of Filonenko is:

$$f = (1.82 \log_{10} Re - 1.64)^{-2} \tag{6.33}$$

Correlations of Gnielinski and Petukhov are given as:

$$Nu = \frac{f/8(Re-1000)Pr}{1.07+12.7(f/8)^{1/2}(Pr^{2/3}-1)} \tag{6.34}$$

$$f = (0.79 \log_{10} Re - 1.64)^{-2} \tag{6.35}$$

Figures 6.4-6.5 show that the results of average Nusselt number and friction factor are within the acceptable ranges with a deviation of 3.2% and 1.82% respectively for smooth tubes. The results are also compared using different turbulent models (k-epsilon and k-omega SST) as shown in Figure 6.5. The results revealed that the estimations by using k-omega SST model are much better than k-epsilon model as it matched well with the experimental correlations with a maximum deviation of 4.1% and 5.3% for Nusselt number and friction factor, respectively.

Figure 6.6a-b shows the comparison of the present numerical results with the experimental results of (Pak and Cho, 1998) [59], and the numerical results of (Mwesigye et al., 2015)

[60] and (Mwesigye et al., 2016) [61] using nanofluids. The results show a good agreement between the two studies with relative deviations of 4.2% for Nusselt number ratios and 2.3% for friction factor ratios. In addition, the thermal efficiency and thermal loss of a smooth receiver are compared with the experimental data of (Dudley et al., 1994) [62] and (Dreyer et al., 2010) [63] to verify the calculations of the present numerical model as shown in Figure 6.7a-b. A good agreement was also obtained with deviations less than 3.6% for the thermal efficiency and 0.62% for the thermal loss. Therefore, the numerical model is valid and provides reliable results.

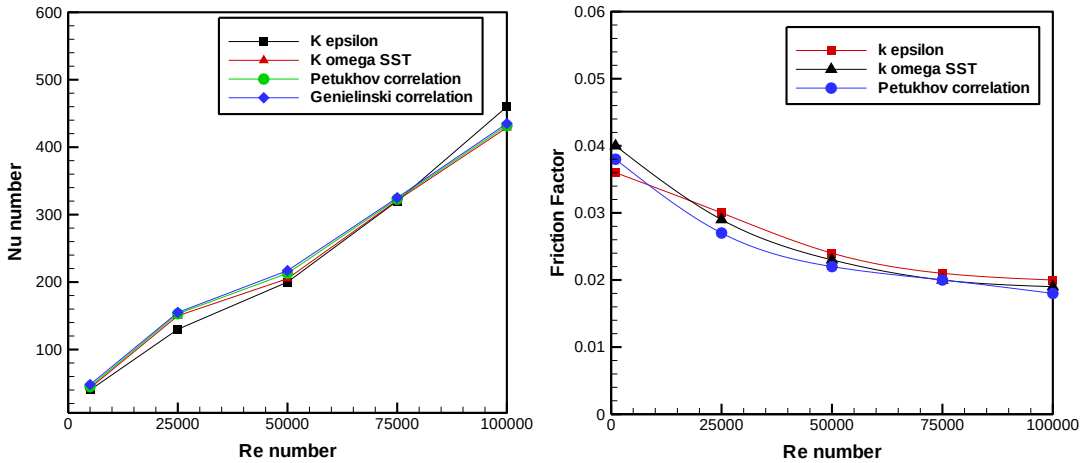

(b) (b)

Figure 6.4 Comparison of the present results with the available empirical correlations data, (a) Nusselt number, (b) Friction factor.

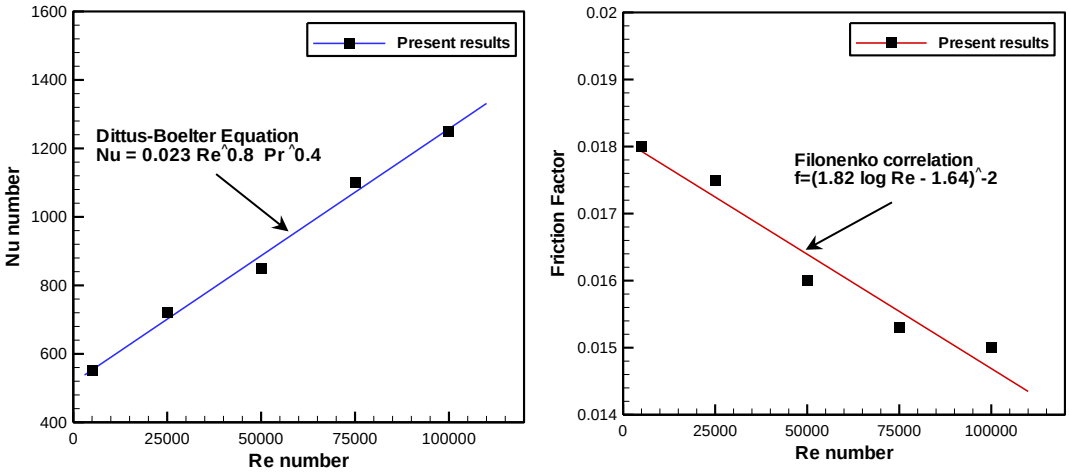

(a) (b)

Figure 6.5 Comparison of the present results with the available empirical correlations data, (a) Nusselt number, (b) Friction factor.

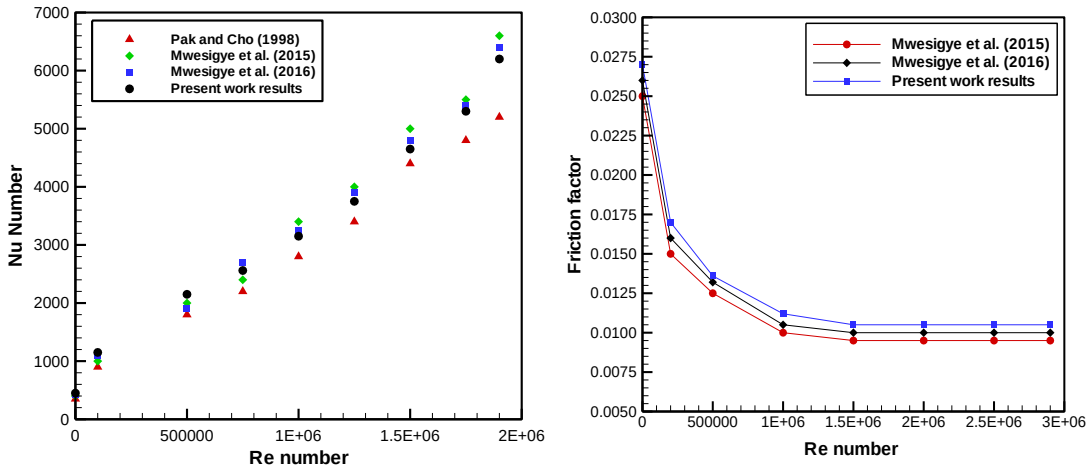

(b) (b)

Figure 6.6 Comparison of the present results with the available experimental and numerical data of (Pak and Cho, 1998) [59], (Mwesigye et al., 2015) [60] and (Mwesigye et al., 2016) [61] using nanofluids, (a) Nu number at $\phi = 6\%$, (b) friction factor at $\phi = 4\%$.

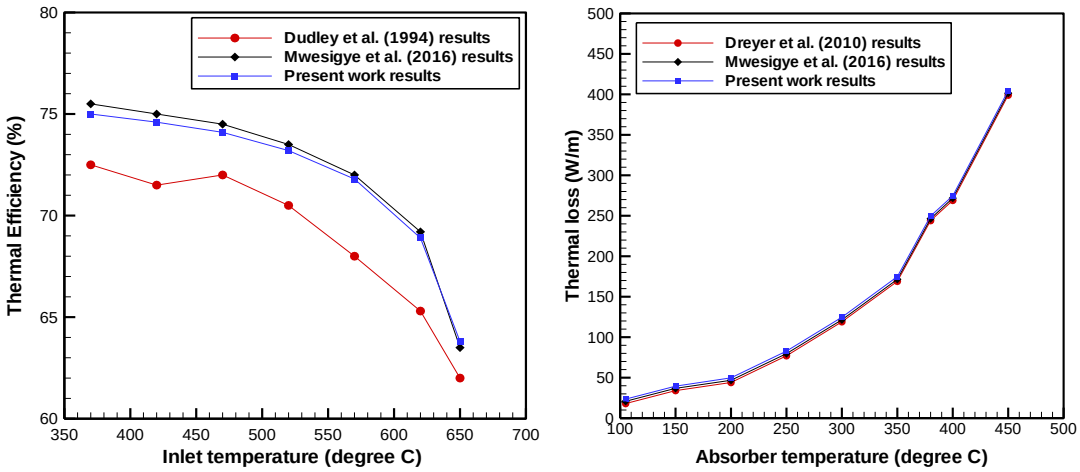

(a) (b)

Figure 6.7 Comparison of the present results with the available experimental and numerical data of (Dudley et al., 1994) [62] and (Dreyer et al., 2010) [63], (a) Thermal efficiency, (b) Thermal loss.

6.2.8 Thermophysical Properties

The effective properties of the resultant hybrid nanofluid (Fe_2O_3-GO/ Syltherm800, Fe_2O_3-SiC/ Syltherm800, and Fe_2O_3-TiO_2/ Syltherm800) mixture substantially rely upon the properties of the individual component of the mixture. In this work, graphene oxide and other selected nanoparticles have been chosen because they are trending material with exceptional electrical, mechanical, and thermal properties and it can significantly improve the properties of host materials and liquids (Raza et al., 2018) [64] and (Aized et al., 2018) [65]. The chosen materials possess highest thermal conductivity, great suspension stability and well-dispersed feature in a base-fluid (Ghosh et al., 2008) [66]. These exceptional characteristics attracted the current study to conduct an in-depth research on these nanoparticle combinations, as they would have a great impact on enhancing the PTSC thermal performance. In this work, the Syltherm800 oil thermophysical properties are considered temperature-dependent using polynomials equations (Dow, 2012) [67] as presented in Table 6.5. The thermophysical properties values of Syltherm-800 and different nanoparticles are tabulated in Table 6.6.

Table 6.5: Thermophysical properties equations of Syltherm-800 (Dow, 2012) [67].

Properties	$a + b\,T + c\,T^2 + d\,T^3 + e\,T^4$				
Constants	**a**	**b**	**c**	**d**	**e**
Dynamic Viscosity, Pa.s	8.4866×10^{-2}	-5.5412×10^{-4}	1.3882×10^{-6}	-1.5660×10^{-9}	6.672×10^{-13}
Thermal conductivity, W/m.K	1.9002×10^{-1}	-1.8752×10^{-4}	-5.7534×10^{-10}	—	—
Specific heat capacity, J/kg.K	1.1078×10^{3}	1.7080	—	—	—
Density, kg/m^3	1.1057×10^{3}	-4.1535×10^{-1}	-6.0616×10^{-4}	—	—

Table 6.6: Properties of Syltherm-800 and different nanoparticles used in this study.

Materials	***ρ (kg/m³)***	***κ (W/m.K)***	***μ (Pa.s)***	***C_p (J/kg.K)***	**Reference**
Syltherm-800	747.2	0.0961	0.00084	1962	(Minea & El-Maghlany, 2018) [68]
Ferric oxide (Fe_2O_3)	5180	6.9	—	670	(Khoshvaght-Aliabadi et al., 2014) [69]
Graphene Oxide (GO)	1800	5000	—	717	(Azimi et al., 2014) [70]
Silicon Carbide (SiC)	3160	117.56	—	723	(Sahoo & Sarkar, 2017) [71]
Titanium dioxide (TiO_2)	4250	8.9538	—	686.2	(Khoshvaght-Aliabadi et al., 2014) [69]

The effective density (ρ_{hnf}) and specific heat $(C_P)_{hnf}$ of the hybrid nanofluid at the reference temperature (T_{in}) are determined by utilising the following equations (Pak & Cho, 1998) [59], (Takabi & Salehi, 2014) [72]:

$$\rho_{hnf} = (1 - \phi_p)\rho_{bf} + \phi_{p1}\,\rho_{p1} + \phi_{p2}\,\rho_{p2} \tag{6.36}$$

where ϕ_p, ρ_p, are the volume fraction and density of nanoparticles and ρ_{bf} is the density of the base fluid. Subscripts 1 and 2 are for nanoparticle number 1 (i.e. Fe_2O_3) and nanoparticle number 2 (i.e. GO, SiC, and TiO_2).

$$(C_p)_{hnf} = \frac{[(1-\phi_p)\,\rho_{bf}C_{bf} + \phi_{p1}\,\rho_{p1}C_{p1} + \phi_{p2}\,\rho_{p2}C_{p2}]}{\rho_{hnf}} \tag{6.37}$$

where C_{bf}, ρ_{bf} are the specific heat and density of the base fluid and C_p is the specific heat of nanoparticles.

Most of the previous studies mentioned in the literature section have considered only the spherical-shaped nanoparticles. Thus, it is very important for this study to consider the effect nanoparticle shapes (spherical, platelets, blades, cylindrical and bricks) on the thermophysical properties of hybrid nanofluids as this would consequently affect the PTSC's overall performance. The following thermal conductivity and dynamic viscosity equations were used (Timofeeva et al., 2009) [73]:

$$k_{hnf} = k_{bf}\left[1 + \left(C_k^{shape} + C_k^{surface}\right)\phi\right] = k_{bf}[1 + C_k\phi] \tag{6.38}$$

where k_{hnf} is thermal conductivity of hybrid nanofluid, k_{bf} is the thermal conductivity of the base fluid, and C_k is the thermal conductivity ratio, which can be obtained by using the available data in Table 6.7.

Table 6.7: The nanoparticle shape effect on the thermal conductivity (Timofeeva et al., 2009) [73].

Type	Schematic	Aspect ratio	C_k	C_k^{shape}	$C_k^{surface} = C_k - C_k^{shape}$
Platelets		1:1/8	2.61	5.72	-3.11
Blades		1:6:1/12	2.74	8.26	-5.52
Cylindrical		1:8	3.95	4.82	-0.87
Bricks		1:1:1	3.37	3.72	-0.35

The effective dynamic viscosity of hybrid nanofluid (μ_{hnf}) is estimated using the following equation (Timofeeva et al., 2009) [73]:

$$\mu_{hnf} = \mu_{bf}\left[\left(1 + a\,\phi_{p1} + b\,\phi_{p1}{}^{2}\right) + \left(1 + a\,\phi_{p2} + b\,\phi_{p2}{}^{2}\right)\right] \tag{6.39}$$

where a and b are the morphology constants which can be obtained from Table 6.8.

Table 6.8: Viscosity coefficients for different nanoparticle shapes (Timofeeva et al., 2009) [73].

Morphology constants	**Platelets**	**Blades**	**Cylindrical**	**Bricks**
a	37.1	14.6	13.5	1.9
b	612.6	123.3	904.4	471.4

6.3 Results and Discussion

The impacts of hybrid nanofluid type, nanoparticles concentration, nanoparticles shape, fluid inlet temperature, and Reynolds number in the range of 5000 to 100000 at nanoparticle diameter of 50 nm on the thermohydraulic assessment, entropy reduction and exergetic efficiency of PTSC equipped with wavy promoters are analysed and interpreted in this section.

6.3.1 Heat Transfer Characteristics

The heat transfer assessment has been conducted in this subsection for various parameters. Figure 6.8(a)-(d) shows the absorber's tube average temperature variation versus Re number for different hybrid nanofluid types, different fluid inlet temperatures, different nanoparticle concentrations, and shapes, respectively. It is noticed from Figure 6.8(a) that the Syltherm oil has the highest outlet temperature of the absorber's tube. Whilst the hybrid nanofluid of Fe_2O_3-GO has the lowest temperature, because of its exceptional thermophysical properties and its higher convective heat transfer (lower temperature). This means that the random movements of Fe_2O_3-GO hybrid nanoparticles enhance the thermal dispersion of the flow better than Syltherm oil and other hybrid nanoparticles. This is then followed by Fe_2O_3-SiC and then Fe_2O_3-TiO_2, which have moderate temperature variation. Figure 6.8(b) displays that the absorber's tube average temperature was highest at an inlet temperature of 650K, while it has the lowest values at an inlet temperature of 400K. Figure 6.8(c) shows that the absorber's tube average temperature diminishes with the increment of the nanoparticle concentration. The results revealed that the Syltherm oil with (ϕ=0%) has the highest average temperature, while the hybrid nanofluid of Fe_2O_3-GO with (ϕ=2%) has the lowest average temperature, which makes it an alternative coolant in PTSC frameworks. This decrease in absorber's tube average temperatures can be attributed to the increased thermal conductivity in the presence of hybrid nanofluids with different nanoparticle types. Consequently, remarkable decrease in the absorber's average temperatures can be achieved particularly at high Re numbers. Figure 6.8(d) shows that the absorber's tube average temperature was highest for platelets shape nanoparticles, while it has the lowest values for bricks shape nanoparticles for hybrid nanofluid of Fe_2O_3-GO with (ϕ=2%) at an inlet temperature of 400K. This is because of the maximum heat transfer coefficient for the brick-shaped nanoparticles. In addition, the utilisation of the platelets shape nanoparticles leads to less nanofluids flow compared to other nanoparticle shapes, which indicates that lower solar energy is absorbed by the top section of the absorber tube. It is worth noting that the absorber's average temperatures are decreased by approximately 7-31°C for all the cases examined in this

work. Though these are considerably small and moderate values, given that temperature is raised to a power of four in the determination of receiver thermal losses, a small reduction in temperature will result in a much higher reduction in the energy transferred by radiation from the absorber tube. Moreover, when the flow rates are lower, significant reductions in absorber tube temperatures can be achieved with heat transfer enhancement (Mwesigye et al., 2016) [61].

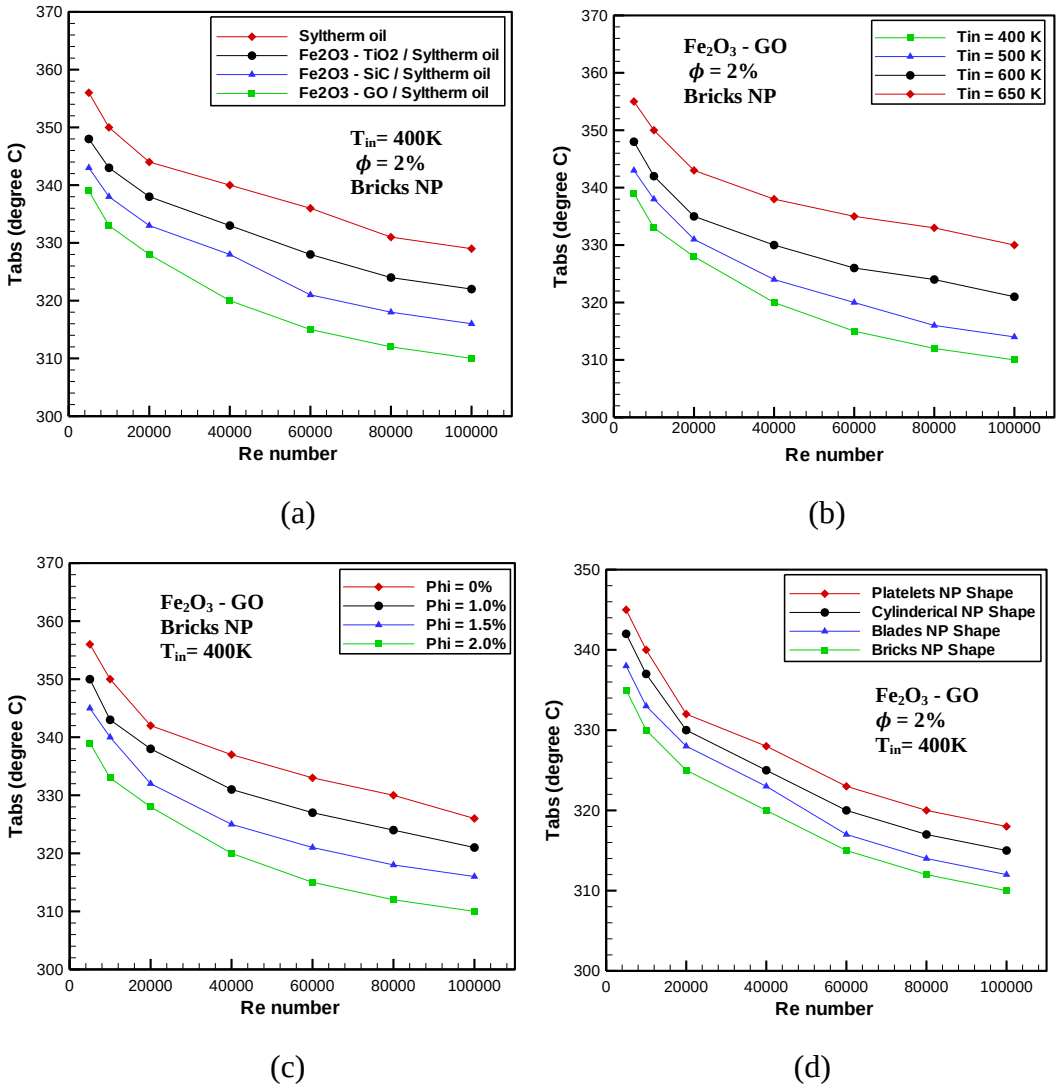

Figure 6.8 The absorber tube average temperature variation versus Re number for various, (a) hybrid nanofluid types, (b) inlet fluid temperatures, (c) nanoparticle concentrations, and (d) nanoparticle shapes.

The average Nusselt number profile versus Re number is plotted in Figure 6.9(a)-(d). The outcomes reveal that all hybrid nanofluids types produce higher average Nusselt number values when Re number increases. This is due to the improved heat transfer performance with increasing Re number due to the thinner thermal boundary layer at high flow rates. It is also apparent that to achieve the same Nusselt number as for the high thermal conductivity hybrid nanofluid, the flow rate of the low thermal conductivity hybrid nanofluid has to be increased. It is evident from Figure 6.9(a) that the nanofluid with Fe_2O_3-GO/Syltherm oil hybrid nanofluid has the highest average Nusselt number, followed by Fe_2O_3-SiC/Syltherm oil and Fe_2O_3-TiO_2/Syltherm oil, and pure Syltherm oil, respectively. This is in line with the thermal conductivity of the nanoparticles used, where Fe_2O_3-GO hybrid nanofluid has the highest thermal conductivity and lowest density (i.e. highest average velocity) compared to other hybrid nanofluids and Syltherm oil. These two significant properties contributed to increase the thermal transport capacity of the mixture, which in turn increases the Nusselt number and then consequently produced high thermal performance. Figure 6.9(b)-(c) reveal that the fluid inlet temperature of 650K and nanoparticle concentration of (ϕ=2%) have the highest Nusselt number values. While the fluid inlet temperature of 400K and nanoparticle concentration of (ϕ=0%) have the lowest values. This is anticipated as at higher fluid inlet temperatures, the hybrid nanofluid is less dense and less viscous and thus it can move the heat energy more viably. Generally, the heat transfer performance will improve as the hybrid nanofluid is heated along the length of the receiver's absorber tube. This is mainly due to the reduction in both fluid density and viscosity with temperature increment. Furthermore, the Nusselt number is enhanced when the nanoparticle volume fraction and Re number rise. This is basically because of the resulted high thermal conductivity of hybrid nanofluid even at low concentrations (Mwesigye et al., 2015) [60]. Figure 6.9(d) reveals that the bricks shape nanoparticles have the highest Nusselt number, while the platelets nanoparticles have the lowest Nusselt number values for hybrid nanofluid of Fe_2O_3-GO with (ϕ=2%) at an inlet temperature of 650K. The brick-shaped nanoparticles show higher thermal conductivity values among other nanoparticle shapes. This means, the thermal conductivity is not the only aspect that increases the Nu number of a PTSC; and the absorption capability is also another

important factor (Tong et al., 2019) [74]. Furthermore, that means the utilisation of the bricks nanoparticles leads to more nanofluids flow compared to other nanoparticle shapes, which indicates that higher solar energy is absorbed by the absorber tube. It is worth noting that the Nusselt number improvement is in the range of 3.1-150.2% for all the parameters and for all cases examined in this work.

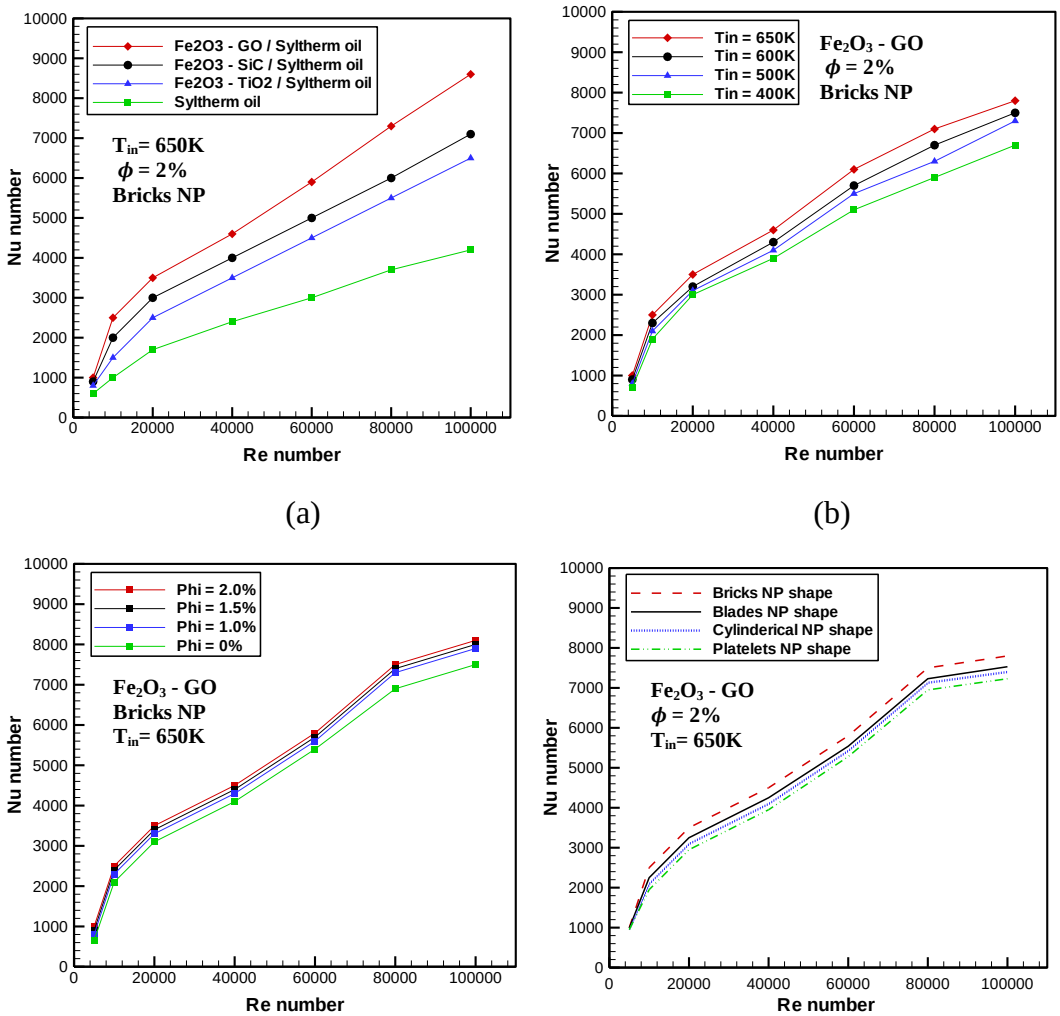

Figure 6.9 The Nu number variation versus Re number for various, (a) hybrid nanofluid types, (b) inlet fluid temperatures, (c) nanoparticle concentrations, and (d) nanoparticle shapes.

6.3.2 Hydraulic Characteristics

The variation of the friction factor for versus Re number is plotted in Figure 6.10(a)-(d). It is noticed that the friction factor rises with the increment of Re number and nanoparticle volume fraction. The results indicate that all hybrid nanofluids types provide higher friction factor values when Re number increases because of the increased viscosity and density of the resulting hybrid nanofluids. It is found from Figure 6.10(a) that at T_{in}=650K and ϕ=2% the hybrid nanofluid of Fe_2O_3-TiO_2/Syltherm oil has the lowest friction factor, followed by Fe_2O_3-SiC/Syltherm oil and Fe_2O_3-GO/Syltherm oil, respectively while pure Syltherm oil shows the least values compared with all hybrid nanofluid types. This is because of the highest viscosity effect of all hybrid nanofluid and lowest density (i.e. highest average velocity) compared to Syltherm oil, which both contributed to the high-pressure drop penalty. Figure 6.10(b)-(c) reveal that the fluid inlet temperature of 400K and nanoparticle concentration of (ϕ=2%) have the highest friction factor values while the fluid inlet temperature of 400K and nanoparticle concentration of (ϕ=0%) have the lowest values. It should be mentioned that the wavy promotors disturb the fluid's movement, which causes a remarkable boost in the flow resistance contrasted to the plain PTSC. It is demonstrated in Figure 6.10(d) that the bricks-shaped nanoparticles have the lowest friction factor, while the platelets-shaped nanoparticles have the highest friction factor values for hybrid nanofluid of Fe_2O_3-GO with (ϕ=2%) at an inlet temperature of 650K. That means the utilisation of the bricks nanoparticles leads to less pressure loss of hybrid nanofluids flow compared to other nanoparticle shapes, which indicates that less pumping power demand is required by the absorber tube. It is worth noting that the friction factor increase is about 22.2-39.1% for all the parameters examined in this work.

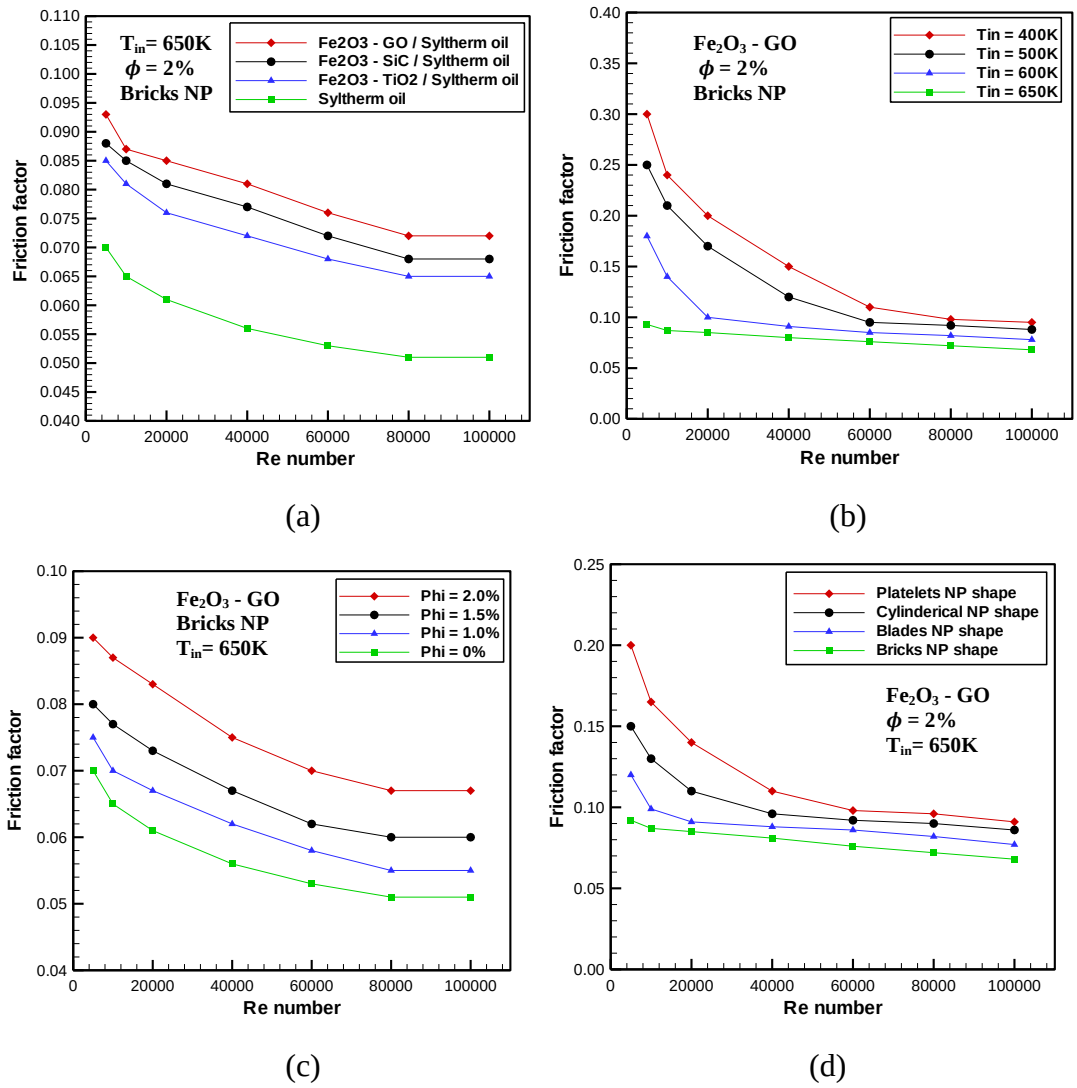

Figure 6.10 The friction factor variation versus Re number for various, (a) hybrid nanofluid types, (b) inlet fluid temperatures, (c) nanoparticle concentrations and (d) nanoparticle shapes.

Figure 6.11 shows the contours of the total pressure of the absorber tube at various Re numbers and concentrations of Fe_2O_3-GO hybrid nanofluid. The range of colors (blue to red) represents the pressure range (minimum to maximum) within the absorber tube. The total pressure of the absorber tube's inner wall increases as the Re increases for Syltherm oil and Fe_2O_3-GO hybrid nanofluid. The results affirmed that the pressure drop depends on the concentration of Fe_2O_3-GO hybrid nanofluid and flow velocity. Additionally, the pressure drop increment can be attributed to the momentum diffusivity of the circulating

fluids. The pressure loss can be directly linked to the fluid's viscosity, where the increase in the latter increases the pumping power, which deemed a detrimental effect on the hydraulic performance of the PTSC.

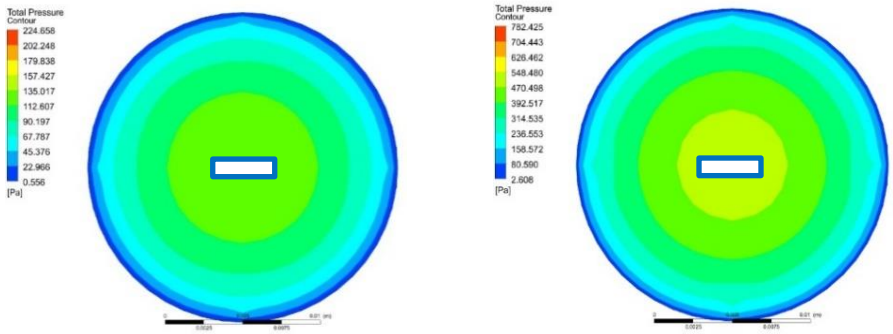

Re = 20000 Re = 100000

Syltherm Oil (ϕ = 0%)

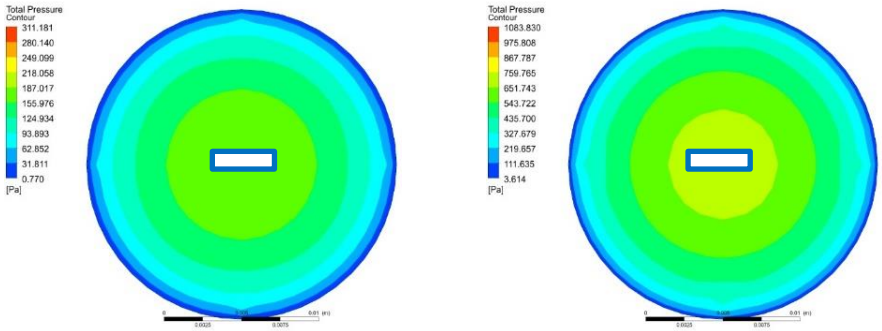

Re = 20000 Re = 100000

Fe_2O_3-GO/Syltherm oil (ϕ = 1.0%)

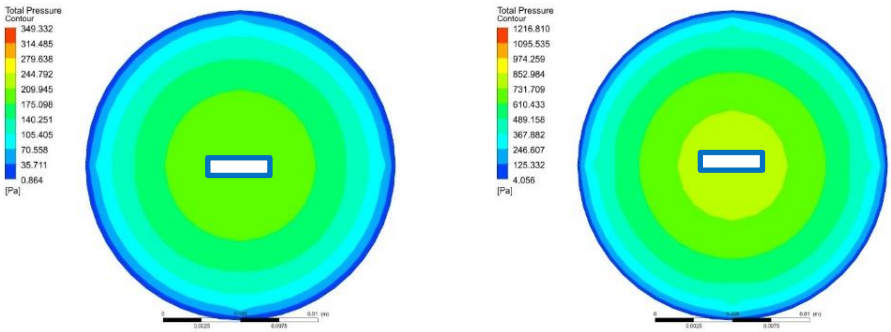

Re = 20000 Re = 100000

Fe_2O_3-GO/Syltherm oil (ϕ = 1.5%)

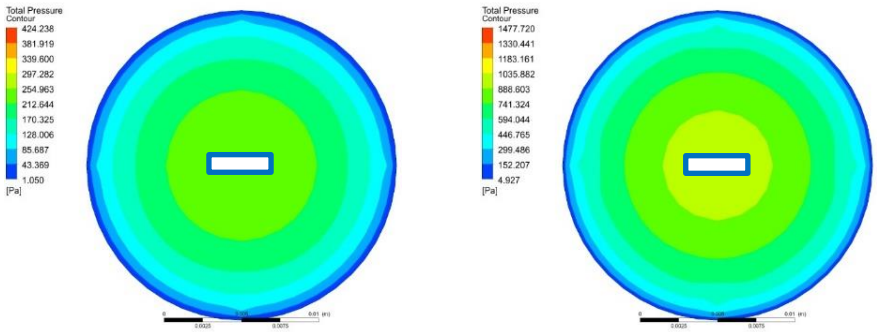

Re = 20000 Re = 100000

Fe_2O_3-GO/Syltherm oil (ϕ = 2.0%)

Figure 6.11 Total pressure contours of Syltherm oil and Fe_2O_3-GO hybrid nanofluid at various Re numbers and concentrations.

The PEC used to evaluate the heat transfer enhancement at similar pumping work demand is depicted in Figure 6.12(a)-(d). The PEC values calculated for PTSC tube with and without nanofluids is called (PEC1) and its values also calculated for PTSC tube equipped with and without wavy promoters is called (PEC2). Figure 6.12(a) indicates that at T_{in}=650K and ϕ=2% all hybrid nanofluids provides higher PEC values at lower Re numbers and it decreases gradually as Re number rises. This is because of the substantial decrement in the heat losses at low Re numbers. The results revealed that hybrid nanofluid of Fe_2O_3-GO/Syltherm oil provides the highest PEC value in the range of 1.24-2.46 followed by Fe_2O_3-SiC/Syltherm oil and Fe_2O_3-TiO_2/Syltherm oil, respectively. From the results of average Nusselt number and PEC, it can be concluded that the wavy promoter can improve the heat transfer performance inside the PTSC's receiver tube by generating swirl flow. This enhancement would be beneficial to the decreases of both PTSC structure temperature and total heat loss. In particular, the wavy promoter differs from other passive techniques in a way that it can lead to highly localized heat transfer enhancement effect near its two flanks. This is very applicable to the PTSC system to cope with the highly concentrated solar load contrapuntally. When the wavy promoter flanks aim at the solar energy focused area, the high-density heat load can be carried away efficiently by the intensive vortexes deployed by the wavy-promoter. Consequently, the structure

temperature of both absorber tube and glass envelop can be greatly decreased. It is noticed that the PEC increases as the inlet fluid temperature increases as shown in Figure 6.12(b). This is due to the enhancement in Nusselt number and decrement in friction factor as observed earlier in Figures 9(b) and Figure 6.10(b), respectively. The PEC is observed to rise with the increment of the nanoparticle volume fraction as shown in Figure 6.12(c). For example, the increase in PEC value at Re = 20000 for 1%, 1.5% and 2% nanoparticle volume fraction of Fe_2O_3-GO/Syltherm oil hybrid nanofluid is 37.5%, 41.2% and 44.4%, respectively. It is realised from Figure 6.12(d), for Fe_2O_3-GO hybrid nanofluid with (ϕ=2%) at an inlet fluid temperature of 400K, that the best PEC belongs to the bricks-shaped nanoparticles as expected and its value is around 2.46, while the least PEC belongs to platelets-shaped nanoparticles and its value is around 1.24. It is also evident from the PEC results that that the PEC value for hybrid nanofluids is significantly higher than the plain PTSC tube. That means the hybrid nanofluid has superior thermal and hydraulic performance than other suspensions.

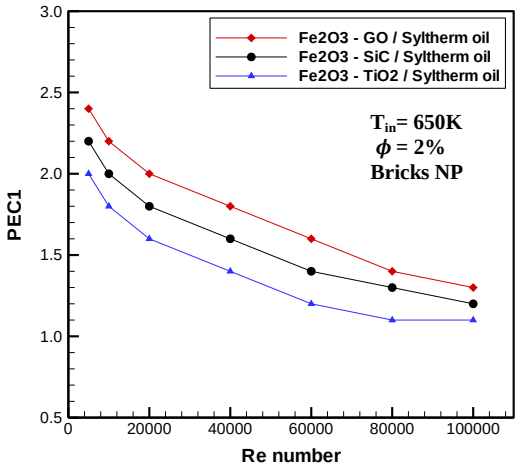

(a)

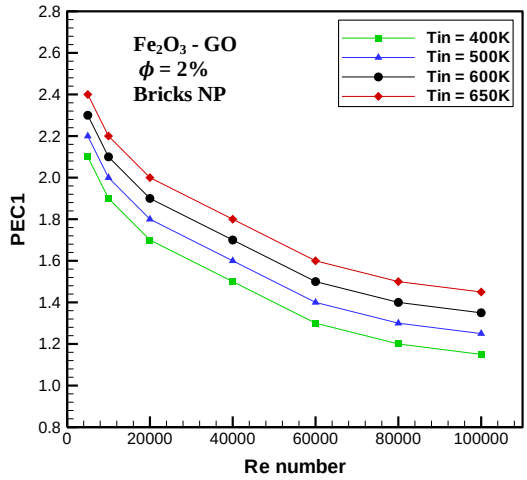

(b)

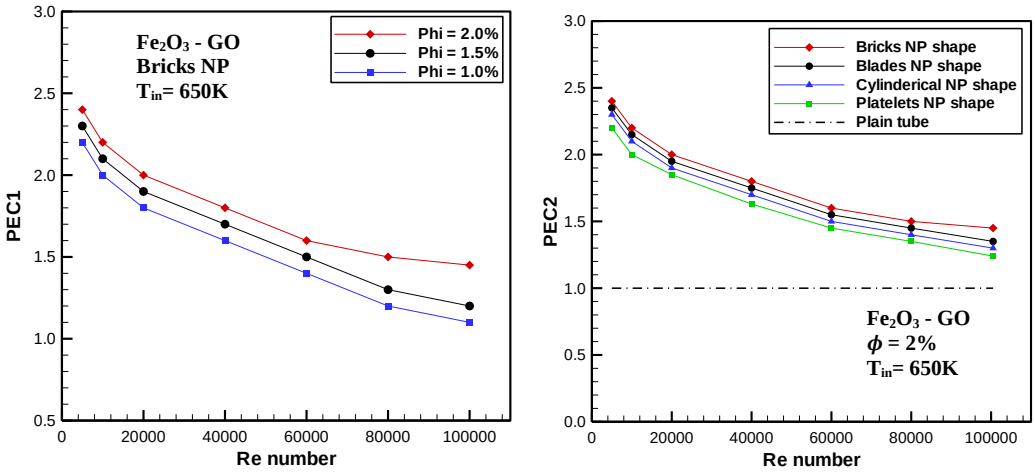

(c) (d)

Figure 6.12 The PEC variation versus Re number for various, (a) hybrid nanofluid types, (b) inlet fluid temperatures, (c) nanoparticle concentrations, and (d) nanoparticle shapes.

6.3.3 Thermal and Exergetic Efficiencies

The PTSC's thermal efficiency deems the performance augmentation due to the enhanced heat transfer at the penalty of thermal losses and pumping work demand. Figure 6.13(a)-(d) shows the thermal efficiency versus reduced temperature parameter various parameters considered in this study. It is generally observed that thermal efficiency rises up to a specific value and then it starts to diminish with the increase of reduced temperature parameter. This is due to the increment of pumping power as Re number increases which gets remarkably higher than the useful heat gain. Additionally, it is due to the decrement in the absorber's tube temperature with thermal augmentation and consequently the decrement of absorber's thermal losses as reported by (Mwesigye et al., 2014) [14]. It is found from Figure 6.13(a) that the thermal efficiency is prevailed highest for Fe_2O_3-GO/Syltherm oil and lowest for Fe_2O_3-TiO_2/Syltherm oil. For instance, hybrid nanofluid of Fe_2O_3-GO/Syltherm oil is increased the thermal efficiency up to 18.51% with reasonable friction factor as shown in Figure 6.13(a). This indicates that this hybrid nanofluid can be utilised and to be the best-suited working fluid among other fluids examined in this study in PTSC frameworks. The thermal efficiency variation with different inlet fluid temperatures at a specific volume fraction of 2% is plotted in Figure

6.13(b). It is noticed that the thermal efficiency has higher values at lower inlet fluid temperatures due to the low absorber's temperature and thus lower thermal losses. It is worth noting that rising the inlet fluid temperature refers to higher absorber's tube temperature, which increases the absorber's tube thermal losses, due to the radiation mode, which occurs from the high temperature medium (absorber's tube) to the low temperature medium (the surroundings). Besides that, as the hybrid nanofluid is dense and more viscous at low temperatures, the thermal efficiency rises to a highest value and then it starts to diminish due to the boosted pumping work demand as Re number increases. The thermal efficiency rises as the nanoparticle volume fraction rises as shown in Figure 6.13(c). As shown, at a given volume fraction, the thermal efficiency is highest at low reduced temperature parameter, which depends on the flow rate or Reynolds number, and it reaches a maximum value and then starts to reduce with a further increase in the reduced temperature parameter. At low reduced temperature parameter, the thermal transfer performance is lower and an increase in the flow rate increases the thermal performance with low pumping power requirements. As the reduced temperature parameter or Reynolds numbers increase, the pumping power also increases until the increase in pumping power becomes more than the increase in the useful energy delivered, which causes the efficiency to start reducing. For example, if hybrid nanofluid of Fe_2O_3-GO/Syltherm oil is to be used at (T_{in}-T_{amb}/I_b) = 0.3 with 1%, 1.5% and 2% nanoparticle concentration instead of base fluid (Syltherm oil in this case), there would be an increment in the thermal efficiency of 4.12%, 6.68% and 8.2%, respectively. It is found that the variation of thermal efficiency presented in Figure 6.13(d) is that same as the PEC results shown in Figure 6.13(d). It is demonstrated that the bricks shape nanoparticles have the highest thermal efficiency, while the platelets nanoparticles have the lowest thermal efficiency values for hybrid nanofluid of Fe_2O_3-GO with (ϕ=2%) at an inlet fluid temperature of 400K. It is important to highlight that the results of the thermal efficiency using hybrid nanofluids are significantly higher than the plain PTSC tube.

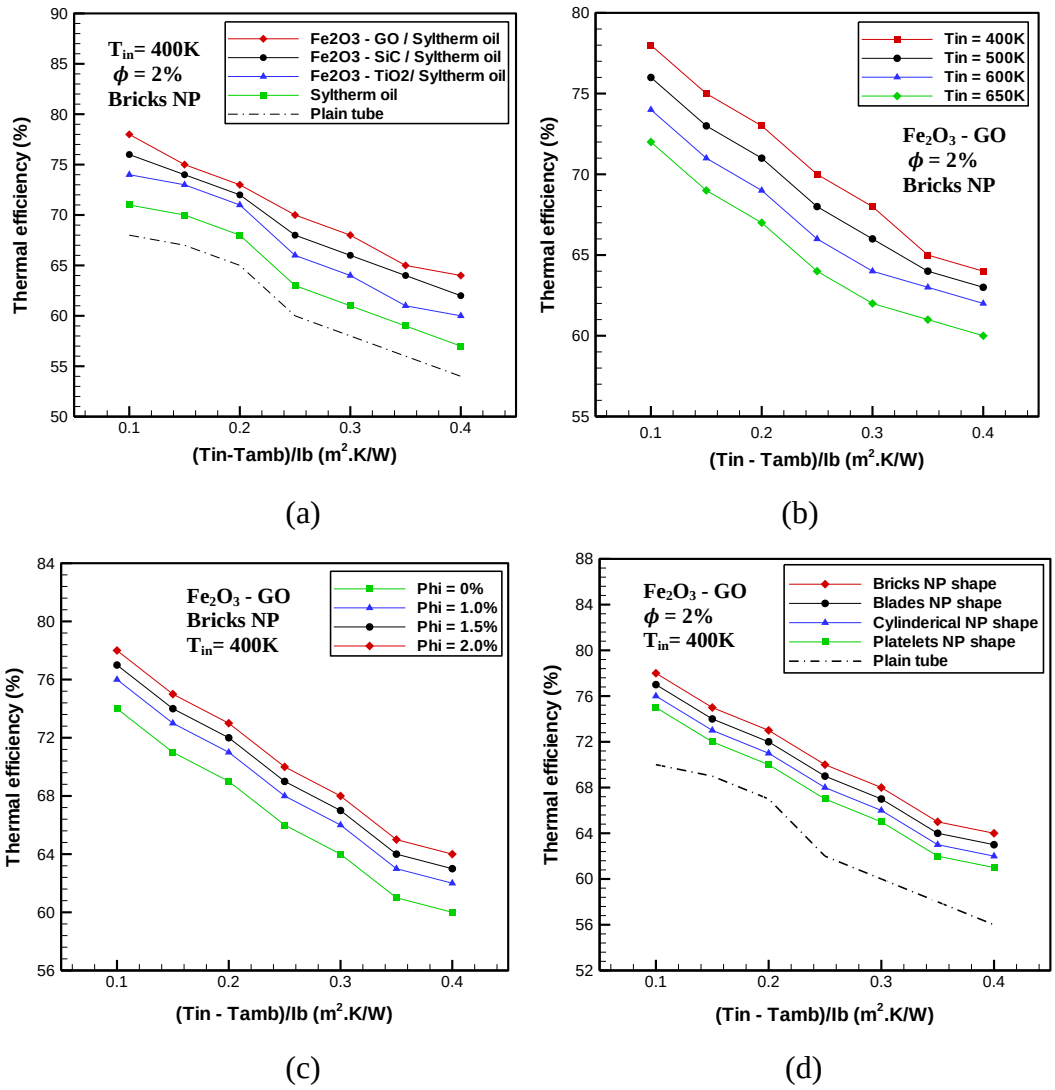

Figure 6.13 The thermal efficiency variation versus reduced temperature parameter for various, (a) hybrid nanofluid types, (b) inlet fluid temperatures, (c) nanoparticle concentrations, and (d) nanoparticle shapes.

It is critical to conduct exergy analysis alongside with energy analysis to evaluate the real work potential of PTSC systems. Exergy analysis will also help to figure out the work potential that is being lost by any particular part of the system. This technique would be helpful in finding where and in which part the useful work is destroyed the most (Hepbasli, 2008) [75]. Thus, the exergetic efficiency was evaluated as an indication of the exergetic performance and its results versus Re number for various parameters are plotted in Figure 6.14(a)-(d). Figure 6.14(a) portrays that the exergetic efficiency diminishes gradually as

Re number rises and becomes relatively steady. It is observed that the hybrid nanofluid of Fe_2O_3-GO/Syltherm oil has the highest exergetic efficiency compared with other hybrid nanofluids. While, the base fluid (Syltherm oil) has the lowest exergetic efficiency value. Figure 6.14(b) indicates that the exergetic efficiency remarkably rises as the fluid inlet temperature rises. It can be noticed that, at lower inlet temperatures, the exergetic efficiency declines as Re number rises due to the high irreversibilities and lower thermal losses. This implies continuous decrement of the available energy and thus the exergetic efficiency. Nevertheless, at high inlet fluid temperatures, the situation is different as the irreversibilities are lower, the thermal losses are higher, and they rise as Re number rises. This increases the available energy and reduces the irreversibilities. As Re number rises further, the irreversibilities due to fluid friction rise and cause a decline in the exergetic efficiency. The maximum exergetic efficiency achieved in this work is 48.6% and the lowest value was around 23.2%. Figure 6.14(c) shows that the exergetic efficiency of Fe_2O_3-GO/Syltherm oil hybrid nanofluid at T_{in}= 650K increases with the increase of the nanoparticle concentrations. It is found that the variation of exergetic efficiency presented in Figure 6.14(d) is that same as the thermal efficiency results shown in Figure 6.13(d). The results reveal that the bricks shape nanoparticles have the highest exergetic efficiency, while the platelets nanoparticles have the lowest exergetic efficiency values for hybrid nanofluid of Fe_2O_3-GO with (ϕ=2%) at an inlet fluid temperature of 650K. It is significant to highlight that the exergetic efficiency of hybrid nanofluids are remarkably higher than the plain PTSC tube. It is also essential to highlight that the maximum augmentation in the exergetic efficiency obtained in this work is about 16.21%.

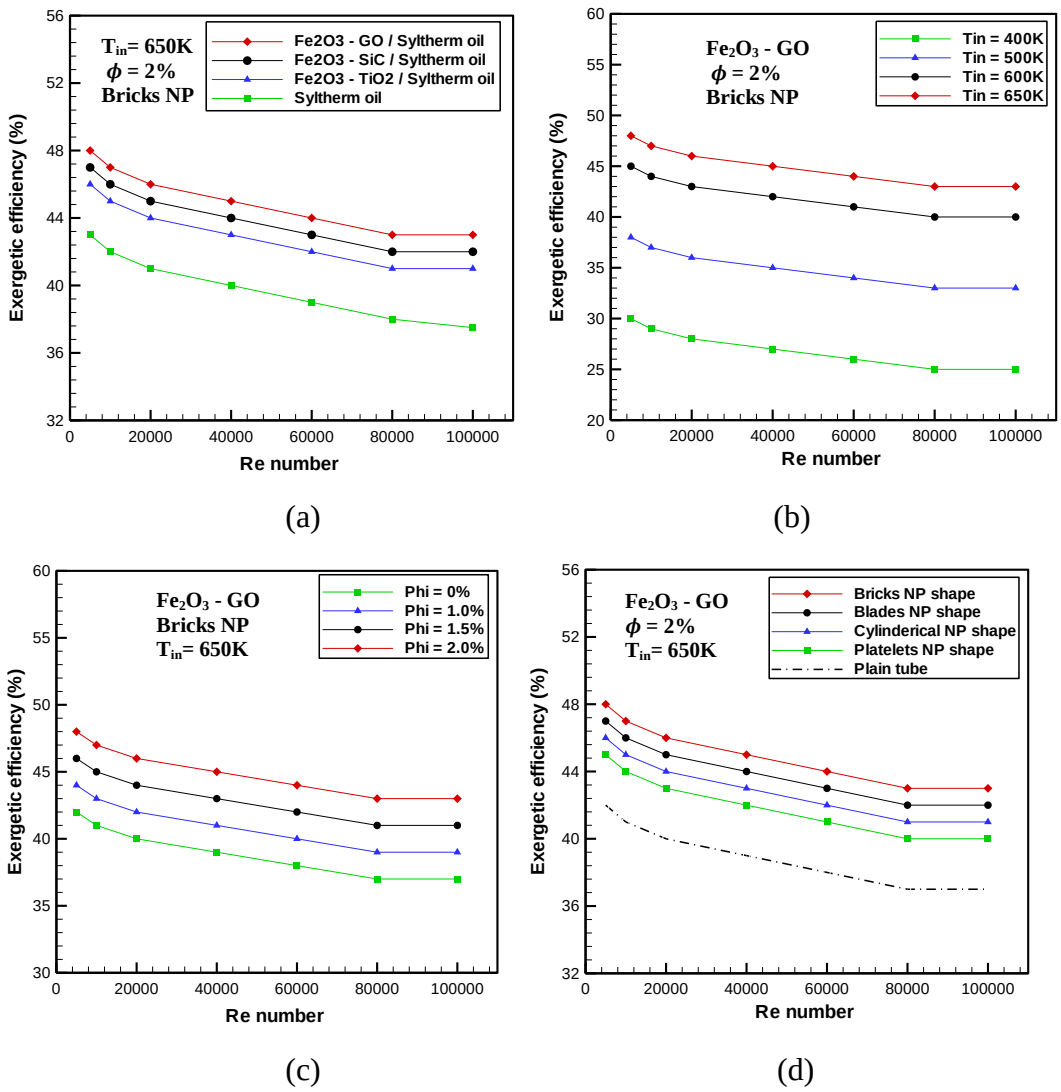

Figure 6.14 The exergetic efficiency variation versus Re number for various, (a) hybrid nanofluid types, (b) inlet fluid temperatures, (c) nanoparticle concentrations, and (d) nanoparticle shapes.

6.3.4 Entropy Generation Rate Characteristics

The total entropy generation rate distribution because of heat transfer and fluid friction versus Re number for various parameters is plotted in Figure 6.15(a)-(d). It is noticed from Figure 6.15(a) that the hybrid nanofluid of Fe_2O_3-GO/Syltherm oil has the lowest value of (S_{gen}^T) compared to other hybrid nanofluids. While, the base fluid (Syltherm oil) exhibits the highest value of (S_{gen}^T). It is also noticed that the entropy generation rate

decreases as Re number increases and becomes relatively steady. This implies that, at lower Re number, the entropy generation because of heat transfer dominates the irreversibility source. Besides that, at high Re numbers, the entropy generated because of heat transfer decreases and the entropy generated because of fluid friction significantly rises and ultimately dominates the irreversibility source. Figure 6.15(b) portrays that the hybrid nanofluid of Fe_2O_3-GO/Syltherm oil with an inlet fluid temperature of 650K has the lowest value of (S_{gen}^T) compared to an inlet fluid temperature of 400K which exhibits the highest value of (S_{gen}^T). The results have shown that higher (S_{gen}^T) rates are anticipated at low inlet fluid temperatures. This implies that, at low inlet fluid temperature, the thermal performance is low which leads to augment the thermal irreversibilities, and the flow irreversibilities are higher because of the high viscosity and density of the hybrid nanofluid used. In addition, as the inlet fluid temperature rises, the properties of the hybrid nanofluid would be changed and led to enhanced thermal performance and less fluid friction as the fluid becomes less dense and less viscous (i.e. less fluid friction irreversibilities). Figure 6.15(c) portrays that the hybrid nanofluid of Fe_2O_3-GO/Syltherm oil with volume fraction of 2% has the lowest value of (S_{gen}^T) compared with other volume fractions considered in this study. While, the base fluid (Syltherm oil) with volume fraction of 0% exhibits the highest value of (S_{gen}^T). This is anticipated as the thermal effectiveness was much greater and thus remarkably diminished the finite temperature differences. Remarkable minimization in the total entropy generation rate is obtainable at lower Re number values of less than 80000. Figure 6.15(d) portrays that the hybrid nanofluid of Fe_2O_3-GO/Syltherm oil with bricks nanoparticle shape has the lowest value of (S_{gen}^T) compared with other hybrid nanofluids considered in this study. While, the plain PTSC tube exhibits the highest value of (S_{gen}^T). It is important to highlight that the optimum reduction of (S_{gen}^T) obtained in this work for various hybrid nanofluid types, various inlet fluid temperatures, various nanoparticle volume fractions and shapes is about 46.42, 52.5%, 45.85% and 48.27%.

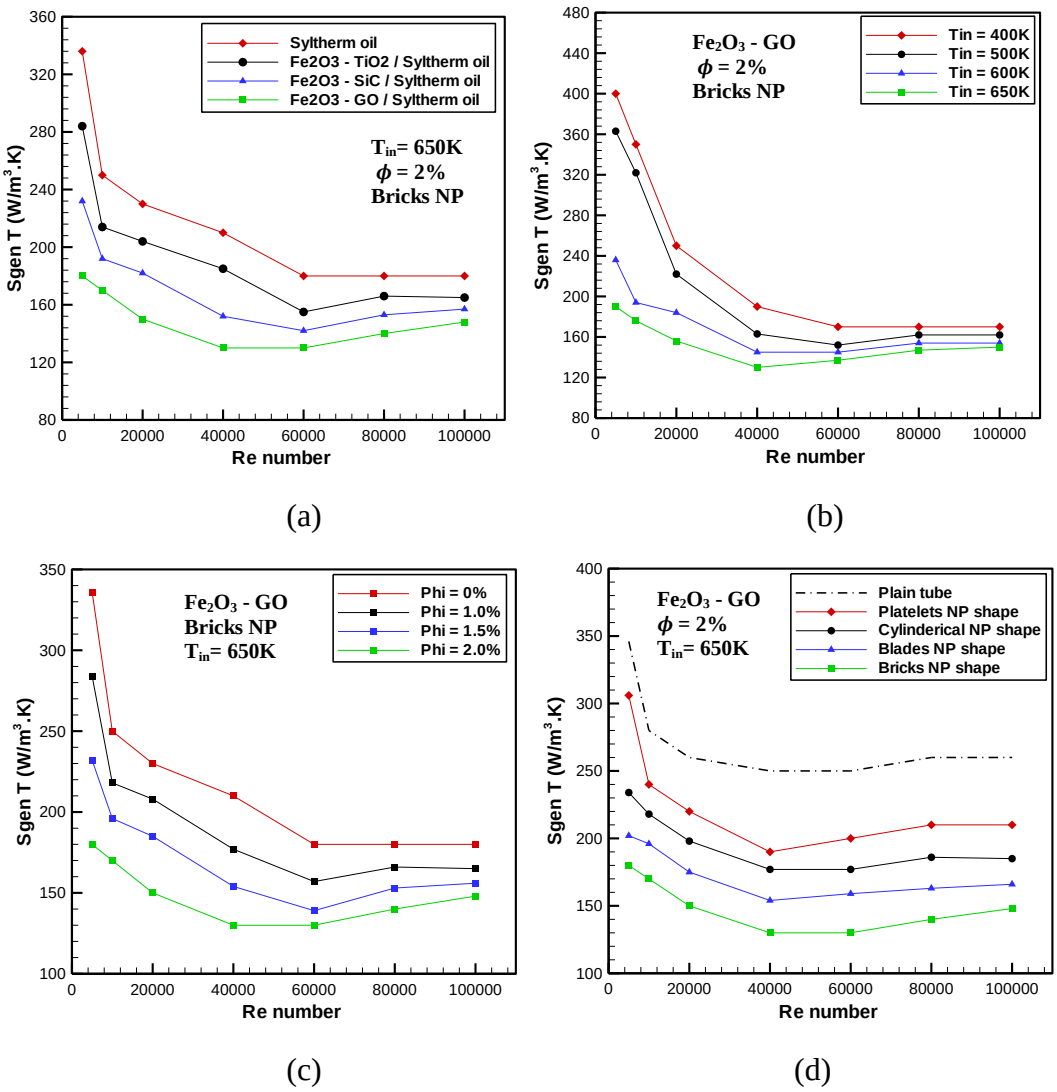

Figure 6.15 The total entropy generation rate variation versus Re number for various, (a) hybrid nanofluid types, (b) inlet fluid temperatures, (c) nanoparticle concentrations, and (d) nanoparticle shapes.

The Be number distribution versus Re number for various parameters is plotted in Figure 6.16(a)-(d). It can be noticed from Figure 6.16(a) that the Be number of hybrid nanofluid of Fe_2O_3-GO/Syltherm oil is the lowest among other hybrid nanofluids. It is also noticed that the inlet fluid temperature of 650K has the lowest value of Be number among other fluid inlet temperatures examined in this work as shown in Figure 6.16(b). This is anticipated as at low temperatures the thermal irreversibility would be greater when the temperature difference is pronounced due to the weak thermal performance.

Nonetheless, at higher inlet temperatures the Be number is seen to be lower due to the distinct temperature differences and lower mass flow rate needed to attain the required Re number which is contrasted to lower fluid inlet temperature cases. At low inlet fluid temperature, the high fluid friction irreversibility is contributed to the Be number reduction. It is noticed from Figure 6.16(c) that the Be number remarkably diminishes as the nanoparticle volume fraction rises at a specific Re number. This is because of the decreased thermal irreversibility and the boosted flow irreversibility as Re and volume fraction values increase. It is worth noting that Fe_2O_3-GO/Syltherm oil hybrid nanofluid with volume fraction of 2% has the lowest value of Be number compared to Syltherm oil which has the highest value. It is noticed from Figure 6.16(d) that the hybrid nanofluid of Fe_2O_3-GO/Syltherm oil with platelets nanoparticle shape has the lowest value of Be number compared to bricks nanoparticle shape which has the highest Be number value. This indicates that there is an increase in the share of frictional entropy produced by increasing the Re number. An increase in the viscosity of the hybrid nanofluid, which happens due to an increase in the shear stress, causes the pattern of the Be number shown in Figure 6.16(d). It is worth noting that the maximum reduction in the Bejan number obtained in this work for different parameters is about 71.8%.

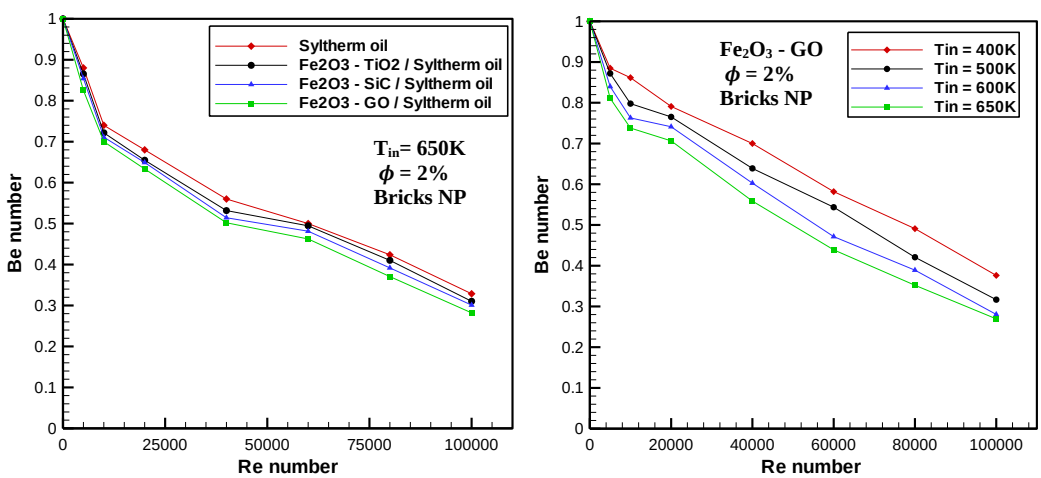

(a) (b)

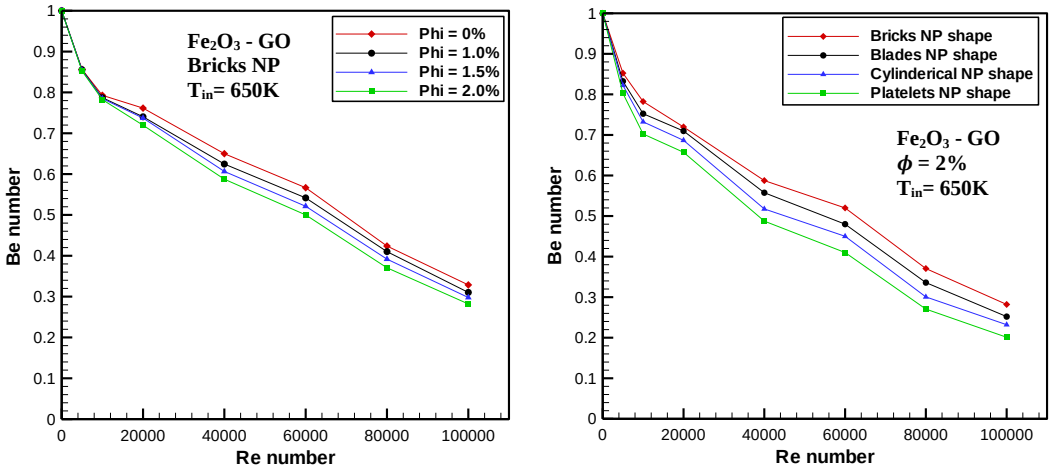

(c) (d)

Figure 6.16 Bejan number variation versus Re number for various, (a) hybrid nanofluid types, (b) inlet fluid temperatures, (c) nanoparticle concentrations, and (d) nanoparticle shapes.

Figure 6.17(a)-(d) shows the entropy generation ratio (N_s) variation versus Re number for various parameters. N_s indicates the wavy promoters can augment the thermodynamic performance when its values are less than 1. It can be obviously noticed from Figure 6.17(a) that the N_s value of each hybrid nanofluid is lower than the plain PTSC and the N_s value of Fe_2O_3-GO/Syltherm oil is the lowest among other hybrid nanofluids used in this study. Figure 6.17(b) portrays that, at lower Re number, the N_s value of each inlet fluid temperature is lower than the plain PTSC tube. In addition, at higher Re number, the N_s results reveal that there is a Re number value (Re= 80000) after which the N_s value becomes close to 1. Thus, it is recommended that the Re number should be less than Re= 80000 to make sure that the N_s value of the PTSC with wavy promoters becomes less than that of the plain PTSC tube. Figure 6.17(c) shows that the N_s value of each nanoparticle volume fraction of Fe_2O_3-GO/Syltherm oil hybrid nanofluid is lower than the plain PTSC tube. It is noticed from Figure 6.17(d) that the hybrid nanofluid of Fe_2O_3-GO/Syltherm oil with platelets-shaped nanoparticle has the lowest value of Ns number compared with the bricks-shaped nanoparticle, which has the highest Ns number value. It is important to highlight that the reduction in the N_s value of various hybrid nanofluids type, inlet fluid

temperature, nanoparticle concentration and shapes are 34.2%, 45.1%, 38.3% and 52.6%, respectively.

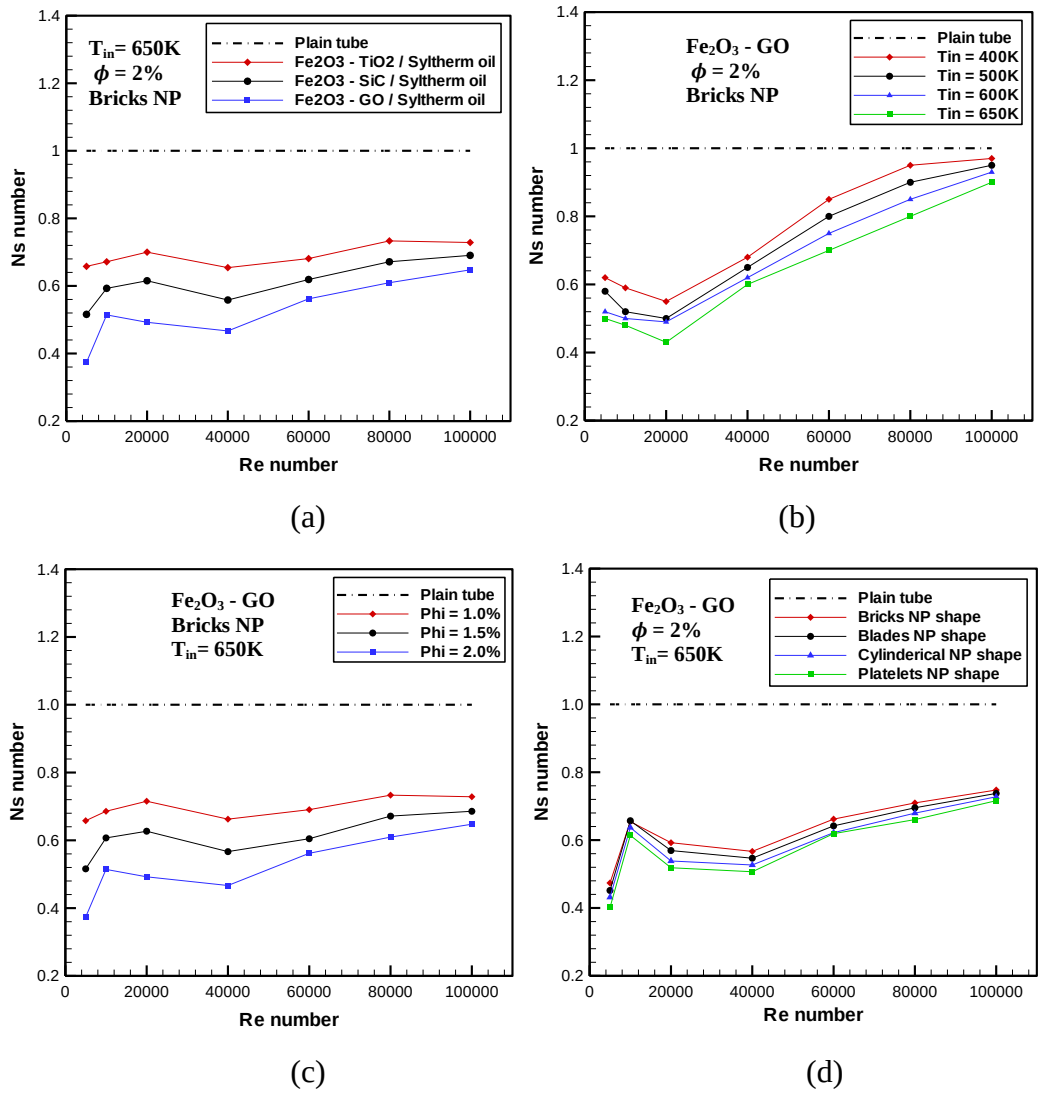

Figure 6.17 The entropy generation ratio variation versus Re number for various, (a) hybrid nanofluid types, (b) inlet fluid temperatures, (c) nanoparticle concentrations, and (d) nanoparticle shapes.

6.3.5 Proposed Correlations

It has been shown from the literature that there is a need for correlations for hybrid nanofluid flows in a PTSC tube equipped with wavy promoters. Thus, the present numerical data were used to develop new empirical correlations for Nu number, friction

factor and thermal efficiency to enhance the knowledgebase in the literature. The adoption of design parameters used in this study were included in the newly developed correlations using the SPSS Statistical Software package with the aid of least square method of regression analysis as presented in the following equations:

$$Nu = Re^{0.76} + \frac{Pr}{(1-\phi)^{151.662}} + T_{in}{}^{1.028} \tag{6.40}$$

$$f = \left(\frac{Pr}{1-\phi}\right)^{0.093} - \frac{0.312\, Re^{0.032}}{T_{in}{}^{-0.162}} \tag{6.41}$$

$$\eta = 1.16 + \left(\frac{T_{in}-T_{amb}}{I_b}\right)^{-0.917} + (\phi - 0.059) \tag{6.42}$$

The R^2 values of these correlations are 0.96, 0.94, 0.96 and the maximum deviation between the estimated data and collected numerical data is ±2.75%, ±4.23% and ±3.55% in terms of Nu number, friction factor (*f*), and thermal efficiency, respectively. The above new equations are valid for the turbulent flow regime with $5000 \leq Re \leq 100000$, $0 \leq \phi \leq 0.02$ and $400\ K \leq T_{in} \leq 650\ K$. These correlations will be very useful for PTSC designers to assess their PTSC thermal and hydraulic performance.

6.3.6 Economic Calculations

This economic calculation shows the financial viability of the developed receiver tubes.

The average value of 1 MWh is approximately $95 (Australian electricity prices 2020) [76] and the cost of producing 1 MWh by solar plant is $50; the Shams 1 power plant 100 MW PTSC electricity thermal plant (Shams 1 2019) [77] is used in the below calculations as an example.

The yearly expected income of the 100MW PTSC electricity plant (using the modified receiver) is:

$95/MWh × 100 MW × 18 hrs/day × 365 days = $62.4 million.

The annual generation cost of the PTSC electricity plant is:

$50/MWh × 100 MW × 18 hrs/day × 365days = $32.8 Million.

Therefore, the solar plant's yearly net financial income equals $29.6 million. Therefore, the additional financial income for the solar plant due to utilizing the developed receiver tube (that enhanced the power plant electricity generation by around 10%) equals approximately $2.96 million.

The cost of the PTSC commercial evacuated receiver tube is approximately $1000.
The total number of the receiver tubes for 100 MW PTSC plant is 27 684.

The expected cost for manufacturing the developed receiver tube is around 130% of the initial receiver tube cost ($1000), thus the developed receiver tubes each cost approximately $1500 including the nanoparticle cost of ($200)
The total additional capital cost for installing the developed receiver tubes of the 100MW PTSC plant = $13.9 million, ($500 × 27684 tubes=13.9 million)

The payback period for the developed receiver tubes is the additional capital cost ($13.9 million) versus the additional income ($2.96 million per year), which is approximately equal to 4.7 years.

6.4 Conclusions

A three-dimensional numerical analysis of various hybrid nanofluid kinds, namely (Fe_2O_3-GO, Fe_2O_3-SiC, and Fe_2O_3-TiO_2) dispersed in a Syltherm800 at various nanoparticle concentrations (ϕ = 1.0-2.0%) and shapes (bricks, blades, cylindrical, and platelets) flowing in a PTSC model fitted with central wavy promoters was investigated. The influence of these aforementioned fluids, inlet fluid temperature and Re number under turbulent flow conditions on the thermohydraulic performance, exergy and entropy reduction was performed. The findings of this work can be listed as follows:

- The maximum decrement in the absorber's average outlet temperature was in the range of 7-31°C. High augmentation in Nu number was produced with the utilisation of Fe_2O_3-GO/Syltherm oil hybrid nanofluid by 150.4% at 2.0% concentration instead

of Syltherm oil. PEC of hybrid nanofluids noticed to be superior in the range of 1.62-2.46 using bricks-shaped nanoparticles compared to base fluid.

- The Fe_2O_3-GO/Syltherm oil hybrid nanofluid has the highest friction factor, while Fe_2O_3-TiO_2/Syltherm oi has the lowest value. Furthermore, the friction factor rose up to approximately 24.7-39.5% for all the cases examined in this study.
- The maximum thermal efficiency of the PTSC remarkably enhanced with the utilisation of Fe_2O_3-GO/Syltherm oil hybrid nanofluid by 18.51%. The maximum exergetic efficiency prominently improved by 16.21% at low Re numbers.
- The maximum decrement in the (S_{gen}^T) and N_s values were approximately 48.27% and 52.6%, respectively, particularly at low Re number.
- From the standpoint of the 2nd law of thermodynamics, hybrid nanofluids reduced the total entropy generations compared to thermal oil. It is considered advantageous working with Re number in the range of 5000 to 60000 for all the volume concentrations. While, it is considered disadvantageous working with higher Re number than 80000.
- New correlations for Nu number, friction factor and thermal efficiency were developed as a function of dropped temperature parameter, nanoparticle concentration and inlet fluid temperature with maximum deviations of ±2.75%, ±4.23% and ±3.55%, respectively.

Thus, for the range of flow rates in actual PTSC energy systems, using hybrid nanofluids would improve the thermal and thermodynamic performance. Furthermore, with heat transfer enhancement using hybrid nanofluids, a higher useful energy output is obtained and less of the available energy is destroyed due to reduced irreversibilities. This improvement in performance is essential to make energy from concentrated solar power systems cost competitive with energy from other sources. With lower energy costs, increased deployment of this technology will be possible and thus ensuring a cleaner and widely available source of energy.

References

[1] Hussein A. K. Applications of nanotechnology to improve the performance of solar collectors-recent advances and overview. Renew Sustain Energy Rev 2016; 62: 767–792.

[2] Kumaresan G., Santosh R., Velraj R., Sudhakar P. Experimental and numerical studies of thermal performance enhancement in the receiver part of solar parabolic trough collectors. Renew Sustain Energy Rev 2017; 77: 1363–74.

[3] Hafez A., Eltwab A. M., ElKousy H. S., Afifi A. O., AbdElhamid A. A., Design analysis of solar parabolic trough thermal collectors. Renew Sustain Energy Rev 2018; 82: 1215–60.

[4] Yang S., Ordonez J. C., Sensoy T. S. Dynamic 3D volume element model of a parabolic trough solar collector for simulation and optimization. Appl Energy 2018; 217: 509–26.

[5] Khanna S., Kedare S. B., Singh S. Analytical expression for circumferential and axial distribution of absorbed flux on a bent absorber tube of solar parabolic trough concentrator. Sol Energy 2013; 92: 26–40.

[6] Bellos E., Tzivanidis C., Antonopoulos K. A. A detailed working fluid investigation for solar parabolic trough collectors. Appl Therm Eng 2017; 114: 374–386.

[7] Kumar K. R., Reddy K. S. Effect of porous disc receiver configurations on performance of solar parabolic trough concentrator. Heat Mass Transf 2012; 48: 555–571.

[8] Cheng Z. D., He Y. L., Cui F. Q. Numerical study of heat transfer enhancement by unilateral longitudinal vortex generators inside parabolic trough solar receivers. Int J Heat Mass Transf 2012; 55: 5631–5641.

[9] Aldali Y., Muneer T., Henderson D. Solar absorber tube analysis: thermal simulation using CFD. Int J Low-Carbon Technol 2013; 8: 14–19.

[10] Ghasemi S. E., Ranjbar A. A., Ramiar A. Three-dimensional Numerical Analysis of Heat Transfer Characteristics of Solar Parabolic Collector with Two Segmental Rings. J Math Comput Sci 2013; 7: 89–100.

[11] Ghadirijafarbeigloo S., Zamzamian A. H., Yaghoubi M. 3-D numerical simulation of heat transfer and turbulent flow in a receiver tube of solar parabolic trough concentrator with louvered twisted-tape inserts. Energy Procedia 2014; 49: 373 – 380.

[12] Waghole D. R., Warkhedkar R. M., Kulkarni V. S., Shrivastva R. K. Experimental investigations on heat transfer and friction factor of silver nanofluid in absorber/receiver of parabolic trough collector with twisted tape inserts. Energy Procedia 2014; 45: 558 – 567.

[13] Song X., Dong G., Gao F., Diao X., Zheng L., Zhou F. A numerical study of parabolic trough receiver with nonuniform heat flux and helical screw-tape inserts. Energy 2014; 77: 771–82.

[14] Mwesigye A., Bello-Ochende T., Meyer J. P. Heat transfer and thermodynamic performance of a parabolic trough receiver with centrally placed perforated plate inserts. Appl Energy 2014; 136: 989–1003.

[15] Jafar K.S., Sivaraman B. Thermal performance of solar parabolic trough collector using nanofluids and the absorber with nail twisted tapes inserts. Int Energy 2014; 14: 189–98.

[16] Mwesigye A., Bello-Ochende T., Meyer J. P. Multi-objective and thermodynamic optimisation of a parabolic trough receiver with perforated plate inserts. Appl Therm Eng 2015; 77:42–56.

[17] Huang Z., Yu G. L., Li Z. Y., Tao W. Q. Numerical study on heat transfer enhancement in a receiver tube of parabolic trough solar collector with dimples, protrusions and helical fins. Energy Procedia 2015; 69: 1306 – 1316.

[18] Lu J., Ding J., Yu T., Shen X. Enhanced heat transfer performances of molten salt receiver with spirally grooved pipe. Appl Therm Eng 2015; 88: 491–8.

[19] Reddy K. S., Kumar K. R., Ajay C. S. Experimental investigation of porous disc enhanced receiver for solar parabolic trough collector. Renew Energy 2015; 77: 308–19.

[20] Diwan K., Soni M. S. Heat transfer enhancement in absorber tube of parabolic trough concentrators using wire-coils inserts. Univers J Mech Eng 2015; 3: 107–12.

[21] Mwesigye A., Bello-Ochende T., Meyer J. P. Heat transfer and entropy generation in a parabolic trough receiver with wall-detached twisted tape inserts. Int J Therm Sci 2016; 99: 238–57.

[22] Bellos E., Tzivanidis C., Antonopoulos K. A., Gkinis G. Thermal enhancement of solar parabolic trough collectors by using nanofluids and converging-diverging absorber tube. Renew Energy 2016; 94: 213–22.

[23] ZhangJing Z., Yang X., Yaling H. Thermal analysis of a solar parabolic trough receiver tube with porous insert optimized by coupling genetic algorithm and CFD. Sci China Technol Sci 2016; 59: 1475–85.

[24] Fuqiang W., Qingzhi L., Huaizhi H., Jianyu T. Parabolic trough receiver with corrugated tube for improving heat transfer and thermal deformation characteristics. Appl Energy 2016; 164: 411–424.

[25] Jaramillo O. A., Borunda M., Velazquez-Lucho K. M., Robles M. Parabolic trough solar collector for low enthalpy processes: An analysis of the efficiency enhancement by using twisted tape inserts. Renew Energy 2016; 93: 125–41.

[26] Benabderrahmane A., Aminallah M., Laouedj S., Benazza A., Solano J. P. Heat transfer enhancement in a parabolic trough solar receiver using longitudinal fins and nanofluids. J Therm Sci 2016; 25: 410–7.

[27] Ghasemi S. E., Ranjbar A. A. Numerical thermal study on effect of porous rings on performance of solar parabolic trough collector. Appl Therm Eng 2017; 118:807–816.

[28] Bellos E., Tzivanidis C., Tsimpoukis D. Thermal enhancement of parabolic trough collector with internally finned absorbers. Sol Energy 2017; 157:514–531.

[29] Zhu X., Zhu L., Zhao J. Wavy-tape insert designed for managing highly concentrated solar energy on absorber tube of parabolic trough receiver. Energy 2017; 141: 1146–55.

[30] Xiangtao G., Fuqiang W., Haiyan W., Jianyu T., Qingzhi L., Huaizhi H. Heat transfer enhancement analysis of tube receiver for parabolic trough solar collector with pin fin arrays inserting. Sol Energy 2017; 144: 185–202.

[31] Huang Z., Li Z. Y., Yu G. L., Tao W. Q. Numerical investigations on fully developed mixed turbulent convection in dimpled parabolic trough receiver tubes. Appl Therm Eng 2017; 114: 1287–1299.

[32] Bellos E., Tzivanidis C. Thermal efficiency enhancement of nanofluid-based parabolic trough collectors. J Therm Anal Calorim 2018; 1: 1–12.

[33] Bitam E., Demagh Y., Hachicha A. A., Benmoussa H., Kabar Y. Numerical investigation of a novel sinusoidal tube receiver for parabolic trough technology. Appl Energy 2018; 218: 494–510.

[34] Okonkwo E. C., Abid M., Ratlamwala T. A. H. Effects of synthetic oil nanofluids and absorber geometries on the exergetic performance of the parabolic trough collector. Int J Energy Res 2018:1–16.

[35] Rawani A., Sharma S. P., Singh K. D. P. Comparative performance analysis of different twisted tape inserts in the absorber tube of parabolic trough collector. Int J Mech Prod Eng Res Dev 2018; 8: 643–56.

[36] Benabderrahmane A., Benazza A., Hussein A. K. Heat transfer enhancement analysis of tube receiver for parabolic trough solar collector with central corrugated insert. J Heat Transfer 2020; 142: 062001–1.

[37] Khan M. S., Yan M., Ali H. M., Amber K. P., Bashir M. A., Akbar, et al. Comparative performance assessment of different absorber tube geometries for parabolic trough solar collector using nanofluid. J Therm Anal Calorim Vol 2020; 142: 2227–2241.

[38] Mwesigye A., Meyer J. P. Optimal thermal and thermodynamic performance of a solar parabolic trough receiver with different nanofluids and at different

concentration ratios. Appl Energy 2017; 193: 393–413.

[39] Bellos E., Tzivanidis C. Parametric investigation of nanofluids utilization in parabolic trough collectors. Therm Sci Eng Prog 2017; 2: 71–79.

[40] Khakrah H., Shamloo A., Hannani S. K. Determination of parabolic trough solar collector efficiency using nanofluid: A comprehensive numerical study. J Sol Energy Eng 2017; 139: 51006–11.

[41] Mwesigye A., Yılmaz I. H., Meyer J. P. Numerical analysis of the thermal and thermodynamic performance of a parabolic trough solar collector using SWCNTs-Therminol VP-1 nanofluid. Renew Energy 2018; 119: 844–62.

[42] Subramani J., Nagarajan P. K., Mahian O., Sathyamurthy R. Efficiency and heat transfer improvements in a parabolic trough solar collector using TiO_2 nanofluids under turbulent flow regime. Renew Energy 2018; 119: 19–31.

[43] Bellos E., Tzivanidis C., Tsimpoukis D. Thermal, hydraulic and exergetic evaluation of a parabolic trough collector operating with thermal oil and molten salt based nanofluids. Energy Convers Manag 2018; 156: 388–402.

[44] Marefati M., Mehrpooya M., Shafii M. B. Optical and thermal analysis of a parabolic trough solar collector for production of thermal energy in different climates in Iran with comparison between the conventional nanofluids. J Clean Prod 2018; 175: 294–313.

[45] Allouhi A., Amine M. B., Saidur R., Kousksou T., Jamil A. Energy and exergy analyses of a parabolic trough collector operated with nanofluids for medium and high temperature applications. Energy Convers Manag 2018; 155: 201–217.

[46] Alsaady M., Fu R., Yan Y., Liu Z., Wu S., Boukhanouf R. An Experimental investigation on the effect of ferrofluids on the efficiency of novel parabolic trough solar collector under laminar flow conditions. Heat Transf Eng 2018; 1:1–9.

[47] Kumar M. K., Yuvaraj G., Balaji D., Pravinraj R., Shanmugasundaram P. Influence of Nano-Fluid and Receiver Modification in Solar Parabolic Trough Collector Performance. IOP Conf Ser Mater Sci Eng 2018; 310: 12140.

[48] Bellos E., Tzivanidis C., Said Z. A systematic parametric thermal analysis of nanofluid-based parabolic trough solar collectors. Sustain Energy Technol Assessments 2020; 39: 100714.

[49] Aminfar H., Mohammadpourfard M., Ahangar Zonouzi S. Numerical study of the ferrofluid flow and heat transfer through a rectangular duct in the presence of a non-uniform transverse magnetic field. J Magn Magn Mater 2013; 327: 31–42.

[50] Bahiraei M., Hangi M. Automatic cooling by means of thermomagnetic phenomenon of magnetic nanofluid in a toroidal loop. Appl Therm Eng 2016; 107: 700-8.

[51] Hong H., Wright B., Wensel J., Jin S., Ye X. R., Roy W. Enhanced thermal conductivity by the magnetic field in heat transfer nanofluids containing carbon nanotube. Synth Met, 157437–40 2007; 157: 437–40.

[52] Aghabozorg M. H., Rashidi A., Mohammadi S. Experimental investigation of heat transfer enhancement of Fe_2O_3-CNT/water magnetic nanofluids under laminar, transient and turbulent flow inside a horizontal shell and tube heat exchanger. Exp Therm Fluid Sci 2016; 72: 182–9.

[53] ANSYS Theory Guide. ANSYS® Academic Research, Release 19.5, ANSYS FLUENT, Theory Guide, ANSYS, Inc. 2019.

[54] Pandey D. K., Lee R. B., Paden J. Effects of atmospheric emissivity on clear sky temperatures. Atmos Environ 1995; 29:2201–2204.

[55] Garcıa-Valladares O., Velazquez N. Numerical Simulation of Parabolic Trough Solar Collector: Improvement Using Counter Flow Concentric Circular Heat Exchangers. Int J Heat Mass Transf 2009; 52:597–609.

[56] Incropera F., Dewitt P. D. Introduction to Heat Transfer, fifth ed., John Wiley & Sons Inc, New York. 2006.

[57] Wirz M., Haselbacher A., Petit J. Potential improvements in the optical and thermal efficiencies of parabolic trough concentrators. Sol Energy 2014; 107(0): 398–414.

[58] Paoletti S., Rispoli F., Sciubba E. Calculation of exergetic losses in compact heat exchanger passages. ASME AES. 1989; 10 (2), 21-29.

[59] Pak B. C., Cho Y. I. Hydrodynamic and heat transfer study of dispersed fluids with submicron metallic oxide particles. Exp Heat Transf 1998; 11: 151–70.

[60] Mwesigye, A., & Huan, Z. Thermal and thermodynamics performance of a parabolic trough receiver with Syltherm 800-Al_2O_3 nanofluid as the heat transfer fluid. Energy Procedia, 2015; *75*, 394 – 402.

[61] Mwesigye, A., Huan, Z., & Meyer, J. P. Thermal performance and entropy generation analysis of a high concentration ratio parabolic trough solar collector with Cu-Therminol VP-1 nanofluid. Energy Conversion and Management, 2016; *120*, 449–465.

[62] Dudley V. E., Kearney R., Kolb J. G. SEGS LS2 solar collector-test results. Rep Sandia Natl Lab 1994; SAN94:1884.

[63] Dreyer S., Eichel P., Gnaedig T., Hacker Z., Janker S., Kuckelkorn T., et al. Heat loss measurements on Parabolic Trough receivers. SolarPaces Conf 2010; 49:1–8.

[64] Raza H., Aized T., Khan M. B., Imran M. Tensile testing of polystyrene graphene 2D nano composite membrane. Int J Adv Manufact Technol 2018; 94: 4343–4349.

[65] Aized T, Imran M, Raza H, Raza MR, Gohar GA, Iqbal A. Effect of nano-filler graphene on nano-composite system of polystyrene-graphene. Int J Adv Manufact Technol 2018; 95: 3707–3715.

[66] Ghosh D., Ghosh1 S., Calizo1 I., Teweldebrhan D., Pokatilov E. P., Nika D. L., et al. Extremely high thermal conductivity of graphene: prospects for thermal management applications in nanoelectronic circuitsjourna. Appl Phys Lett 2008; 92:151911.

[67] Dow. SYLTHERM 800 Heat Transfer Fluid: Product Technical Data 2012.

[68] Minea A. A., El-Maghlany W. M. Influence of hybrid nanofluids on the performance of parabolic trough collectors in solar thermal systems: Recent findings and numerical comparison. Renew Energy 2018; 120: 350–64.

[69] Khoshvaght-Aliabadi M., Zamzamian A., Hormozi F. Wavy channel and different nanofluids effects on performance of plate-fin heat exchangers. J Thermophys Heat Transf 2014; 28 (3): 474-484.

[70] Azimi M., Azimi A., Mirzaei M. Investigation of the unsteady graphene oxide nanofluid flow between two moving plates. J Comput Theor Nanosci 2014; 11: 2104–8.

[71] Sahoo R. R., Sarkar J. Heat transfer performance characteristics of hybrid nanofluids as coolant in louvered fin automotive radiator. Heat Mass Transf 2017; 53: 1923–31.

[72] Takabi B., Salehi S. Augmentation of the heat transfer performance of a sinusoidal corrugated enclosure by employing hybrid nanofluid. Adv Mech Eng 2014; 6: 147059.

[73] Timofeeva E. V., Routbort J. L., Singh D. Particle shape effects on thermophysical properties of alumina nanofluids. J Appl Phys 2009; 106: 014304.

[74] Tong,Y., Lee, H., Kang, W. and Cho, H. Energy and exergy comparison of a flat-plate solar collector using water, Al_2O_3 nanofluid, and CuO nanofluid, *Appl. Therm. Eng.*, 2019; 159, 113959.

[75] Hepbasli A. A key review on exergetic analysis and assessment of renewable energy resources for a sustainable future. Renewable and Sustainable Energy Reviews, 2008; 12(3), 593-661.

[76] Australian electricity prices 2020, Australian electricity prices; the cost of electricity in Australia per kWh, BulkEnery, accessed 20 June 2020, <https://gobulk.com.au/australian-electricity-prices/.>.

[77] Shams 1 2019, Concentrating Solar Power Projects, National Renewable Energy Laboratory, accessed 20 June 2020, <https://solarpaces.nrel.gov/shams-1.>.

Chapter 7 Conclusions and Recommendations

7.1 Conclusions

Non-renewable energy sources (fossil fuels) remain economically advantageous because of their abundance and capacity to generate a large amount of energy in single location. However, pollution is the main issue of utilising this energy as in each second approximately 1.2 million kilograms of CO_2 are released into the atmosphere. Therefore, due to the increase in the world's fossil fuel energy consumption, limit to its resources and growing pollution issues, there is an urgent need for environmentally-friendly and sustainable energy resources. Renewable energy resources are sustainable resources that produce zero greenhouse gas emissions while producing the energy. Solar energy is the most abundant and geographically widespread resource and it has tremendous advantages over other renewable energy resources.

Among all of the CSP technologies, Parabolic Trough Solar Collectors (PTSC) are the most mature, efficient and cost-effective technology. The PTSC systems can be used to generate electricity in most power plants and to provide thermal energy for various applications such as pressurization, drying, sterilization, boiler feed water, bleaching, and process heat for the chemical, paper, textile, dairy, food, and mining industries. However, there are some challenges with the operation of PTSC systems. PTSC thermal efficiency and outlet temperature are principally low. These challenges are associated with low thermal conductivity of heat transfer fluids and thus low heat transfer characteristics and pressure drop penalty associated with the usage of some flow turbulators. Although there have been different working fluids and various passive techniques have been widely reported during the past decade to enhance the heat transfer in PTSC. However, there is still a room for improvement to make the heat transfer and fluid dynamics process more effective in PTSC systems. Therefore, the coupling of passive techniques and nanofluids can have unbelievably great impacts on the PTC's thermal effectiveness.

In this thesis, different advanced working fluids and various passive techniques, which have advantages over the other conventional fluids and techniques, to improve the PTSC's thermal and thermodynamics performance and to reduce the entropy generation. From this perspective, numerical investigations using CFD with the aid of FVM and MRCT methods of PTSC's receiver tube equipped with various turbulators. Three different scenarios of PTSC system geometry were employed: Four nanoparticles (Al_2O_3, CuO, SiO_2, and ZnO) dispersed in water were numerically tested in a uniformly heated receiver tube with different conical insert shapes (DR and CR); Three hybrid nanofluids (Ag-MgO, Ag-SWCNT, and Ag-MWCNT) dispersed in Syltherm oil were numerically tested in a PTSC receiver tube with conical turbulator; and three hybrid nanofluids (Fe_2O_3-GO, Fe_2O_3-SiC and Fe_2O_3-TiO_2) dispersed in Syltherm oil were employed in a PTSC's receiver tube with wavy promoter at different operating conditions. The synergistic effect between nanofluid/hybrid nanofluid parameters and the influence of passive techniques on the PTSC's thermal and thermodynamics performance were explored in this thesis. Several general conclusions can be made from the observations during the research involving the topic "Heat transfer enhancement in a parabolic trough solar collector (PTSC) using passive technique and nanofluids/ hybrid nanofluids".

7.1.1 Two-Phase Forced Convection of Nanofluids Flow in Circular Tubes using Convergent and Divergent Conical Rings Inserts

The following conclusions can be drawn as follows:

- The DR inserts provide higher value of heat transfer augmentation, pressure drop and PEC index in comparison with CR inserts. It is found that the insertion of conical rings has enhanced the Nusselt number for the DR arrangement up to 365%, and for the CR arrangement up to 280%.
- Nanofluid with SiO_2 particle achieved the highest Nusselt number and it was followed by Al_2O_3, ZnO and CuO respectively, while the pure water gave the lowest values. The heat transfer in terms of Nusselt number improved well for the higher particle volume fraction (4%) and the lower particle diameter (20 nm).

- There was no considerable increase in the friction factor noticed when using different types of nanofluids. The average Nusselt number increases with increasing Reynolds number, while friction factor represents reverse trend for both water and nanofluids.
- The comparison of calculated results for different models shows that the two-phase mixture model is more precise than the single-phase model.

7.1.2 Heat Transfer Augmentation of Parabolic Trough Solar Collector Receiver's Tube using Hybrid Nanofluids and Conical Turbulators

The following findings of this research can be listed as follows:

- The Nu number is improved by approximately 233.4%, 150%, and 66.7% when utilising Ag-SWCNT/Syltherm oil, Ag-MWCNT/Syltherm oil, and Ag-MgO/Syltherm oil hybrid nanofluids, respectively, at 2.0% concentration instead of Syltherm oil.
- The pumping power rose up to approximately 23.4-35.4% as the nanoparticle concentration increased from 1-2%.
- The maximum decrement in the absorber's outlet temperature and the temperature gradient was approximately 28.1% and 38.3%, respectively.
- Thermal performance of hybrid nanofluids is noticed to be superior compared to base fluid as the PEC value of PTSC equipped with conical turbulators is in the range of 0.9-1.82.
- The maximum boost in the thermal efficiency and the exergetic efficiency were about 11.5% and 18.2%, respectively, using Ag-SWCNT/Syltherm oil hybrid nanofluid.
- The maximum decrement in the entropy generation rate and the entropy generation ratio were approximately 42.7% and 33.7%, respectively, particularly at low Re number.
- At specific parameters, there was a Re number (Re= 65000) beyond which the entropy generation rate became higher than 1 and the entropy generation ratio became higher than the smooth PTSC.

7.1.3 Thermohydraulic and Thermodynamics Performance of Hybrid Nanofluids based Parabolic Trough Solar Collector equipped with Wavy Promoters

The findings of this work can be listed as follows:

- The maximum decrement in the absorber's average outlet temperature was in the range of 7-31°C. High augmentation in Nu number was produced with the utilisation of Fe_2O_3-GO/Syltherm oil hybrid nanofluid by 150.4% at 2.0% concentration instead of Syltherm oil. PEC of hybrid nanofluids noticed to be superior in the range of 1.62-2.46 using bricks-shaped nanoparticles compared to base fluid.
- The Fe_2O_3-GO/Syltherm oil hybrid nanofluid has the highest friction factor, while Fe_2O_3-TiO_2/Syltherm oi has the lowest value. Furthermore, the friction factor rose up to approximately 24.7-39.5% for all the cases examined in this study.
- The maximum thermal efficiency and maximum exergetic efficiency of the PTSC prominently improved with the utilisation of Fe_2O_3-GO/Syltherm oil hybrid nanofluid by 18.51% and 16.21%, respectively, at low Re numbers.
- The maximum decrement in the (S_{gen}^T) and N_s values were approximately 48.27% and 52.6%, respectively, particularly at low Re number.
- It is considered advantageous working with Re number in the range of 5000 to 60000 for all the volume concentrations. While, it is considered disadvantageous working with higher Re number than 80000.
- New correlations for Nu number, friction factor and thermal efficiency were developed as a function of dropped temperature parameter, nanoparticle concentration and inlet fluid temperature with maximum deviations of ±2.75%, ±4.23% and ±3.55%, respectively.

7.2 Commercial Implications

Both the thermal and thermodynamics receiver tube enhancements contribute to significant potential commercial benefits for PTSC technology, especially using non-evacuated receiver tubes instead of the available evacuated receiver tubes (which are so

expensive as they cost approximately 30% of the total solar field's components). Both enhancements will produce more heat energy, and therefore more income. For example, the developed receiver tubes have the potential to earn an additional $3 million per annum for a 100 MW parabolic trough solar thermal electric power plant, providing a payback period of less than 4.7 years (Section 6.3.6 of Chapter 6 shows the details of these financial calculations). The developed receiver tubes can also be used effectively for PTSC solar thermal plants in addition to other PTSC heating applications.

7.3 Recommendations

Further to the reported literature, the following recommendations can be considered for future studies:

- There is a high need for a more detailed experimental investigation with simultaneous numerical analysis using nanofluids/hybrid nanofluids for PTSC systems-based in real power generation systems in order to find solutions of nanofluids issues such as its stability, agglomeration, arrangement, and so on.
- Experimental investigation on the utilisation of inserting metal foams, continuous and discontinuous helical screw-tape inserts, conical rings in various angles, porous media and other insert types are needed to optimise the design of PTSC systems.
- Further numerical structural analysis of a PTSC's absorber tube supported at multiple points is needed to identify its impact on the PTSC's temperature profile, bending, deflection, and service time.
- Further studies on different HTF types (i.e. other magnetic nanoparticles, ferrofluids, tri nanofluids/tri hybrid nanofluids, ionic liquid-based nanofluids) and different gases will be needed to investigate its impact on the PTSC's overall efficiency.
- There is an imperative need for two-phase flow research in PTSC systems using hybrid nanofluids and it needs to be extensively explored further.
- The cross-area of the PTSC's absorber pipe is suggested to be in various shapes such as elliptical, and oval to evaluate its impacts on the thermal performance.

Appendix I: Attribution Tables

Paper "Two-phase Forced Convection of Nanofluids Flow in Circular Tubes using Convergent and Divergent Conical Rings Inserts", International Communications in Heat and Mass Transfer, Vol. 101, pp.10-20, 2019.

Ibrahim A.M. Ali Abuobeida, Hari B. Vuthaluru, Shaomin Liu.

Author's Name	Conception and Design	Acquisition of data & method	Data condition & manipulation	Analyses & statistical method	Interpretation & discussion	Final approval
Ibrahim A. M. Ali Abuobeida						**X**
I acknowledge that these represent my contribution to the above research output Signature:						
Hari B. Vuthaluru						**X**
I acknowledge that these represent my contribution to the above research output Signature:						
Shaomin Liu						**X**
I acknowledge that these represent my contribution to the above research output Signature:						

Appendix I: Paper Contribution Table

Paper "CFD based Investigations on The Effects of Blockage Shapes on Transient Mixed Convective Nanofluid Flow over a Backward Facing Step", Powder Technology, Vol. 345, pp.608-620, 2019.

F. Fathinia, Hari B. Vuthaluru, Shaomin Liu

Author's Name	Conception and Design	Acquisition of data & method	Data condition & manipulation	Analyses & statistical method	Interpretation & discussion	Final approval
F. Fathinia						**X**
I acknowledge that these represent my contribution to the above research output Signature:						
Hari B. Vuthaluru						**X**
I acknowledge that these represent my contribution to the above research output Signature:						
Shaomin Liu						**X**
I acknowledge that these represent my contribution to the above research output Signature:						

Paper "Heat Transfer Augmentation of Parabolic Trough Solar Collector Receiver's Tube using Hybrid Nanofluids and Conical Turbulators", Journal of the Taiwan Institute of Chemical Engineers, Vol. 125, pp.215-242, 2021.

Hari B. Vuthaluru, Shaomin Liu

Author's Name	Conception and Design	Acquisition of data & method	Data condition & manipulation	Analyses & statistical method	Interpretation & discussion	Final approval
Hari B. Vuthaluru						**X**
I acknowledge that these represent my contribution to the above research output Signature: V. Hari Babu						
Shaomin Liu						**X**
I acknowledge that these represent my contribution to the above research output Signature: Liushaomin						

Appendix I: Paper Contribution Table

Paper "Thermohydraulic and Thermodynamics Performance of Hybrid Nanofluids based Parabolic Trough Solar Collector equipped with Wavy Promoters", Renewable Energy, Vol. 182, pp.401-426, 2022.

Hari B. Vuthaluru, Shaomin Liu

Author's Name	Conception and Design	Acquisition of data & method	Data condition & manipulation	Analyses & statistical method	Interpretation & discussion	Final approval
Hari B. Vuthaluru						**X**
I acknowledge that these represent my contribution to the above research output Signature:						
Shaomin Liu						**X**
I acknowledge that these represent my contribution to the above research output Signature:						

Book “Parabolic Trough Solar Collectors - Thermal and Hydraulic Enhancement Using Passive Techniques and Nanofluids, to be published by Springer Nature Switzerland, 2022.

Hari B. Vuthaluru, Shaomin Liu

Author’s Name	Conception and Design	Acquisition of data & method	Data condition & manipulation	Analyses & statistical method	Interpretation & discussion	Final approval
Hari B. Vuthaluru						**X**
I acknowledge that these represent my contribution to the above research output Signature:						
Shaomin Liu						**X**
I acknowledge that these represent my contribution to the above research output Signature:						

Appendix II: Copyright Permission Statements

A. Chapter 4, reprinted with permission from "Hussein A. Mohammed, Ibrahim A.M. Ali Abuobeida, Hari B. Vuthaluru, Shaomin Liu, Two-phase Forced Convection of Nanofluids Flow in Circular Tubes using Convergent and Divergent Conical Rings Inserts, *International Communications in Heat and Mass Transfer*, Vol. 101, pp.10-20, 2019".

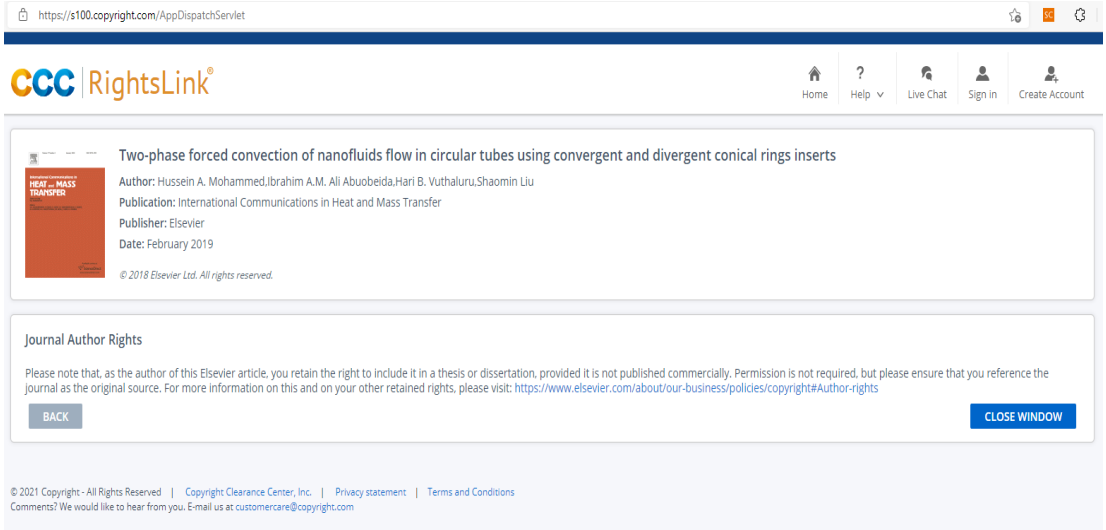

B. Chapter 5, reprinted with permission from "Hussein A. Mohammed, Hari B. Vuthaluru, Shaomin Liu, Heat Transfer Augmentation of Parabolic Trough Solar Collector Receiver's Tube using Hybrid Nanofluids and Conical Turbulators, *Journal of the Taiwan Institute of Chemical Engineers*, Vol. 125, pp.215-242, 2021".

C. Chapter 6, reprinted with permission from "Hussein A. Mohammed, Hari B. Vuthaluru, Shaomin Liu, Thermohydraulic and Thermodynamics Performance of Hybrid Nanofluids based Parabolic Trough Solar Collector equipped with Wavy Promoters, *Renewable Energy*, Vol. 182, pp. 401-426, 2022".

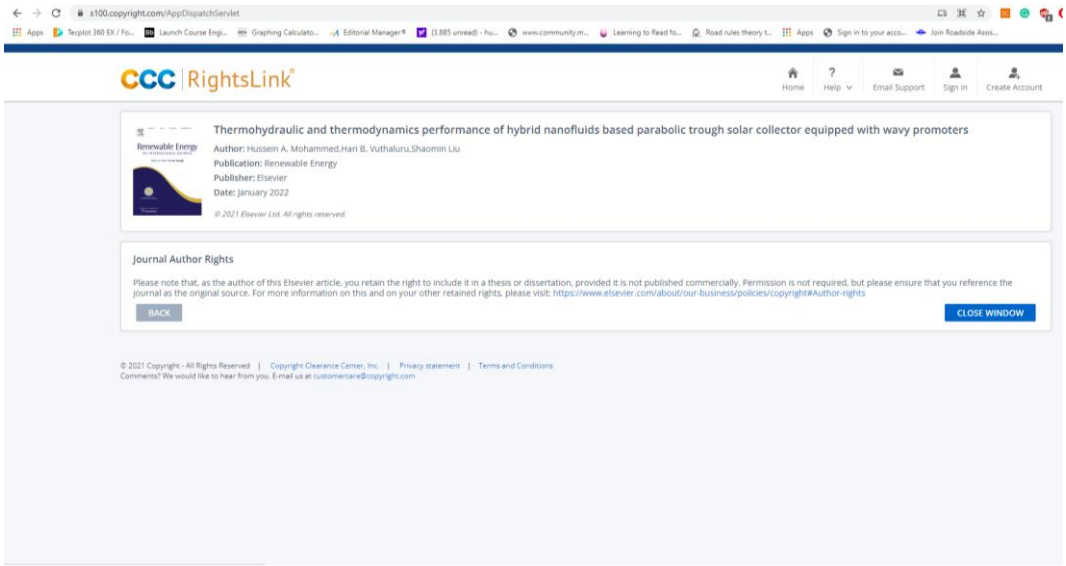

D. "Hussein A. Mohammed, F. Fathinia, Hari B. Vuthaluru, Shaomin Liu, CFD based Investigations on The Effects of Blockage Shapes on Transient Mixed Convective Nanofluid Flow over a Backward Facing Step, *Powder Technology*, Vol. 345, pp.608-620, 2019.